Multi-level modeling of gold nanoparticles in various environment : a theoretical approach

Rika Tandiana

To cite this version:

Rika Tandiana. Multi-level modeling of gold nanoparticles in various environment : a theoretical approach. Theoretical and/or physical chemistry. Université Paris-Saclay, 2022. English. NNT : 2022UPASF059 . tel-04010768

HAL Id: tel-04010768
https://theses.hal.science/tel-04010768

Submitted on 2 Mar 2023

Multi-level Modeling of Gold Nanoparticles in Various Environments: A Theoretical Approach

Modélisation multi-échelle de nanoparticules d'or dans divers environnements : une approche théorique

Thèse de doctorat de l'université Paris-Saclay

École doctorale n° 571 : sciences chimiques : molécules, matériaux,
instrumentation et biosystèmes (2MIB)
Spécialité de doctorat: Chimie
Graduate School : Chimie, Référent : Faculté des sciences d'Orsay

Thèse préparée à l'**Institut de Chimie Physique** (Université Paris-Sacay, CNRS),
sous la direction de **Carine CLAVAGUERA**, Directrice de recherche,
et le co-encadrement de **Van-Oanh NGUYEN-THI**, Maîtresse de conférences

Thèse soutenue à Paris-Saclay, le 21 septembre 2022, par

Rika TANDIANA

Composition du jury

Talal MALLAH Professeur, Université Paris-Saclay	Président
Jérôme CUNY Maître de conférences (HDR), Université Paul Sabatier Toulouse	Rapporteur & Examinateur
Tzonka MINEVA Directrice de recherche, CNRS-Institut Charles Gerhardt	Rapporteur & Examinatrice
Jean-Philip PIQUEMAL Professeur, Sorbonne Université	Examinateur
Stephan STEINMANN Chargé de recherche, CNRS-ENS de Lyon	Examinateur
Carine CLAVAGUERA Directrice de recherche, CNRS/Université Paris-Saclay	Directrice de thèse

THESE DE DOCTORAT

NNT : 2022UPASF059

ÉCOLE DOCTORALE
Sciences Chimiques : Molécules, Matériaux, Instrumentation et Biosystèmes (2MIB)

Titre: Modélisation multi-échelle de nanoparticules d'or dans divers environnements : une approche théorique

Mots clés: Analyse vibrationelle, Dynamique électronique, Analyse topologique, Nanoparticules, Réactivité, Champs de force polarisables

Résumé: Les nanoparticules d'or (GNP) sont des matériaux prometteurs dans divers domaines de recherche, grâce à leurs propriétés chimiques, physiques et optiques accordables. Leur complexité peut être en partie attribuée aux interactions dynamiques avec les ligands de surface et le solvant. Ainsi, une compréhension précise de ces interactions dynamiques permettrait de concevoir de manière rationnelle des matériaux aux propriétés souhaitées. Alors que diverses techniques spectroscopiques ont été largement utilisées dans ce but, les approches computationnelles se sont avérées être elles aussi des méthodes puissantes pour fournir des informations atomistiques importantes. Par conséquent, l'objectif de ce travail est d'utiliser des approches de calcul à plusieurs niveaux pour comprendre l'interaction des GNP avec divers environnements.

Tout d'abord, l'interaction interfaciale de l'eau sur une série de GNP de taille croissante a été systématiquement sondée par dynamique moléculaire classique et des méthodes semi-empiriques. Les propriétés structurelles de la première couche de solvatation ont été étudiées à l'aide de la durée de vie de relaxation orientationnelle, des fonctions de distribution radiale et de l'orientation des molécules d'eau. Ces analyses ont montré un réarrangement des molécules d'eau pour former un réseau de liaison hydrogène 2D étendu lorsque la taille de la GNP augmente. La densité d'états vibrationnels calculée pour la première couche de solvatation a mis en évidence un déplacement vers le bleu des modes d'étirement OH par rapport à la gouttelette d'eau, ce qui confirme l'observation d'un réarrangement du réseau de liaisons hydrogène.

Malgré ces résultats intéressants, le champ de forces utilisé pour cette étude présente des limitations, en particulier l'absence de terme de polarisation. Par conséquent, nous avons implémenté le champ de forces GAL, récemment développé pour les interactions entre l'eau et les surfaces métalliques, dans le logiciel Tinker pour permettre le couplage avec le champ de forces polarisable AMOEBA. Nos résultats ont souligné une excellente description des effets à n-corps lorsque nous avons incorporé les interactions eau-eau. En outre, la stabilité de l'implémentation a été testée dans les ensembles NVT et NPT. D'autres propriétés structurelles issues de la dynamique sont comparées aux données de référence.

En plus de l'eau, la dynamique de l'interaction entre la GNP et les ligands de surface est importante. Par conséquent, l'adsorption de molécules organiques sur la GNP a été systématiquement étudiée en DFT. Tout d'abord, la géométrie d'une série de composés aromatiques substitués adsorbés sur Au32 a été optimisée. Des analyses topologiques ont été réalisées pour identifier multiples interactions non covalentes. Les analyses de décomposition de l'énergie ont montré que les interactions électrostatiques et dispersives étaient les principaux contributeurs. Enfin, des analyses vibrationnelles ont été réalisées pour étudier comment l'adsorption sur la GNP affecte la spectroscopie infrarouge des composés organiques. L'information sur l'orientation du cycle aromatique peut être déduite de la variation de l'intensité des modes d'étirement CH. De plus, nous avons trouvé qu'il y a un effet limité de la taille de la GNP sur l'énergie d'interaction. Ensuite, avec l'acide benzoïque comme cas d'étude, nous avons comparé qualitativement les spectres infrarouges et Raman obtenus par l'expérience.

Enfin, nous avons utilisé la méthode DFT dépendante du temps en temps réel pour étudier une propriété importante des systèmes sous irradiation, le pouvoir d'arrêt électronique. Nous avons évalué sa sensibilité aux bases atomiques utilisées et des grandes bases, capables de décrire l'état de continuum, ont été générées. Avec un modèle d'eau, nous avons évalué l'efficacité de ces bases pour obtenir une courbe du pouvoir d'arrêt comparable à celles obtenues par des méthodes d'onde plane et une approche empirique.

ÉCOLE DOCTORALE
Sciences Chimiques: Molécules,
Matériaux, Instrumentation
et Biosystèmes (2MIB)

Title: Multi-level Modeling of Gold Nanoparticles in Various Environments: A Theoretical Approach

Keywords: Vibrational Analysis, Electron Dynamics, Topological Analysis, Nanoparticles, Reactivity, Polarizable Force Fields

Abstract: Gold Nanoparticles (GNP) are promising materials across various research fields, thanks to their tunable chemical, physical, and optical properties. The complexity of GNP systems can be partly attributed to the dynamic interactions with surface ligands and the solvent. Therefore, with the precise understanding of these dynamic interactions, a rational design of materials with desired properties would be achievable. While various spectroscopic techniques have been widely employed for this effort, computational approaches have been proven to be powerful methods to provide important atomistic insights. Therefore, the objective of this work is to employ multi-level computational approaches to understand the interaction of GNPs with various environments.

Firstly, the interfacial interaction of water on a series of increasing-size GNP has been systematically probed with classical molecular dynamics and semi-empirical methodologies. The structural properties of the first solvation shell have been investigated with orientational relaxation lifetime, radial distribution functions, and orientations of water molecules. These analyses have suggested re-arrangement of the water network to form an extended 2D hydrogen bond network as the size of GNP increases. The computed vibrational density of states of the first solvation shell of the GNP series has highlighted a blue shift of OH stretching modes in comparison with the water droplet, which further supported the observation of re-arrangement of the hydrogen-bond network.

Despite the interesting results obtained, there are still limitations in the forcefield used for this study, in particular the absence of polarization term. Therefore, we have implemented GAL forcefield, *i.e.* a recently developed forcefield for water-metal surfaces interactions, in Tinker software to allow the coupling with the polarizable AMOEBA forcefield. Our result suggested an excellent description of many-body effects as we incorporated water-water interactions. In addition, the stability of the implementation has been tested in both NVT and NPT ensembles. Further structural properties from the dynamics are compared with reference data.

In addition to water molecules, the dynamics of interaction between GNP and surface ligands is important. Therefore, the adsorption of organic molecules on GNP has been systematically investigated at the DFT level. Firstly, the geometry of a series of substituted aromatic compounds adsorbed on Au32 has been optimized. Topological analyses have subsequently been performed to identify the formation of multiple non-covalent interactions with varied strengths. The energy decomposition analyses suggested that the electrostatic and dispersive interactions were the main contributors to the interaction. Vibrational analyses were lastly performed to investigate how the adsorption on GNP affects the infrared spectroscopy of the organic compounds. Interestingly, the information on the orientation of the aromatic ring can be deduced from the variation in the intensity of the CH stretching modes of the phenyl ring. Moreover, we have systematically found that there is minimal effect of the size of GNP on the interaction energy with a series of small organic molecules. Afterwards, with benzoic acid as a case study, we have qualitatively compared the obtained infrared and Raman spectra with experiments.

Lastly, we have employed the real-time time-dependent DFT method to study an important property of systems under irradiation, *i.e.* the electronic stopping power. We evaluated the sensitivity of stopping power with respect to the basis sets used to describe the molecules. In this study, large basis sets, capable of describing continuum state, have been generated. With water cluster as the model system, we have evaluated the effectiveness of these basis sets in obtaining the curve of stopping power that is comparable to the plane-wave methods and the semi empirical approach.

Multi-level Modeling of Gold Nanoparticles in Various Environments: A Theoretical Approach

Modélisation multi-échelle de nanoparticules d'or dans divers environnements : une approche théorique

Thèse de doctorat de l'université Paris-Saclay

École doctorale n° 571 : sciences chimiques : molécules, matériaux, instrumentation et biosystèmes (2MIB)
Spécialité de doctorat: Chimie
Graduate School : Chimie, Référent : Faculté des sciences d'Orsay

Thèse préparée à l'**Institut de Chimie Physique** (Université Paris-Saclay, CNRS),
sous la direction de **Carine CLAVAGUERA**, Directrice de recherche,
et le co-encadrement de **Van-Oanh NGUYEN-THI**, Maîtresse de conférences

Thèse soutenue à Paris-Saclay, le 21 septembre 2022, par

Rika TANDIANA

Talal MALLAH Professeur, Université Paris-Saclay	Président
Jérôme CUNY Maître de conférences (HDR), Université Paul Sabatier Toulouse	Rapporteur & Examinateur
Tzonka MINEVA Directrice de recherche, CNRS-Institut Charles Gerhardt	Rapporteur & Examinatrice
Jean-Philip PIQUEMAL Professeur, Sorbonne Université	Examinateur
Stephan STEINMANN Chargé de recherche, CNRS-ENS de Lyon	Examinateur
Carine CLAVAGUERA Directrice de recherche, CNRS/Université Paris-Saclay	Directrice de thèse
Van-Oanh NGUYEN-THI Maîtresse de conférences, Université Paris-Saclay	Co-encadrante de thèse
Fabien CAILLIEZ Maître de conférences, Université Paris-Saclay	Invité

Acknowledgments

This PhD journey would not have been possible if not for the different people who have been there at every step, regardless of them being physically here or not. First of all, I would like to express my gratitude to Carine, for her constant guidance and support, despite all the crazy and irrational ideas I had throughout the three years. Also, for the constant encouragement and challenges that help me grow as a researcher and as a person. I would also like to thank Van-Oanh for her guidance during this time as well. Many thanks to the collaborators who have assisted and contributed to the research works that are reported here: Cécile Sicard-Roselli, Aurélien de la Lande, Stephan Steinmann, Paul Clabaut, Dominik Domin. Also for the internship students, who have also participated enthusiastically in the research works: Judith, Marine, Sylvain, Cécile, and Nitik. I am forever grateful for all of them. I am thankful for each of the members of jury for making time to be part of my thesis defense, and in particular Fabien and Talal who have followed my research progress for the past three years. Their advice and suggestions have been highly appreciated.

I am also very grateful for all of the members of Théosim group, who have created the warm and welcoming culture daily. I have greatly enjoyed their company during lunch time, coffee time, and after work gatherings. I consider myself to be very lucky to be a part of this group.

Lastly, I would like to thank my family, who have consistently provided emotional support during the three years. And my friends, who have always been there to listen and to encourage me, Marija, Riya, Gilbert, Diana, Diaz, Nacho, Jed, Marija, and Divya. Also to everyone else whom i have met during my stay in France, many thanks for all the support.

Synthèse en français

Les nanoparticules d'or (GNPs) sont des matériaux prometteurs dans divers domaines de recherche, grâce à leurs propriétés chimiques, physiques et optiques accordables. Leur complexité peut être en partie attribuée aux interactions dynamiques avec les ligands de surface et le solvant. Ainsi, une compréhension précise de ces interactions dynamiques permettrait de concevoir de manière rationnelle des matériaux aux propriétés souhaitées. Alors que diverses techniques spectroscopiques ont été largement utilisées dans ce but, les approches computationnelles se sont avérées être elles aussi des méthodes puissantes pour fournir des informations atomistiques importantes. Par conséquent, l'objectif de ce travail est d'utiliser des approches de calcul à plusieurs niveaux pour comprendre l'interaction des GNPs avec divers environnements.

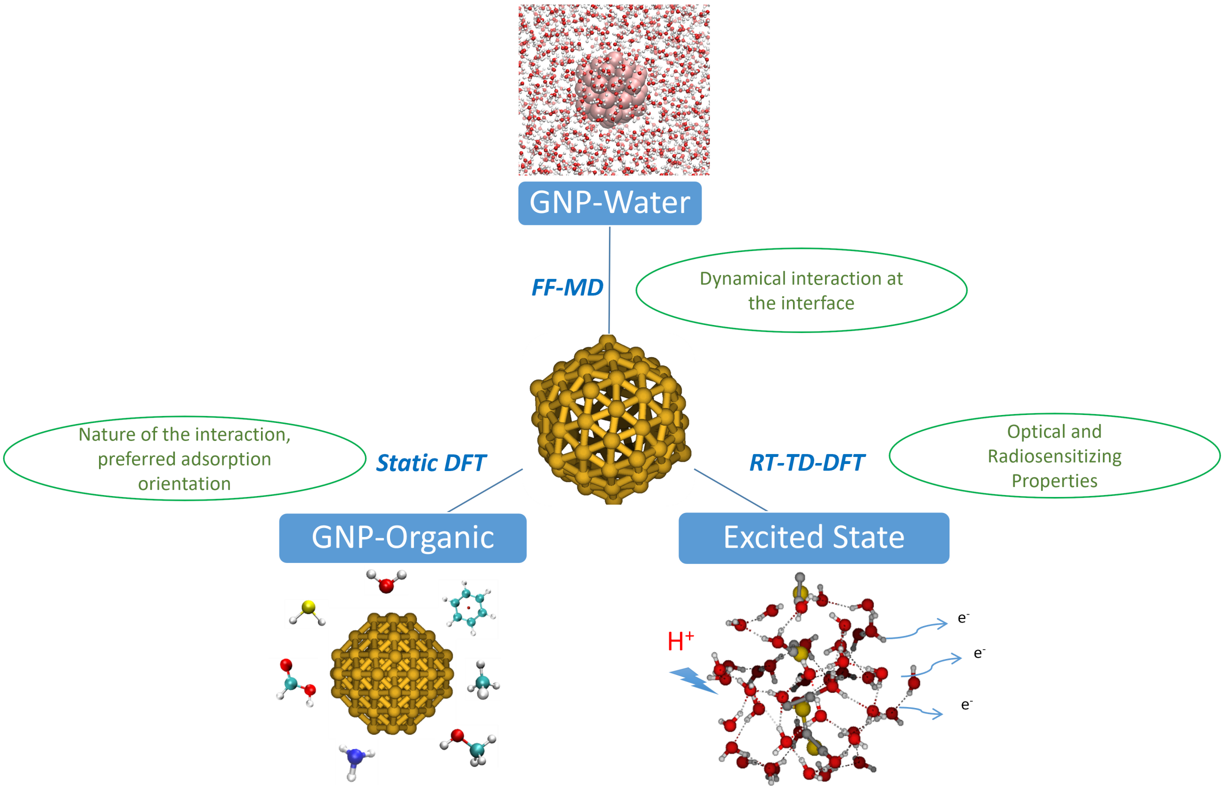

Figure 1: Représentation schématique des objectifs de la thèse utilisant différents niveaux de méthodes de calcul pour étudier des propriétés spécifiques d'intérêt.

Tout d'abord, l'interaction interfaciale de l'eau sur une série de GNP de taille croissante a été systématiquement sondée par dynamique moléculaire classique et des méthodes semi-empiriques. Les propriétés structurales de la première couche de solvatation ont été étudiées à l'aide de la durée de vie de relaxation orientationnelle, des fonctions de distribution radiale et de l'orientation des molécules d'eau.

Ces analyses ont montré un réarrangement des molécules d’eau pour former un réseau de liaison hydrogène étendu à deux dimensions lorsque la taille de la GNP augmente. La densité d’états vibrationnels calculée pour la première couche de solvatation a mis en évidence un déplacement vers le bleu des modes d’étirement OH par rapport à la gouttelette d’eau, ce qui confirme l’observation d’un réarrangement du réseau de liaisons hydrogène.

Malgré ces résultats intéressants, le champ de forces utilisé pour cette étude présente des limitations, en particulier l’absence de terme de polarisation pour traiter les effets à n-corps. Par conséquent, nous avons implémenté le champ de forces GAL, récemment développé pour les interactions entre l’eau et les surfaces métalliques, dans le logiciel Tinker pour permettre le couplage avec le champ de forces polarisable AMOEBA. Nos résultats ont souligné une excellente description des effets à n-corps lorsque nous avons incorporé les interactions eau-eau. En outre, la stabilité de l’implémentation a été testée dans les ensembles NVT et NPT. D’autres propriétés structurelles issues de la dynamique sont comparées aux données de référence.

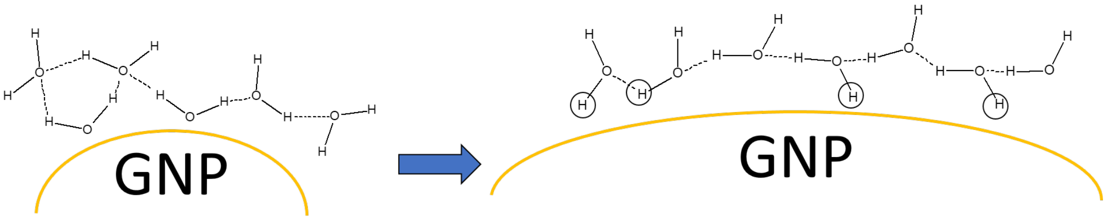

Figure 2: Schéma représentant le réarrangement du réseau des molécules d’eau en présence de GNP de tailles croissantes.

En plus de l’eau, la dynamique de l’interaction entre la GNP et les ligands de surface est importante. Par conséquent, l’adsorption de molécules organiques sur la GNP a été systématiquement étudiée en DFT. Tout d’abord, la géométrie d’une série de composés aromatiques substitués adsorbés sur Au32 a été optimisée. Des analyses topologiques ont été réalisées pour identifier multiples interactions non covalentes. Les analyses de décomposition de l’énergie ont montré que les interactions électrostatiques et dispersives étaient les principaux contributeurs. Enfin, des analyses vibrationnelles ont été réalisées pour étudier comment l’adsorption sur la GNP affecte la spectroscopie infrarouge des composés organiques. Par exemple, l’information sur l’orientation du cycle aromatique peut être déduite de la variation de l’intensité des modes d’étirement CH. De plus, nous avons trouvé qu’il y a un effet limité de la taille de la GNP sur les valeurs de l’énergie d’interaction. Ensuite, avec l’acide benzoïque comme cas d’étude, nous avons comparé qualitativement les spectres infrarouges et Raman obtenus par l’expérience.

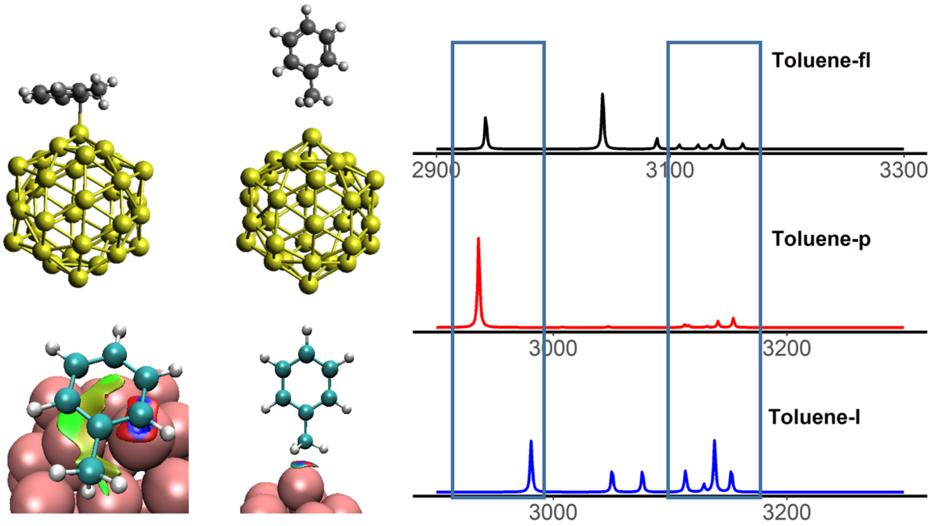

Figure 3: Interaction entre les composés aromatiques substitués et la GNP, sondée par analyse topologique et analyse vibrationnelle.

Enfin, nous avons utilisé la méthode DFT dépendante du temps en temps réel pour étudier une propriété importante des systèmes sous irradiation, le pouvoir d'arrêt électronique. Nous avons évalué sa sensibilité aux bases atomiques utilisées et des grandes bases, capables de décrire l'état de continuum, ont été générées. Avec un modèle d'eau, nous avons évalué l'efficacité de ces bases pour obtenir une courbe du pouvoir d'arrêt comparable à celles obtenues par des méthodes d'onde plane et une approche empirique.

Les travaux rapportés dans cette thèse ont démontré l'apport des simulations multi-échelles à la compréhension de l'interaction entre les GNP et leur environnement chimique. Cette étude ouvre les portes vers de nombreuses perspectives tant du côté du développements de méthodes théoriques que du côté des applications à la spectroscopie vibrationnelle et aux outils d'apprentissage automatique.

Contents

Chapter 1

INTRODUCTION

Contents

Gold Nanoparticles (GNP) have been a material of choice across many different fields of applications, such as catalysis, sensors, biomedicals, drug delivery, nanomedicines, cancer treatment, among many others. These widespread applications have been made possible thanks to the unique optical and physical properties exhibited by GNP of various size and shape. Moreover, GNP can be easily conjugated with functionalizing agents, such as drugs, DNA, proteins, surfactants, etc., further expanding and improving their potential applications. The scientific interests in its applications in biomedical fields are rapidly increasing. Figure 1.1 gives an illustration on the different possible functional groups that could be added on the surface, and their potential applications in different medical applications.

The highly tunable properties of GNP can be attributed to the variability of the size and shape of GNP and the interactions with the surface ligands. The GNP prepared in the laboratory are increasingly more sophisticated, as shapes like nanorods, nanostars, nanopyramids, nanocages, nanoshells have been successfully prepared and characterized. Each of this shape exhibits unique physical, and optical properties, and additionally toxicity profile. As an example, gold nanorods have been shown to exhibit two modes of plasmonic behavior that absorb at two different wavelengths, *i.e.* transversal and longitudinal modes. As the length of the rod increases, a red shift in one of the modes towards the near IR range in the plasmonic behavior is observed.[1] This red shifted absorption is desirable for the biomedical application in either imaging or photothermal therapy, as infrared can penetrate through biological tissues. Additionally, the plasmonic activity of GNP has been shown to induce the dissociation of H_2 and D_2, forming HD.[2] As a potential drug carrier agent, GNP have been functionalized with poly-ethylene glycol to avoid being eliminated by mononuclear phagocytic system (MPS), allowing it to reach the targeted site inside the body.[3] This functionalization of course has a significant impact on the physical and optical properties of GNP. Yet in another application, where GNP has been used as radiosensitizers, the presence of surface ligand might trap the secondary electrons induced by irradiation, thus lowering the radiosensitizing effect.

All these examples highlight the importance of the interaction between GNP and the ligands at the surface. Another additional contributing factor is the solvation effect, that cannot be ignored. Solvent molecules provide competitive interaction between GNP-solvent and GNP-ligand, and also ligand-solvent, providing another layer of complexity to the interaction. Experimental investigations have been proven quite challenging to provide such atomistic interactions, whereas computational tools can provide valuable insights. The understanding of the interactions can eventually lead to rational design and synthesis of GNP with desired properties. In the following section, the current computational approaches that have been employed to study either gold surfaces and GNP are being reviewed.

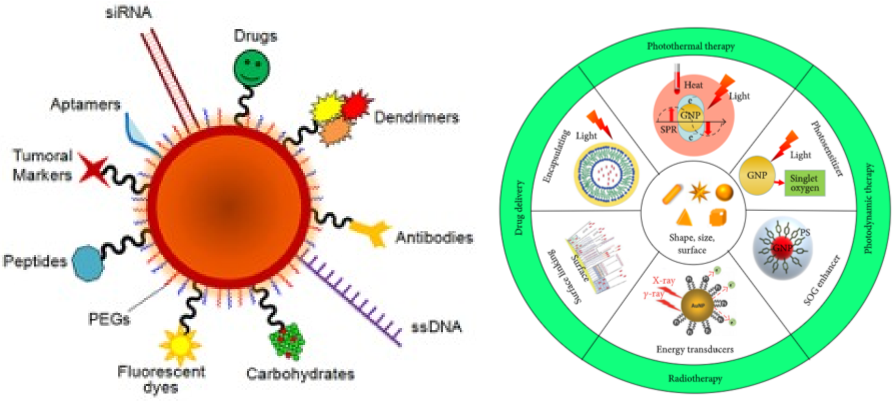

Figure 1.1: The schematic illustration of multifunctionalized GNP[4] (left) and their possible application in biomedical fields[5] (right)

1.1 Literature Review

We will start our literature review by discussing the different experimental approaches taken to study the interaction at the interface of GNP. With the advancement in the surface sensitive spectroscopy techniques, there is an increasing amount of research efforts directed at the study of the interaction at the interface of GNP, to answer the question on the orientation of molecules or the number of binding sites on GNP, among many other interesting questions.[6–8]

Figure 1.2 illustrates the different in-situ experimental techniques along with the different questions to be solved, adapted from a review article by Xue *et al.*.[9]

Iosin *et al.* have employed surfaced enhanced Raman spectroscopy (SERS) to investigate the interaction between protein and GNP, and to localize the molecular group responsible for the interaction.[10] Another study employing SERS technique has focused on the protein aggregation process as a function of temperature and solvent.[11] The surface enhanced hyper-Raman scattering (SEHRS), a non-linear analogue of SERS, has been used to probe the adsorption geometry of amino acids, DNA bases, on GNP.[12–15] The authors have observed that SERS and SEHRS techniques have different selection rules, and comparing the two spectra allows an accurate interpretation of the orientation of the ligands adsorbed at the surface of metal nanoparticles. Based on the SERS and SEHRS, the authors reported a different adsorption geometry of thiophenol on the surface of GNP and AgNP.

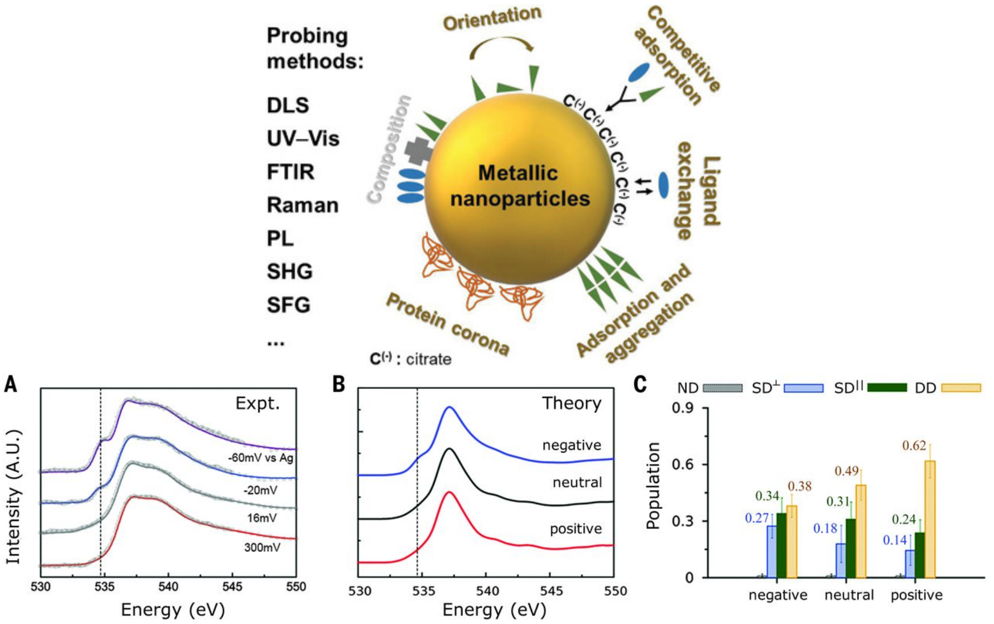

Figure 1.2: (top)The schematic illustration of different experimental techniques to characterize the surface of metal nanoparticles[9] ; (bottom) Comparison between experimental (A) and calculated (B) X-Ray Absorption Spectroscopy for quantifying the orientation of water molecules on the surface of charged and neutral gold surfaces (C).[16]

In another study, reflection-absorption infrared spectroscopy (RAIRS) has also been used to probe the halogenated benzene adsorbed on Copper surfaces ([111] and [110] surfaces), and how the substituent affects the orientation.[17] Terahertz (THz) spectroscopy and sum-frequency vibrational spectroscopy have also been increasingly used to especially probed the collective translational and librational motions of hydrogen bond network at the vicinity of GNP.[18] In another article, X-ray absorption (XAS) has been employed to study and quantify the distribution of water structure and the hydrogen bond network at the interface of gold electrode (see Figure 1.2).[16]

Meanwhile, there is an increasing number of works reported with computational approaches at various scales providing important insight into interaction at the interface of GNP. Some works have also combined experimental and theoretical approaches to probe GNP interactions with various molecules.[19–22] For the following sections, the reported works will be grouped into three main categories based on the computational approaches applied, which are the molecular dynamics approach, focusing on the study of dynamic processes of ligands and solvents on the surface, the static electronic structure calculation, focusing on the study of the electronic properties of the interaction for example for catalytic properties, and lastly the calculation of GNP in excited state, mainly to study the plasmonic properties and radiosensitizing properties of GNP.

1.1.1 Molecular Dynamics Methods

The dynamical interaction of surface ligands, such as organic molecules, polymers, proteins, and ions, with the surface of GNP, and also with solvent molecules can be captured with molecular dynamics (MD) method. The delicate balance between the competing interaction of surface-ligand, surface-solvent, and ligand-solvent is important for prediction of the properties of GNP. MD simulations offer atomistic outlook on the time evolution of the interactions, which can provide valuable insights into the underlying processes. The theoretical foundation of MD simulations is explained thoroughly in Chapter 2. For introductory and clarity purposes, MD simulations are performed with classical treatment of the atomic nuclei, and the trajectories of the atoms are accumulated by solving Newton's equation of motion for each atoms. The potential energy and the forces associated to the atoms can be calculated at different levels of computation, depending on the desired accuracy, and the properties of interest.

For high accuracy in computations of the potential energy and forces, quantum level of theory will be necessary, and among which, DFT method is gaining increasing popularity due to the balance between accuracy and computational cost. However, the computational cost is still prohibitively high, which results in the limitation in the size of the system (number of atoms) and the simulation time (usually in the picosecond time scale). To reduce the computational cost and hence, accelerating the calculations, different levels of approximations can be introduced. Firstly, the semi-empirical method, among which is the tight-binding approach (DFTB), has recently been increasingly employed. The Hamiltonian of the interacting atom pairs is stored as a parameter file, that is derived from DFT calculation by using minimal basis set.[23] As such, this computational level can reach high level of accuracy, and important electronic effects (such as charge transfer and polarization) are still explicitly treated. With DFTB, the computational cost is significantly reduced as compared to DFT, and hence expanding the limit of the system size and simulation time (up to a few nanoseconds time scale). The limitation of such method will be the availability of atom pair specific parameters.

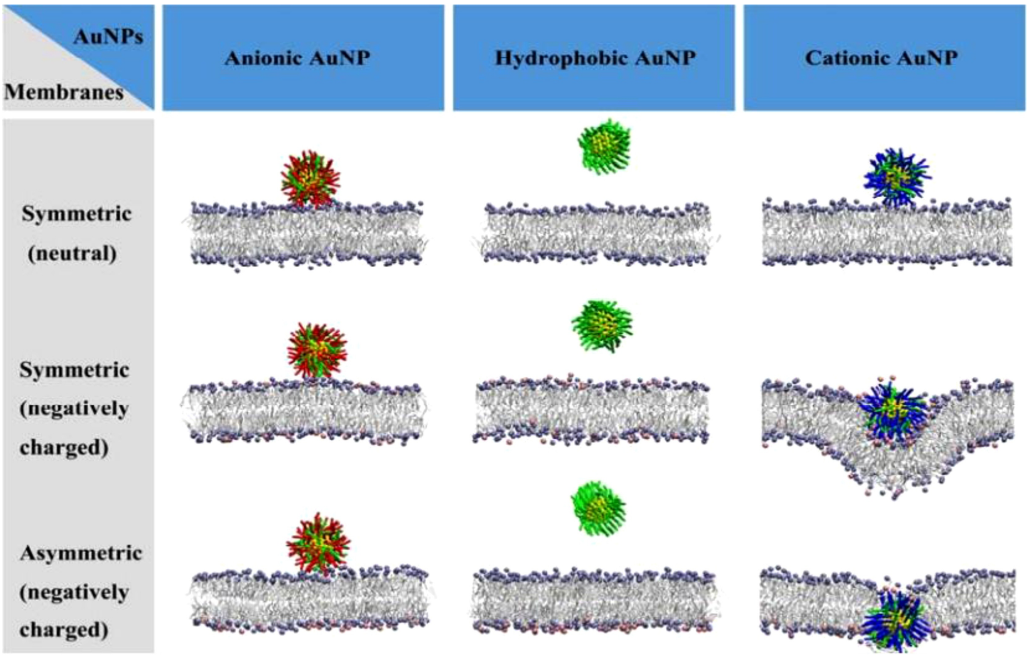

Figure 1.3: The coarse-grained approach to investigate the translocation of GNP through membrane in different conditions.[24]

Considering that GNP have been increasingly used in biomedical contexts, as demonstrated earlier in the chapter, the interaction between GNP and various biomolecules and in various biological processes have to be considered. Many biological processes span across different time scales and it can reach up to seconds, for example protein folding or protein reorganization on GNP surfaces can vary from a few nanoseconds up to hundreds of nanoseconds, and translocations of drug functionalized GNP across a membrane (see Figure 1.3)[24], which can take between minutes and hours. Moreover, both GNP and biomolecules usually contain large number of atoms, up to hundreds of thousands of atoms in total. Therefore, these events cannot be observed neither with the quantum level nor the semi-empirical level of calculations. To enable such large scale simulation, other levels of approximation for the calculation of potential energy, called atomic force field and coarse grained model, have been developed.

In force field model, the potential energy information is stored in atom-type specific parameters and then computed with a mathematical function. Within this model, the molecules are considered as collection of balls connected with a spring, and the electronic information is not explicitly treated. But, the gain in the computational acceleration enables the simulation of large biomolecules over a longer period of simulation time (up to microsecond time scale). In coarse grained model, molecules are grouped together as beads during the potential energy calculation. As a result, the individuality of the atoms is replaced by group-based parameters. However, sometimes such approximation is necessary to allow simulations of processes that involve large systems, for example in the study of formation of protein corona on GNP, which is a critical aspect for its application in nanomedicine.[25] An important limitation of these models is that processes requiring explicit electron treatment cannot be simulated, such as bond forming and breaking processes, charge transfer, among many others. To overcome this limitation, a reactive force field (Reax-FF) has recently been introduced that allows the simulation of bond formation and bond breaking.[26] The parameters describing the gold-thiol systems have been proposed, and employed to study the adsorption of thiolated ligands on gold surfaces.[27–29]

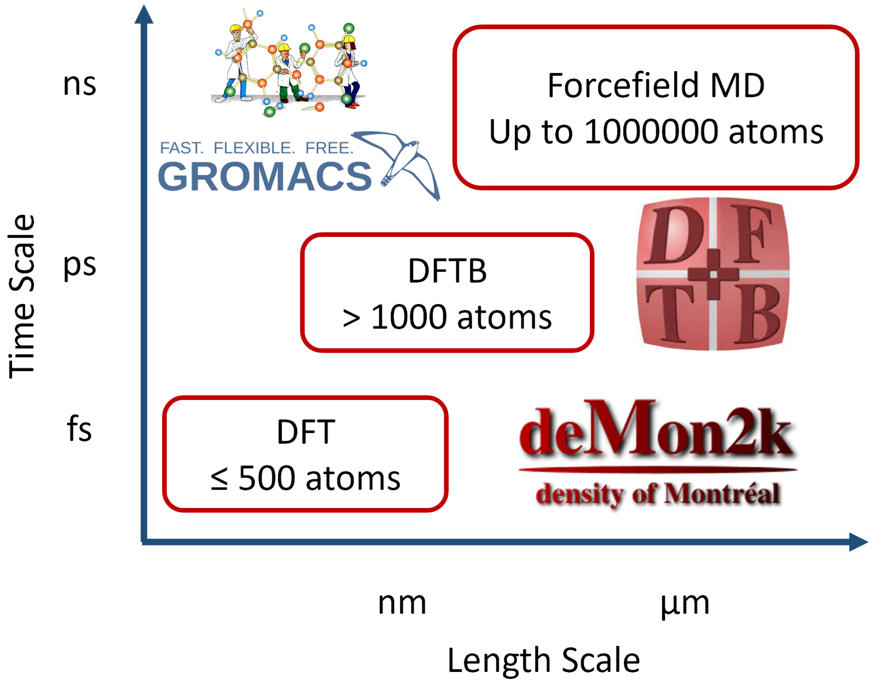

Figure 1.4: The comparison of the different computational levels used in this thesis with respect to the time and length scale of the systems of interest.

In the cases where the electronic effect is important, *i.e.* in the cases of gold electrodes, the utilization of ab-initio simulations might be inevitable. Alternatively, combination of the ab-initio and force field methodology, within a QM/MM framework, has been proposed and developed. In the framework, the ab-initio region (QM), where the important processes will be simulated, is surrounded by the molecular mechanic region (MM), where the environment will be simulated with the force field methods. This method has recently gained popularity, as it gives access to both the important processes requiring explicit electron treatment and also including the response of the environment to these processes. Hence, it brings us into a more realistic simulation and yet at a much lower computational cost as compared to the full ab-initio simulations. The challenge in this method is however, selecting the suitable boundary between the QM processes and the MM simulation. Despite the advantages that QM/MM methodology propose, it has not been used widely yet to simulate GNP interface.[30]

In short, the illustration of the relationship between the different calculation levels and the time and length scale is shown in Figure 1.4. In the following sections, the simulations of GNP based systems at different levels of MD simulations in the last few years are discussed.

1.1.1.1 DFT-MD

Since calculation at DFT level is associated with high computational cost, simulations of GNP at intermediate sizes (few nanometers in diameter) can be very costly. Furthermore, by employing plane wave approaches that are efficient in calculation of periodic surfaces, DFT-MD simulations of gold systems have been generally performed with gold [111] or [100] surface slabs, consisting of a few layers of gold atoms repeated in xy directions. Indeed, several publications have reported MD simulations on gold surfaces by employing this plane wave approach. Various investigations on the solvation structure of water molecules on neutral and charged surfaces, in the context of electrocatalysis and electrodes have been reported, whose electronic aspects of the interaction are crucial.[16,31–36] These researches have provided valuable insights not only into the water structure at the interface of neutral or charge gold surfaces, but also into the development of force field specific for Au-water interface.

Moreover, DFT-MD simulations have been used to investigate the interactions between oxygen atoms, CO, and CO_2, in the context of catalysis.[37–39] Yoo *et al.* have performed MD simulations to investigate the role of oxygen vacancy on the catalytic activity of gold nanocatalyst supported on reduced titania support (see Figure 1.5).[40] Upon a closer inspection on the band alignment diagram, they have concluded that the charge transfer occurs from Au cluster to the conduction band of TiO_2, and that the role of oxygen vacancy is indirect in nature. In short, the charge redistribution at the interface results in the increase in the reactivity of supported GNP.

On the contrary, there is a lesser amount of works in DFT-MD reported with GNP as the model, due to the reasons discussed previously. Additionally, there is no straightforward reason for any particular choice of size or shape of GNP as the model, other than when experimental results are available. Still, Darvish Ganji *et al.* have performed DFT-MD study to investigate the adsorption of several amino acids on the surface of Au_{32} and followed by the adsorption of nucleobases on Au_{13}. In these studies, they investigated the preferred adsorption mode of the small biomolecules on the surface of GNP, which is through either the amine or carbonyl functional groups for amino acid, and either through the N/O or the aromatic ring for nucleobases. Furthermore, the interaction is reported to be chemisorption by nature.[41,42] All in all, DFT-MD is not exactly the most popular tool to investigate the dynamical properties of gold interfaces, despite the high level of accuracy achieved and the detailed information on the electronic contribution.

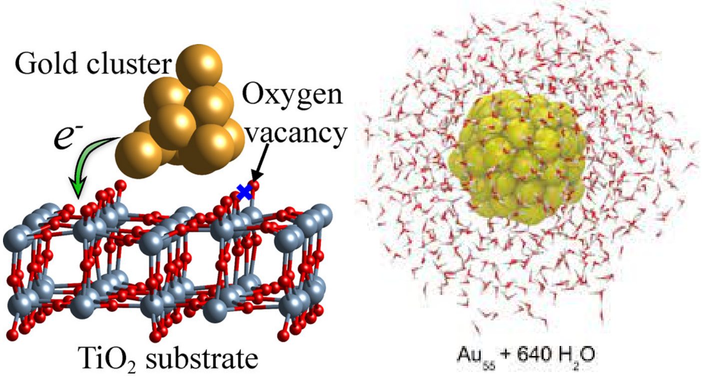

Figure 1.5: (left) The dynamic interaction between oxygen vacancy, gold cluster, and reduced titanium dioxide substrate, underlies the catalytic activity on oxidative reactions,[40] and (right) the schematic representation of Au_{55} surrounded by 640 water molecules in a cluster model.[43]

1.1.1.2 DFTB-MD

There are also reported works employing the semi-empirical level of MD simulations with tight binding approximation, as in DFTB method. At this level of simulation, an important bottleneck would be the development of highly accurate parameters for the atom pairs in the systems of interest. The parameters for gold thiolated systems, including the Au, S, C, H, N, and O atoms, have been reported by Fihey *et al.*.[44] The parameters describing the Au-Au interactions have subsequently been benchmarked for gold systems varying from cluster size to bulk systems.[45] This has led to the exploration and the detailed investigation on the electronic properties of different sizes and shapes of GNP.

In addition, Fazio *et al.* have used the reported parameters to perform DFTB-MD simulations to study the water structure at the interface of Au_{55} with cluster model (see Figure 1.6).[43] They reported an MD simulation performed for 20 ps for a system that includes 640 water molecules, for which the charge of GNP has been varied from 0 to +1 and to +2. Their objective is to investigate the dependence of the solvation structure on the charge. They have demonstrated that the orientation of water molecules residing at the first solvation shell is sensitive to the charge state, which is consistent with the observation from DFT-MD method discussed above. In another study, Domínguez-Castro *et al.* have investigated the interaction of peptides on the surface of Au$_{25}$, which represents the [111] facet. They have observed that the interaction was formed through the carboxylic functional group (see Figure 1.6).[46] Since phosphine-based ligand can be an alternative capping agent for GNP, the parameter describing the Au-P interaction has been recently reported, thus enabling the simulation of phosphine stabilized gold nanoclusters.[47]

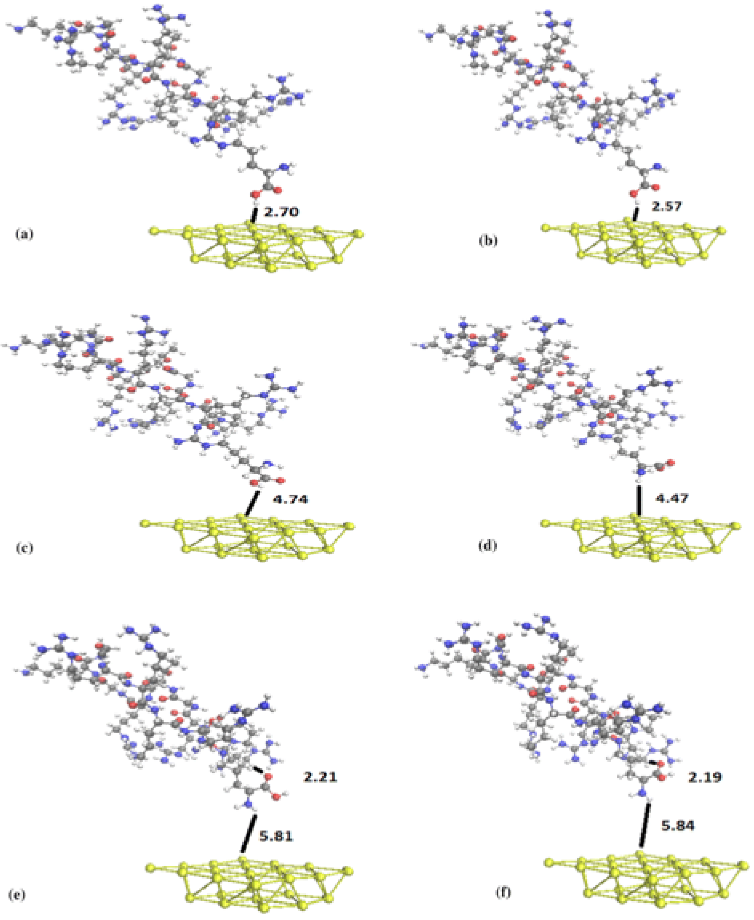

Figure 1.6: The DFTB-MD simulations of peptides interacting on gold [111] surface, highlighting the change in Au-peptide bond over time.[46]

Despite being a promising methodological tool, the major limitation for DFTB methodology is still the parameters development, firstly, and the transferability of the parameters, secondly. The Slakos parameters are usually stored for pair of the interacting atoms, and their derivation does not usually include the effect of the environment. Consequently, the parameter of the interactions can be system specific. Therefore, when the parameter is used in another system, the accuracy of the calculation might drop. There are constant efforts in improving the DFTB parameters, and one such approach relies on an artificial neural network to introduce energy correction for a particular interacting pair.[48,49]

1.1.1.3 Force Field-based MD

Force field-based MD (FF-MD) is a popular method of choice to study the interfacial interaction of gold surfaces and GNP. The strong scientific interest in the GNP materials has driven the development of force field specifically describing the interaction of gold surfaces with various molecules. Initially, the interaction has been described with various Lennard Jones (LJ) potentials, and the integration of the gold parameters within the different force fields available is straightforward.[50,51] The compatibility of the parameters with the existing biomolecular force field leads to their widespread use for the simulation of gold surfaces. The parameters developed by Heinz *et al.* have been fitted against experimental properties, *i.e.* surface tension and density, and they have been shown to perform well in simulating the interaction of gold surfaces with various molecules.[50] However, the simplistic approach to the interaction does not reflect accurately the underlying interaction, in particular the differentiation between physisorption and chemisorption, in addition to the contribution from polarization and charge transfer.

Thereafter, different force fields have been proposed, such as the GolP (Gold-protein) force field as proposed by Corni's group. The force field takes into account the polarization effect, chemisorption term, van der Waals interaction term (through LJ potential and addition of virtual sites), and an additional term for pi-conjugated systems.[52] Initial parameters have been fitted for models of amino acids and validated against a series of small organic molecules (*i.e.* alkanes, alkenes, toluene) adsorbed on Au [111] surface. The parametrization was performed for the interaction energy and optimal distance from the surface.

The force field was later extended to include the adsorption on Au [100] to allow investigation of facet-specific adsorption. The force field is compatible with CHARMM force field, and hence called GolP-CHARMM.[53] These force fields have been extensively used for studies involving amino acid, peptides, and proteins. Subsequently, the force field is further adapted to the interaction between Au [111] surface and DNA within AMBER force field framework.[54] Futera *et al.* later assessed the accuracy of the parameters for amino acid and introduced new Au-S bonding parameters that improve the description of S-linkages.[55] Biriukov and Futera later on investigated the adsorption geometry of amino acids at the interface of aqueous gold electrode (see Figure 1.7).[56] They observe that the external electric field has stronger influence for the positively charged than both the negatively charged and neutral amino acids, which also depends on the ability of these amino acids to penetrate the solvent layer to approach the surface. However, the adsorption geometry of water and all amino acids is found to be moderately perturbed by the applied electric fields.

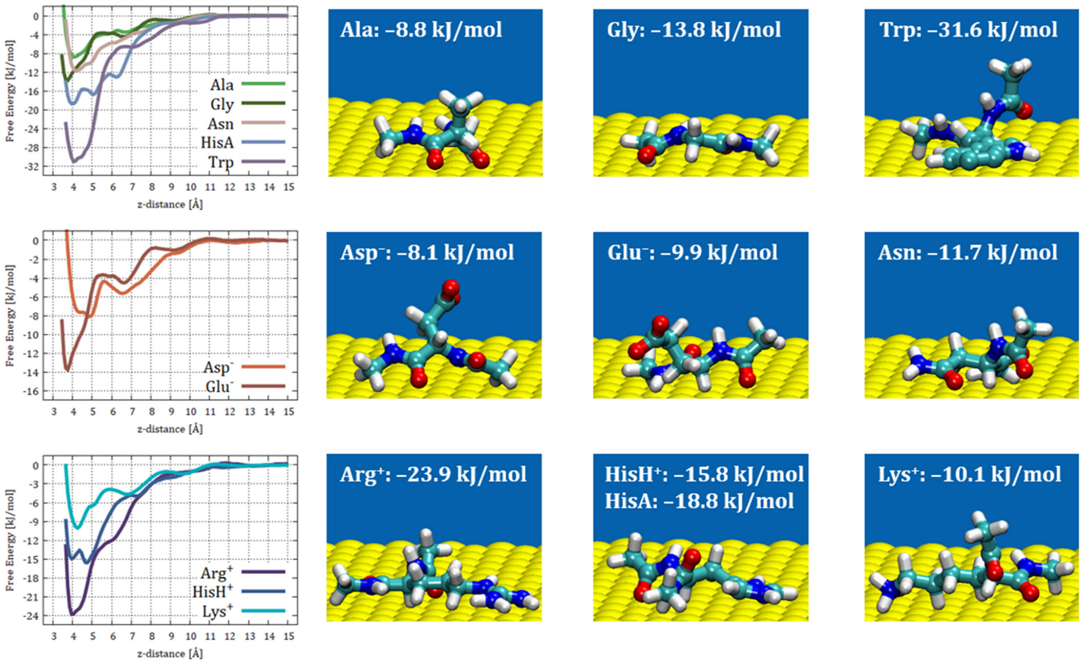

Figure 1.7: The adsorption free energy profile (left) and the representative configurations of amino acids (right) on zero-field condition as simulated with GolP-CHARMM FF by Futera *et al.*[56]

Focusing on the interaction between metal surfaces, both [100] and [111] facets, and water molecule, GAL force fields have been developed.[57,58] The functional form of GAL is different from the generally available force fields, and it will be discussed thoroughly in Chapter 2. GAL force field includes the angular dependence contribution in addition to the physisorption and chemisorption terms. The force field is able to replicate correctly the preferred orientation of water molecules on Au [111] surface obtained at DFT level. The force field has been demonstrated to reproduce well the interfacial water structure on metal surfaces, as well as alloy surfaces (see Figure 1.8).

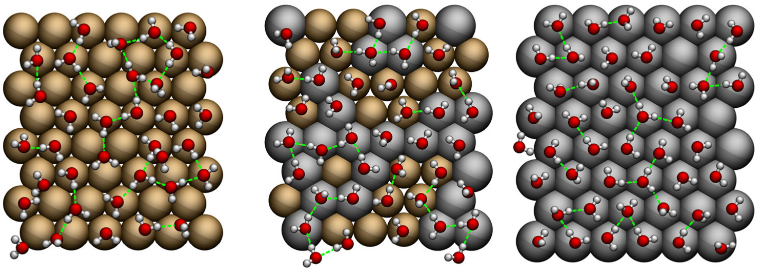

Figure 1.8: The structure of the first water layer adsorbed on Cu [111] (left), $Cu_{0.5}Ag_{0.5}$[111] (middle), and Ag[111] (right), taken from a snapshot of MD simulations with GAL force field.[58]

The interactions between gold surfaces and biomolecules have also been probed with force field-based MD simulations. Brancolini *et al.* have thoroughly investigated the interaction between ubiquitin, a ubiquitous protein in eukaryotes, and gold surfaces (see Figure 1.9).[59] They have found that the driving force for the interaction is dominated by the van der Waals interaction with smaller contribution from the electrostatic interactions, and the interaction is assisted by binding to citrate, a common surface ligand of GNP. The computational results have subsequently been found to agree with and to explain experimental observation.

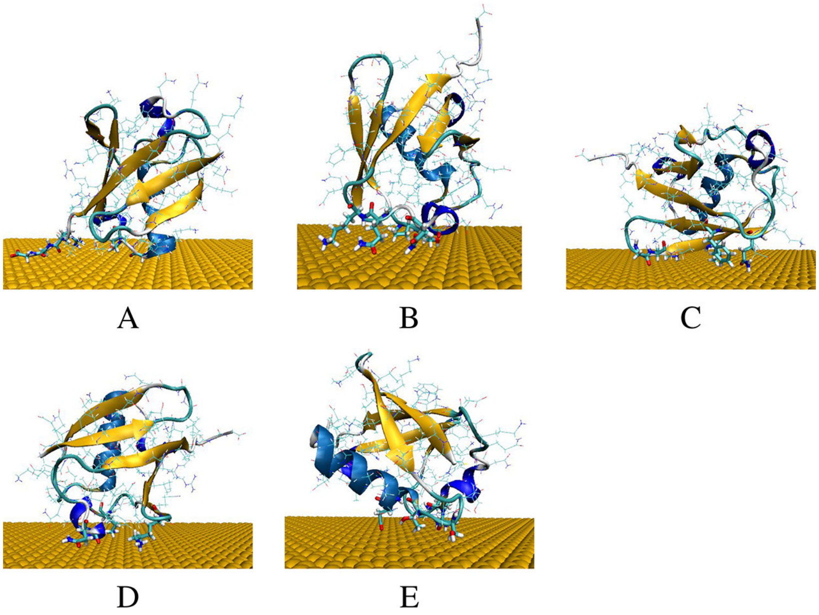

Figure 1.9: The most possible binding geometries of ubiquitin on bare gold surfaces as obtained with BD Docking, and serve as the starting geometry for MD simulations with GolP force field.[59]

The simulations of GNP systems have largely been carried out by employing one of these reported force fields, since the surface of GNP is represented by Au

[111] or [100] facets. The force field-based MD has generally been employed for a wide range of objectives, to investigate the water solvation of GNP of various sizes, shapes and in the presence of surface ligands,[60–63] to assess the binding preference of amino acids on GNP,[64] to investigate the adsorption of large biomolecules on GNP,[59,65–67] etc.

1.1.2 Static Approach: Electronic Structure Calculations

Besides molecular dynamics simulations, a large number of articles has been reported based on the static approach at DFT level of computation. The objective of the study mainly focuses on understanding the electronic aspect of the interaction and searching for the optimized geometries of molecules interacting at the surface. Similarly, the preferred model is usually the gold surfaces with either [111] or [100] facets, thanks to the efficiency of plane wave-based codes. Few articles have been reported to use intermediate sizes of GNP,[68] and most has been reported to study gold clusters as a representative model for GNP,[21,69] due to the computational cost associated with the calculation of gold systems. However, with the constant efforts in improving the computational architecture,[70] *i.e.* parallelization of the code and implementation in GPU, the size limit accessible to DFT computation is increasingly being expanded. Therefore, a rise in the computational study for intermediate sizes of GNP should be expected in the near future.

An important aspect of electronic structure calculation is the investigation of the reactivity of GNP. Gold has always been thought to be catalytically inert material, and the discovery of its catalytic activity at nanometer scale by Haruta *et al.* in 1987, has led to an explosion of interest in the material.[71,72] Different propositions have been made to understand the emergence of catalytic activity of GNP, such as the quantum confinement effect, presence of defects, or low-coordinated gold atoms at the surface of GNP, among others. Theoretical approaches can eventually help to provide atomistic details of the structural and electronic insights on the GNP. Haruta first discovered its activity in the oxidation of carbon monoxide, and thereafter, GNP has been shown to be active for other reactions as well, such as various carbon-carbon coupling reactions,[73] hydrogenation of the unsaturated hydrocarbons,[74] water-gas shift reaction,[75] etc.

The approach in probing the catalytic activity through computational tools usually involves firstly the evaluation of reactivity descriptors, *i.e.* Fukui function[76] (see Figure 1.10 top) or d-band analysis[77], and followed by the calculation of binding energy of the reactant of interest (include CO, O_2, H_2O, among others),[78] and lastly the calculation of reaction paths based on transition state theory[79]. In general, the calculations have agreed that the corners and edges of multi-faceted GNP, *i.e* atoms with low coordination number, exhibit higher reactivity and interact stronger with the reactants, highlighting the importance of defects on the surface. The calculations of gold clusters ranging between 65 to 8000 atoms, have also agreed with experimental observation that the reactivity decreases with the increasing size of the GNP, due to the diminishing number of atoms with low coordination number.[80] Additionally, theoretical insights can also provide detailed information on the reaction coordinate of catalytic pathway and the interaction with the supporting substrate to assess the catalytic activity of deposited GNP, for example charge transfer (see Figure 1.10 bottom).[79]

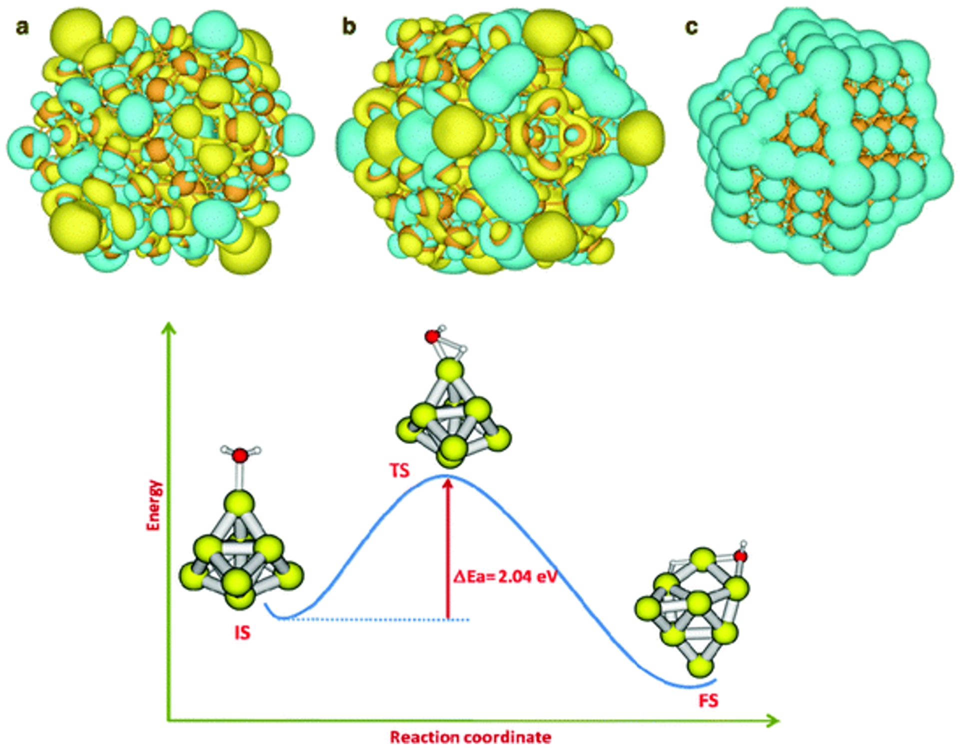

Figure 1.10: (top) The plot of HOMO (a), LUMO (b), and Fukui function (c) for radical attack of Au_{147}[76]; (down) The schematic representation of the catalytic pathway of water dissociation on gold cluster.[79]

Other computational studies have been directed towards rational design of GNP-based catalysts. Since, the electronic structure of GNP can be modified by introducing other metallic atoms, either as defects or in a core-shell structure, computational approaches provide an avenue for evaluating the reactivity before performing the catalytic tests. The modified electronic structure can then result in either favorable or not favorable change in the catalytic activity. Fang *et al.* have systematically investigated the stability and reactivity of the core shell structure of $Au_{32}M_6$, with M including Cu, Pt, Pd, Rh, and Ir, for the water-gas shift reaction.[81] With another approach, Cheng *et al.* have tuned the catalytic activity of the catalyst model of Au_{55} in CO oxidation, by introducing an increasing number of Pd atoms in the structure. They reported that $Au_{43}Pd_{12}$ has the highest reactivity among the other clusters considered.[82]

Furthermore, the static approach has also been used to study the adsorption behavior and the conformation adopted by different molecules on either gold surfaces or GNP, such as water molecule,[20,32,33,35,83,84] amino acids,[21,85,86] aromatic compounds,[19,69,87,88], and fatty acid.[89] These various studies have the objective of localizing the part of the molecules that interacts on the surface. For amino acids, the -C=O, -NH-, S, and aromatic side chain are generally found to be the anchoring functional groups.[21,85] In the case of the fatty acid, the carboxylic acid functional group is the moiety that forms interactions with the surface.[89]

The motivations of these studies are firstly to understand the possible binding sites of various biomolecules on GNP, and secondly to assist in the interpretation of experimental vibrational spectroscopy analysis, such as the surface sensitive IR and Raman methodologies. Yao *et al.* illustrated the synergistic between experimental and theoretical calculations of SERS spectra for cysteine adsorbed on GNP (see Figure 1.11).[21] For the DFT calculations, the GNP has been modeled by small gold clusters, such as Au$_5$, Au$_6$, Au$_8$, and Au$_{10}$. The simulated spectra of different conformations of cysteine are then compared with the experimental data. Across the different sizes of gold clusters, the interactions are formed through both S and O sites, with minimal effect from the size and shape of the cluster. This insensitivity of vibrational spectra on the size and shape of gold clusters has also been reported by Prakash *et al.* for their study on the adsorption of imidazole.[69] They proposed that gold clusters, such as Au$_8$, Au$_{10}$, and Au$_{20}$ are good models to represent Au [111] surfaces.

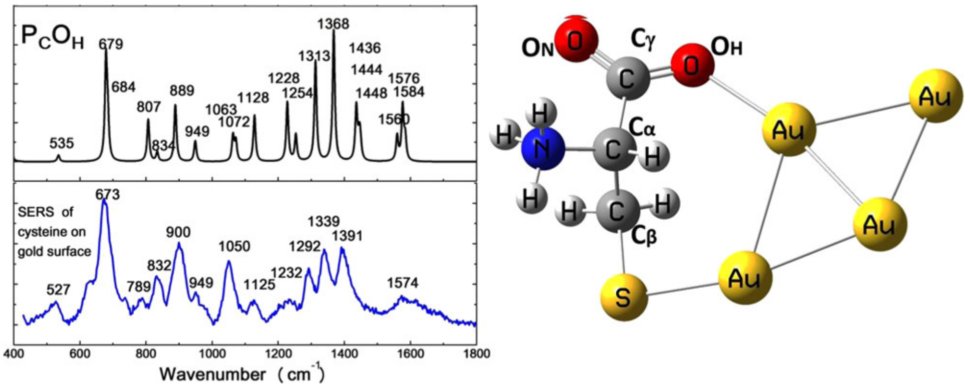

Figure 1.11: The calculated Raman spectra of cysteine adsorbed on Au$_4$ cluster through S and O sites.[21]

1.1.3 Systems In Excited States

The unique optical property of GNP that arises from the surface plasmon properties has been exploited for sensors and imaging, and recently photocatalysis and photothermal therapy, as discussed at the beginning of the chapter. There have been vast research efforts directed at the understanding and prediction of the optical properties of either bare or thiolated GNP. Specifically, there is an interest in resolving the question on the the critical number of gold atoms to be considered as a metallic state nanocluster.[90] A sharp transition has been observed from the nonmetallic $Au_{246}(SR)_{80}$ to metallic $Au_{279}(SR)_{84}$, whose electronic properties have been thoroughly investigated experimentally and theoretically.[91] A computational tool would be able to offer important insights into the understanding of the relationship between size and optical excitation. For example, Li *et al.* investigated $Au_{317}(SR)^{110}$, to conclude that the nanocluster is indeed metallic in nature.[92] Besides the size of GNP, the surface ligands could have a significant impact on the absorption spectra.[93,94]

There are also reported works simulating the optical absorption of bare GNP. Stener *et al.* have evaluated the application of frozen core electrons associated with scalar relativistic in TD-DFT calculation of the optical excitation spectra for a series of bare GNP, which are Au_{64}^{+}, Au_{6444}^{+}, and Au_{1462}^{+}.[95] Burgess *et al.* have performed TD-DFT calculations to calculate and compare the optical absorption spectra of bare gold clusters consisting of 20 to 171 atoms, with varying shapes.[96] The TD-DFT method coupled with Ehrenfest dynamics has also been applied to investigate the underlying mechanism of water splitting induced by the plasmonic property of GNP.[97] In another study, Senanayake *et al.* studied the optical absorption of a series of bare and linear gold nanowires with Real-Time TD-DFT method (time propagation of electron dynamics), to observe a redshift in the longitudinal mode as the length of the nanowire increases, while the transverse mode remains constant.[98]

Furthermore, the radiosensitizing property of GNP has been widely observed, and they are promising for the application in radiotherapy for cancer treatment. The underlying mechanism of the radiosensitization is, however, still under debate, which has sparked the development of theoretical approaches to investigate the physical stages involved in radiosensitization. The physical stages include the interaction between the projectile (high energy charged particle, γ ray, etc.) and GNP, and the subsequent production of secondary electrons. The widely used approach is the Monte Carlo based model called Geant4, which allows detailed calculations of local dose in the vicinity of GNP, and followed by the calculation of the impact of the secondary electrons on the surroundings.[99–105] Salado-Leza *et al.* have employed Geant4-DNA to investigate the radio-enhancing properties of bimetallic AuPt nanoparticles in comparison to the monometallic nanoparticles.[102] A typical simulation setup in Geant4 is shown in Figure 1.12.

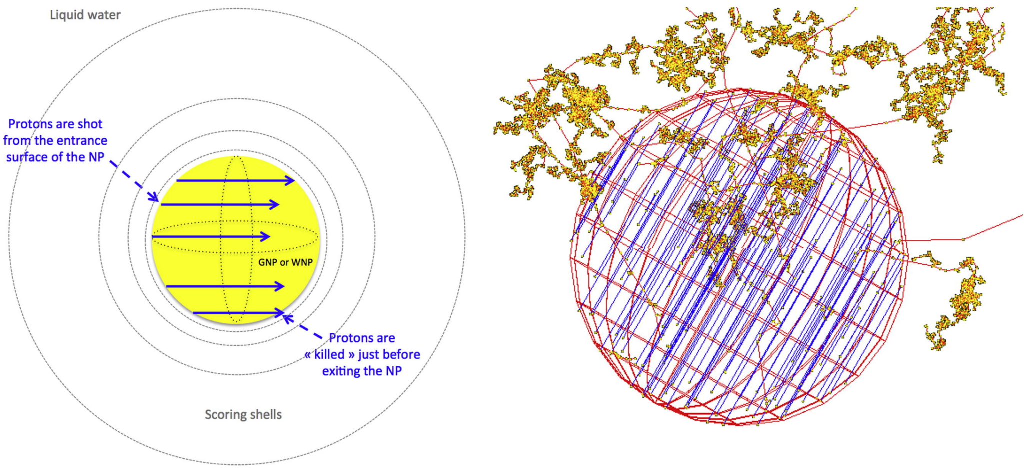

Figure 1.12: (left) The schematic diagram of a typical simulation setup in Geant4, in which the incident parallel protons are shot to the nanoparticle (yellow sphere) that is surrounded by the scoring spherical shells, and (right) the visualization of the secondary electron interactions (red tracks) upon irradiation.[100]

Real time TD-DFT method, in which the notion of propagation is introduced, has recently been developed and proposed as an alternative method to simulate the collision of projectiles and matters of interest.[106,107] This method has been successfully employed for the calculation of electronic stopping power of liquid water, DNAs, and metal slab (see Figure 1.13).[108–112] However, this method has not been used to simulate the collision of projectiles with GNP or gold slabs yet. It could be due to the high computational cost associated to the simulation.

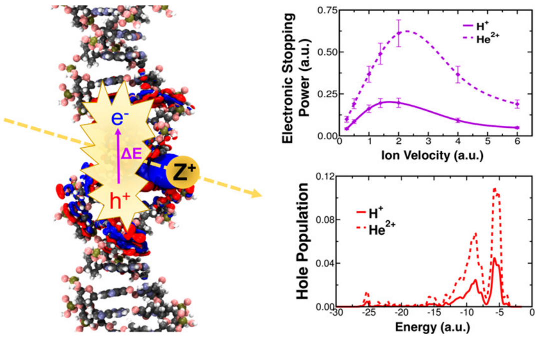

Figure 1.13: (left) The schematic illustration of the collision between DNA and high energy charged particles; (right) The calculated electronic stopping power and the hole population generated by the collision with the proton and alpha particle.[108]

The theoretical approaches to simulate large systems under excited state are relatively young and currently undergoing a rapid development, to enable the simulation of increasingly more complex systems. Particularly in the case of TD-DFT, efforts to introduce tight-binding approximation are under way both to accelerate the computation time, as well as to simulate even larger systems.[113] These reported works have indeed demonstrated the computational approaches as a valuable tool to provide insight into the plasmonic and radiosensitizing properties of GNP.

1.2 The Objectives

Through the literature review, computational tools have indeed been exploited to model and investigate the interfacial interaction of either gold surfaces and gold nanoparticles within a wide range of context. While the current state of the art has provided great insight into experimental observations, there remain questions to be answered, and models to be improved. Coupled with the advancement in computational power and architecture, and constant development of theories, theoretical models that increasingly reflect the realistic system are within our reach.

The problem in simulating GNP systems, as illustrated in the literature review, is a complex and also a multi-scale problem. The goal of the current thesis is, therefore, to exploit the different levels of computational tools to investigate the interaction of GNP with the environment. The choice of computational tools strongly depends on the properties of interest. The schematic representation of the objective of the thesis can be seen in Figure 1.14.

The thesis is separated into 3 chapters with different and yet interconnected focuses. The first chapter is dealing with the dynamic interaction of water molecules on GNP. In this chapter, the force field-based MD has been selected as the method of choice for several reasons. We are interested firstly in the competitive interaction between formation of hydrogen bond network and the optimal interaction with GNP surfaces. Secondly, a system containing hydrated GNP in periodic boundary conditions is required to probe the dynamics, which necessitates the force field representation to reduce the computational cost. The main objective of the chapter is to employ force field-based MD to explore and probe the structure of water at the first solvation shell of GNP. Afterwards, a new and accurate force field derived from GAL force field, and adapted specifically for multi-faceted GNP-water systems, is developed.[57,58] The polarization effect is subsequently introduced within the AMOEBA framework.

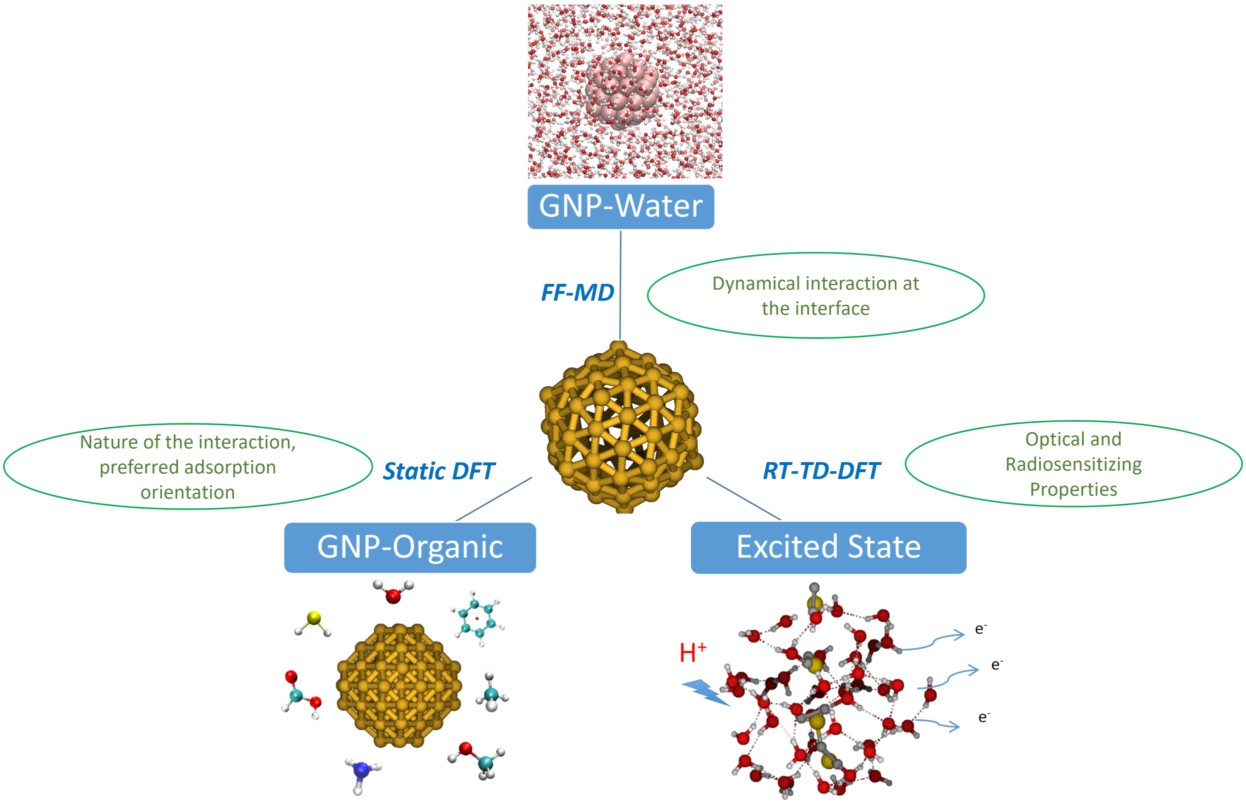

Figure 1.14: The schematic representation of the objectives of the thesis in employing various levels of computational methods to investigate specific properties of interest.

The second chapter will be dealing with the interaction of small organic molecules on GNP, in which we have performed the geometry optimization of a series of representative organic molecules on the model systems of Au$_{32}$, Au$_{55}$, and Au$_{79}$. There are multiple objectives for this chapter, which are, firstly, a systematic investigation and characterization of the nature of the interaction between GNP and ligands. Secondly, we are interested in investigating the size and shape effects of GNP on the interaction energy, as well as on the vibrational signatures of the organic molecules. Lastly, we are interested in qualitatively comparing our calculated vibrational spectra with experimental spectra, which usually is not straightforward. Therefore, the calculations performed in this section are all at DFT level and followed by vibrational analysis in the harmonic approximation. The optimized complexes are subsequently subjected to various quantum chemical topological analysis to gain insight into the nature of the interactions and to identify potential descriptors of the interaction. Lastly, the energy decomposition analysis has also been performed to further probe into the underlying physical forces of the interaction.

In the last section of the thesis, the radiosensitizing and optical properties of hydrated GNP with real-time time-dependent DFT (RT-TD-DFT) have been investigated. The simulation of the collision between high kinetic energy projectile and water clusters has been performed to investigate the sensitivity of the calculation of electronic stopping power, an important property of radiosensitizers, on the choice of basis set. For that purpose, basis sets capable of describing continuum functions have been generated. This study will serve as a reference before investigating the hydrated GNP system. The absorption spectra of various sizes of GNP have also been calculated, with the objective of studying the size and shape effect of GNP on their optical properties. This study will also serve as a reference for further investigation of the optical properties of hydrated GNP systems.

Bibliography

[1] X. Huang, I. H. El-Sayed, W. Qian and M. A. El-Sayed, *J Am Chem Soc*, 2006, **128**, 2115–2120.

[2] S. Mukherjee, F. Libisch, N. Large, O. Neumann, L. V. Brown, J. Cheng, J. B. Lassiter, E. A. Carter, P. Nordlander and N. J. Halas, *Nano Lett*, 2013, **13**, 240–247.

[3] L. Shi, J. Zhang, M. Zhao, S. Tang, X. Cheng, W. Zhang, W. Li, X. Liu, H. Peng and Q. Wang, *Nanoscale*, 2021, **13**, 10748–10764.

[4] J. Conde, J. T. Dias, V. Grazú, M. Moros, P. V. Baptista and J. M. de la Fuente, *Front Chem*, 2014, **2**, 2014.

[5] C. Yao, L. Zhang, J. Wang, Y. He, J. Xin, S. Wang, H. Xu and Z. Zhang, *J Nanomater*, 2016, **2016**, 5497136.

[6] M. Hoarau, S. Badieyan and E. N. G. Marsh, *Org Biomol Chem*, 2017, **15**, 9539–9551.

[7] G. P. Szekeres and J. Kneipp, *Analyst*, 2018, **143**, 6061–6068.

[8] S. G. Harroun, *ChemPhysChem*, 2018, **19**, 1003–1015.

[9] S. Xue, P. Guha, Q. Yuan and W. Gan, *Part. Part. Syst. Char.*, 2021, **38**, 2000316.

[10] M. Iosin, F. Toderas, P. L. Baldeck and S. Astilean, *J Mol Struct*, 2009, **924-926**, 196–200.

[11] N. Schwenk, B. Mizaikoff, S. Cárdenas and A. I. Lṕpez-Lorente, *Analyst*, 2018, **143**, 5103–5111.

[12] F. Madzharova, Z. Heiner and J. Kneipp, *J Phys Chem C*, 2020, **124**, 6233–6241.

[13] F. Madzharova, Z. Heiner and J. Kneipp, *J Phys Chem C*, 2017, **121**, 1235–1242.

[14] F. Madzharova, Z. Heiner, M. Gühlke and J. Kneipp, *J Phys Chem C*, 2016, **120**, 15415–15423.

[15] F. Madzharova, Z. Heiner and J. Kneipp, *J Phys Chem C*, 2020, **124**, 6233–6241.

[16] J.-J. Velasco-Velez, C. H. Wu, T. A. Pascal, L. F. Wan, J. Guo, D. Prendergast and M. Salmeron, *Science*, 2014, **346**, 831–834.

[17] C. Schunke, D. P. Miller, E. Zurek and K. Morgenstern, *Phys Chem Chem Phys*, 2022, **24**, 4485–4492.

[18] Y. R. Shen and V. Ostroverkhov, *Chem Rev*, 2006, **106**, 1140–1154.

[19] J. Gao, Y. Hu, S. Li, Y. Zhang and X. Chen, *Spectrochim Acta, Part A*, 2013, **104**, 41–47.

[20] J.-F. Li, Y.-F. Huang, S. Duan, R. Pang, D.-Y. Wu, B. Ren, X. Xu and Z.-Q. Tian, *Phys Chem Chem Phys*, 2010, **12**, 2493.

[21] G. Yao and Q. Huang, *J Phys Chem C*, 2018, **122**, 15241–15251.

[22] A. Królikowska, J. Cukras, M. Witkowski, D. Tymecka, A. Hernik-Magoń, A. Misicka and W. Dzwolak, *J Phys Chem C*, 2020, **124**, 7097–7116.

[23] M. Elstner, D. Porezag, G. Jungnickel, J. Elsner, M. Haugk, T. Frauenheim, S. Suhai and G. Seifert, *Phys Rev B*, 1998, **58**, 7260–7268.

[24] E. Okoampah, Y. Mao, S. Yang, S. Sun and C. Zhou, *Colloids Surf , B*, 2020, **196**, 111312.

[25] M. S. Jahan Sajib, P. Sarker, Y. Wei, X. Tao and T. Wei, *Langmuir*, 2020, **36**, 13356–13363.

[26] T. P. Senftle, S. Hong, M. M. Islam, S. B. Kylasa, Y. Zheng, Y. K. Shin, C. Junkermeier, R. Engel-Herbert, M. J. Janik, H. M. Aktulga, T. Verstraelen, A. Grama and A. C. T. van Duin, *npj Comput Mater*, 2016, **2**, 1–14.

[27] T. T. Järvi, A. C. T. van Duin, K. Nordlund and W. A. Goddard, *J Phys Chem A*, 2011, **115**, 10315–10322.

[28] G.-T. Bae and C. M. Aikens, *J Phys Chem A*, 2013, **117**, 10438–10446.

[29] S. Monti, V. Carravetta and H. Ågren, *J Phys Chem Lett*, 2016, **7**, 272–276.

[30] D. Liang, J. Hong, D. Fang, J. W. Bennett, S. E. Mason, R. J. Hamers and Q. Cui, *Phys Chem Chem Phys*, 2018, **20**, 3349–3362.

[31] J. Le, A. Cuesta and J. Cheng, *J Electroanal Chem*, 2018, **819**, 87–94.

[32] G. Cicero, A. Calzolari, S. Corni and A. Catellani, *J Phys Chem Lett*, 2011, **2**, 2582–2586.

[33] A. Huzayyin, J. H. Chang, K. Lian and F. Dawson, *J Phys Chem C*, 2014, **118**, 3459–3470.

[34] L. S. Pedroza, P. Brandimarte, A. R. Rocha and M.-V. Fernández-Serra, *Chem Sci*, 2018, **9**, 62–69.

[35] R. Nadler and J. F. Sanz, *J Chem Phys*, 2012, **137**, 114709.

[36] Z. K. Goldsmith, M. F. Calegari Andrade and A. Selloni, *Chem Sci*, 2021, **12**, 5865–5873.

[37] T. A. Baker, C. M. Friend and E. Kaxiras, *J Chem Theory Comput*, 2010, **6**, 279–287.

[38] Y. Li, W. Dononelli, R. Moreira, T. Risse, M. Bäumer, T. Klüner and L. V. Moskaleva, *J Phys Chem C*, 2018, **122**, 5349–5357.

[39] Y. Li, S. Li, M. Bäumer, E. A. Ivanova-Shor and L. V. Moskaleva, *ACS Catal*, 2020, **10**, 3164–3174.

[40] S.-H. Yoo, N. Siemer, M. Todorova, D. Marx and J. Neugebauer, *J Phys Chem C*, 2019, **123**, 5495–5506.

[41] M. Darvish Ganji, H. Tavassoli Larijani, R. Alamol-hoda and M. Mehdizadeh, *Sci Rep*, 2018, **8**, 11400.

[42] G. Hashemkhani Shahnazari and M. Darvish Ganji, *Sci Rep*, 2021, **11**, 435.

[43] G. Fazio, G. Seifert, M. Rapacioli, N. Tarrat and J.-O. Joswig, *Z Phys Chem*, 2018, **232**, 1583–1592.

[44] A. Fihey, C. Hettich, J. Touzeau, F. Maurel, A. Perrier, C. Köhler, B. Aradi and T. Frauenheim, *J Comput Chem*, 2015, **36**, 2075–2087.

[45] L. F. L. Oliveira, N. Tarrat, J. Cuny, J. Morillo, D. Lemoine, F. Spiegelman and M. Rapacioli, *J Phys Chem A*, 2016, **120**, 8469–8483.

[46] A. Domínguez-Castro, D. Hernández and F. Guzmán, *Theor Chem Acc*, 2017, **136**, 84.

[47] V. Q. Vuong, J. M. L. Madridejos, B. Aradi, B. G. Sumpter, G. F. Metha and S. Irle, *Chem Sci*, 2020, **11**, 13113–13128.

[48] J. Zhu, V. Q. Vuong, B. G. Sumpter and S. Irle, *MRS Commun*, 2019, **9**, 867–873.

[49] C. L. Gómez-Flores, D. Maag, M. Kansari, V.-Q. Vuong, S. Irle, F. Gräter, T. Kubař and M. Elstner, *J Chem Theory Comput*, 2022, **18**, 1213–1226.

[50] H. Heinz, R. A. Vaia, B. L. Farmer and R. R. Naik, *J Phys Chem C*, 2008, **112**, 17281–17290.

[51] K. Kanhaiya, S. Kim, W. Im and H. Heinz, *npj Comput Mater*, 2021, **7**, 17.

[52] F. Iori, R. Di Felice, E. Molinari and S. Corni, *J Comput Chem*, 2009, **30**, 1465–1476.

[53] L. B. Wright, P. M. Rodger, S. Corni and T. R. Walsh, *J Chem Theory Comput*, 2013, **9**, 1616–1630.

[54] M. Rosa, S. Corni and R. Di Felice, *J Chem Theory Comput*, 2014, **10**, 1707–1716.

[55] Z. Futera and J. Blumberger, *J Chem Theory Comput*, 2019, 12.

[56] D. Biriukov and Z. Futera, *J Phys Chem C*, 2021, **125**, 7856–7867.

[57] S. N. Steinmann, R. Ferreira De Morais, A. W. Götz, P. Fleurat-Lessard, M. Iannuzzi, P. Sautet and C. Michel, *J Chem Theory Comput*, 2018, **14**, 3238–3251.

[58] P. Clabaut, P. Fleurat-Lessard, C. Michel and S. N. Steinmann, *J Chem Theory Comput*, 2020, **16**, 4565–4578.

[59] G. Brancolini, D. B. Kokh, L. Calzolai, R. C. Wade and S. Corni, *ACS Nano*, 2012, **6**, 9863–9878.

[60] K. Tay and F. Bresme, *J Mater Chem*, 2006, **16**, 1956.

[61] S.-P. Ju, *J Chem Phys*, 2005, **122**, 094718.

[62] E. Heikkilä, A. A. Gurtovenko, H. Martinez-Seara, H. Häkkinen, I. Vattulainen and J. Akola, *J Phys Chem C*, 2012, **116**, 9805–9815.

[63] O. A. Perfilieva, D. V. Pyshnyi and A. A. Lomzov, *J Chem Theory Comput*, 2019, **15**, 1278–1292.

[64] Q. Shao and C. K. Hall, *Langmuir*, 2016, **32**, 7888–7896.

[65] C. P. Shaw, D. A. Middleton, M. Volk and R. Lévy, *ACS Nano*, 2012, **6**, 1416–1426.

[66] M. Tang, N. S. Gandhi, K. Burrage and Y. Gu, *Langmuir*, 2019, **35**, 4435–4444.

[67] F. Ramezani, M. Amanlou and H. Rafii-Tabar, *J Nanopart Res*, 2014, **16**, 2512.

[68] C.-H. Chan, F. Poignant, M. Beuve, E. Dumont and D. Loffreda, *J Phys Chem Lett*, 2019, **10**, 1092–1098.

[69] M. Prakash, G. Chambaud, M. M. Al-Mogren and M. Hochlaf, *J Mol Model*, 2014, **20**, 2534.

[70] G. Geudtner, *Theor Chem Acc*, 2021, **140**, 87.

[71] M. Haruta, T. Kobayashi, H. Sano and N. Yamada, *Chem Lett*, 1987, **16**, 405–408.

[72] M. Haruta, *Chem Rec*, 2003, **3**, 75–87.

[73] G. Li and R. Jin, *Nanotechnology Reviews*, 2013, **2**, 529–545.

[74] A. S. K. Hashmi and G. J. Hutchings, *Angew Chem - Int Ed*, 2006, **45**, 7896–7936.

[75] J. J. Plata, F. Romero-Sarria, J. Amaya Suárez, A. M. Márquez, Ó. H. Laguna, J. A. Odriozola and J. Fdez Sanz, *Phys Chem Chem Phys*, 2018, **20**, 22076–22083.

[76] T. C. Allison and Y. J. Tong, *Phys Chem Chem Phys*, 2011, **13**, 12858–12864.

[77] B. Yoon, P. Koskinen, B. Huber, O. Kostko, B. von Issendorff, H. Häkkinen, M. Moseler and U. Landman, *ChemPhysChem*, 2007, **8**, 157–161.

[78] X. Cheng, F. Li and C. Wang, *Comput Theor Chem*, 2016, **1097**, 1–7.

[79] N. K. Jena, K. R. S. Chandrakumar and S. K. Ghosh, *RSC Adv*, 2012, **2**, 10262–10267.

[80] S. H. Brodersen, U. Grønbjerg, B. Hvolbæk and J. Schiøtz, *J Catal*, 2011, **284**, 34–41.

[81] L. Fang, T. Chen, Y. Meng, Y. Wang, J. Xue, Z. Ni and S. Xia, *Mol Catal*, 2020, **483**, 110757.

[82] D. Cheng, H. Xu and A. Fortunelli, *J Catal*, 2014, **314**, 47–55.

[83] S. Meng, E. G. Wang and S. Gao, *Phys Rev B*, 2004, **69**, 195404.

[84] A. Huzayyin and F. Dawson, *J Electroanal Chem*, 2015, **748**, 8–15.

[85] M. Hoefling, F. Iori, S. Corni and K.-E. Gottschalk, *ChemPhysChem*, 2010, **11**, 1763–1767.

[86] G. Hong, H. Heinz, R. R. Naik, B. L. Farmer and R. Pachter, *ACS Appl Mater Interfaces*, 2009, **1**, 388–392.

[87] Q. Zhao, *J Mol Model*, 2021, **27**, 132.

[88] Q. Zhao, *J Mol Model*, 2021, **27**, 328.

[89] J.-g. Wang and A. Selloni, *J Phys Chem C*, 2009, **113**, 8895–8900.

[90] M. Zhou, X. Du, H. Wang and R. Jin, *ACS Nano*, 2021, **15**, 13980–13992.

[91] N. A. Sakthivel, M. Stener, L. Sementa, A. Fortunelli, G. Ramakrishna and A. Dass, *J Phys Chem Lett*, 2018, **9**, 1295–1300.

[92] L. Li, P. Wang and Y. Pei, *Nanoscale*, 2022, **14**, 5694–5700.

[93] L. Sementa, G. Barcaro, A. Dass, M. Stener and A. Fortunelli, *Chem Commun*, 2015, **51**, 7935–7938.

[94] A. Fihey, F. Maurel and A. Perrier, *J Phys Chem C*, 2014, **118**, 4444–4453.

[95] M. Stener, A. Nardelli, R. De Francesco and G. Fronzoni, *J Phys Chem C*, 2007, **111**, 11862–11871.

[96] R. W. Burgess and V. J. Keast, *J Phys Chem C*, 2014, **118**, 3194–3201.

[97] J. Huang, X. Zhao, X. Huang and W. Liang, *Phys Chem Chem Phys*, 2021, **23**, 25629–25636.

[98] R. D. Senanayake, D. B. Lingerfelt, G. U. Kuda-Singappulige, X. Li and C. M. Aikens, *J Phys Chem C*, 2019, **123**, 14734–14745.

[99] W.-G. Shin, J. Ramos-Mendez, B. Faddegon, H. N. Tran, C. Villagrasa, Y. Perrot, S. Okada, M. Karamitros, D. Emfietzoglou, I. Kyriakou, M. C. Bordage, D. Sakata, S. Guatelli, H. J. Choi, C. H. Min, S. B. Lee and S. Incerti, *J Appl Phys*, 2019, **126**, 114301.

[100] H. N. Tran, M. Karamitros, V. N. Ivanchenko, S. Guatelli, S. McKinnon, K. Murakami, T. Sasaki, S. Okada, M. C. Bordage, Z. Francis, Z. El Bitar, M. A. Bernal, J. I. Shin, S. B. Lee, P. Barberet, T. T. Tran, J. M. C. Brown, T. V. Nhan Hao and S. Incerti, *Nucl Instrum Methods Phys Res Sect B Beam Interact Mater At*, 2016, **373**, 126–139.

[101] Z. Francis, G. Montarou, S. Incerti, M. Bernal and S. A. Zein, *Phys Medica*, 2019, **67**, 148–154.

[102] D. Salado-Leza, A. Traore, E. Porcel, D. Dragoe, A. Muñoz, H. Remita, G. García and S. Lacombe, *Int J Mol Sci*, 2019, **20**, 5648.

[103] J. C. L. Chow, M. K. K. Leung, S. Fahey, D. B. Chithrani and D. A. Jaffray, *J Phys : Conf Ser*, 2012, **341**, 012012.

[104] J. C. L. Chow, M. K. K. Leung and D. A. Jaffray, *Phys Med Biol*, 2012, **57**, 3323–3331.

[105] E. Engels, S. Bakr, D. Bolst, D. Sakata, N. Li, P. Lazarakis, S. J. McMahon, V. Ivanchenko, A. B. Rosenfeld, S. Incerti, I. Kyriakou, D. Emfietzoglou, M. L. F. Lerch, M. Tehei, S. Corde and S. Guatelli, *Phys Med Biol*, 2020, **65**, 225017.

[106] A. Parise, A. Alvarez-Ibarra, X. Wu, X. Zhao, J. Pilmé and A. de la Lande, *J Phys Chem Lett*, 2018, **9**, 844–850.

[107] A. Alvarez-Ibarra, A. Parise, K. Hasnaoui and A. de la Lande, *Phys Chem Chem Phys*, 2020, **22**, 7747–7758.

[108] D. C. Yost, Y. Yao and Y. Kanai, *J Phys Chem Lett*, 2020, **11**, 229–237.

[109] K. G. Reeves, Y. Yao and Y. Kanai, *Phys Rev B*, 2016, **94**, 041108.

[110] D. C. Yost and Y. Kanai, *J Am Chem Soc*, 2019, **141**, 5241–5251.

[111] A. Schleife, Y. Kanai and A. A. Correa, *Phys Rev B*, 2015, **91**, 014306.

[112] I. Maliyov, J.-P. Crocombette and F. Bruneval, *Phys Rev B*, 2020, **101**, 035136.

[113] N. Asadi-Aghbolaghi, R. Rüger, Z. Jamshidi and L. Visscher, *J Phys Chem C*, 2020, **124**, 7946–7955.

Chapter 2

SIMULATING GNP-WATER INTERFACE

Contents

2.1 Introduction

This chapter focuses on modeling the interaction of water at the interface of GNP by employing force field-based MD (FF-MD). Our initial motivation was based on the experimental observation of overproduction of hydroxyl radicals and secondary electrons in the presence of GNP under irradiation, where the author proposed the important contribution of unique water structure at the interface of GNP in facilitating the water bond breaking.[1] Experimental studies have additionally demonstrated a different water structure in the vicinity of nanoparticles and surfaces.[2–4] However, the understanding of GNP-water dynamics has important implications in other applications as well, such as the effect on the orientation of surface ligands and in the field of electrocatalysts.

The choice of employing FF-MD, and not static approach, is firstly, because we are interested in the dynamical processes of water, and secondly, to reduce the computational time and cost for the simulation that could consist of thousands of atoms depending on size of the GNP. While different sets of force fields are available for Au [111] surfaces, and they have successfully been used to model GNP systems in literature, force field specifically developed to model the multifaceted nanoparticle is not yet available. Additionally, currently available force fields are not accurate enough to describe the many body interactions at the interface of water and GNP.[5] This has illustrated the urgent need for an accurate force field describing the GNP-water systems.

This chapter consists of two main parts, and preceded by the methodological section that describes in details FF-MD. In the first part of this chapter, the structure of water solvation shell of a series of increasing size of GNPs is studied by systematically investigating the change in dynamical and structural properties of the first water solvation shell. The study is followed by the investigation of vibrational density of states calculated with harmonic approximation. Then, in the second part of this chapter, the development of an accurate force field is reported for the description of GNP-water interface by adding polarization term, based on AMOEBA framework, to the GAL21 force field.

2.2 Computational Methodologies

This chapter mainly employs FF-MD simulations. The study reported in Section 2.3 has been performed with GROMACS software package,[6] while the one reported in Section 2.4 has been performed with Tinker Molecular Package, with openMP parallelization.[7] The various data analysis derived from the simulations will also be described here.

2.2.1 Theories and Fundamentals of MD Simulation

MD simulation, a method that simulates the physical movements of atoms in a given period of time, is among the powerful computational tools for exploration of interfaces of metal surfaces. From the accumulated trajectories over a given period of time, various physical properties can be derived. These trajectories are generated by solving the Newton's equation of motion (see Equation 2.1), which describes the relationship between the forces ($\vec{F_i}$), mass (m_i), and acceleration ($\vec{a_i}$) of a particle.

Essentially, the MD simulations are performed by calculating the forces exerted on each atom by all the other atoms based on the initial position ($\vec{r_i}$(t)), and are followed by calculation of their velocities.[8] From the velocities, the positions of the atoms are updated at $t + \Delta t$, (represented as $\vec{r_i}$(t+Δ t)) , and with the updated positions, the energy of the system and the forces felt by the individual atoms will be recalculated, to give new velocities. This step is then repeated until the simulation time has been reached. Verlet algorithm (also shown in Equation 2.1), which is derived from the Taylor expansions up to the fourth power, is frequently used as the integrator in MD simulations, thanks to its simplicity and stability. However, it is important to use a very small time step to ensure the stability of the propagation. Even so, a small time step would mean millions of MD steps have to be performed to reach the desired time scale. This leads to an increase in computational time, which is not desirable. A rule of thumb for the choice of time step would be a tenth of the fastest motion within the system, which is usually the motions of light atoms. Considering that the vibrational motion of O-H bond takes several femtoseconds, which means subfemtosecond time step is crucial to ensure the stability of the propagation. Alternatively, it is possible to impose constraints on the OH bond length and hence allowing an increase in the time step up to 2 fs, at a cost of losing information on the vibrational movement of OH.

$$\vec{F_i} = m_i a_i = -\frac{dV}{dr_i} \tag{2.1}$$

Meanwhile, the interatomic potential necessary for the calculation of energies and forces of the system can be calculated through ab-initio method, where the Hamiltonian of each individual atom has to be solved. This method has high accuracy, but it comes at high computational cost. An alternative to the ab-initio method is the classical force field model. The force field model introduces approximation in the calculation of potential energy, in which each molecule is represented as a series of classical charged balls linked by springs, and the interatomic potential is calculated based on a mathematical function, with atom/molecule specific parameters derived from quantum calculation. A typical form of the mathematical function of a force field is a sum of the intramolecular and intermolecular energy terms, as represented by Equation 2.2.

$$\begin{aligned} U = \sum_{bonds} \frac{1}{2} k_b (r - r_0)^2 + \sum_{angles} \frac{1}{2} k_a (\Theta - \Theta_0)^2 + \sum_{torsions} \frac{V_n}{2}[1 + cos(n\theta - \delta)] \\ + \sum_{improper} V_{imp} + \sum_{LJ} 4\varepsilon_{ij}\left(\frac{\sigma_{ij}^{12}}{r_{ij}^{12}} - \frac{\sigma_{ij}^{6}}{r_{ij}^{6}}\right) + \sum_{elec} \frac{q_1 q_2}{r_{ij}} \end{aligned} \tag{2.2}$$

The intramolecular interactions include bond stretching, angle bending, dihedral, and improper torsions energies, which correspond to the first four terms in the equation. The bond stretching and angle bending energies are calculated with harmonic approximation, with force constant (k_b) and equilibrium length (r_0) parameters associated with the bonding terms, and k_a and Θ_0 representing the angular force constant and equilibrium angle, respectively. The torsion term is needed to describe the dihedral angle for at least four connected atoms, and to discriminate between the cis and trans conformation resulted from single bond rotation. The functional form for torsion term corresponds to the third term in the Equation 2.2, with V_n is the barrier height and n is an integer to determine the periodicity of the potential. The last intramolecular term is the improper torsion, which helped to select the correct geometry or chirality of atoms.

The intermolecular interactions, *i.e.* the last two terms in Equation 2.2, include the van der Waals interactions and the Coulombic interactions. The van der Waals potential usually takes the form of Lennard-Jones potential, that describes the repulsive term at small separation and the attractive term at longer distances between atom pair of i and j. The parameter σ is defined as the distance of the atom pair when the energy is zero, and the parameter ε corresponds to the energy at the equilibrium distance, though the definition might change slightly depending on the force field. The Coulombic interaction describes the interaction of the partial charges between atom pair of i and j (q_i and q_j). All these parameters are derived from ab-initio calculations, and are specific for each atom type. Therefore, careful assignments of atom type are crucial to obtain the correct representation of molecules. Many force fields are currently available in the literature, describing a wide range of organic molecules, metal ions, biomolecules, such as CHARMM,[9] GROMOS,[10] OPLS,[11] AMBER,[12] and COMPASS[13]. In addition, these force fields are constantly updated to achieve an improved accuracy, and to describe increasingly more complex systems.

The traditional force field model normally works quite well, until electrostatic and electronic effects become non-negligible, for example in describing charged particles, metal surfaces, and also the transition between gas phase to condense phase. The inability of these force fields to respond to the environmental electrostatic and polarization effect, due to the fixed charge model, has been demonstrated to be lacking for an accurate representation of interactions at metal surfaces, among many other systems.[14] For that purpose, different polarizable models have been proposed, such as fluctuating-charges,[15] Drude oscillator,[16] charge scaling,[17] induced dipole approaches,[18] among many others.

The fluctuating charges approach, which is based on the principle of electronegativity equalization, treats charges as variables that fluctuate as a response to the external electrostatic potential of the environment. The fluctuation is calculated based on the electronegativity and hardness of the respective atoms, and as a result, this model allows charge transfer to occur between the atoms. The Drude-oscillator approach introduces an auxiliary massless particle that is attached via a harmonic spring to each of the polarizable atoms. The electronic induction, is therefore, a result of the displacement of this particle under the influence of the local electric field. With charge scaling approach, the electronic polarization is scaled based on the medium's permittivity, and hence including it in a mean field way. Alternatively, with the induced dipole approach, the induced dipole moment is based on the atomic polarizability, and is defined as the multiplication of the polarizability of the atom and the total electric field felt by the atom. Within this approach, the induced dipole moment at an atom site induces polarization at other atom sites, which leads to mutual polarization. The polarization, therefore, has to be solved iteratively via self-consistent field.

The AMOEBA force field, *i.e.* Atomic Multipole Optimized Energetics for Biomolecular Applications, is one of the polarizable force fields based on the induced dipole model.[19] The force field treats explicitly both the inter- and intramolecular polarization, and it includes 4 major components, which are the atomic multipoles, the permanent electrostatic components that are separated from the intramolecular polarization, Thole's interactive dipole polarizability model,[20] and group-based intramolecular polarization.

$$\mu_{i,\alpha}^{ind} = \alpha_i(\sum_j T_\alpha^{ij}(M_j) + \sum_{j'} T_{\alpha\beta}^{ij'} \mu_{j',\beta}^{ind}) \tag{2.3}$$

Within the interactive polarizability Thole's model, the induced dipole of each atom polarizes all the other atom sites. Therefore, the electric field experienced by atom i is the summation of both permanent multipoles (first term in Equation 2.3) and induced dipoles by the surrounding atoms (second term in Equation 2.3). α_i represents the polarizability of atom i, and j represents the atoms belonging to another molecule other than i, and j' includes all the other atoms, other than atom i, and the subscript α and $\beta \in x, y, z$. The $\mathbf{T}$ represents the interaction matrix elements, and $\mathbf{M}$ represents the vector of permanent atomic multipole components in Cartesian polytensor form. Therefore, the first term in Equation 2.3 can be referred as direct induction, while the second term is referred as mutual induction. The equation is then solved iteratively to achieve convergence. In general, the intramolecular polarization at short distances is excluded, but for larger molecules, the intramolecular polarization beyond a certain distance might be necessary to be included. In the case of intermolecular polarization, a damping scheme has to be introduced at short distances to prevent a phenomenon called polarization catastrophe. The damping scheme in Thole's model suggested a smearing of the charge distribution, based on Equation 2.4. The term u represents the effective distance (R_{ij}) as a function of atomic polarizabilities, and a is the dimensionless damping factor controlling the width of the smeared charge distribution.

$$\begin{aligned} \rho =& \frac{3a}{4\pi} exp(-au^3) \\ u =& \frac{R_{ij}}{(\alpha_i \alpha_j)^{1/6}} \end{aligned} \tag{2.4}$$

Subsequently, the atomic multipoles of a given compound (see Equation 2.5) refers to the sum of the permanent electrostatic components of a particular atom i, which are q (charges), d (dipoles), and Q (quadrupoles). They can be derived via the rigorous redistribution of electron density associated with overlap integral products, called the Distributed Multipole Analysis (DMA) protocol.[21] The resulting multipoles are considered as summation of permanent and induced moments. Since, the induced moment can be calculated based on the Equation 2.6, the permanent moments can then be separated and obtained as the difference between the total multipoles and the induced moments. Permanent moments have been demonstrated to be transferable across different conformations of a given compound.[19]

$$M_i = [q_i, d_{i,x}, d_{i,y}, d_{i,z}, Q_{i,xx}, Q_{i,xy}, Q_{i,xz}, Q_{i,yx}, Q_{i,yy}, Q_{i,yz}, Q_{i,zx}, Q_{i,zy}, Q_{i,zz}]^T \tag{2.5}$$

$$M_i = M_i^{perm} + M_i^{ind} \tag{2.6}$$

As a result, in terms of computational cost, polarizable force fields are considerably more costly than traditional force fields. However, the computational cost of AMOEBA force field is considered as an intermediate among the different available polarizable force fields. Additionally, the performance of the force field has been reviewed recently for its applications in simulating aqueous peptide solvation, calculation of solvation free energies, stability studies of aqueous solvated proteins, computational X-Ray crystallography, and protein-ligand binding.[22] Therefore, AMOEBA force field will be our method of choice for the treatment of polarization term.

In the context of simulating gold surfaces, Heinz was among the first to develop the non-polarizable force field for gold surfaces based on the Lennard-Jones potential.[23] He later adapted the force field to include the polarization effect based on harmonically coupled core-shell charge pair for every gold atom at the surface.[24] Another force field, called GolP, has been developed to study the interfacial interaction of Au [111] and Au [100] facets with proteins, sulfur, and nucleobases.[25–27] Still another force field has recently been reported, which focuses on the interfacial interaction between water and metal surfaces.[28,29] With the availability of different force fields, a careful consideration has to be taken in selecting the suitable one. Berg *et al.* have evaluated the performance of several water-gold surfaces non-polarizable force field, and showed that the interfacial structure of water is strongly dependent on the parameters.[5] Their study highlights the need for an accurate force field for the interfacial interactions.

2.2.2 Molecular Dynamics Simulation Setup

In setting up a force field-based MD simulation, there are several important aspects that need to be considered. In general, simulating realistic system requires the inclusion of environment (*i.e.* solvent) into a simulation box. However, when the system is confined into a simulation box, the surface effect, due to the non-negligible fraction of atoms interacting with vacuum, will result in an artefact. Therefore, to remove the surface effect, periodic boundary condition (PBC) needs to be applied, in which the simulation box is repeated infinitely in either two or three dimensions, depending on the system of interest. The particles are then allowed to move freely across the box, in the sense that when a particle leaves the main simulation box, an image particle will enter into the main simulation box from the opposite side as a replacement. This scheme will, therefore, conserve the number of particles within the main simulation box. But, as a result, a cutoff distance for long distance interactions has to be applied to prevent the inclusion of interaction between the particle with its image counterpart in another box. The cutoff distance is generally set to be less than half of the length of the box. As for the electrostatic interactions, Ewald summation method has to be applied since the potential energy does not decay as quickly with the distance.

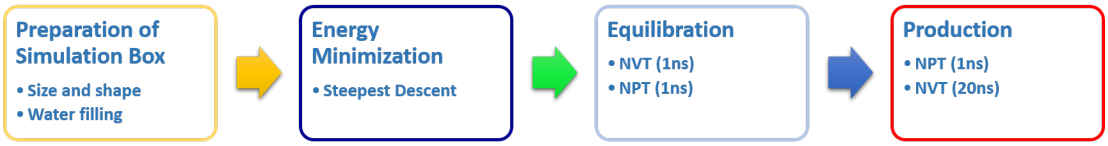

Figure 2.1: The schematic representation of a typical workflow for a molecular dynamics simulation

A typical molecular dynamics simulation is carried out within a thermodynamic ensemble, such as the microcanonical ensemble (NVE), canonical ensemble (NVT), and isothermal-isobaric ensemble (NPT). In the microcanonical ensemble, the number of particles, the volume of the cell, and the total energy of the system remain constant. The potential and the kinetic energies are, however, allowed to change until they reach an equilibrium at a certain temperature. Meanwhile, in the NVT ensemble, the number of particles, the volume, and the temperature of the system are kept constant. For the temperature to be kept constant, a thermostat has to be applied, such as the Nosé-Hoover thermostat,[30] in which the system is coupled to a heat bath, and an extra degree of freedom for heat bath is introduced in the Hamiltonian. Lastly, in the isothermal-isobaric ensemble, the number of particles, the pressure, and the temperature of the system are kept constant, while the density and volume of the box are allowed to vary. In addition to the thermostat, the barostat will have to be introduced as well. The barostat couples the system to a pressure bath, and the volume will be scaled periodically. In practice, the choice of ensembles is less important, as long as the equilibrated system has been achieved before time averages properties are computed.

Performing a molecular dynamics simulation usually follows the workflow represented in Figure 2.1. Firstly, the preparation of the system includes building the box with the desired size and shape. The size of the box has to be sufficiently large to ensure that as many interactions as possible can be taken into account, but small enough that the computational cost is not too large. The system is then filled with desired solvent (see Figure 2.2). Afterwards, an energy minimization procedure, with steepest decent algorithm, is performed to relax the system and to remove steric clashes and inappropriate geometry. The box is now ready for equilibration step in either NVT or NPT ensemble, or both. Once the system reaches equilibrium, the system is allowed to evolve further, and the trajectories from this last step, also called production step, can be used for data analysis.

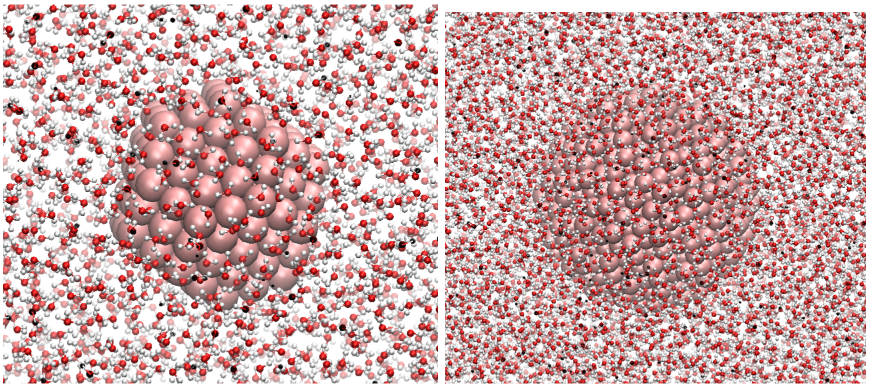

Figure 2.2: The schematic representation of GNP in a box of water Au$_{201}$ (left) and Au$_{887}$ (right)

2.2.3 Data Analysis

Different types of analysis can be calculated from the trajectories of molecular dynamics simulations. Firstly, the thermodynamic properties of the system can be obtained, such as the temperature, pressure, density, potential energy, and kinetic energy, among many others. These properties are usually calculated at each step, and they could be important indicators of instability during the simulation.

$$g(r) = \frac{1}{4\pi r^2 N\rho} \sum_i \sum_j \langle \delta(r - |r_i - r_j|) \rangle \tag{2.7}$$

Secondly, the structural properties can also be computed as time averages. One important example is the calculation of radial/pair distribution function ($g(r)$, see Equation 2.7), which provides information on the packing of the molecules, with ρ representing the density of the system, N representing the number of pair atoms, and r representing the atom pair distances. This property can sometimes be directly comparable with the neutron scattering experiments or X-ray diffraction.

In the context of this work, we are interested in the packing of water molecules around gold nanoparticles. On top of the radial distribution function, we are also interested in calculating the distribution of water orientations in the first solvation shell of GNP. The characterization of these orientations is based on the α and β angle (see Figure 2.3).[5] Instead of the surface normal, our point of reference is the vector between the center of mass of GNP and the respective water molecule. Therefore, for this characterization to be valid, the GNP has to adopt an almost spherical structure. The α is then defined as the angle between the vector of water's dipole and the GNP com-water vector, and β is the angle between the normal of water's molecular plane and the GNP com-water vector. The criteria for the characterization are shown in Table 2.1

Table 2.1: The characterization of water configurations based on α and β angles

Configuration	α	β
Up	$\alpha < 70°$	any
Flat	$70° < \alpha < 110°$	$\beta > 30°$ or $\beta < 150°$
Dangling	$70° < \alpha < 110°$	$70° < \beta < 110°$

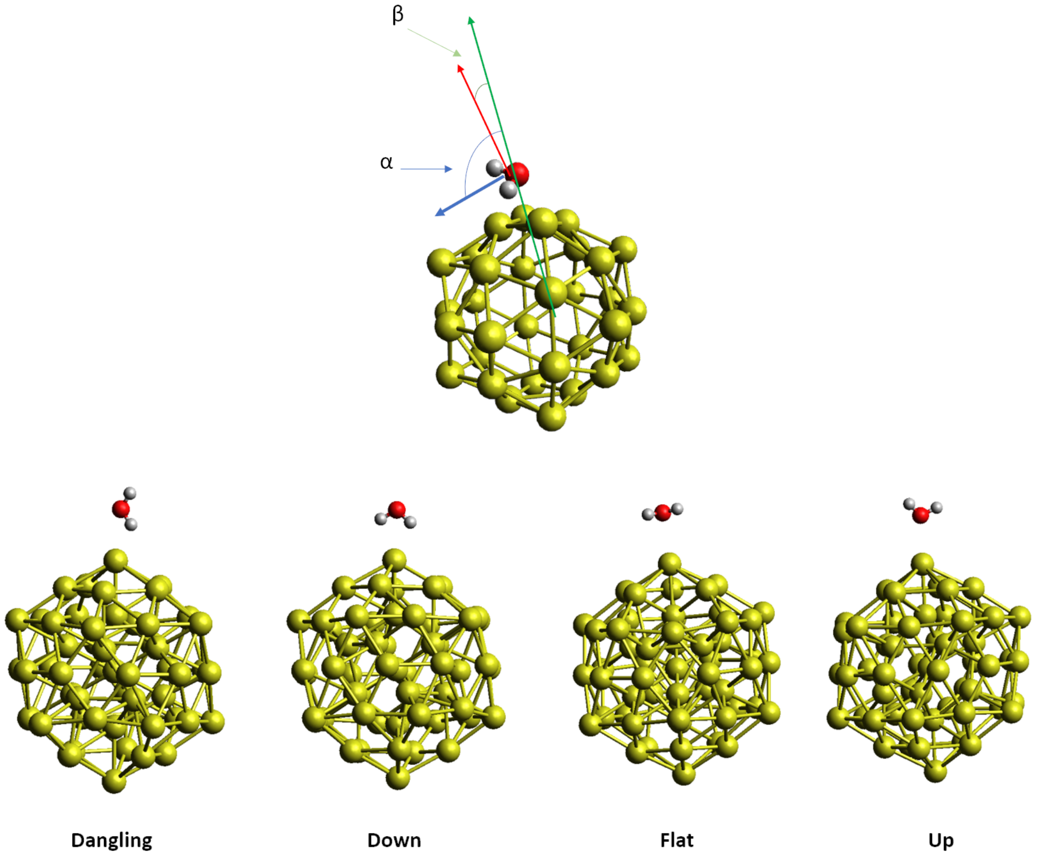

Figure 2.3: The schematic representation of the geometry descriptors for angle analysis, α and β, (top) and the different possible orientations of water on GNP (bottom)

Thirdly, the dynamic properties can also be computed, depending on the properties of interest. In our context, we are interested in the dynamic properties of hydrogen bond network of water solvation shell in the presence of increasing sizes of GNP. The self-diffusion coefficient (D) has been computed based on Einstein relation, according to Equation 2.8, with N represents the number of atoms, and $r(t)$ represents the displacement of the atoms. The time correlation function (C), as shown in Equation 2.9, gives information on the dynamic properties, with A or B corresponding to any property of interest, such as dipole moment or velocity. The autocorrelation functions of dipole moments of water molecules can be computed to obtain the re-orientational lifetime of water molecules, which is an important descriptor for hydrogen bond network. Additionally, vibrational properties can be calculated by applying Fourier transform on the correlation function of the velocities.

$$D = \lim_{t\to\infty} \frac{1}{6N} \frac{d}{dt} \sum_{\alpha=1}^{3} \sum_{i=1}^{N} \langle [r_{\alpha,i}(t) - r_{\alpha,i}(t_0)]^2 \rangle \tag{2.8}$$

$$C(t) = \lim_{\tau\to\infty} \frac{1}{\tau} \int_0^{\tau} A(t_0)B(t_0+t)dt_0 = \langle A(t_0)B(t_0+t) \rangle \tag{2.9}$$

2.3 Probing the Structural Properties of the Water Solvation Shell Around Gold Nanoparticles: A Computational Study

This section focuses on the systematic investigation of water structure around GNP, as experimental observations have indeed demonstrated the difference in the water structure in the vicinity of nanoparticles and surfaces. The strategy adopted in this study is investigating the change in the dynamics and structural properties of water surrounding an increasing size of GNP, which are Au_{32}, Au_{54}, Au_{55}, Au_{72}, Au_{79}, Au_{105}, Au_{147}, Au_{201}, Au_{344}, and Au_{887}. Furthermore, the vibrational density of states of the first solvation shell is calculated, to assess their hydrogen bond network. This work has been published in Journal of Chemical Physics and can be found in the following section, and the supporting information has been added in Appendix A.1.1.[31]

Probing the structural properties of the water solvation shell around gold nanoparticles: a computational study

Rika Tandiana,[1] Emilie Brun,[1] Cécile Sicard-Roselli,[1] Dominik Domin,[1] Nguyen-Thi Van-Oanh†,[1, a)] and Carine Clavaguéra†[1, b)]
Université Paris-Saclay, CNRS, Institut de Chimie Physique, UMR8000, 91405 Orsay, France

(Dated: December 27, 2020)

While subjected to radiation, gold nanoparticles (GNP) have been shown to enhance the production of radicals when added to aqueous solutions. It has been proposed that the arrangement of water solvation layers near the water-gold interface plays a significant role. As such, the structural and electronic properties of the first water solvation layer surrounding GNP of varying sizes were compared to bulk water using classical molecular dynamics, quantum and semi-empirical methods. Classical molecular dynamics was used to understand the change in macroscopic properties of bulk water in the presence of different sizes of GNP, as well as by including salt ions. The analysis of these macroscopic properties has led to the conclusion that larger GNPs induce the rearrangement of water molecules to form a 2D hydrogen-bond network at the interface. Quantum methods were employed to understand the electronic nature of the interaction between water molecules and GNP along with the change in the water orientation and the vibrational density of states. The stretching region of vibrational density of states was found to extend into the higher wavenumber region, as the size of the GNP increases. This extension represents the dangling water molecules at the interface, as a result of reorientation of the water molecules in the first solvation shell. This multi-level study suggests that in the presence of GNP of increasing sizes, the first water solvation shell undergoes a rearrangement to maximize the water-water interactions as well as the water-GNP interactions.

I. INTRODUCTION

Unwittingly, gold nanoparticles (GNP) have been used since ancient times, primarily as color additives. These nanoparticles are of nanometer size at least in one dimension, leading to quantum-size effects, resulting in their interesting optical properties. In the last few decades, scientists have successfully synthesized GNP of well-controlled size and geometry. This has led to the interest in utilizing GNP in various fields: catalysis, sensing, imaging, drug delivery, and radiotherapy treatments.[1–4] Recently, Sicard-Roselli *et. al.*[5–7] have developed a protocol for the quantification of hydroxyl radical production during water radiolysis and demonstrated the enhanced production of hydroxyl radicals in the presence of GNP and nano-diamonds. Contrary to the generally accepted explanation, which involves the ejection of secondary electrons (Auger's electron) and Compton's scattering by nanoparticles composed of heavy elements, they proposed that GNPs induced overproduction of hydroxyl radicals and solvated electrons is due to specific restructuring of water molecules at the interface. Such solvent structure has been observed experimentally, with X-ray Absorption Spectroscopy, at the interface of nano-diamonds.[8–11] Recently, Novelli *et al.*[12] have probed water structure surrounding GNP with Terahertz and mid-IR spectroscopy, and it is characterized by weaker hydrogen bonds than those found in bulk water. However, only limited atomistic detail can possibly be obtained from these experiments. Molecular simulation studies may provide a significant insight into this interesting GNP-water interfacial phenomenon.

Many theoretical approaches have been used to probe the interfacial behavior of solvent on metal NPs, including atomistic approaches that model the interaction with atomic clusters (up to 100 atoms) using quantum and semi-quantum approaches,[13–17] and classical molecular dynamics (MD) studies of solvents near gold metal surfaces (either [111] or [100] phase) with a few layers of gold atoms repeated along the xy plane.[18–21] In the classical MD framework, the quality of the force field which contains the important physical effects, is crucial in achieving the right interfacial behavior. Heinz *et al.*[22] were among the first to develop a force field for metal surfaces based on the Lennard-Jones potential. The r_0 and ε_0 parameters were refined against experimental data for cell parameters and surface tensions. Their compatibility with existing biomolecular force fields leads to their application in many simulation studies of gold surfaces and GNPs in interaction with their environment. The force field provides reasonable agreement with experiments or density functional theory (DFT) results.[18,21,23,24] Though, Heinz's force field provides good results in reproducing the interfacial structure of metal surfaces, there are still limitations in describing their interaction with biomolecules or a polar solvent. For example they have neglected polarization effects that are crucial in accurately describing the interaction with highly polar molecules. Geada *et al.*[25] later developed a polarizable Lennard-Jones potential to describe interaction between metal surfaces with ions. Iori *et al.*[26] then developed the *GolP* force field that focuses on the interaction between Au [111] surfaces and proteins in water. The interaction energy was decomposed into a gold polarization term, a chemisorption term, a van der Waals term, and a π conjugation system term. This force field has been demonstrated to perform well for

---

[a)] Electronic mail: van-oanh.nguyen-thi@universite-paris-saclay.fr

[b)] Electronic mail: carine.clavaguera@universite-paris-saclay.fr

†These authors contributed equally to this work.

the surface interaction with small representative molecules, such as water, imidazole and phenol. This force field has also been further refined to include more specific corrections to the interaction of the gold surface with proteins,[27] sulfur,[28] and nucleobases.[20,29] Recently, Clabaut *et al.*[30] have also developed a new force field for noble metal interfaces, called *GAL19*, to represent ten different facets of interfaces. Their interaction includes physisorption, chemisorption and angular dependence, to accurately replicate the preferred adsorption geometry obtained in DFT calculations. Meanwhile, Berg *et al.*[19] evaluated the different force field parameters and their transferability for gold surface [001 and 111 lattices] interacting with water molecules against DFT calculations. They concluded that the different choices of parameters give rather different interfacial behaviours pointing out the need for better model for gold-water interface and hence, they propose a set of optimized parameters especially catered to this interaction. As such, the molecular dynamics simulation needs to be carefully compared and interpreted with respect to the desired properties (e.g. water structural features or self diffusion coefficient).

Quantum chemistry methods have also been applied to study the interfaces of GNP systems, with atomic clusters and/or small nanoparticles used to represent bulk surfaces. For example, Huang *et al.*[13] have employed DFT to probe the nature of the interaction between O_2 and a series of small gold cluster anions (n=1-7). DFT was also used to investigate the interaction between Au_{32} and amino acids[14] or between naringin and gold clusters.[15] The adsorption of monomer and bilayer water molecules on a series of metal nanoparticles, including Au [111] surface, has been reported by Meng *et al.*,[31] using a plane wave representation. They probed the electronic aspect of water-metal interaction by looking at charge transfer and OH vibrational stretching modes. The catalytic activity of a GNP on a carbon nanotube for water dissociation has been studied at the DFT level.[32] They reported a lowered activation energy as water interact with the GNP. Chan *et al.*[33] have also looked into the stability of the shapes of GNP (up to 100 atoms) interacting with a water solvation shell at the DFT level, highlighting the importance of GNP stability for their application in radiotherapy. Though the fully quantum methodology allows accurate determination of the electronic and structural properties of small GNPs, the method is computationally limited in the size of systems that may be treated. Therefore, many have turned their attention to the approximate quantum methods, such as Density Functional Based Tight-Binding (DFTB), to reduce the computational time and to extend the range of system sizes that are accessible. Fihey *et al.*[34] have recently developed parameters for gold-thiolates systems in the DFTB framework to accurately reproduce geometries, energies and electronic properties obtained at the DFT level. Oliveira *et al.*[35] have conducted a benchmark of the Au-Au parameters for a series of gold clusters against DFT. These parameters have been used in different studies to determine the properties of gold and silver clusters, nanoparticles and bulk,[36] the role of surface charge on the orientation of water at the interface for the application in electrodes,[37] and the interaction between gold clusters and biomolecules.[38]

These various theoretical approaches have definitely provided valuable insights into the interfacial interaction between gold surfaces and water molecules. However, the number of studies that directly model the interfacial structure of GNPs, is still limited. The geometrical features of nanoparticles have generally been accepted to affect the orientation and stability of adsorbed molecules, in particular biomolecules.[24,39] Therefore, it is highly possible that water structures itself differently around these GNPs as well. In this current article, we propose systematic approaches to probe the water structure at the GNP interface. The investigation starts by using classical MD simulations to probe the physical and structural properties of water molecules in the presence of GNPs of increasing sizes. This step allows one to systematically follow the restructuring of water molecules as the size of GNP increases. With the same methodology, the effect of salt on the restructuring of water molecules is studied as the ions have been found to affect the production of hydroxyl radicals under irradiation.[6] Then, the electronic properties are investigated to probe the interaction between GNP with one water molecule. This is done in order to understand how the presence of vertices on GNP affects the orientation of the water molecule, both at the DFT and DFTB quantum levels. Since hydrogen bond networks play an important role in the arrangement of water molecules, the systems are extended to include the first solvation shell. Electronic and structural properties such as orientation of water molecules and vibrational density of states are investigated. The results obtained by the combination of these classical and quantum approaches are then used to describe and support the experimental observations and hypotheses.[5–7]

II. METHODOLOGY

A. Structures

A series of GNP was studied from the size of 0.8 nm to ca. 3 nm. Their corresponding geometries, shown in Figure 1 were taken from the database for silver nanoparticles[40,41] except for Au_{32} and Au_{72} for which the geometries were previously optimized at the DFT level.[42] The initial geometries of each of the GNP were re-optimized without constraints at the DFTB level. As shown in the Figure 1, each of the nanoparticles adopts a different geometry, exposing surfaces of different shapes to water. Au_{32} and Au_{72} are almost spherical and symmetrical with a cavity in the center. Au_{54} and Au_{105} are decahedron with different height and width. Au_{55} and Au_{147} adopt an icosahedral structure, Au_{79} adopts an irregular truncated octahedron and Au_{201} resembles a regular truncated octahedron. Au_{344} adopts an octahedral structure. Au_{887}, the largest structure studied here, is almost spherical in shape. The calculated structural and electronic properties of the GNP at DFTB level are tabulated in *Table S1*. The calculated Au-Au bond lengths are comparable with the experimental values, which are around 2.73 Å obtained from EXAFS for Au nanoparticles and 2.88 Å for bulk Au.[43] As mentioned in the previous section, the DFTB parameters for Au-Au interactions were benchmarked by Cuny et. al. and the Au-Au distances have

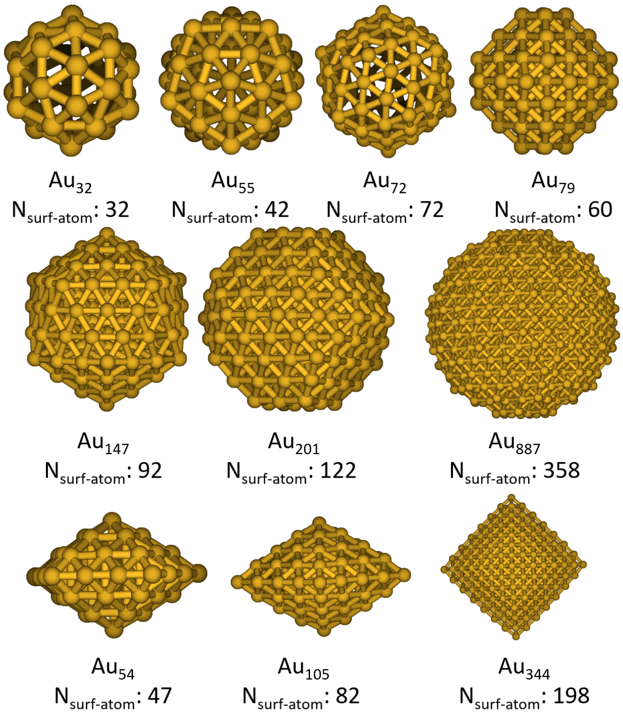

Figure 1. Series of GNP in this study with the number of surface atoms: (top row; from left to right) Au_{32}, Au_{55}, Au_{72}, Au_{79}, (middle row) Au_{147}, Au_{201}, Au_{887}, (bottom row) the non-spherical group: Au_{54}, Au_{105}, and Au_{344}.

been found comparable to the DFT values.[36] Therefore, the GNP structures obtained from DFTB geometry optimizations are likely to be reliable.

B. Computational strategy

With the inherent limitation of different computational methods, the following systematic multi-level approach is proposed to answer the questions regarding the interfacial water/GNP interactions. Firstly, classical MD is employed to investigate the physical and structural properties of water molecules in the presence of increasing size of GNPs. This step allows us to follow systematically the restructuring of water molecules as the size of GNP increases. In addition, the effect of salt on the restructuring of water molecules at the interface is studied. All the molecular dynamics simulations were performed with the GROMACS package.[44–50] The force field parameters for GNP were taken from a previous study in which the parameters were optimized for water-gold interactions on a gold surface (see *Table S2*).[19] Water molecules are modeled using the rigid SPC/E model.[51–55] Preliminary simulations indicated that the structure of GNP changed during the simulation in the presence of water. Rigid Au-Au bonds were imposed during the MD simulation to preserve the GNP 3D structure. Such practice has also been adopted in previous studies of GNP interacting with organic molecules.[21,23,24,27–30] The technical details of the MD simulations are given in Supplementary Material. The relevant properties of the systems, such as energetic properties, radial distribution function, and self-diffusion coefficient of solvent, were analyzed using tools available in the GROMACS software package. For systems that include salt, several solvent molecules were replaced by the desired number of sodium and chloride ions, while maintaining the neutrality of the system. To ensure the reliability of the simulations, the potential energy, average pressure, average temperature, average density and average total energy of the system were computed for each simulation ensemble. Several examples of such properties are provided in *Figure S1* to show the stability of the simulations.

Secondly, quantum methods were used to investigate the electronic properties that underlie the interaction between GNP with one water molecule. Subsequently, since hydrogen bond network plays important role in the arrangement of water molecules, the systems are extended to include the first solvation shell. The electronic and structural properties are then investigated, such as orientation of water molecules and the vibrational density of states. DFT calculations were made with the deMon2k code.[56] The calculations used an auxiliary density reduced computational cost algorithm which reduces the scaling of the calculation of Coulomb interactions and the numerical integration of exchange correlation energies to the number of generated auxiliary functions instead of the size of the system. The PBE functional, associated to empirical dispersion corrections, was used with the DZVP basis set for Oxygen and Hydrogen atoms, and the Stuttgart relativistic effective core potential (60 core electrons) with 19 valence electrons explicitly treated in combination with its basis set for Au.[57]

Meanwhile, the self-consistent charge DFTB (SCC-DFTB) formalism was used in which the total energy is a second-order Taylor expansion of the Kohn-Sham energy with respect to the charge density variations.[58–61]. All DFTB calculations were performed with DFTB+ code.[62,63] The parameters used for the systems under study were obtained from previously reported publication.[34,36] The geometry optimization of the systems was done with the conjugate gradient algorithm without any constraint. Dispersion corrections were systematically introduced using the DFTB3 framework[64] along with hydrogen bond corrections, as proposed in previous publications.[65] Normal mode analysis was performed by Hessian calculations. The resulting vibrational density of states (VDOS) spectrum was then plotted in the form of histogram because infrared intensities are not provided by DFTB+. The technical details are also provided in Supplementary Material.

Interaction energies E_{tot} of the system at the DFT and DFTB level were obtained via

$$E_{int} = E_{tot} - E_{Au} - E_{wat}$$

with E$_{Au}$ the electronic energy of GNP, and E$_{wat}$ the total electronic energy of the water molecules considered in the geometry of the full system.

The deformation energies E$_{def}$ of GNP at the DFTB level were obtained by the following formula:

$$E_{def} = E_{Au-wat} - E_{Au-vac}$$

with E$_{Au-wat}$, the electronic energy of GNP in water and E$_{Au-vac}$ the electronic energy of GNP in vacuum.

1. *Water angle analysis*

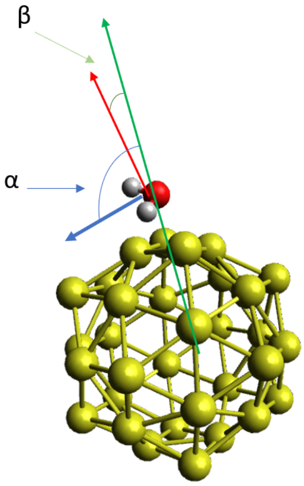

Figure 2. Schematic diagram to define the α and β angles.

The orientation of water molecules with respect to the center of mass (*com*) of GNP is analyzed and is defined by the α and β angles as shown in Figure 2. The definition of the angles were adopted from previous publication on the orientation of water molecules with respect to a gold surface.[19]. α corresponds to the angle between the dipole of water molecule to the vector which is formed between the *com* of GNP and the oxygen atom of the water molecule; β corresponds to the angle between the normal of water molecule to the vector between *com* of GNP and the oxygen atom of the water molecule. According to this definition, the flat configuration of water molecules is characterized by the α angle of ca. 90° and β angle of either close to 0° or close to 180°. The up configuration is characterized by the α angle of less than 90° regardless of the β angle value. The dangling configuration is characterized by the α angle of ca. 90° and β angle of ca. 90°. To quantify the different configurations of water molecules, the criteria set for flat configuration was when α is within 80° to 120° and β is either below 30° or above 150°. The criteria for up configuration has been set to be as long as α is less than or equal to 70°. As for the dangling configuration, both α and β have to be within 70° to 110°.

2. *Choice of DFTB parameters*

In the literature, there is currently one parameter set available for Au-Au, Au-O, and Au-H interactions, named as "auorg", which was benchmarked for the Au-Au interactions and Au interactions with organic molecules (O, S, H, C) in an aqueous environment.[34] Furthermore, water-water interaction can be described by different available sets. We tested water-water parameters from mio-1-1 set which was extensively used for water and solvated Titanium systems.[66] The results of different parameter set associations were compared with DFT calculation for three different GNP interacting with one water molecule (see *Table S3*) and on Au$_{54}$ with one solvation shell (see *Table S4*) with the possibility of addition of hydrogen bond corrections. The "auwater" parameter set corresponds to the "auorg" parameter for GNP and Au-water interaction, and mio-1-1 parameter for water and water-water interaction. Comparing the interaction energies and the Au-water distance for one water molecule interaction in *Table S3*, the "auwater" parameter set gives the closest values to that of DFT results. In the case of one solvation shell, the addition of hydrogen correction gives a higher interaction energy between the two. Therefore, all DFTB calculations will be performed using the "auwater (Hbond)" set.

III. RESULTS

A. Structural investigation

The investigation started by analyzing the physical properties of water molecules in the presence of GNP, such as the density, self-diffusion coefficient and re-orientational lifetimes. These properties, computed from classical MD trajectories, are shown in Figure 3 and are tabulated in *Table S5* with the goal of analyzing the change in solvation properties of water in the presence of GNP. The simulation of a pure water box, consisting of 1504 water molecules, was performed for reference. The calculated density was 998.5 kg.m^{-3}, while the calculated self-diffusion coefficient was 2.65×10^{-5} cm^2.s^{-1}. These values are comparable to the experimental values of 997 kg.m^{-3} and 2.299×10^{-5} cm^2.s^{-1}, respectively.[52] The self-diffusion coefficient of water molecules in the presence of GNP is also tabulated in *Table S5*. Since the self-diffusion coefficient has been calculated for all the water molecules (inclusive of the solvation shell of GNP), changes in this value correspond to an implication of the retardation of water molecules at the solvation shell. Hence this retardation is attributed to interfacial interaction between GNP and water molecules. From Figure 1, it is clear that the GNP studied adopt different geometries, and were classified into almost spherical GNP and non-spherical GNP. Therefore, the number of surface atoms of GNP that are exposed to water molecules varies with both size and geometry. To further understand the effect of the exposed surface atoms, the value of the self-diffusion coefficient is plotted with respect to the number of surface atoms in Figure 3 (top). It shows a decreasing trend in the self-diffusion coefficient as the surface area of

GNP increases. For the non-spherical GNPs (represented by black squares), the change in the self-diffusion coefficient is not notably high as the number of surface atoms increases, as compared to the spherical GNP (red triangles).

Another important property to probe the water network at the interface is the re-orientational relaxation lifetime of water molecules, because this movement requires the breaking and formation of new hydrogen bonds with their respective neighbors. In pure water, each water molecule forms hydrogen bonds with their neighboring molecules, and the re-orientational relaxation lifetime was calculated to be 4.81 ± 0.01 ps. In the presence of GNP, there is a competition between the interaction of GNP-water and water-water, especially at the interface. This competition then strongly influences the hydrogen-bond network formation at the interface, which can be probed by measuring this lifetime. Similarly, the correlation between this lifetime and the number of surface atoms is plotted in Figure 3 (bottom). In the graph, an increase of the lifetime is observed as the number of surface atom increases, which implies that the structure of the hydrogen-bond network has been disturbed by the presence of GNP. It could be assumed that as the surface area of the interface increases, the water molecules have been forced to rearrange to maximize the interaction with the neighboring water molecules as well as with GNP. As such, in the presence of GNP as small as Au$_{32}$, diameter of 8 Å, the relaxation lifetime noticeably increases. It can be noticed that there is a smaller retardation of the lifetime as the size of the surface atom of the non-spherical GNP increases as compared to that of the almost spherical GNPs. A maximum retardation is noticed before it decreases for the larger GNP.

To rationalize the retardation for small atom clusters shown in Figure 3, the ratio between the number of water molecules at the first solvation shell to the number of surface Au atoms was calculated. For the almost spherical GNPs, the ratio slowly decreases from 2:1, for Au$_{32}$, to almost 1:1 for Au$_{887}$. With increasing size of almost spherical GNPs, the average number of water molecules directly in contact with surface atoms decreases, but on the other hand, the effect on the alignment of water molecules increases, which leads to reduction in flexibility of the water structure. But, as the ratio approaches 1:1 for Au$_{887}$, the retardation on water molecules decreases as the water structure re-arranges to accommodate GNP. On the other hand, the ratio calculated for the non-spherical GNPs is 1:1, 1:1, and 1:1.5 respectively. The presence of vertices on the non-spherical GNPs decreases the average number of water molecules directly in contact with Au atoms. This explains the rather small change in retardation observed in both properties. This decrease in the density of water molecules adjacent to almost spherical GNP when size increases, is also known as dewetting as the water molecules progressively move away from the surface as a result of formation of interface and the re-arrangement of water molecules to maximize the formation of hydrogen bond network with their surroundings.[67] The progressive change of this water orientation with increasing size of GNP could be the reason for the initial maximum (for re-orientational lifetime) or minimum (for self-diffusion coefficient) before eventually a decrease or an increase, respectively. It could signify the formation of an interface at the large GNP. However, with the limited number of points, it is still too far-fetched to draw a trend.

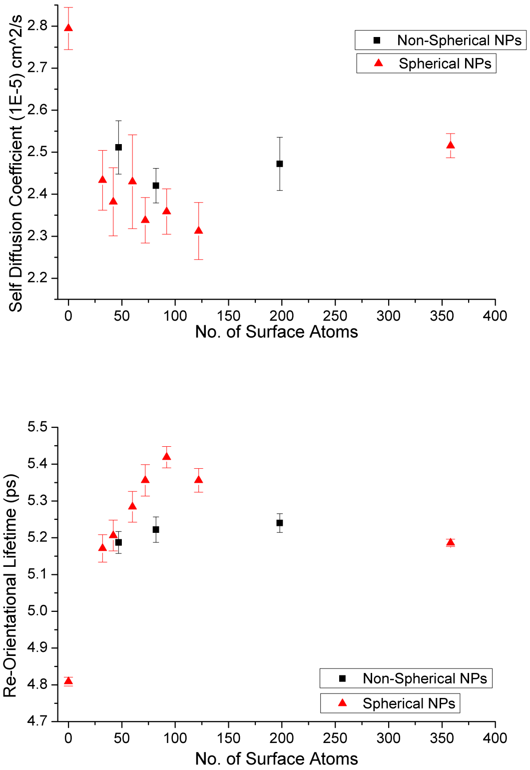

Figure 3. Change in self-diffusion coefficient (top) and orientational relaxation lifetime (bottom) with respect to number of surface Au atoms (black squares for the non-spherical GNPs and red triangles for the spherical GNPs).

To further examine the arrangement of water molecules within the first solvation shell of GNP, the α and β angles previously defined for water molecules with respect to the center of mass (*com*) of GNP were investigated for the almost spherical structures (e.g. Au$_{32}$, Au$_{55}$, Au$_{72}$, Au$_{79}$, Au$_{147}$, Au$_{201}$, and Au$_{887}$). The definition as represented in Figure 2 does not hold for the non spherical GNP as they contain edges and corners and induce a different way of packing. The plot of distribution of α and β for the different GNP is shown in Figure 4. At a glance, during the dynamics, water molecules adopt the up and flat configurations more than the down configuration. Looking at the effect of the size of GNP on the orientation of water molecules, there is an increase in the number of water molecules adopting dangling configurations as the size increases (both α and β within 70° to 110°). This clearly suggests the rearrangement of water molecules as proposed previously. Based on the quantification of the angle distribution, the ratio between flat:up configurations increases very slowly as the size of GNP increases. As such, the increase of the number of dangling configurations, supported also by the increase in the ratio between flat:up configurations, strongly suggests the rearrangement of water molecules to presumably form a 2D hydrogen-bond network, as observed at the air-water interface proposed by Pezzotti *et al.*[68]. Performing this angle analysis on the second solvation shell has revealed that there is considerably larger percentage of water molecules that adopt the down configuration, to connect to the first layer of hydrogen bond network. Beyond the second solvation shell however, the distribution of the angles reflects the one in bulk water. This implies that the re-arrangement of water molecules is not limited to the first solvation shell, but it also affects the second solvation shell all the more so as the first shell was impacted.

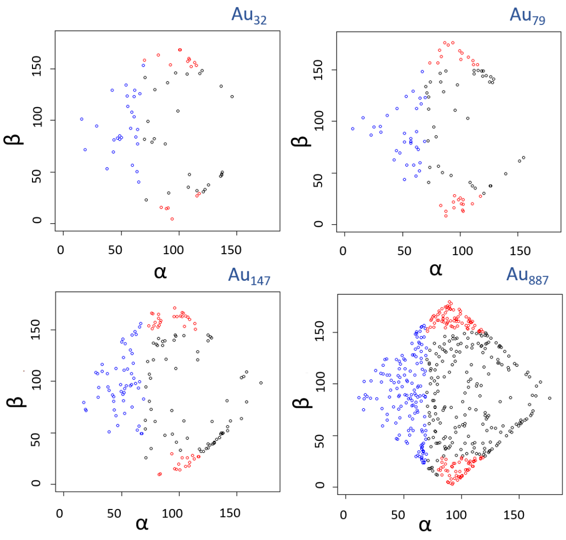

Figure 4. The distribution of α and β angles for Au_{32}, Au_{79}, Au_{147}, and Au_{887}, respectively. Blue circles represent up configuration, red circles represent flat configuration, and black circles represent other configurations.

To understand the spatial arrangement of the water molecules, the radial distribution function (RDF) of water oxygen was computed with respect to the *com* of GNPs as the reference, and it was corrected with respect to the GNP radius to study the geometry effect of GNPs. The plot of the RDF of different GNP systems is shown in Figure 5 (top). Alongside the shape, the position and the width of the first solvation peak vary depending on the geometry. This carries significant implication in defining the boundary between the first solvation shell and the bulk for further analysis. RDFs were also computed with respect to the surface of GNP and shown in the middle of Figure 5. One important observation is that the distance of the first RDF peak coincides for all the studied systems, which implies that the distance of water molecules to the surface of GNP is independent of the size and geometry of GNP. Since the it is not normalized, the y-axis of the plot corresponds to the number of water molecules at that particular distance. As expected, with increasing surface area of GNP, the number of water molecules within the first solvation shell also increases proportionally. In fact, when the number of shell water molecules is normalized against the number of surface Au atoms of the respective GNP, a decreasing trend is observed to achieve a 1:1 ratio eventually for the large and spherical GNP. This implies that more water molecules (or even organic ligands) can be packed at the interface when the curvature of the GNP is small. This curvature, in fact, plays a crucial role in determining the packing density at the interface of NPs. It is also observed that the width of the first RDF peak is narrow, while the next peak is broader. This implies that the water molecules in the first solvation shell are highly structured, due to the interaction with GNP, while the influence of GNP decreases in the subsequent shells, supporting similar observations that have been reported in other studies.[37]

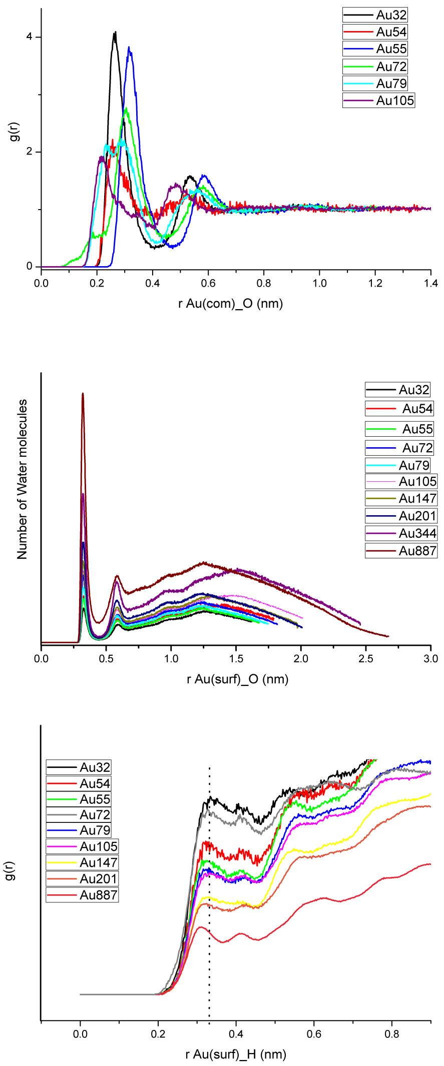

Figure 5. Radial distribution functions of water oxygen with respect to the center of mass of the GNPs (top) or surface of GNPs (middle), and radial distribution function of water hydrogen with respect to surface of GNP (bottom).

Finally, the RDF of hydrogen atoms with respect to the surface of GNP is shown at the bottom of Figure 5. Here, there is a shift in the first peak closer to the surface of GNP which corresponds to the increase in the presence of dangling water molecules that are pointing towards the surface of GNP. This water reorganization is represented by a schematic view in Figure 6. The increasing presence of the dangling configurations of water molecules in larger GNP system is supported by the observed angle distributions.

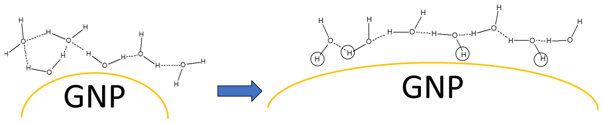

Figure 6. Scheme of the change from 3D to 2D network at the GNP interface.

B. Investigation of the salt effect

Experimentally, the presence of salt plays an important role in regulating the ionic strength and hence the stability of GNPs in a solution. At high concentration of salts, GNPs start to aggregate, while at low concentration, the presence of ions influences the zeta potential of GNP. In addition, Sicard-Roselli *et al.*[6] demonstrated that the addition of salt impacts significantly the radical production as 0.1% (m/v) of NaCl induces a decrease of more than 40% of hydroxyl radical. Based on their hypothesis on the role of water structure at the interface, this change in production of hydroxyl radicals indicates a change in water structure due to the presence of salt. So far, no experimental evidence has been published that indicates the perturbation of the interfacial water structure in the presence of salt. Therefore, a few water molecules were replaced by Na^+ and Cl^- maintaining the neutrality of the system during the simulations. Here, there are two variables of interest: the number of ions in the system and the size of GNP. Then, the angle distribution of the solvation shell and the RDF of the water molecules with respect to the ions is investigated to understand the organization of water molecules at the interface. The main results are provided in Table I.

The effect of increasing the number of ions in the system is considered taking Au_{32} as a model system. The number of chloride ions is increased from 1 to 5, 10, 15, and 20 atoms, along with the same amount of sodium ions. The average pair distances between Au_{32} and Na^+ and Cl^- highlight that Cl^- ions are present closer to the surface in average, as compared to Na^+. In addition, with increasing the number of ions, the average pair distance for both Na^+ and Cl^- is decreasing, which means that both types of ions are getting closer to the surface of GNP. According to the RDF, the ions are present far from the surface of GNP in the cases of a low ratio, and they are present right at the boundary between the first and second solvation shells at the highest ratio. The analysis on the angle of water molecules at the surface of Au_{32} (see Table I and *Figure S4*) shows an increasing trend in the proportion of dangling water molecules when the number of ions are increased. As the ions approach the surface of GNP (in the case of 1:1 to 1:10), they start to exert influence on the vicinity of the interfacial arrangement, as it can be seen from the fluctuation in the proportion of dangling water molecules (both α and β within 70° to 110°). As more ions are added, the proportion of dangling water molecules further increases. Therefore, the arrangement of water molecules at the interface is disrupted in the presence of salt ions.

Then, the effect of increasing the size of GNP is investigated, while leaving the number of ions constant (1:10 ratio) for Au_{32}, Au_{55} Au_{79}, Au_{147}, Au_{201} and Au_{887}. Similarly, we start our investigation with calculating the average pair distance between GNP and Na^+ and Cl^-, respectively. The averaged pair distance of GNPs reveals that the ions are located close to the surface of GNP, and based on RDF, they are present at the border between first and second solvation shell. In this case, the proportion of dangling water molecules with respect to the proportion of the system without salt (see Table I and *Figure S5*) shows a rather significant change in the proportion of dangling water molecules, as also observed in the previous case. For smaller sized GNP, the proportion increases in the presence of salt. Meanwhile, for larger sized GNPs, this proportion decreases in the presence of salt. This different modification for the small GNP (Au_{32}, Au_{55}, and Au_{79}) and the large GNP (Au_{147}, Au_{201}, and Au_{887}) could arise due to the different water structure of the respective system in the absence of ions. Consequently, the ions modify the water structure accordingly. However, the presence of salt does not alter the flat and up configurations significantly.

Table I. Percentage of the different water orientations residing at the solvation shell of GNPs without (1:0 ratio) and with the presence of salt ions, and Au-ion distances.

System	Ratio of GNP:Cl^-	Flat (%)	Up (%)	Dangling (%)	Au-Cl^- (nm)	Au-Na^+ (nm)
Au_{32}	*1:0*	*26.05*	*32.99*	*4.20*	-	-
Au_{32}	1:1	26.59	32.84	3.78	1.168	1.235
Au_{32}	1:5	25.63	32.31	4.37	0.729	0.756
Au_{32}	1:10	25.93	32.24	3.85	0.613	0.639
Au_{32}	1:15	26.26	31.99	4.02	0.548	0.572
Au_{32}	1:20	27.30	31.26	4.88	0.518	0.528
Au_{55}	*1:0*	*26.77*	*31.87*	*3.48*	-	-
Au_{55}	1:10	28.65	31.20	3.80	0.565	0.608
Au_{79}	*1:0*	*27.46*	*32.13*	*3.64*	-	-
Au_{79}	1:10	27.55	30.66	4.50	0.565	0.603
Au_{147}	*1:0*	*28.99*	*30.42*	*4.79*	-	-
Au_{147}	1:10	31.69	30.95	3.62	0.581	0.635
Au_{201}	*1:0*	*30.54*	*30.85*	*4.58*	-	-
Au_{201}	1:10	30.14	30.55	4.13	0.552	0.605
Au_{887}	*1:0*	*23.99*	*28.93*	*5.33*	-	-
Au_{887}	1:10	24.71	28.93	4.99	0.694	0.788

C. Quantum chemistry investigation of water structure at the interface with GNPs

Considering the classical MD does not take into account the electronic properties of the interaction, we turned to the approximate quantum DFTB method to investigate the role of electronic effect on the interaction. DFTB is heavily dependent on the quality of the parameters in order to achieve accurate calculations. Therefore, we started the investigation by validating the DFTB method against DFT calculations.

1. Validation of DFTB results

A benchmark of DFTB was performed against DFT/PBE calculations in terms of interaction energies and charge transfer. The model used for this benchmark was Au_{32} interacting with one water molecule and one solvation shell (see *Table S6, Table S7, and Figure S8*). The interaction energies of the Au_{32}-water system follow the same global trend between the two methods. However, the minimum distance between Au_{32} and the water oxygen is ca. 2.6 Å at the DFT level, while the distance is ca. 3.0 Å at the DFTB level. Furthermore, the charge transfer was defined as the change in total charge of GNP after interacting with water. The values of charge transfer follow the same trend at both levels, even if the quantity is larger for DFT as compared to DFTB, due to the minimal and localized basis set used in DFTB. For Au_{32} surrounded by one solvation shell, the interaction energy per water molecule at DFT and DFTB levels agrees pretty well, with a difference less than 0.1 eV (*Table S7 and Figure S8*). With the consistent trend observed for both interaction energy and charge transfer between the two levels, we considered it to be reasonable to perform qualitative structural analysis on the calculations at DFTB level for the different size of GNP, despite the overestimation of the optimal distance between GNP and one water molecule shown in *Table S3*. In addition, similar parameter set has also been used by Fazio *et al.* to perform molecular dynamics on the charged and neutral Au_{55} surrounded by water shells.[37]

2. Interaction of GNP with one water molecule

The interaction between a single water molecule and GNP was studied to search for the most stable water configurations and GNP's preferred adsorption sites. The investigation started with the smallest GNP available, Au_{32}. The different possible configurations of the water molecule interacting with GNP were compared. The flat configuration is found to be the most stable configuration and the up configuration is slightly higher in energy (see *Figure S9*). The optimization step at both DFT and DFTB levels subsequently yields the same configuration, albeit at different distances. Furthermore, being almost spherical, Au_{32} does not have a preferred adsorption site. It is also observed that there is a charge transfer from the water molecule to GNP which is characteristic of chemisorption phenomenon. In *Table S6*, the charge transfer decreases as the distance between GNP and water increases, which is explained by the change in the extent of orbital's overlap as the distance grew.

As such, the frontier molecular orbitals (MOs) of Au_{32} and the water molecule are investigated with the electron transfer occurring from the HOMO of the water molecule toward the LUMO of GNP. Having two lone pairs localized on the oxygen atom, these HOMOs are available to donate electrons. Figure 7 shows that the HOMOs of the water molecule can be either perpendicular to or along the water molecule's plane. Therefore, the water molecule can adopt either the flat or up configuration to an optimized overlap of the interacting orbitals, with the flat configuration preferred as indicated from the calculated interaction energy in *Figure S9*.

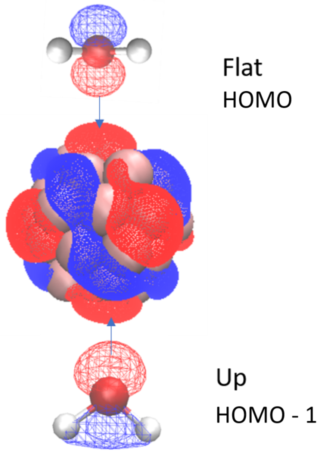

Figure 7. The favored up or flat configuration as a result of overlapping frontier orbitals for Au_{32} with one water molecule.

Subsequently, the interaction energies between the different sizes of GNP with one water molecule were computed and provided in *Table S8*. The optimized geometries are therefore shown in *Figures S10, S11, S12 and S13* for the GNPs of various sizes. Since the larger GNPs under study are not all spherical, there are various possible adsorption sites (Figure 8). In the case of Au_{54} and Au_{105}, there are four different possible sites, whose interactions will in turn differ (see *Figure S10 and S13*). Au_{55} is slightly spherical, with one likely interaction site, and Au_{79} possesses edges, with two possible interaction sites. Therefore, the structure of each GNP with one water molecule initially positioned at the different interaction sites was optimized. But it was performed in a local configuration phase, therefore, the minima may not include the most stable one on the potential energy surface.

Following the previous observation of charge transfer and orbital overlap in Au_{32}, the chemisorption characteristics are present for the larger GNPs. The highest occupied MOs are degenerated resulting in fractionally occupied MOs (see the five highest occupied and five lowest unoccupied MOs for

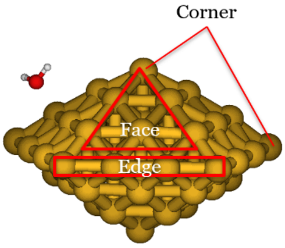

Figure 8. Possible configurations and adsorption sites for a water molecule interacting with GNP.

Au_{54} in *Figure S14*). As a result, these fractionally occupied orbitals can also accept electrons from the incoming water molecule. Therefore, the determination of the participating MOs is not as straightforward as that of Au_{32}, where the first LUMO is the most possible orbital to accept electron. Indeed due to the presence of these multiple possible accepting MOs, the water molecule at different initial positions can interact with whichever MOs that are the nearest to it. For example for Au_{54}, the first configuration is optimized with the water molecule positioned at the top corner of GNP and it can in turn interact with either the fourth or fifth orbitals (*Figure S14*). For the second configuration, the water was positioned close to the edge site, and hence was able to interact with also either fourth and fifth orbitals (*Figure S14*). The water molecule was placed at the face site for the third configuration, and in turn it can interact with the second or third orbitals. For the last configuration, where the water molecule was placed at the side corner site, it can interact with either the second, third, fourth or fifth MOs. However, the nature and the strength of the overlap between the participating orbitals differ, and affect the interaction energy and the charge transfer. For Au_{54}, the fourth configuration is found to be the most energetically favored. Similar observations can be deduced for the other GNP interacting with a single water molecule.

3. *One-shell solvation of GNP*

It has been recently demonstrated that water molecules get organized in a 2D hydrogen-bond network with dangling O-H bonds at air-water interface.[68] Furthermore, dangling water molecules were found at the surface of the GNP in the classical MD simulations presented above. As a result, there is a competition between Au-water and water-water interactions at the interface, which then dictates the orientation of water molecules. The objective was to investigate the arrangement of one-shell water molecules at the DFTB level to take into account electronic effects. The structure of the GNP + one-shell water molecules has been initially derived from the classical MD trajectory, by selecting the water molecules that are within a certain distance from the center of mass of GNP (the distance obtained from the first RDF peak).

Firstly, the electronic and energetic properties of the systems were analyzed and provided in Table II. The interaction energy, normalized over the total number of water molecules, is found to fluctuate around the same values. The charge transfer from water to GNP increases globally with the increase of the size of GNP, and is found to be proportional to the increase of interacting water molecules in the shell. This implies that these properties are independent of the size of GNP,[33] but rather dependent on the surface area of GNP. This is expected, as the surface area directly correlates with the number of molecules interacting at the surface. The deformation energy of GNP is relatively small for all the systems pointing to no change in the shape of GNP as it comes into contact with water molecules, which implies stability of the GNP structures. This information is very important considering the application of GNP in many diverse fields, such as catalysis, sensing, drug delivery, that the GNP has to maintain their structural integrity to achieve the desired effect.[33]

Then, the structural properties of the water molecules in the solvation shell were compared to that of a water droplet of 109 molecules. These properties are the distribution of α and β angles of water molecules with respect to the *com* of GNP, the distribution of O-H bond lengths and H-O-H angles, in an attempt to understand the impact of the presence of GNP to the structural features. Figure 9 shows the distribution of the α and β angles for different sizes of GNP. For the smallest system of Au_{32}, 57 % of the water molecules adopt the flat configuration and 33 % the up configuration, with the remaining adopting dangling or down configurations. Similarly for Au_{79}, 59 % of the water molecules adopt the flat configuration and 22 % the up configuration, and the rest of the water molecules adopting dangling or down configurations. Moving to larger GNP, Au_{147} and Au_{201} have 58 % and 26 %, and 52 % and 20 %, for flat and up configurations, respectively. The percentage of water molecules adopting a flat configuration remains constant across the size of the nanoparticle, but the number of up configurations noticeably decreases with the size of GNP. In turn, these water molecules increasingly adopt dangling configurations, signature of interfacial water, or down configurations. This trend can be rationalized such that when the size of GNP increases, the water molecules, which prefer either the flat or up configurations when present in isolation, are forced to rearrange themselves to maximize the hydrogen-bond formation in the solvation shell. This trend seen in increasing proportion of dangling water molecules is consistent with the observation from classical MD simulations. The quantification of the various configurations of water molecules is different, however. This difference arises from the geometry optimization step, the missing temperature effect, and the smaller total number of water molecules in the DFTB calculations. In any case, consistent trend in the rearrangement of water molecules is observed between DFTB and classical MD simulations.

Next, the distribution of O-H bond lengths of water molecules shows that there is an increase in the population of shorter bond length for the solvation shell, resulting in the decrease of the mean O-H bond length as the GNP size increases (*Figure S15*). These shorter bond lengths can be correlated to the presence of almost isolated water molecules at the inter-

Table II. DFTB Interaction energies, interaction energies per water, deformation energies, charge transfer and percentage of the different water orientations for a series of GNP with one water solvation shell.

System	No. of water	E_{int} (eV)	E_{int}/water (eV)	E_{def} (eV)	Charge Transfer (e)	Flat (%)	Up (%)	Dangling (%)
Au_{54}	96	-11.363	-0.118	0.033	-1.465	-	-	-
Au_{55}	77	-9.1047	-0.118	0.028	-1.037	57.1	31.2	0
Au_{79}	110	-13.639	-0.142	0.065	-1.688	59.1	21.8	1.8
Au_{105}	148	-15.547	-0.105	0.043	-1.577	-	-	-
Au_{147}	160	-19.678	-0.205	0.099	-2.181	58.8	25.6	0.6
Au_{201}	212	-25.229	-0.263	0.160	-2.775	52.4	20.3	2.4
Au_{344}	320	-38.483	-0.120	0.064	-3.815	-	-	-

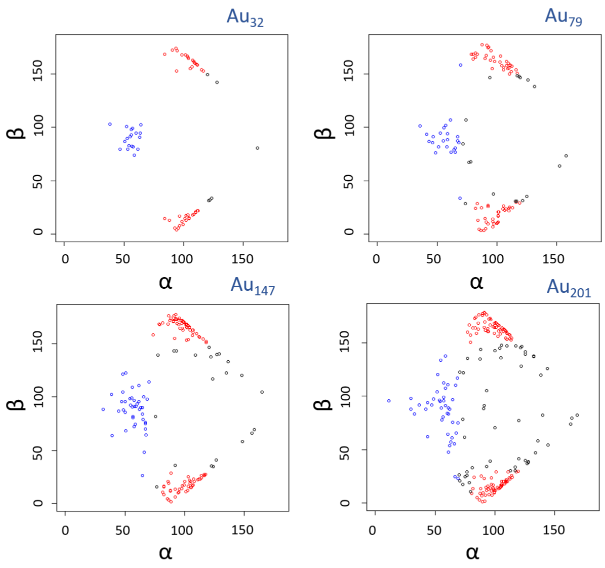

Figure 9. α and β angles of the water molecules in the solvation shell with respect to the *com* of GNP for Au_{32}, Au_{79}, Au_{147}, and Au_{201}, respectively, with red circles representing the flat configurations, blue circles for the up configurations, and black circles for the other configurations.

face or the weakening of hydrogen bonds in the system. As observed in the distribution of the α and β angles, as the size of GNP increases, the number of water molecules pointing towards the interface (both dangling and down configurations) increases. As such these water molecules form fewer hydrogen bonds with their neighbors, as compared to those in flat and up configurations, which results in the observed shorter O-H bond lengths. The H-O-H bond angles has also been analyzed but there is no significant change observed as the size of GNP increases (*Figure S16*).

To further probe the structure of water molecules in the solvation shell, normal mode analysis was performed to obtain the vibrational density of states (VDOS) as shown in Figure10 for the 3000 - 4000 cm^{-1} frequency range (see *Figure S17* for full frequency-range VDOS). The VDOS of the water droplet was also calculated as a reference. Bending modes of water molecules near 1500 cm^{-1} are not perturbed by the presence of GNP. These bending modes are typically linked to the H-O-H angle of water molecules, and as mentioned earlier the angle does not significantly change in the presence of GNP. On the other hand, the stretching modes of water molecules between 3200 - 4000 cm^{-1} are influenced by the presence of GNP. Notably, the stretching frequencies are extended towards higher frequencies, as compared to those in pure water. Consistent with the O-H bond length analysis mentioned above, the high stretching frequencies are a result of the increasing number of water molecules that are forming fewer hydrogen bonds as a result of the configurations pointing towards the interface (down and dangling configurations).[12]

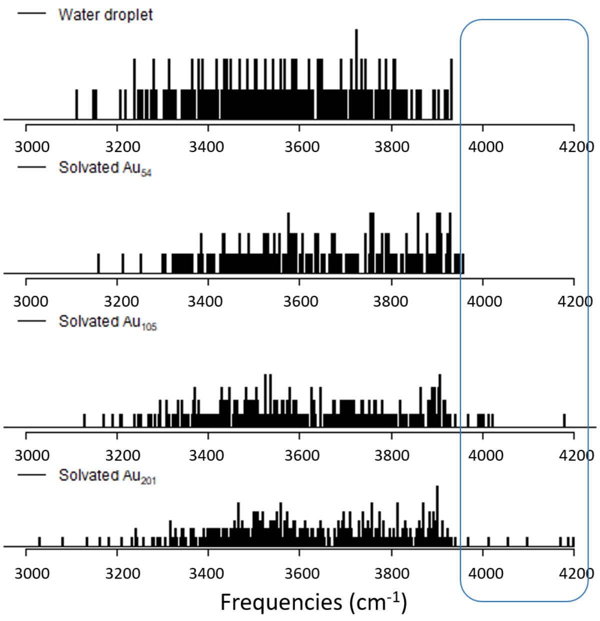

Figure 10. VDOS of water in water droplet, Au_{54}, Au_{105}, and Au_{201}, respectively.

IV. DISCUSSION

This systematic analysis has demonstrated a rearrangement of the water molecules at the interface of increasing size of GNP, in support of the experimental observation of specific water organization at the surface of nanoparticles.[8,12] For small structures, GNP introduces a perturbation to the resulting physical properties (e.g. self-diffusion coefficient and re-orientational lifetime) as the water molecules come into contact with the surface Au atoms. This perturbation increases with the GNP size until eventually the perturbation leads to the rearrangement of water molecules to form 2D hydrogen-bond networks for larger GNPs. This could explain the behavior of the self-diffusion coefficient and the re-orientational lifetime (Figure 3) which initially shows an increase in retardation before decreasing for the largest GNPs, as the water molecules re-arrange to form a 2D network. As seen in the DFTB results, charge transfer occurs between GNP and one water molecule, and the effect is modulated based on the orientation of the water molecule. This charge transfer also plays an important role in the structuring of water. Particularly for the large GNPs, the combination between this electronic property and the hydrogen-bond formation between water molecules contributes to the change in the water structure at the interface. In the experiment performed by Sicard-Roselli *et al.*,[5,6,69] the GNP used was large in size (∼6 and 32 nm in diameter) in comparison to the system studied here (∼2 nm in diameter) and minimal amount of citrate ligands are present at the surface. However, by extrapolating these data, it is safe to assume that water molecules at the interface have rearranged to form 2D hydrogen-bond network. Even though directly comparable properties are not available experimentally, especially on increasing size of GNPs or the effect of charge transfer on the water structure, the current analysis corroborates the hypothesis that the presence of GNP induces rearrangement of water molecules at the interface, which could be responsible for specific nanoparticle properties. Several experimental and theoretical studies on the structure of water molecules at the interface of gold surface and GNP have been reported, with different approaches and descriptors.[31,37,70–73] The current results have been not only consistent with the previous studies, but also have provided a deeper insight as well as additional descriptors into both the electronic and structural properties of water molecules at the interface of GNP.

The addition of salt ions in the simulations demonstrates that the structure of interfacial water is perturbed due to the presence of ions that reside close to the surface. They introduce a competition between the Au-water and ions-water interactions. With increasing concentration of salt ions, both Na^+ and Cl^- generally reside closer to the surface of GNP. This could be the underlying reason for the aggregation of GNPs induced by high concentration of salt, as the repulsion between GNPs is diminished. Meanwhile, at the intermediate concentration of ions (1:10), the arrangement of water molecules is considerably changed as shown in Table I. Considering that the unique water structure at the interface facilitates the production of hydroxyl radical, hence, perturbation introduced into this structure by the presence of salt ions might be responsible for the change in hydroxyl radical yield measured experimentally.[6]

Both structural and electronic properties of the water molecules at the interface were studied using DFTB. The structure of water molecules at the solvation shell was analyzed with vibrational density of states and evolution of the water bond lengths and angles. This analysis highlights that the OH bond lengths decrease with the increasing size of GNP, which implies change in the strength of the hydrogen-bond network at the solvation shell. Such structural change was observed experimentally by Novelli *et al.*, by using both the THz and mid-IR spectroscopy.[12] This shortening of OH bonds, which indirectly implies increased activation energy for bond breaking, could contradict the initial expectation that the presence of GNP facilitates the bond breaking, resulting in high production of hydroxyl radicals. However another point of view could also be, that the presence of extended hydrogen-bond network actually protects the water molecules, because the deposited energy can be delocalized throughout the molecules, so resulting in lower localized OH bond breaking. But, when the hydrogen-bond network is weakened, the energy deposition is localized to several water molecules, resulting in higher probability of bond breaking, as compared to the extended hydrogen-bonded network. However, the scope of this work only involves system at ground state. The study of systems at excited states is, however, possible with the recent development of Real-Time Time-Dependent DFT. Recent applications of this method include the topological analysis of charge migration after irradiation[74] and the calculation of stopping power of lithium cluster,[75] or biomolecules.[76] By employing this method, it would then be interesting to model and study the irradiation of the different water structures either in bulk or at the interface.

Despite the advantages of classical MD for the structural study, there are limitations due to the lack of description of electronic effects or physical properties, such as polarizability. Similarly, the inherent limitation of DFTB also lies in the parameters describing the interaction between different atoms, as demonstrated in the current study. Though DFT is generally accepted as an accurate method, it comes with high computational cost that increases quickly with increasing size of the systems. Therefore, classical MD and DFTB are still attractive alternatives provided that the parameters are built and developed very carefully. The force field currently used in the study was developed for gold surfaces, and it does not take into account the polarizability of the molecules. Particularly in the case of salt addition, the effect of polarization was largely ignored, which might have played important roles on the alignment of water molecules at the interface as well. Therefore, development of a force field tailored to NPs, that includes the polarization effect should be a further step in a future work in a fully flexible description. Similarly, the DFTB methodology holds a great promise in treating very large systems that consist of large nanoparticles (more than 5 nm) and their surrounding environments (solvent and ligands), once the parameters have carefully been set up. Then, DFTB will allow the computation of GNP plasmonic properties at the atomic level, and the investigation of their interaction with small ligands in relation with SERS experimental spectra.

V. CONCLUSION

In conclusion, we have successfully probed the re-orientation of water molecules at the interface by a step-wise approach involving different theoretical methodologies. The presence of increasing size of GNP affects the structural and physical properties of water molecules, to result in the formation of a 2D hydrogen-bond network. Addition of salt also perturbs the water structure as the ions reside close to the surface of GNP, leading to possible aggregation at high concentration which may change the production of hydroxyl radicals under irradiation. DFTB was used to study the electronic and structural properties of the interaction between GNP with water molecule(s). The presence of vertices in GNP results in different preferred orientations of water molecules across the series of GNP. Yet, the formation of 2D hydrogen-bond network has been also observed in large GNPs, i.e. Au_{201}, consistent with the observation seen in classical MD simulations. The vibrational density of states analysis suggests a weaker hydrogen-bond network with increasing GNP size, which has been previously observed experimentally using Terahertz IR spectroscopy. Therefore, despite the inherent limitations introduced by the methodologies, the approach adopted in this study provides a glimpse into re-arrangement of water molecules and the effects on structural and electronic properties. These results provide supporting evidence that the water structure at the interface of GNP is different from that in bulk water.

SUPPLEMENTARY MATERIAL

See Supplementary Material for a detailed description of the methodology, tables with supplementary data from MD, DFT and DFTB calculations, and complementary figures as described and cited in the text.

ACKNOWLEDGMENTS

This work was supported by GDR 2035 SolvATE GDR funded by CNRS. This work was performed using HPC resources from GENCI [CINES/IDRIS] (Grant 2019-[A0060806830]).

DATA AVAILABILITY STATEMENT

The data that support the findings of this study are available within the supplementary material and from the corresponding author upon reasonable request.

REFERENCES

[1] Z. Kuncic and S. Lacombe, Phys. Med. Biol. **63**, 02TR01 (2018).

[2] X. Huang, I. H. El-Sayed, W. Qian, and M. A. El-Sayed, J. Am. Chem. Soc. **128**, 2115 (2006).

[3] T. T. T. N'Guyen, H. T. T. Duong, J. Basuki, V. Montembault, S. Pascual, C. Guibert, J. Fresnais, C. Boyer, M. R. Whittaker, T. P. Davis, and L. Fontaine, Angew. Chem. Int. Ed. **52**, 14152 (2013).

[4] O. Tahiri Alaoui, A. Herissan, C. Le Quoc, M. e. M. Zekri, S. Sorgues, H. Remita, and C. Colbeau-Justin, J. Photochem. Photobiol. A **242**, 34 (2012).

[5] C. Sicard-Roselli, E. Brun, M. Gilles, G. Baldacchino, C. Kelsey, H. McQuaid, C. Polin, N. Wardlow, and F. Currell, Small **10**, 3338 (2014).

[6] M. Gilles, E. Brun, and C. Sicard-Roselli, J. Colloid Interface Sci. **525**, 31 (2018).

[7] M. Kurzyp, H. A. Girard, Y. Cheref, E. Brun, C. Sicard-Roselli, S. Saada, and J.-C. Arnault, Chem. Commun. **53**, 1237 (2017).

[8] T. Petit, H. Yuzawa, M. Nagasaka, R. Yamanoi, E. Osawa, N. Kosugi, and E. F. Aziz, J. Phys. Chem. Lett. **6**, 2909 (2015).

[9] M. Zobel, R. B. Neder, and S. A. J. Kimber, Science **347**, 292 (2015).

[10] M. Zobel, Acta Cryst. A **72**, 621 (2016).

[11] S. L. J. Thomä, S. W. Krauss, M. Eckardt, P. Chater, and M. Zobel, Nature Comm. **10**, 995 (2019).

[12] F. Novelli, M. Bernal Lopez, G. Schwaab, B. Roldan Cuenya, and M. Havenith, J. Phys. Chem. B **123**, 6521 (2019).

[13] W. Huang, H.-J. Zhai, and L.-S. Wang, J. Am. Chem. Soc. **132**, 4344 (2010).

[14] M. Darvish Ganji, H. Tavassoli Larijani, and R. Alamol-hoda, Sci. Rep. **8**, 11400 (2018).

[15] B. Singh, M. Rani, J. Singh, L. Moudgil, P. Sharma, S. Kumar, G. S. S. Saini, S. K. Tripathi, G. Singh, and A. Kaura, RSC Adv. **6**, 79470 (2016).

[16] G. Chadha and P. Chug, Materials Research Express **5**, 065038 (2018).

[17] S. Liu, Materials Research Express **6**, 1150g3 (2019).

[18] D. Liang, J. Hong, D. Fang, J. W. Bennett, S. E. Mason, R. J. Hamers, and Q. Cui, Phys. Chem. Chem. Phys. **20**, 3349 (2018).

[19] A. Berg, C. Peter, and K. Johnston, J. Chem. Theory Comput. **13**, 5610 (2017).

[20] M. Rosa, R. Di Felice, and S. Corni, Langmuir **34**, 14749 (2018).

[21] M. Tang, N. S. Gandhi, K. Burrage, and Y. Gu, Langmuir **35**, 4435 (2019).

[22] H. Heinz, R. A. Vaia, B. L. Farmer, and R. R. Naik, J. Phys. Chem. C **112**, 17281 (2008).

[23] E. Heikkilä, A. A. Gurtovenko, H. Martinez-Seara, H. Häkkinen, I. Vattulainen, and J. Akola, J. Phys. Chem. C **116**, 9805 (2012).

[24] Q. Shao and C. K. Hall, Langmuir **32**, 7888 (2016).

[25] I. L. Geada, H. Ramezani-Dakhel, T. Jamil, M. Sulpizi, and H. Heinz, Nature comm. **9**, 716 (2018).

[26] F. Iori, R. Di Felice, E. Molinari, and S. Corni, Journal of Computational Chemistry **30**, 1465 (2009).

[27] L. B. Wright, P. M. Rodger, S. Corni, and T. R. Walsh, J. Chem. Theory Comput. **9**, 1616 (2013).

[28] Z. Futera and J. Blumberger, J. Chem. Theory Comput. **15**, 613 (2019).

[29] M. Rosa, S. Corni, and R. Di Felice, J. Chem. Theory Comput. **10**, 1707 (2014).

[30] P. Clabaut, P. Fleurat-Lessard, C. Michel, and S. N. Steinmann, J. Chem. Theory Comput. **16**, 4565 (2020).

[31] S. Meng, E. G. Wang, and S. Gao, Phys. Rev. B **69**, 195404 (2004).

[32] N. K. Jena, K. R. S. Chandrakumar, and S. K. Ghosh, RSC Adv. **2**, 10262 (2012).

[33] C.-H. Chan, F. Poignant, M. Beuve, E. Dumont, and D. Loffreda, J. Phys. Chem. Lett. **10**, 1092 (2019).

[34] A. Fihey, C. Hettich, J. Touzeau, F. Maurel, A. Perrier, C. Köhler, B. Aradi, and T. Frauenheim, J. Comput. Chem. **36**, 2075 (2015).

[35] L. F. L. Oliveira, N. Tarrat, J. Cuny, J. Morillo, D. Lemoine, F. Spiegelman, and M. Rapacioli, J. Phys. Chem. A **120**, 8469 (2016).

[36] J. Cuny, N. Tarrat, F. Spiegelman, A. Huguenot, and M. Rapacioli, J. Phys. Condens. Matter **30**, 303001 (2018).

[37] G. Fazio, G. Seifert, M. Rapacioli, N. Tarrat, and J.-O. Joswig, Zeitschrift für Physikalische Chemie **232**, 1583 (2018).

[38] A. Domínguez-Castro, D. Hernández, and F. Guzmán, Theor. Chem. Acc. **136**, 84 (2017).

[39] I. Lynch and K. A. Dawson, Nano Today **3**, 40 (2008).

[40] A. Barnard, B. Sun, B. Motevalli Soumehsaraei, and G. Opletal, (2017), silver nanoparticle data set, https://data.csiro.au/collections/%23collection/CIcsiro:23472v3/DItrue.

[41] B. Sun, M. Fernandez, and A. S. Barnard, J. Chem. Inf. Model. **57**, 2413 (2017).

[42] A. J. Karttunen, M. Linnolahti, T. A. Pakkanen, and P. Pyykkö, Chem. Commun. , 465 (2008).

[43] W. Szczerba, H. Riesemeier, and A. F. Thünemann, Anal. Bioanal. Chem. **398**, 1967 (2010).

[44] M. J. Abraham, T. Murtola, R. Schulz, S. Páll, J. C. Smith, B. Hess, and E. Lindahl, SoftwareX **1-2**, 19 (2015).

[45] H. Berendsen, D. van der Spoel, and R. van Drunen, Computer Physics Communications **91**, 43 (1995).

[46] E. Lindahl, B. Hess, and D. van der Spoel, Molecular Modeling Annual **7**, 306 (2001).

[47] D. Van Der Spoel, E. Lindahl, B. Hess, G. Groenhof, A. E. Mark, and H. J. C. Berendsen, J. Comput. Chem. **26**, 1701 (2005).

[48] S. Páll, M. Abraham, C. Kutzner, B. Hess, and E. Lindahl, *Lecture Notes in Computer Science*, Vol. 8759 (Springer,Cham, 2015).

[49] S. Pronk, S. Páll, R. Schulz, P. Larsson, P. Bjelkmar, R. Apostolov, M. R. Shirts, J. C. Smith, P. M. Kasson, D. van der Spoel, B. Hess, and E. Lindahl, Bioinformatics **29**, 845 (2013).

[50] B. Hess, C. Kutzner, D. van der Spoel, and E. Lindahl, J. Chem. Theory Comput. **4**, 435 (2008).

[51] H. J. C. Berendsen, J. R. Grigera, and T. P. Straatsma, J. Phys. Chem **91**, 6269 (1987).

[52] P. Mark and L. Nilsson, J. Phys. Chem. A **105**, 9954 (2001).

[53] J. Zielkiewicz, J. Chem. Phys. **123**, 104501 (2005).

[54] M. W. Mahoney and W. L. Jorgensen, J. Chem. Phys. **114**, 363 (2001).

[55] L. A. Báez and P. Clancy, J. Chem. Phys. **101**, 9837 (1994).

[56] G. Geudtner, P. Calaminici, J. Carmona-Espíndola, J. M. del Campo, V. D. Domínguez-Soria, R. F. Moreno, G. U. Gamboa, A. Goursot, A. M. Köster, J. U. Reveles, T. Mineva, J. M. Vásquez-Pérez, A. Vela, B. Zúñinga-Gutierrez, and D. R. Salahub, WIREs Computational Molecular Science **2**, 548 (2012).

[57] P. Schwerdtfeger, M. Dolg, W. H. E. Schwarz, G. A. Bowmaker, and P. D. W. Boyd, J. Chem. Phys. **91**, 1762 (1989).

[58] W. M. C. Foulkes and R. Haydock, Phys. Rev. B **39**, 12520 (1989).

[59] M. Elstner, D. Porezag, G. Jungnickel, J. Elsner, M. Haugk, T. Frauenheim, S. Suhai, and G. Seifert, Phys. Rev. B **58**, 7260 (1998).

[60] T. Frauenheim, G. Seifert, M. Elstner, T. Niehaus, C. Köhler, M. Amkreutz, M. Sternberg, Z. Hajnal, A. D. Carlo, and S. Suhai, J. Phys. Condens. Matter **14**, 3015 (2002).

[61] M. Elstner and G. Seifert, Philosophical Transactions of the Royal Society A: Mathematical, Physical and Engineering Sciences **372**, 20120483 (2014).

[62] B. Aradi, B. Hourahine, and T. Frauenheim, J. Phys. Chem. A **111**, 5678 (2007).

[63] B. Hourahine, B. Aradi, V. Blum, F. Bonafé, A. Buccheri, C. Camacho, C. Cevallos, M. Y. Deshaye, T. Dumitrică, A. Dominguez, S. Ehlert, M. Elstner, T. van der Heide, J. Hermann, S. Irle, J. J. Kranz, C. Köhler, T. Kowalczyk, T. Kubař, I. S. Lee, V. Lutsker, R. J. Maurer, S. K. Min, I. Mitchell, C. Negre, T. A. Niehaus, A. M. N. Niklasson, A. J. Page, A. Pecchia, G. Penazzi, M. P. Persson, J. Řezáč, C. G. Sánchez, M. Sternberg, M. Stöhr, F. Stuckenberg, A. Tkatchenko, V. W.-z. Yu, and T. Frauenheim, J. Chem. Phys. **152**, 124101 (2020).

[64] M. Gaus, Q. Cui, and M. Elstner, J. Chem. Theory Comput. **7**, 931 (2011).

[65] J. Řezáč, J. Chem. Theory Comput. **13**, 4804 (2017).

[66] G. Dolgonos, B. Aradi, N. H. Moreira, and T. Frauenheim, J. Chem. Theory Comput. **6**, 266 (2010).

[67] D. Chandler, Nature **437**, 640 (2005).

[68] S. Pezzotti, D. R. Galimberti, and M.-P. Gaigeot, J. Phys. Chem. Lett. **8**, 3133 (2017).

[69] G. Baldacchino, E. Brun, I. Denden, S. Bouhadoun, R. Roux, H. Khodja, and C. Sicard-Roselli, Cancer Nanotechnology **10**, 3 (2019).

[70] J.-J. Velasco-Velez, C. H. Wu, T. A. Pascal, L. F. Wan, J. Guo, D. Prendergast, and M. Salmeron, Science **346**, 831 (2014).

[71] S.-P. Ju, J. Chem. Phys. **122**, 094718 (2005).

[72] C.-I. Chang, W.-J. Lee, T.-F. Young, S.-P. Ju, C.-W. Chang, H.-L. Chen, and J.-G. Chang, J. Chem. Phys **128**, 154703 (2008).

[73] K. Tay and F. Bresme, J. Mater. Chem. **16**, 1956 (2006).

[74] A. Parise, A. Alvarez-Ibarra, X. Wu, X. Zhao, J. Pilmé, and A. de la Lande, J. Phys. Chem. Lett. **9**, 844 (2018).

[75] I. Maliyov, J.-P. Crocombette, and F. Bruneval, Eur. Phys. J. B **91**, 172 (2018).

[76] A. Schleife, Y. Kanai, and A. A. Correa, Phys. Rev. B **91**, 014306 (2015).

2.3.1 Conclusion and Perspectives

Our analysis has shown that there is a rearrangement of water network at the vicinity of increasing sizes of GNP to form 2D hydrogen bond network, due to the increase in the proportion of planar surfaces at larger size of GNP. This rearrangement occurs as a result of maximizing both the water-water and water-surface interactions. Despite the limitation in the theoretical approach employed in the study, the observations are still consistent with experimental results. However, the correct dynamics of water molecules in the presence of other surface ligands (ions, organic molecules, etc.) on GNP surfaces is still crucial to describe correctly the dynamical processes at the interface, particularly the balance between ligand-surface, water-surface, and ligand-water interactions. Our work has shown that the presence of ions perturbed slightly the hydrogen bond network when they reside close to the surface. Similarly, previous study by Futera *et al.* have also indicated that surface ligands need to penetrate through the water layer to approach gold surface.[32] Furthermore, Berg *et al.* has demonstrated the variation in water orientation at the surface with the parameters, which could result in incorrect behavior of ligands at the surface.[5] Therefore, in the following section, an accurate force field describing the GNP-water interface, derived from GAL21 will be developed.

2.4 Development of an Accurate Force Field for the Au-Water Interaction

Despite the observation of unique water structure at the vicinity of metal surfaces and metal nanoparticles and the implications in various contexts, the investigation of the interaction at the interface of GNP is still proven challenging both experimentally and from theoretical approach. The challenges arise due to the complexity of the interaction at the surface, which includes the competitive interaction between surface, solute, and solvent. From the perspective of computational approach, a force field model is necessary to simulate systems containing hydrated GNP. However, the availability of accurate force field describing the GNP-water interaction becomes a serious limitation in providing correct behavior of water at the interface, as illustrated by Berg *et al.*.[5]

In the previous section, the classical force field molecular dynamics has been employed to probe the structure of water solvation shell on a series of increasing size of GNP. Despite using the force field parameters adapted to gold surface, we have obtained a consistent result as observed in experimental condition, where the re-arrangement of the first water solvation shell as the size of GNP increases was observed. However, there is still a need for a tailored force field for GNP (multifaceted particles), along with the inclusion of polarization term, which is important to correctly describe the interfacial interactions, especially in the cases where ions or charged ligands are included in the system.

Clabaut *et al.* has recently reported a highly accurate force field describing the interfacial interactions between noble metal surfaces and water.[28,29] This force field, called GAL, includes the angular dependence term in addition to the physisorption and chemisorption terms, and it has been shown to accurately replicate the DFT level optimized geometries, and the respective interaction energies. The force field has been implemented in CP2K package,[33] that is optimal for surface system with periodic boundary condition. Therefore, a molecular approach of modeling GNP as an alternative would be desirable, and hence, this work reports on the implementation of the force field in Tinker molecular package. The advantage of implementing in Tinker package is the ease of incorporation of AMOEBA polarizable force field into this functional form, which is another objective of ours in this study. Furthermore, different force fields for biomolecules is available within the package, which eventually enables the inclusion of biomolecules in the systems of interest.

All in all, this work is carried out in collaboration with S. Steinmann (Laboratoire de Chimie, ENS Lyon), and our objective in this section is threefold. Firstly, the implementation of GAL force field within Tinker software package is tested and validated. Secondly, we performed parametrization of GAL parameters fitted against

DFT reference data. Lastly, we coupled AMOEBA polarizable force field with GAL, and evaluated its performance.

2.4.1 GAL Functional Form

The general GAL force field (herein called GAL19)[28,29] has a different form from the typical force field, explained in the methodology section. This force field is a sum of pairwise interaction potential between Au-O and Au-H, as shown in Equation 2.10. The geometrical descriptors necessary for the calculation of the interaction are represented in Figure 2.4. The normal of the surface ($\vec{n}$) is defined as the summation of Au-Au interatomic pair vectors (represented by blue lines) within the cut-off of 3.0 Å, to include all the first neighbor atoms. In GNP, the normal of the different Au atoms at the surface is not always the same, due to their non-planar surfaces. Therefore, the calculation of surface normal has to be performed for each Au-water pair considered. The orientation of the water molecule is then described with several angles, which are $\varTheta$ representing the angle between the normal of the surface and the dipole moment vector of the water (represented as green line), ϕ (called propeller angle) and ω (called helicopter angle) angles describing the orientation of water with respect to the surface. When ϕ = 0°, the molecular plane of water is parallel to the surface.

$$V_{GAL19} = \sum_{H} \sum_{M \in \Omega(H)} V_{M,H}(\vec{r}_{M,H}) + \sum_{O} \sum_{M \in \Omega(O)} V_{M,O}(\vec{r}_{M,O}, \theta) \tag{2.10}$$

GAL force field can be further separated into the potential terms corresponding to Au-H interactions and the Au-O interactions. Firstly, the interaction potential between Au-H is described by the exponential repulsive wall, shown in Equation 2.11, with A_H representing the strength of the repulsion and the R_H representing the distance of the exponential decay.

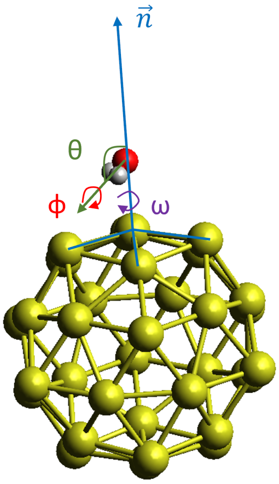

Figure 2.4: The schematic representation of the geometric descriptors for GAL: $\vec{n}$, the surface normal, is represented by the blue line; the water dipole is represented by the green line; the angles θ, ϕ, and ω are the angular descriptor to determine the water orientation with respect to the surface of GNP

The interaction potential between Au-O pairs, shown by Equation 2.12, can be decomposed into its components, which are the chemisorption term, consisting of V_G, attractive Gaussian potential, and V_A, the explicit angular dependence, and the physisorption term described by Tang and Toennies potential, V_{TT}.[34] Their respective tunable parameters are A, B, $C_6, \varepsilon_a, b_{||}, b_{\perp}, R_O, a_1, a_2, a_3$, and a_4.

$$V_{M,H}(\vec{r}_{M,H}) = A_H e^{-r_{M,H}/R_H} \tag{2.11}$$

$$\begin{aligned} V_{M,O}(\vec{r}_{M,O},\theta) =& V_G(\varepsilon_a, b_{||}, b_{\perp}; \vec{r}_{M,O}) + V_A(R_O, a_{1-4}; r_{M,O}, \theta) \\ &+ V_{TT}(A, B, C_6; r_{M,O}) \end{aligned} \tag{2.12}$$

The physisorption potential, V_{TT}, can be calculated based on the Equation 2.13, which consists of the exponential soft-wall potential, long-range London attraction, and a damping term. This potential introduces a continuous repulsive potential in the short range.

$$V_{TT}(r) = Ae^{-Br} - [1 - \sum_{k=0}^{6} \frac{(Br)^k}{k!} e^{-Br}] \frac{C_6}{r_6} \tag{2.13}$$

The chemisorption term comprises the Gaussian attractive term, V_G, and the angular dependent term, V_A, that can be written as Equation 2.14 and Equation 2.15, respectively. The asymmetry in the perpendicular ($\perp$), and parallel ($||$) direction of water molecule with respect to the surface is introduced by this Gaussian attractive term. With this asymmetry, a stabilization in the top site with respect to the hollow site can be imposed, which is the preferred site both in the DFT and experimental observation.[3,35] Additionally, the angular dependent term introduces a damped, truncated Fourier series of 4 terms, to reproduce the preferred orientation where the molecular plane of water is parallel to the metal surface. Finally, there are 13 adjustable parameters for GAL19, that have to be parametrized for each metal surface.

$$V_G(\vec{r}_{M,O}) = \varepsilon_a e^{-b_\parallel r_\parallel^2} e^{-b_\perp r_\perp^2} \tag{2.14}$$

$$V_A(M_i \in \Omega(O); r, \theta) = \frac{(e^{-r/R_O})^2}{\sum_{M_i \in \Omega(O)} e^{-r_{M_i,O}/R_O}} \sum_{n=1}^{4} a_n cos(n\theta) \tag{2.15}$$

2.4.1.1 Introducing Reactivity of GNP in GAL21

To further account for the environment (*i.e.* reactivity) of the individual metal atoms at the surfaces, the term generalized coordination number (GCN) has been proposed by Calle-Vallejo *et al.* and can be computed with Equation 2.16. This term has been demonstrated to have exceptional performance as a reactivity descriptor for the adsorption of small organic molecules on nanoparticles, over the traditional coordination number.[36] By definition, this generalized term conveys the information on the incomplete coordination sphere better than that of standard coordination number. GCN can be calculated by the sum of the coordination number of the closest neighboring atoms, divided by the maximum coordination number of metal in bulk (in general 12 for fcc metal). The GCNs for core atoms are within the range of 9 to 12, and those for surface atoms are within the range of 4 to 9, depending on their respective sites. Therefore, low values of GCN are associated with higher reactivity, and vice versa. The GCN of surface atoms of Au_{39}, Au_{55}, and Au_{79} are shown in Figure 2.5. Incorporating this term in the GAL19 force field will likely improve the transferability of the force field in multi-faceted metal nanoparticles, and it will be called GAL21 from here onwards.

$$GCN(i) = \sum_{j}^{n} \frac{CN(j)}{CN_{max}} \tag{2.16}$$

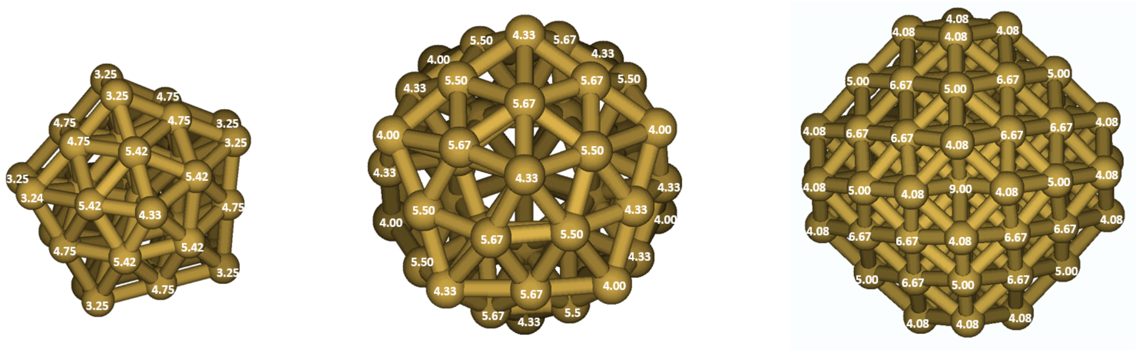

Figure 2.5: The computed GCN values corresponding to individual surface atoms of Au$_{39}$, Au$_{55}$, and Au$_{79}$.

With the addition of GCN parameter, the different parameters of GAL have become either linearly or exponentially dependent on GCN, which take the form in Equation 2.17 and Equation 2.18, respectively. The choice of either linear or exponential dependence has been decided based on the observation of either linear or quadratic correlation between the interaction of water molecule and the metal adsorption site. For the Au-H potential, the A_H and B_H parameters (replacing R_H of GAL19) become linearly dependent on the GCN. In the Au-O potential, the A and B terms in V_{TT} and the $b_\perp$ and $b_\|$ in Gaussian attraction term become linearly dependent on GCN, while the ε term in Gaussian attraction term becomes quadratically dependent. Lastly, the a_n terms in the angular terms become quadratically dependent on GCN. This dependency results in 29 adjustable parameters for GAL21.

$$L = L_{(1)}.GCN(M) + L_{(0)} \tag{2.17}$$

$$Q = Q_{(2)}.GCN(M)^2 + Q_{(1)}.GCN(M) + Q_{(0)} \tag{2.18}$$

2.4.2 Dataset and Fitting Procedure

2.4.2.1 Reference Dataset

Clabaut *et al.* fitted the GAL19 parameters with DFT interaction energy as reference data, which consists of single water molecule adsorbed at increasing distances and at varying orientations with respect to the metal surface.[29] Similarly, our dataset consists of the interaction between one water molecule with Au$_{39}$, Au$_{55}$, Au$_{79}$, Au$_{147}$, and Au$_{201}$ at increasing distances (from 2.0 Å- 4.0 Å) and at different orientations (which are flat, up, down, and dangling, as seen in Figure 2.3). Additionally, for Au$_{39}$ and Au$_{79}$, additional configurations of water molecules interacting at different interaction sites (such as edge, top, and face sites) are included (see Figure 2.6). In total, our dataset contains 115 structures for Au$_{39}$, 43 structures for Au$_{55}$, 132 structures for Au$_{79}$, 81 structures for Au$_{147}$, and 82 structures for Au$_{201}$. Lastly, to include many body effects, 357 additional structures with multiple water molecules, *i.e.* dimer (D), trimer (T), and tetramer (Te), interacting with Au$_{55}$ and Au$_{79}$ have been generated.

The interaction energies for all the configurations have been obtained with dispersion corrected DFT method with PBE functional (refer to the methodological section of Chapter 3 for more details on DFT calculation). The gold atom is described by a relativistic effective core potential (RECP) and its associated basis set, with 68 core electrons replaced by a potential, and 11 valence electrons treated explicitly. The water molecule is described with DZVP basis set. The interaction energy, E_{INT}, is then calculated with Equation 2.19, with E_{Au-H_2O} representing the energy of the complex, E_{Au} representing the energy of GNP, and E_{H_2O} representing the energy of water.

$$E_{INT} = E_{Au-H_2O} - (E_{Au} + E_{H_2O}) \tag{2.19}$$

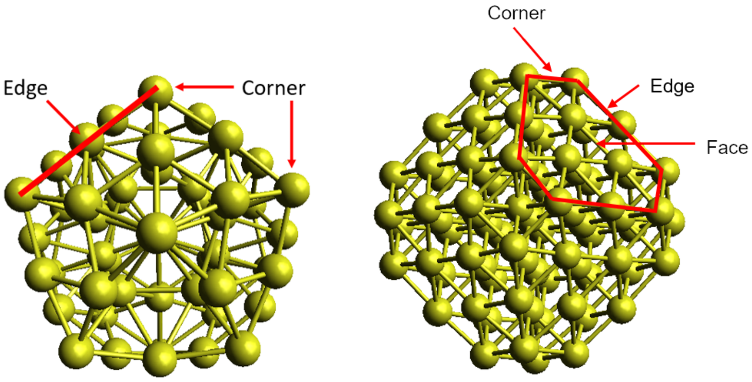

Figure 2.6: The schematic representation of Au$_{55}$ and Au$_{79}$ with the possible interaction sites highlighted.

2.4.2.2 Fitting Procedure

The Forcebalance software, interfaced with Tinker Molecular Package, was previously used to improve parameters of polarizable water models.[37] In this work, Forcebalance software has been used to optimize the parameters for GAL force field. The schematic representation of the systematic parametrization procedure is shown in Figure 2.7. The water model TIP3P has been used to represent water. The non-linear optimization has been performed with Newton-Raphson mode. The optimization is considered converged when two of the following criteria have been achieved: convergence criteria of 0.1 for objective function, convergence criteria 0.01 for gradient, or convergence criteria of 0.01 for step. During the fitting, only the interaction energy lower than 20.0 kcal/mol is considered in the calculation of objective function, to keep only the small repulsive behavior at short distances.

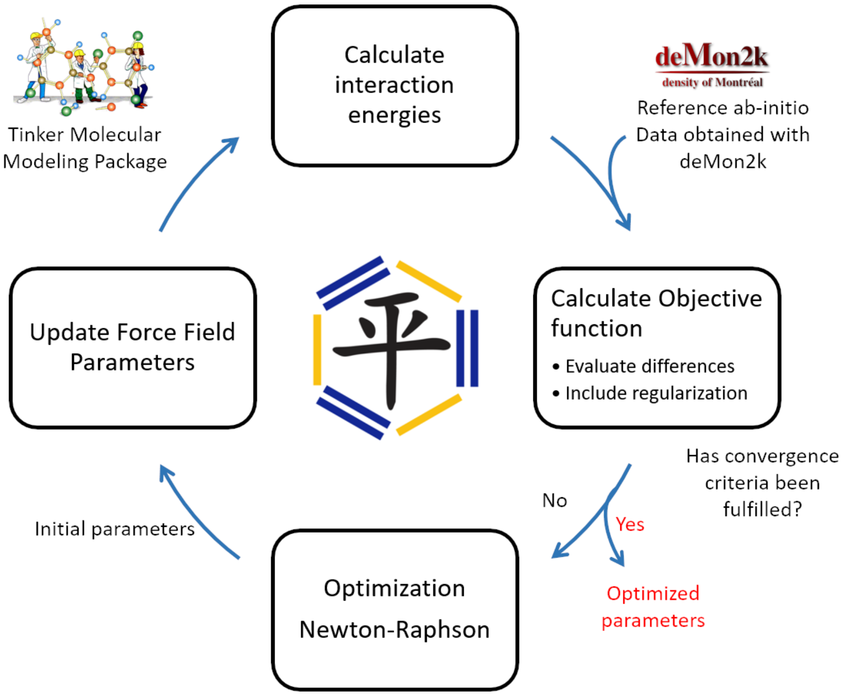

Figure 2.7: The schematic representation of the optimization procedure in Forcebalance adapted from the reference.[37]

2.4.3 Fitting for GAL19

The reported parameters for Au [100] (GAL-100) and Au [111] (GAL-111) (see Table A.1) have firstly been used to calculate the interaction energy of one water molecule interacting with Au_{39}, Au_{55}, and Au_{79}. The plots of the calculated interaction energies with both GAL-100 and GAL-111, with respect to the DFT reference data are shown in Figure 2.8. The plots indicate that the parameters fitted for surface system are not directly transferable for nanoparticle systems. The question that follows would be the selection of reference dataset, such as, which kind of structure (size and shape) of GNP should be taken for the fitting of the parameters, and then whether the parameters will be transferable to other structures not included in the dataset. To answer the question, a systematic fitting procedure has been carried out with different geometries included in the fitting dataset.

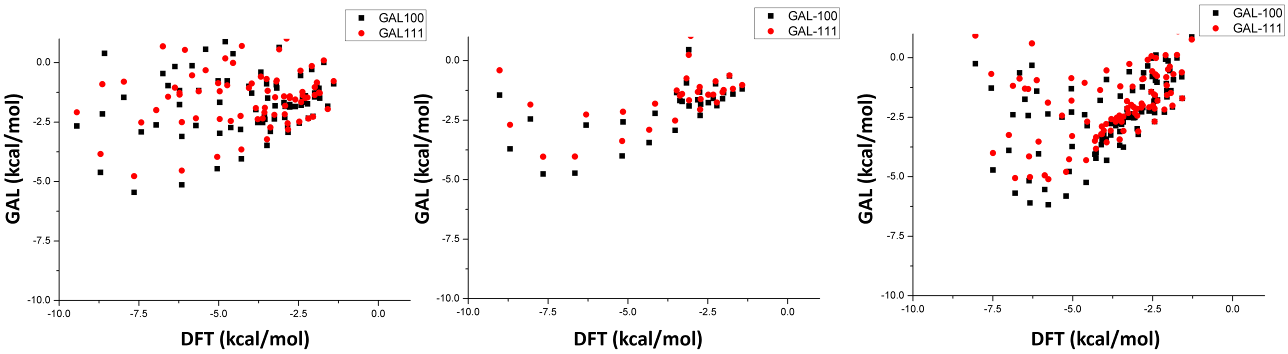

Figure 2.8: The calculated GAL interaction energies of 1 water molecule interacting with Au_{39} (left), Au_{55} (middle), and Au_{79} (right), with respect to the DFT energies: GAL calculation performed with the reported parameters fitted for Au [100] and Au [111] surfaces.

In the first fitting procedure, labelled as AuNP-fmix, the fitting was carried out for the interaction between one water molecule and Au_{39}, Au_{55}, and Au_{79}. In this set, the different interaction sites across different sizes and shape of GNP is explored. The second fitting procedure, labelled as AuNP-f79, only the interactions of 1 water molecule with Au_{79} at various interaction sites have been included in the fitting dataset. In this set, only the different interacting sites on Au_{79} are explored. In the last fitting procedure, labelled as AuNP-fall, on top of the interaction between one water molecule (monomer, M) with Au_{39}, Au_{55}, and Au_{79}, the interaction of multiple water molecules, *i.e.* dimer (D), trimer (T), and tetramer (Te), has also been included, to account for many body effects. In all of these fitting procedures, the values for C, R_O, and R_H have been taken from the reported Au [100] values, with the assumption that these values will not change much during optimization, and hence leaving 10 adjustable parameters. Table A.1 reports the optimized parameters for all the sets.

The parameters are then evaluated by calculating the RMSD of the predicted interaction energies against the DFT energies, and they are shown in Figure 2.9, Figure 2.10, and Table A.4. The calculation of RMSD has been done on the geometries whose interaction energies in DFT are less than 1 kcal/mol, excluding strongly repulsive interactions. The performance of the sets of parameters is evaluated based on their predictions for the systems that are not part of the fitting dataset, such as interaction of water on Au_{147} and Au_{201}, and also the interaction of multiple water molecules on Au_{55} and Au_{79}.

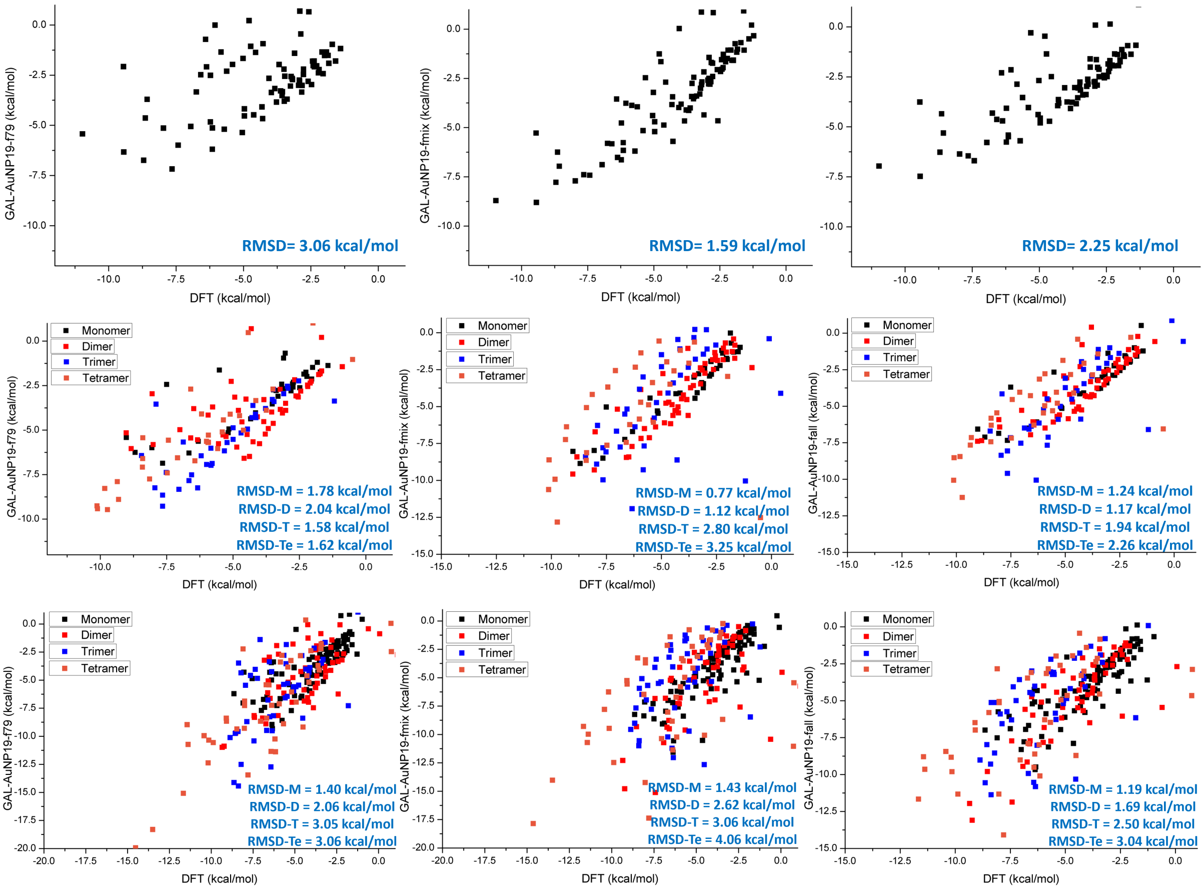

Figure 2.9: The calculated GAL interaction energies of Au_{39} (top), Au_{55} (middle), and Au_{79} (bottom) interacting with monomer (M), dimer (D), trimer (T), and tetramer (Te) of water with respect to the DFT reference energies, with the optimized parameters: (left) AuNP-f79, (middle) AuNP-fmix, and (right) AuNP-fall

For AuNP-fmix set, the parameters predict quite well the interaction energies of 1 water molecule with Au_{147} and Au_{201} (see Figure 2.10 middle column), with the calculated RMSDs being 2.91 and 1.62 kcal/mol, respectively. However, the RMSD increases as more water molecules interact at the surface of Au_{55} and Au_{79}(see Figure 2.9 the middle column of middle and bottom rows), for example the interaction energy of Au_{79} increased from 2.62 kcal/mol for adsorption of two water molecules to 4.06 kcal/mol for adsorption of four water molecules. As such, the transferability of these parameters across different GNPs size and shape is quite good, while the description of many body effects is moderate.

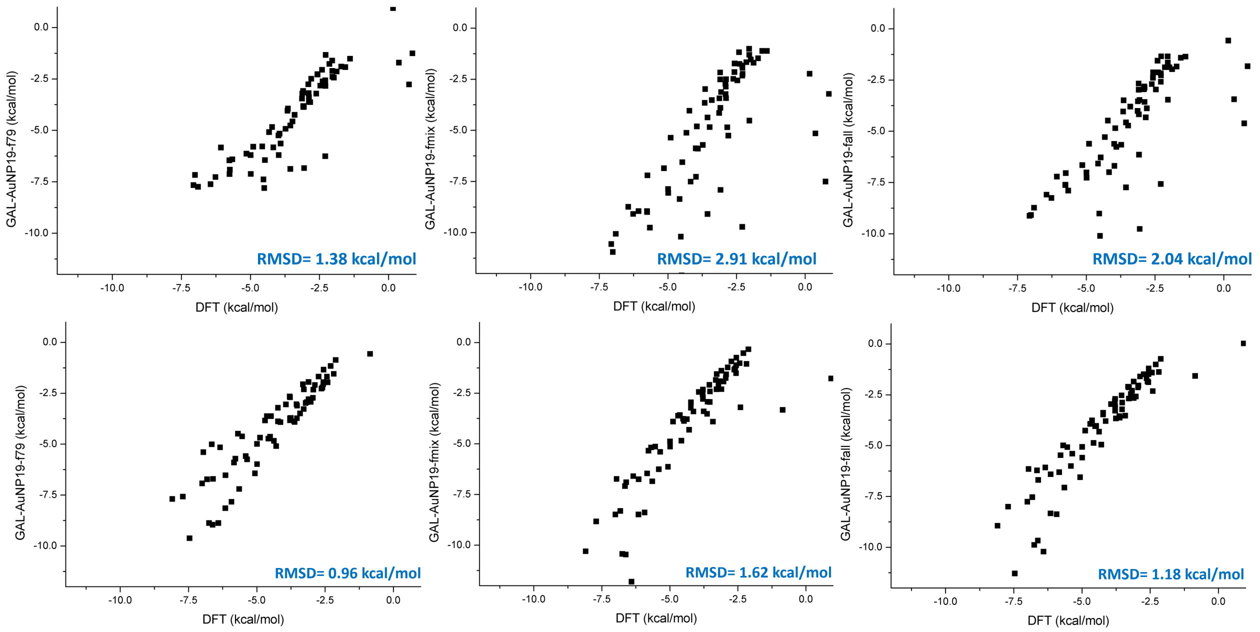

Figure 2.10: The calculated GAL interaction energies of 1 water molecule interacting with Au$_{147}$ (top) and Au $_{201}$ (bottom) with respect to DFT reference energies, with the following optimized parameters: (left) AuNP-fmix, (center) AuNP-f79, and (right) AuNP-fall

As for the AuNP-f79 set, the RMSDs for the interaction of one water molecule with Au$_{39}$, Au$_{55}$, Au$_{147}$, and Au$_{201}$ are excellent, which are 3.06, 1.78, 1.38, and 0.96 kcal/mol, respectively (see Figure 2.9 and 2.10 left column). It appears that the set performs increasingly better for the increasing size of GNP. However, the structure could also play a role, since the structure of Au$_{39}$ is very different from the rest of the GNP, resulting in the relatively high RMSD. The RMSD for the interactions of multiple water molecules are quite good for both Au$_{55}$ and Au$_{79}$, with smaller increase in the RMSD as more water molecules are added into the system, for example the RMSD increased from 2.06 kcal/mol for two water molecules to 3.06 kcal/mol for four water molecules interacting with Au$_{79}$ (see Figure 2.9 left column of bottom row). Therefore, this set seems to be transferable for across the size of GNP, and it gives good description for the interaction with multiple water molecules.

For the last set, the AuNP-fall parameter, in which all the structures, except for those of Au$_{147}$ and Au$_{201}$, are included, perform excellently for large GNP, (2.04 and 1.18 kcal/mol respectively for Au$_{147}$ and Au$_{201}$), and for interaction of multiple water molecules (see Figure 2.9 and 2.10 right column). Therefore, this parameters will be employed to carry out MD simulations. In other words, in the case for GAL19, for better description of many body effects and the transferability, the adsorption of multiple water molecules on various GNP needs to be included. Consequently, the force field is not quite practical and careful consideration has to be taken before employing the force field.

2.4.3.1 Molecular Dynamics Simulations with GAL19

MD simulations with GAL19 implemented in Tinker Molecular Package have been carried out for a series of GNP in water using PBC, which are Au$_{55}$, Au$_{147}$, Au$_{201}$, and Au$_{887}$. Considering the good performance of AuNP-fall to describe the interaction with multiple water molecules, it has been selected to be the parameter set of choice for the simulation, and additionally to test the stability of the implementation. The system has been taken from previously equilibrated cubic box of solvated GNPs, with the size of the boxes being 33.9208 Å, 39.8494 Å, 40.5951 Å, and 68.3825 Å, respectively for Au$_{55}$, Au$_{147}$, Au$_{201}$, and Au$_{887}$. The total number of water molecules is, therefore, 1288, 2042, 2170, and 10241, respectively. The TIP3P water model has been employed, while the Au-water interaction has been described only by GAL force field. The dynamics have been performed with constraints on water structure, imposed with the rattle algorithm, and on the Au-Au positions. Verlet integrator has been used with time step of 1.0 fs during equilibration for around at least 200 ps and time step of 2.0 fs during production for at least 1 ns. The dynamics have been performed in NVT ensemble, with Nosé-Hoover thermostat, maintaining the temperature at 300 K. The thermostat will kick in every 0.1 ps. The long range interactions have been treated with Ewald summation with cutoff of 8 Å. The periodic boundary condition has also been applied at all axis, with the cutoff for non-bonding interactions set to be 8 Å.

The evolution of temperature and potential energy over the simulation in NVT ensemble is shown in Figure 2.11, and these data imply the stability of the dynamics of the different systems of GNP, for up to one nanosecond. The water structuration around the GNP is then assessed with radial distribution function (RDF) for pairs of Au-O and Au-H, which are shown in Figure 2.12. The RDF plot of Au-O shows the presence of slightly more structured first solvation shell at around 2.85 Å, which agrees with reported AIMD simulations.[3] The subsequent peaks are broader as the influence of GNP on the structure diminishes, and they start to resemble bulk water. According to the RDF, the first solvation shell extends up to 4.0 Å. However, there does not seem to be a large difference in terms of the water structure across the different sizes of GNP. Additionally, the RDF plot of Au-H indicates the hydrogen to be almost at the same distance as Au-O. Upon closer inspection, there seems to be a slight shift in this peak towards the surface of GNP, as the size of GNP increases, which agrees with our previous study. However, more studies with larger GNP will be necessary to confirm this observation.

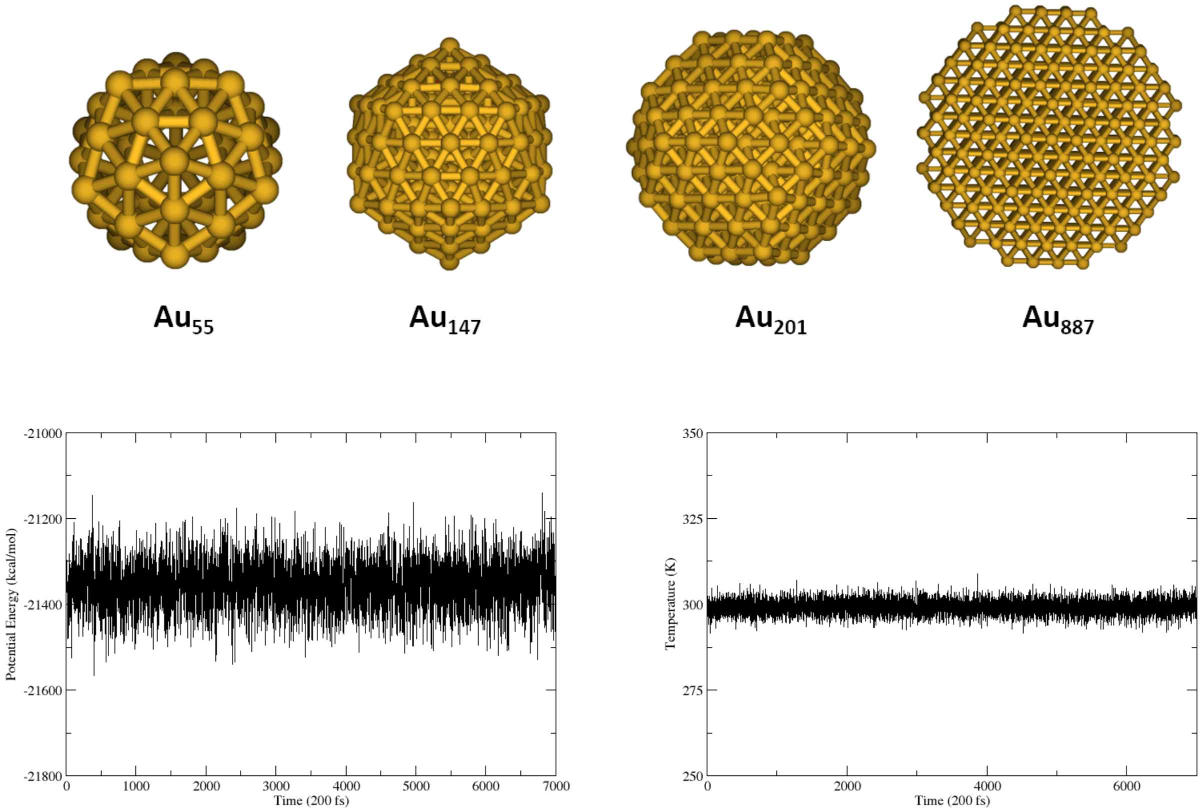

Figure 2.11: (top) The schematic representation of GNP studied in the MD simulations; (bottom) The evolution of potential energy (left) and temperature (right) for MD simulation of Au_{201}, with data points collected at every 200 fs.

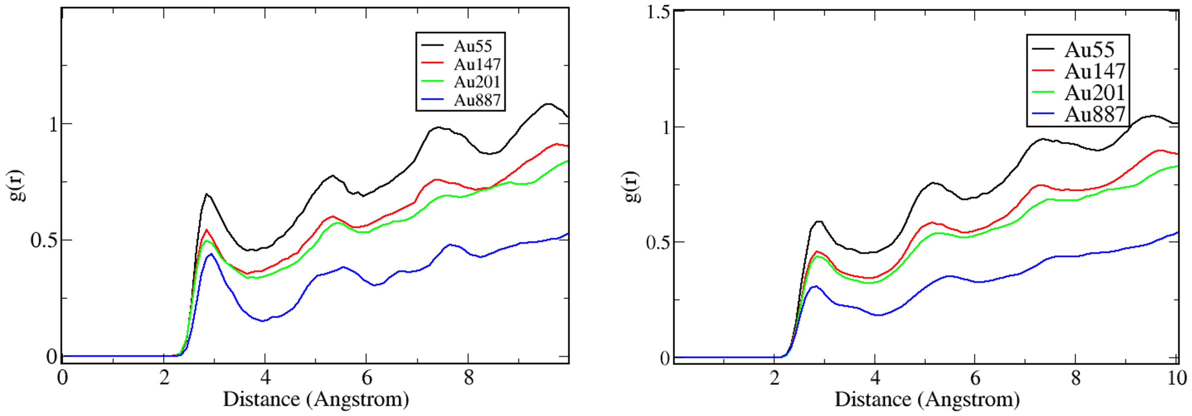

Figure 2.12: The plot of radial distribution function of O (left) and H (right) with respect to a series of GNP: Au_{55}, Au_{147}, Au_{201}, Au_{887}

Additionally, the distribution of water orientation has been calculated based on the α and β angle, and the result is tabulated in Table 2.2. As the size of GNP increases, there is naturally an increase in the average number of water molecules in the first solvation shell. A large portion of water molecule is oriented with the hydrogen atoms pointing away from the surface (up). These water molecules are forming hydrogen bond networks with the next solvation shell. The proportion of water molecule adopting the flat configuration seems to decrease with increasing size of GNPs. However, the proportion of water molecules adopting the dangling configuration does not change drastically. The rest of the water molecules adopts the orientation where the 2 hydrogen atoms are pointing towards the surface (down).

Table 2.2: The average distribution of the orientations of water in the first solvation shell of increasing sizes of GNP calculated based on the snapshots taken from MD simulations performed with GAL19

System	No. of Water	Up (%)	Flat (%)	Dangling (%)
Au$_{55}$	80	41.2	28.0	1.8
Au$_{147}$	139	43.4	26.8	1.3
Au$_{201}$	173	44.0	24.9	1.3
Au$_{887}$	469	50.6	15.3	1.3

2.4.4 Fitting for GAL21

Similarly, the parameters of GAL21 generated for metal surfaces are not optimized for GNP systems yet.[38] Therefore, the parameters have been fitted with our data set. Following the previous approach, different fitting sets have been carried out depending on the systems included in the dataset. In the AuNP21-fmix, the fitting dataset includes the interaction between one water molecule and Au$_{39}$, Au$_{55}$, and Au$_{79}$. In the AuNP21-f79, only the geometries of Au$_{79}$ are included. Contrary to the fitting for GAL19, the interaction between multiple water molecules on GNP is not included in any of the sets. The optimized parameters are tabulated in Table A.2. With the inclusion of reactivity descriptor (GCN), the performance of GAL21 is expected to be better than GAL19. These parameters will be evaluated also based on their predictions for the interaction energies of 1 water molecule with Au$_{147}$ and Au$_{201}$, and the multiple water molecules with Au$_{55}$ and Au$_{79}$ (see Table A.5, Figure 2.13, and Figure 2.14).

With the AuNP21-fmix set, the RMSD for the predicted interaction energies of one water molecule with Au$_{147}$ and Au$_{201}$ are 2.27 and 1.10 kcal/mol, respectively (see Figure 2.14 right column). Their prediction for the interaction energies of multiple water molecules with Au$_{55}$ and Au$_{79}$ is moderately well (see Figure 2.13 right column).

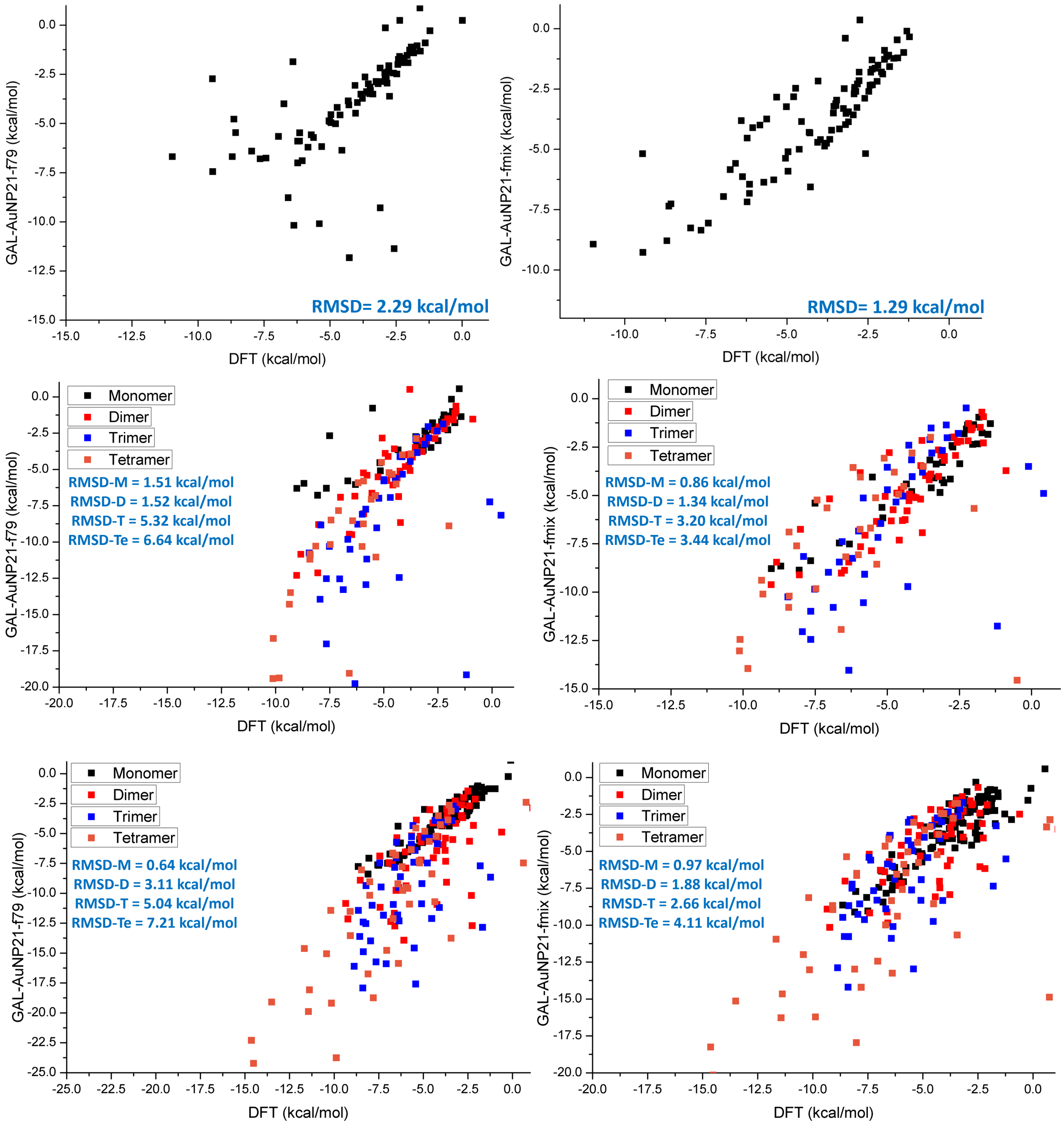

Figure 2.13: The calculated GAL interaction energies of Au$_{39}$ interacting with monomer (top); and of Au$_{55}$ (middle) and Au$_{79}$ (bottom) interacting with monomer (M), dimer (D), trimer (T), and tetramer (Te) of water with respect to the DFT reference energies, with the following optimized parameters: (left) AuNP21-f79 and (right) AuNP21-fmix

With the AuNP21-f79 set, the interaction energies of one water molecule interacting with Au$_{39}$, Au$_{55}$, Au$_{147}$, and Au$_{201}$ are predicted in excellent agreement with the reference dataset (see Figure 2.13 and Figure 2.14 left column). But, they do not seem to predict the interaction energies for multiple water molecules well, with error as large as 7 kcal/mol for the interaction of four water molecules with Au_{79}.

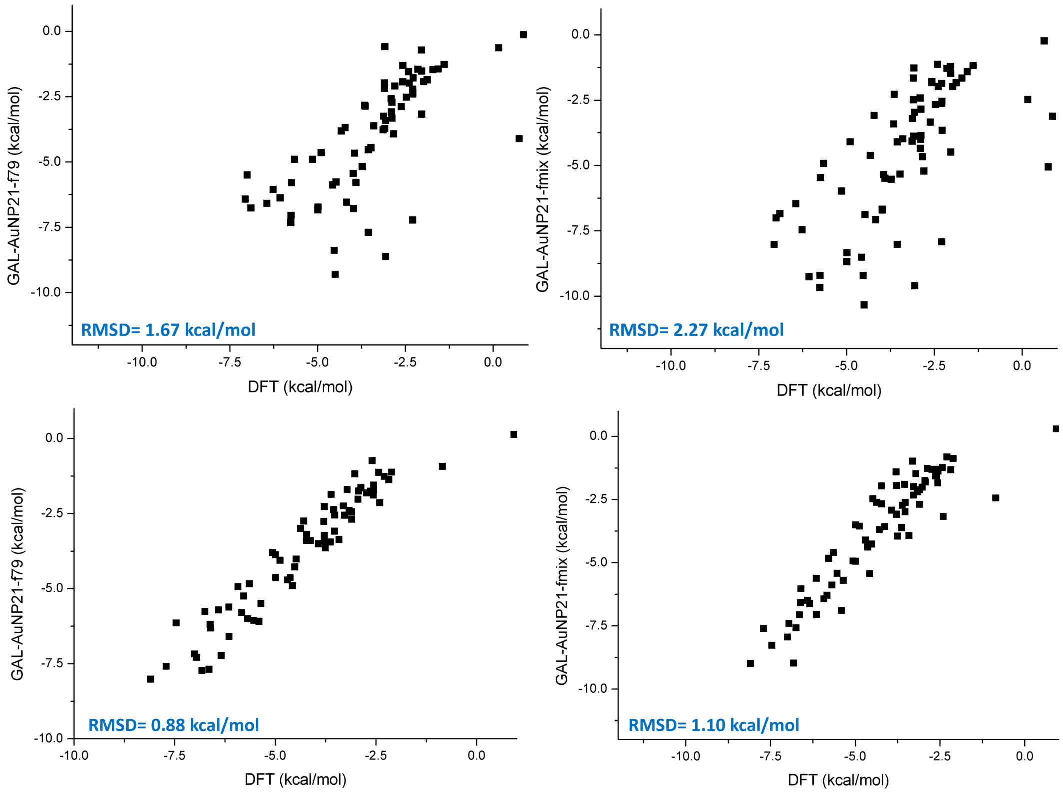

Figure 2.14: The calculated GAL interaction energy of Au_{147} (top) and Au_{201} (bottom) with respect to DFT reference energies, with the following optimized parameters: (left) AuNP21-f79 and (right) AuNP21-fmix

As expected, GAL21 is better in describing the interaction with one water molecule, as compared to GAL19. However, it still does not describe well the interaction with multiple water molecules, particularly with the AuNP21-f79 parameters. One possible reason could be due to the fact that GAL21 places too much importance on the reactivity descriptor, and hence overestimates the interaction with individual water molecule. Therefore, it might still be necessary to include the multiple water molecules within the fitting dataset to include the many body interactions, which will not be practical. For the subsequent molecular dynamics simulation, the AuNP21-fmix parameter set will be employed, because of their relatively lower RMSD for the interaction of multiple water with GNP.

2.4.4.1 Molecular Dynamics Simulations with GAL21

Similarly, the stability of the implementation of GAL21 in Tinker has been tested by performing MD simulations in NVT ensemble, with the same setup as mentioned for GAL19. The AuNP21-fmix set of parameters has been used in the simulations, and the GCN descriptors of each GNP have to be provided in the parameter file.

The stability of the simulation is validated by the stable evolution of potential energy and temperature during the simulation (see Figure 2.15). The water structure has similarly been studied with radial distribution function of O and H with respect to Au (see Figure 2.16). In comparison to GAL19, the first solvation peak obtained with GAL21 seems to have smaller width at 2.86 Å, with deeper dip at around 3.75 Å. This implies a more structured configuration at the first solvation shell for GAL21, as compared to that of GAL19. In GAL21, the larger GNP seems to exert larger effect on the water structure at the first solvation shell, which is not really the case for GAL19.
Meanwhile, the RDF of Au-H shows that the first solvation peak is at 2.77 Å, closer to the GNP surface, as compared to the oxygen. This is in contrary to what is observed in GAL19, where the first peak of Au-O and Au-H almost coincides. In addition, in the case for Au$_{55}$, the first peak solvation peak seems to extend quite far from the surface, due to the indistinguishable hydrogen atoms. However, as the size of GNP increases, more structuration occurs at the first solvation shell, with a slight shift of the first solvation shell closer to the surface of GNP.

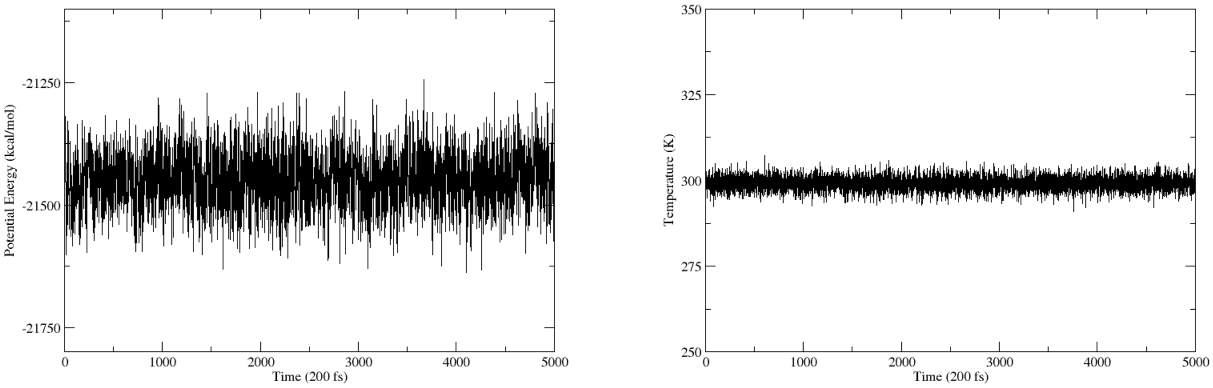

Figure 2.15: The evolution of potential energy (left) and temperature (right) for MD simulation of Au$_{201}$, with data points collected at every 200 fs.

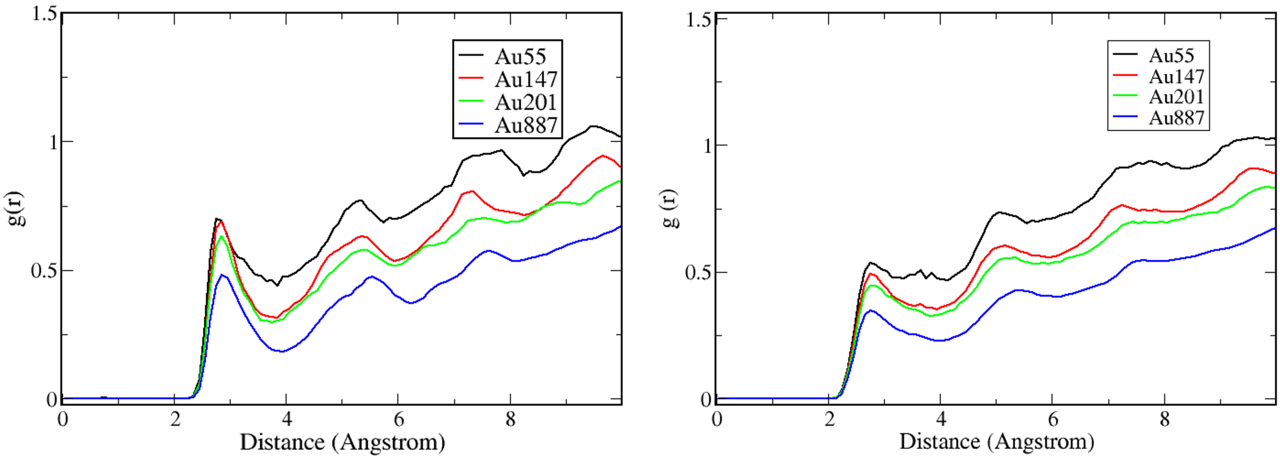

Figure 2.16: The plot of RDF of O (left) and H (right) with respect to a series of GNP: Au_{55}, Au_{147}, Au_{201}, and Au_{887}

Table 2.3: The average distribution of the orientations of water in the first solvation shell of increasing sizes of GNP, calculated based on the snapshots taken from MD simulations performed with GAL21

System	No. of Water	Up (%)	Flat (%)	Dangling (%)
Au_{55}	75	40.8	24.4	2.4
Au_{147}	141	39.0	30.3	1.9
Au_{201}	174	40.1	28.3	1.8
Au_{887}	457	42.0	21.2	1.8

Similarly, the distribution of the orientation of water molecules at the first solvation shell is quantified and shown in Table 2.3. The orientation of water molecules simulated with GAL21 is quite different from that simulated with GAL19. In average, the proportion of up configuration is slightly lesser than that obtained with GAL19. The proportion of the flat configuration, in the contrary, does not decrease with the size of GNP, as seen in GAL19. In GAL21, the flat configuration seems to increase for the intermediate GNP sizes. Lastly, there seems to be more water molecules adopting the dangling configuration. The proportion of water molecules oriented with the two hydrogen atoms pointing towards the surface (down configurations) has increased as well in the simulations with GAL21.

All in all, the data analysis extracted from the MD simulations performed with GAL21 shows a different behavior of water molecules in the vicinity of GNP as compared to those performed with GAL19. However, with the lack of reference data, it is still quite hard to conclude which force field performs better. However, for the interaction with one water molecule, GAL21 performs better and it is more transferable to different sizes of GNP. In the following section, the polarization and electrostatic terms within AMOEBA framework will be coupled with GAL21, and the performance of the resulting force field will be assessed.

2.4.5 Including Polarization in GAL21

The performance of both GAL19 and GAL21 has been demonstrated to be quite good, but, their description of the many body interaction is still lacking. This could arise due to the absence of the polarization and charge transfer term that has been demonstrated to be important. Especially, the polarization effect of GNP should have an effect on the arrangement of water at the interface. Therefore, in this work, the addition of polarization term will be carried out by coupling GAL21 with AMOEBA force field, which has been extensively used for the simulation of ions solvation, and biomolecules with high accuracy. As discussed under the methodology section, the AMOEBA force field includes additional terms for electrostatic and polarization, on top of the bonding interactions and van der Waals interactions. Since the interaction of Au-water has to be treated exclusively with GAL21, double counting of particular terms has to be carefully avoided, especially during the fitting.

Before going further, energy decomposition analysis with block localized wavefunction scheme (BLW-EDA) has been carried out to compute the contributions of polarization and charge transfer terms to the interaction energy. The detailed description of BLW-EDA can be found in the methodology section of Chapter 3. Table 2.4 shows the different terms (*i.e.* frozen energy, polarization, and charge transfer) for the interaction of one water molecule with Au$_{55}$. The configurations refer to the geometry and distance of one water molecule interacting with Au$_{55}$. The term HU, HF, HDown, and HDangling refers to up, flat, down, and dangling orientation, respectively (see Figure 2.3). The number 1-11 refers to the increasing distances of water with respect to Au$_{55}$ surface, and they vary between 2.0 Å to 4.0 Å.

Table 2.4: The frozen, polarization, and charge transfer energies (in kcal/mol) of the interaction between one water molecule and Au$_{55}$ based on the BLW-EDA scheme

Configuration	Frozen Energy	Polarization	Charge Transfer	Interaction Energy
HU-1	58.89	-21.29	-22.06	15.55
HU-2	18.35	-9.13	-10.38	-1.16
HU-3	6.21	-4.64	-6.01	-4.44
HU-4	1.87	-2.84	-3.98	-4.94
HU-5	-0.76	-1.53	-2.31	-4.60
HU-6	-1.52	-1.01	-1.50	-4.03
HU-7	-1.80	-0.69	-1.00	-3.48
HU-8	-1.80	-0.40	-0.65	-2.86
HU-9	-1.69	-0.30	-0.43	-2.42
HU-10	-1.49	-0.22	-0.25	-1.96
HU-11	-1.28	-0.16	-0.16	-1.60
HF-2	22.97	-9.32	-13.49	0.16
HF-3	6.00	-3.75	-7.39	-5.14
HF-4	1.09	-1.87	-4.66	-5.44
HF-5	-0.63	-1.16	-3.27	-5.07
HF-6	-1.65	-0.60	-1.88	-4.13
HF-7	-1.81	-0.32	-1.36	-3.49
HF-8	-1.77	-0.21	-0.88	-2.86
HF-9	-1.55	-0.13	-0.48	-2.16
HF-10	-1.33	-0.10	-0.30	-1.73
HDown-1	156.47	-27.75	-51.63	77.09
HDown-2	76.87	-12.11	-30.11	34.65
HDown-3	34.50	-4.88	-16.69	12.93
HDown-4	17.87	-2.49	-10.45	4.93
HDown-5	8.79	-1.38	-6.46	0.96
HDown-6	3.42	-0.78	-3.68	-1.05
HDown-7	1.10	-0.53	-2.24	-1.68
HDown-8	-0.10	-0.34	-1.38	-1.82
HDown-9	-0.66	-0.26	-0.84	-1.75
HDown-10	-0.87	-0.20	-0.48	-1.55
HDown-11	-0.90	-0.16	-0.35	-1.41
HDang-1	116.54	-21.36	-38.55	56.62
HDang-2	66.22	-11.38	-24.75	30.09
HDang-3	35.38	-5.66	-15.31	14.41
HDang-4	15.88	-2.59	-8.33	4.96
HDang-5	8.31	-1.51	-5.22	1.58
HDang-6	3.27	-0.84	-2.91	-0.49
HDang-7	0.64	-0.47	-1.52	-1.35
HDang-8	-0.25	-0.30	-0.96	-1.51
HDang-9	-0.75	-0.17	-0.57	-1.49
HDang-10	-0.88	-0.13	-0.35	-1.35
HDang-11	-0.87	-0.10	-0.21	-1.18

Since the frozen energy is a sum of the electrostatic, dispersive and repulsive energies, this term is generally positive at small distances. This term then decreases as the distance increases, where eventually the contributions from dispersion and electrostatic become dominant, resulting in negative energy at larger distances. The polarization and charge transfer terms, in contrary, are strongly stabilizing at small distances, and they decrease as the distance increases. The interaction energy is, by definition, the summation of all these terms. The combination of polarization and charge transfer compensates the positive frozen term to result in favorable interaction energy. An interesting observation is that the charge transfer is generally larger than the polarization term, except for the up configuration. Therefore, this analysis has demonstrated the important contribution of both the polarization and charge transfer to the interaction energy,[39] which have not been included in the GAL force field.

The contribution of polarization and charge transfer at the optimal interacting distance varies between -2.84 and -0.30 kcal/mol and -3.98 and -0.96 kcal/mol, respectively. It generally decreases from the up, flat, down, and dangling configurations. Part of the reason is due to the increasing optimal interacting distance across the configurations. Similar observations have been made for Au_{39} and Au_{79} (see Table A.6 and Table A.7), which led us to conclude that there is no significant size effect of GNP on the polarization and charge transfer at the surface. It is an important basis for the transferability of polarization effect across different sizes of GNPs.

2.4.5.1 Fitting for GAL21 coupled with AMOEBA

To include the polarization term within AMOEBA framework, on top of the GAL21 force field parameters, additional parameters have to be included. As mentioned earlier, there is a risk of double counting during the energy calculation. GAL21 force field has explicitly included the non-bonded interactions between Au and water, except for the polarization and electrostatic terms. Even though, they might have been included implicitly during the fitting of the parameters, it has not been sufficient to describe the many body effects as demonstrated by the RMSD of predicted interaction energies for multiple water molecules on GNP with GAL19 and GAL21. AMOEBA functional form includes van der Waals interaction as part of the non-bonded interaction. Therefore, the parameters relating to this term and bonded term have been set to 0 to prevent double counting. For the permanent electrostatic term, only the charge is included, and excluding the higher order multipoles. As for the polarization term, both the polarizability and Thole damping factor are needed.

The range of values for polarizability of the gold atoms have been obtained from quantum calculation, and set to be 3.2349 $Å^3$ in this work, and the standard

Thole damping factor of 0.39 has been used. However, the choice of charge is not as straightforward. Firstly, there is a question on the sign and the magnitude of the charge. Secondly, it is not obvious whether introducing a universal charge for all the Au atoms or separating the charge based on the surface or core Au atoms would provide a better result. Therefore, careful consideration has been taken in deciding the sign and magnitude of the charge.

To take into consideration the correlation between charge and polarization, a small charge of 0.02 will be applied, because it will give a good energy range for the polarization term. Additionally, the positive charge is found to behave better with the distance, as compared to the negative charge. Subsequently, the two charge settings will be systematically compared, in which the first one has the universal charge of 0.02 for all Au atoms (labelled P1T), and the second one having 0.02 charge at the surface atoms, and the counter balancing negative charge is distributed in the core atoms (labelled P2T). The first setting results in excess positive charge on the GNP, while the second setting results in neutral GNP, which may be preferrable in a MD simulation.

$$E_{ref} = E_{int-DFT} - E_{pol-amoeba} - E_{multi-amoeba} \tag{2.20}$$

Since the parameters for AMOEBA are not going to be adjusted, the contribution arising from the polarization and multipole terms has to be subtracted from the DFT reference energy to prevent double counting (see Equation 2.20), with the E_{ref} corresponding to the new reference data for fitting, $E_{int-DFT}$ corresponding to the interaction energy as obtained from DFT, $E_{pol-amoeba}$ and $E_{multi-amoeba}$ referring to the polarization and multipole energy calculated with Tinker. The remaining parameters of GAL21 will be fitted against E_{ref}. In this way, the polarization terms are separated from the GAL terms quantitatively during the fitting.

Similar to our previous approach, the fitting will also be systematically carried out with different dataset. The first set includes the interaction between one water molecule with a mixture of GNP in the dataset (fmix) and the second set includes only the interaction between one water molecule with Au$_{79}$ structures in the dataset (f79). All in all, we tested four different sets of fitting procedure, which are P1T-fmix, P2T-fmix, P1T-f79, and P2T-f79, and their respective optimized parameters are shown in Table A.3.

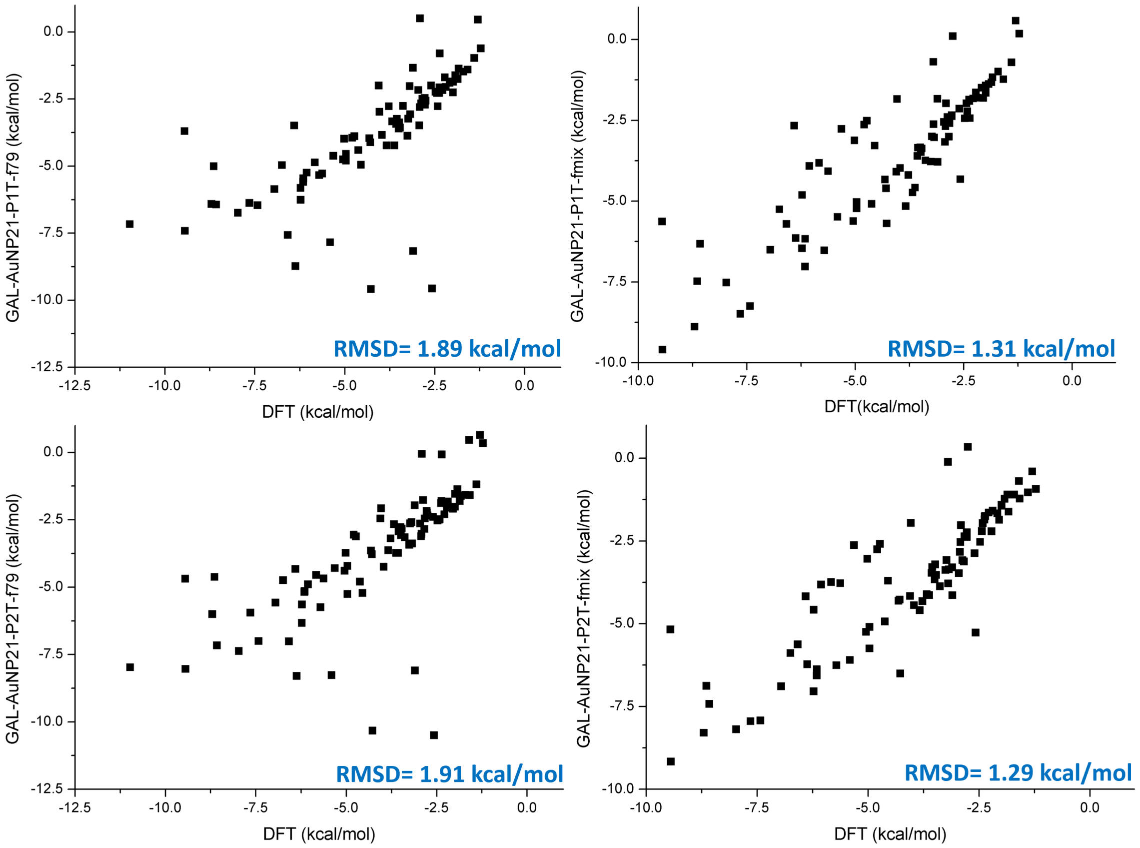

Figure 2.17: The calculated GAL interaction energies of Au_{39} with one water molecule with the following optimized parameters:(top) P1T-f79 and P1T-fmix, (bottom) P2T-f79 and P2T-fmix

The performance of the parameters has similarly been evaluated based on the RMSD of the predicted interaction energies of one water molecule with Au_{39}, Au_{147}, and Au_{201} (see Figure 2.17, Figure 2.20 and Figure 2.21), and those of the multiple water molecules interacting with Au_{55} and Au_{79} (see Figure 2.18, Figure 2.19, and Table A.5).

Comparing between the P1T and P2T scheme, with both fmix and f79, the RMSD calculated for interaction of one water molecule with the larger GNP (Au_{147} and Au_{201}) are found to be generally lower for the P2T scheme (see Figure 2.20 and Figure 2.21). The RMSD calculated for Au_{147} are 2.09 kcal/mol and 2.32 kcal/mol for P2T associated with f79 and fmix, respectively. In comparison, the RMSD calculated for the same structures for P1T scheme are 2.36 kcal/mol and 3.00 kcal/mol, respectively. However, for interaction of multiple water molecules on GNPs, P1T gives lower RMSD for Au_{55} complexes (see Figure 2.18), while P2T gives lower RMSD for Au_{79} complexes(see Figure 2.19). Hence, they are comparable. However, with the lower error observed for the interaction of one water molecule and the resulting neutral GNP system, P2T scheme is favored.

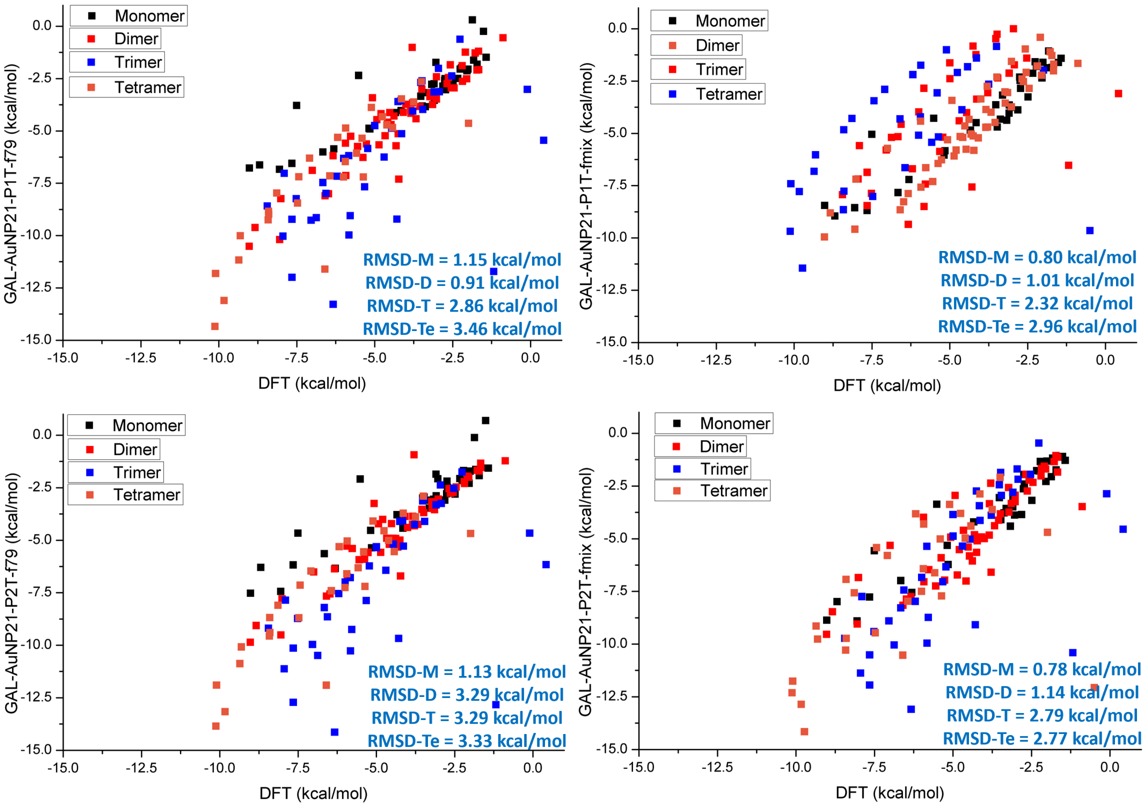

Figure 2.18: The calculated GAL interaction energies of Au_{55} interacting with monomer (M), dimer (D), trimer (T), and tetramer (Te) of water with respect to the DFT reference energies, with the following optimized parameters: (top) P1T-f79 and P1T-fmix, (bottom) P2T-f79 and P2T-fmix

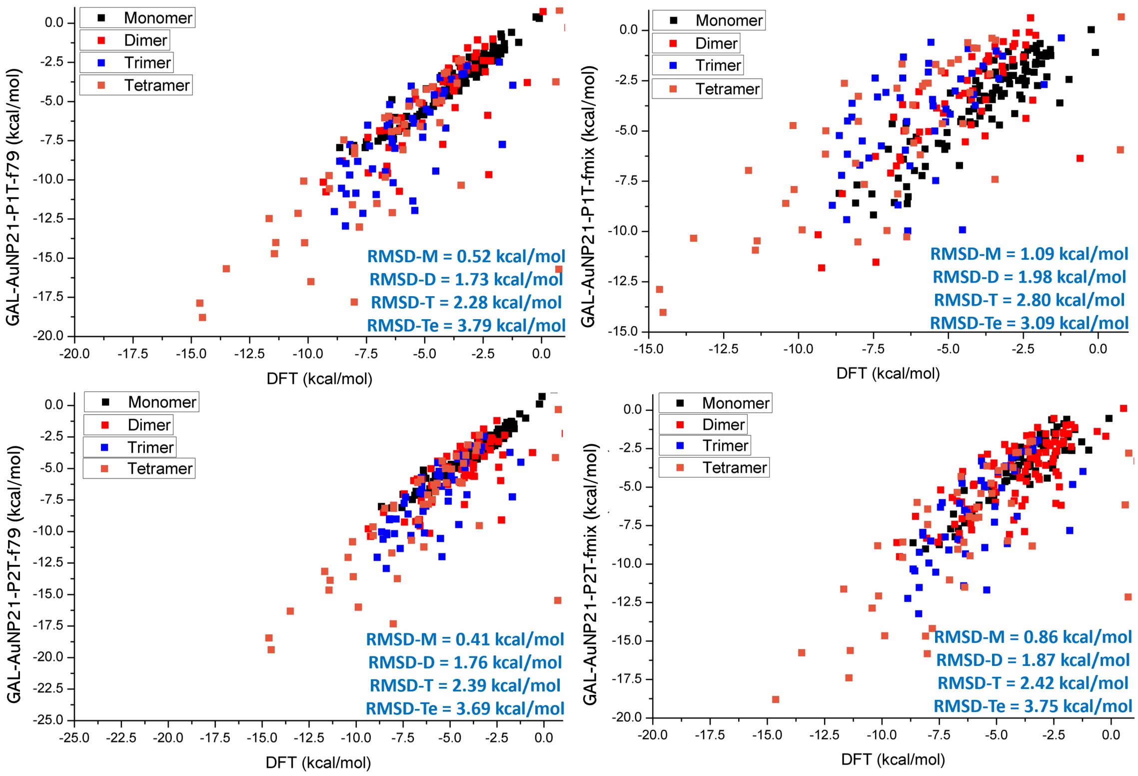

Figure 2.19: The calculated GAL interaction energies of Au_{79} interacting with monomer (M), dimer (D), trimer (T), and tetramer (Te) of water with respect to the DFT reference energies, with the following optimized parameters: (top) P1T-f79 and P1T-fmix, (bottom) P2T-f79 and P2T-fmix.

Since, the P2T has been considered the scheme of choice for the charge, the RMSD are calculated to evaluate and compare the performance of P2T-f79 and P2T-fmix. The two sets seems to be comparable for both the interaction of one water molecule (see the bottom plots of Figure 2.17, Figure 2.20, and Figure 2.21) and multiple water molecules on GNP (see the bottom plots of Figure 2.18 and Figure 2.19).

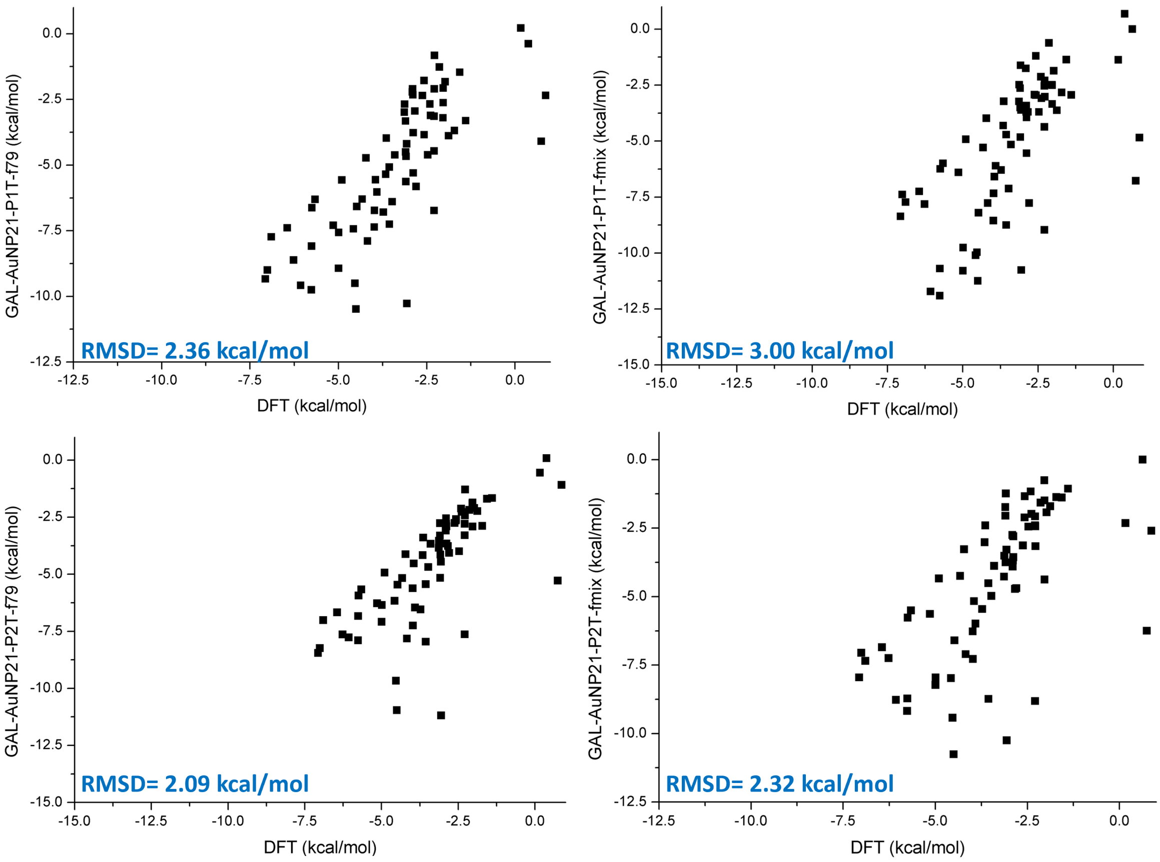

Figure 2.20: The calculated GAL interaction energies of Au_{147} interacting with monomer (M), dimer (D), trimer (T), and tetramer (Te) of water with respect to the DFT reference energies, with the following optimized parameters:(top) P1T-f79 and P1T-fmix, (bottom) P2T-f79 and P2T-fmix.

In the case for the one water molecule systems, P2T-fmix gives lower RMSD for Au_{147}, while P2T-f79 gives lower RMSD for Au_{201}. As for the interaction of multiple water molecules on GNP, the P2T-f79 performs slightly better for Au_{79} complexes (see Figure 2.19), and slightly worse for Au_{55} complexes (see Figure 2.18). Nevertheless, RMSD for the interaction with multiple water molecules are better than the non-polarizable GAL21. This results show the superior performance of polarizable GAL21 in the description of many body interaction.

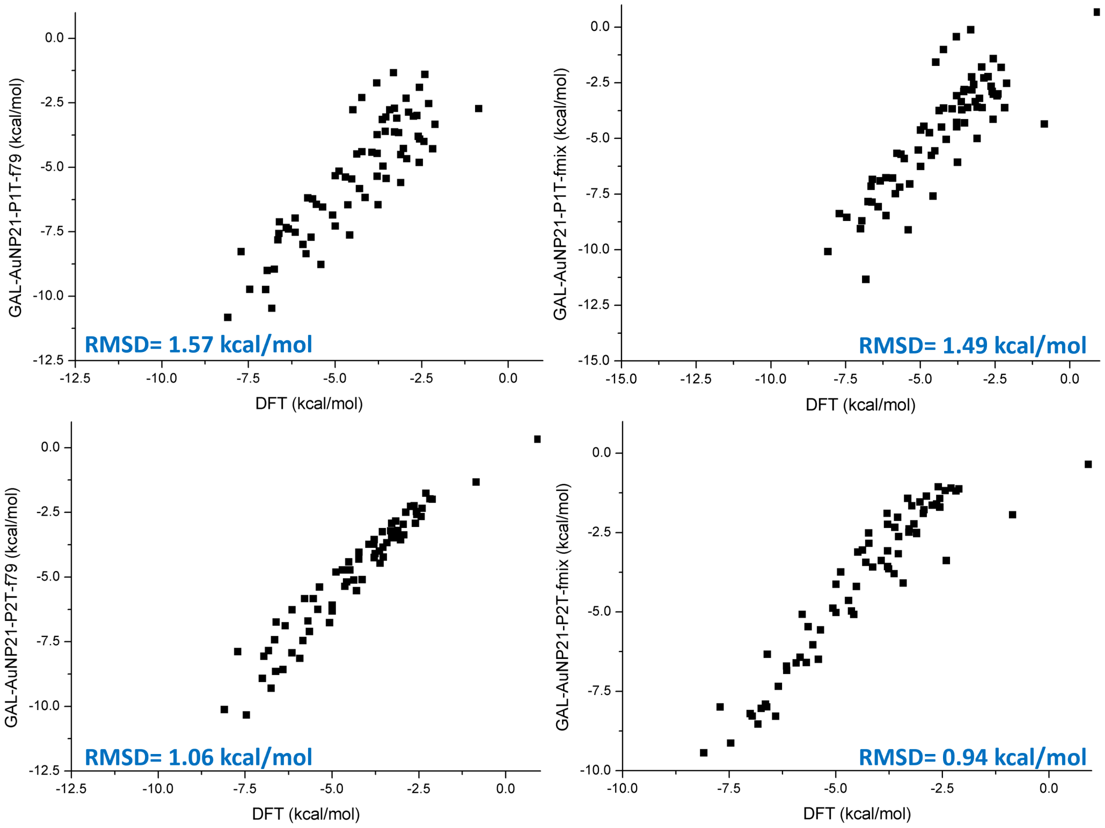

Figure 2.21: The calculated GAL interaction energies of Au_{201} interacting with monomer (M), dimer (D), trimer (T), and tetramer (Te) of water with respect to the DFT reference energies, with the following optimized parameters: (top) P1T-f79 and P1T-fmix, (bottom) P2T-f79 and P2T-fmix.

Furthermore, this analysis demonstrates that the polarizable force field obtained with Au_{79} (P2T-f79) fitting dataset can produce satisfactory interaction energies across sizes of GNP, and also for the interaction between multiple water molecules and GNP. This could imply that the parameters fitted in this work can be directly applicable for different sizes and shapes of GNP without re-parametrization. Therefore, our parameter of choice to run MD simulations will be P2T-f79 to further test the transferability of the force field.

2.4.5.2 Molecular Dynamics Simulations with Polarizable GAL21

MD simulations, with the same simulation setup and systems as the previous sections, have been carried out to evaluate the stability of the coupling between GAL21 and AMOEBA force field, in NVT ensemble. As mentioned, the P2T-f79 parameters have been selected as the parameter of choice, in which the surface atoms will have 0.02 charge, and the counter balancing negative charge will differ depend on the size of GNP. Similarly, the GCN of the GNP has to be included in the parameter file. Since there is a significant increase in simulation time for this force field, only a few hundred steps of simulation has been performed.

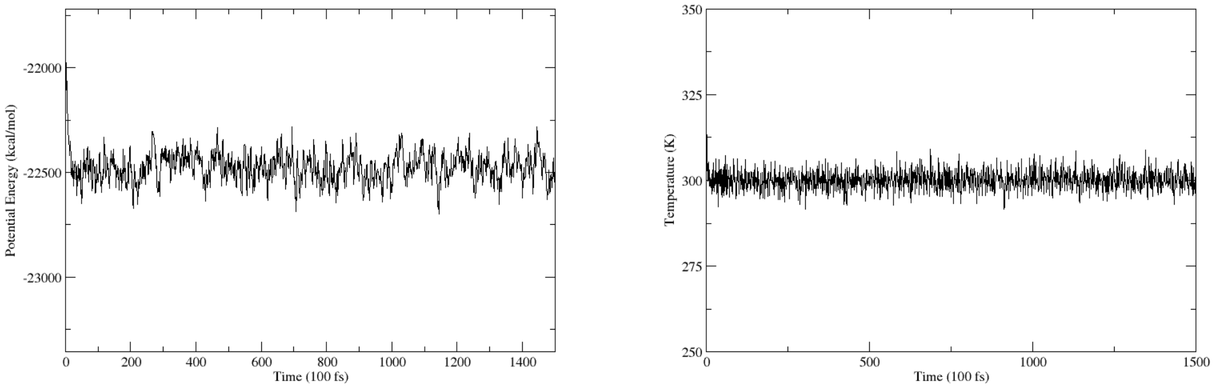

Figure 2.22: The evolution of potential energy (left) and temperature (right) for MD simulation of Au$_{201}$, with data points collected every 100 fs.

Similarly, the evolution of potential energy and temperature during the simulation is stable, as they fluctuate around the average value (see Figure 2.22). The water structure has also been investigated at the vicinity of GNP by calculating the RDF of both O and H with respect to Au atoms (see Figure 2.23 top). For the RDF of oxygen atom with respect to gold atoms, the first solvation shell has not changed much across the size of GNP and the peak is at 2.80 Å. Meanwhile, for the RDF of hydrogen atom with respect to gold atoms, the shape of the first solvation shell has not changed much, but the peak has shifted to larger distance for the large GNP, *i.e.* from 2.85 Å for Au$_{55}$ to 2.96 Åfor Au$_{147}$ and Au$_{201}$. The hydrogen atoms are found to be a bit further away from the surface as compared to the oxygen atoms.

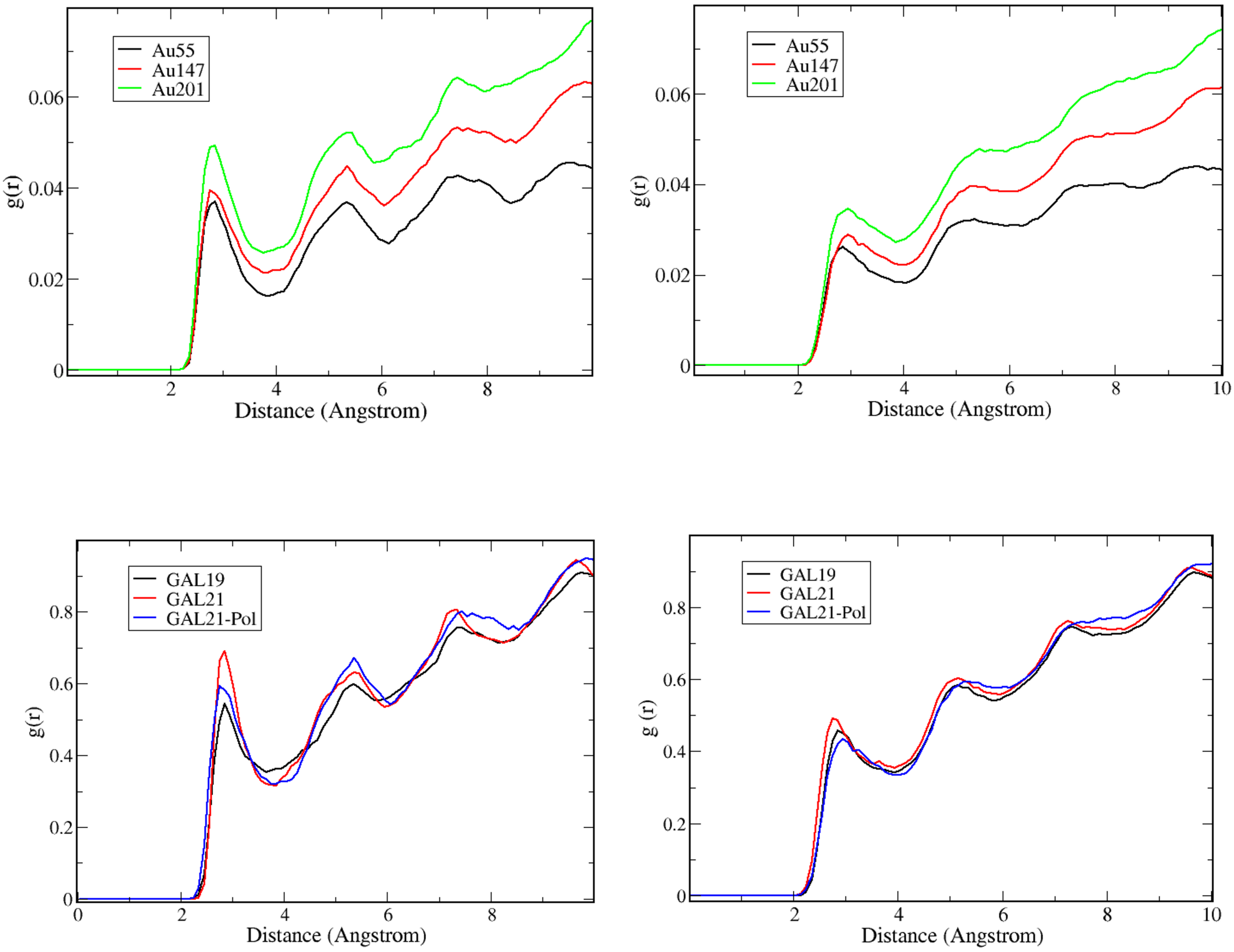

Figure 2.23: The RDF of O (left) and H (right) with respect to a series of GNP: Au_{55}, Au_{147}, andAu $_{201}$ (top); The comparison of RDF for Au_{147} between the different force field (bottom).

Subsequently, the RDF of oxygen and hydrogen with respect to Au_{147} are compared between the different force fields, and shown in Figure 2.23 bottom. The RDF for oxygen is not very different across the different force fields, while the first peak for RDF of hydrogen has shifted a little, with the one corresponding to the GAL21-Pol being the furthest away from the surface, and the GAL21 being the closest to the surface. However, further investigation needs to be carried out to validate the polarizable force field.

Table 2.5: The average distribution of the orientations of water in the first solvation shell of increasing sizes of GNP, calculated based on the snapshots taken from MD simulations performed with polarizable GAL21

System	No. of Water	Up (%)	Flat (%)	Dangling (%)
Au_{55}	79	54.9	15.5	2.9
Au_{147}	135	59.1	13.4	2.9
Au_{201}	167	57.8	13.8	3.3

The orientation of water molecules at the first solvation shell has been quantified and shown in Table 2.5. The distribution shows that the water structure simulated with polarizable GAL21 is different from GAL19 and non-polarizable GAL21. A majority of the water molecules is adopting the orientation where the two hydrogen atoms are pointing away from the surface (up configuration). Though, there seems to be a decrease in the flat proportion as the size of GNP increases, similar trend observed in GAL19. Intriguingly, the proportion of dangling water molecules has increased in the polarizable GAL21, as compared to the other force fields. Additionally, it slightly increases as the size of GNP increases, which is consistent with the general expectation of an increase in planar surface in larger GNP, thus resembling metal surfaces.

2.4.6 Conclusion and Perspectives

Our preliminary tests have shown that including polarization in GAL21 force field, in which the reactivity of surface atoms is accounted by GCN, improves the many body interactions at the interface of GNP. Additionally, the transferability of the force field is excellent across the different sizes and shapes of GNP considered here, which could imply the direct applicability of the reported parameters for simulations of gold systems.

For further validation of the force field, however, additional tests are still needed to be carried out. Particularly, the computation of the RDF is currently performed with individual atoms of Au as the reference, which leads to the plots reported in this chapter. Different approaches in studying the water packing in the vicinity of GNP are needed to obtain better description, for example setting the center of mass of GNP as the point of reference. The interaction of GNP with water in the presence of ions and charged molecules, especially, needs to be tested as an evaluation of the force field. Furthermore, as the force field has been implemented in Tinker molecular package, the integration with other force fields should be straightforward, in particular for biomolecule simulations. Moreover, with the MPI parallelization in Tinker HP package,[40] long simulations with polarizable GAL21 will be possible.

All in all, an accurate force field describing GNP-water interaction has been developed. With the availability of accurate force field for GNP-water interaction, it would be possible to calculate and compare the properties of hydrogen bond networks in greater detail. It will be particularly interesting to extract different trends and descriptors for the hydrogen bond network surrounding GNP exhibiting unusual shapes, such as nanostars, nanocubes, nanowires, nanorods. Additionally, the dynamics of the interaction between GNP-ligand can be extensively sampled, and based on which vibrational spectra could be derived to compare with experimental data.

2.5 General Conclusion and Perspectives

In this chapter, the focus has been on the modelling of GNP-water interface by employing force field-based MD simulations. The dynamical and structural properties of water solvation shell of GNP have been systematically studied, and the rearrangement of water structure to 2D hydrogen bond network has been observed as the size of GNP increases. Furthermore, an accurate and polarizable force field, derived from GAL21 force field, has been shown to be excellent in predicting the interaction energies of multiple water molecules on GNP. Additionally, the force field is also transferable across the different sizes and shapes of GNP studied here.

In section 2.3, the optimum distance of Au-water interaction has been found to differ between DFT method and semi-empirical DFTB method. Since the property of interest was the vibrational density of states of the solvation shell of GNP, the distance of Au-water may be negligible, as long as the water-water interactions are well described. However, this is an important limitation inherent to this semi-empirical method.

The parameters employed in section 2.3 have been generated specifically for gold thiolated systems, and our results show that these parameters, in particular the parameters generated for O-O, O-H, and H-H interactions (water interactions) are not fully transferable for GNP-water systems. Therefore, in cases where an accurate potential energy surface is important, the errors due to the parameters could lead to wrong interpretation. Moreover, this method cannot be used as the reference method for force field parametrization involving large systems. Therefore, to obtain accurate simulation, new parameters have to be derived to describe the Au-water interface. However, generating new DFTB parameters can be quite tedious, especially if each addition of different molecules in the system requires new parameters.

Alternatively, artificial neural networks have recently been proposed as a powerful method to predict the energy correction to increase the accuracy of DFTB to DFT or ab-initio methods.[41,42] Therefore, such an approach can be applied for Au-water interactions. The work is currently ongoing, and is carried out together with N. Bhatia (Master 2 student) and in collaboration with Prof. Marcus Elstner's group. The challenges of the method include, the sampling of the potential energy surface to be included in the training set, the optimization of hyper parameters for the geometry descriptors, and finally the optimization of the neural network parameter itself. However, the preliminary results are promising with the ML corrected DFTB interaction energies are comparable with DFT reference energies as compared to initial DFTB energies (see Figure 2.24). The next challenge being to test the transferability of this neural network model in predicting energy corrections for GNP systems other than those included in the training dataset.

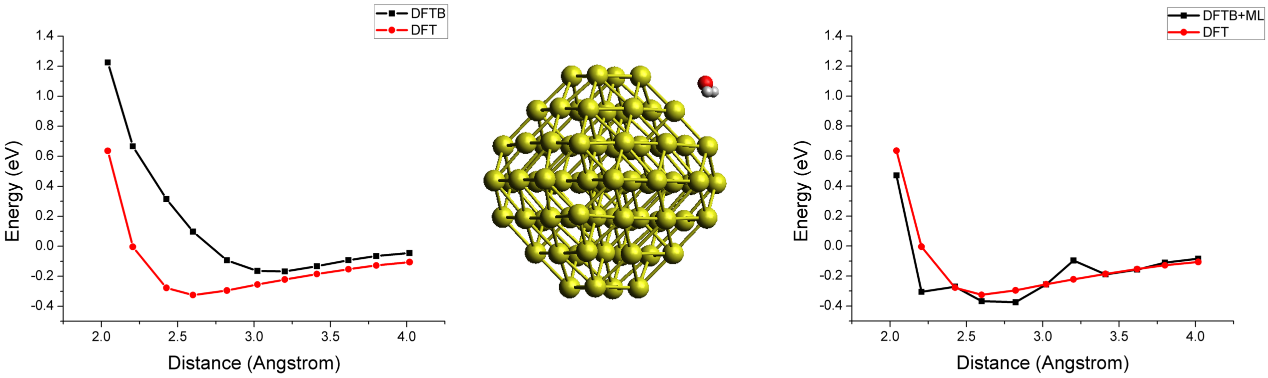

Figure 2.24: The interaction energies of one water molecule at varied distances calculated with DFTB (left) and DFTB-ML (right) as compared to DFT reference energies.

Bibliography

[1] C. Sicard-Roselli, E. Brun, M. Gilles, G. Baldacchino, C. Kelsey, H. McQuaid, C. Polin, N. Wardlow and F. Currell, *Small*, 2014, **10**, 3338–3346.

[2] T. Petit, H. Yuzawa, M. Nagasaka, R. Yamanoi, E. Osawa, N. Kosugi and E. F. Aziz, *J Phys Chem Lett*, 2015, **6**, 2909–2912.

[3] J.-J. Velasco-Velez, C. H. Wu, T. A. Pascal, L. F. Wan, J. Guo, D. Prendergast and M. Salmeron, *Science*, 2014, **346**, 831–834.

[4] F. Novelli, M. Bernal Lopez, G. Schwaab, B. Roldan Cuenya and M. Havenith, *J Phys Chem B*, 2019, **123**, 6521–6528.

[5] A. Berg, C. Peter and K. Johnston, *J Chem Theory Comput*, 2017, **13**, 5610–5623.

[6] M. J. Abraham, T. Murtola, R. Schulz, S. Páll, J. C. Smith, B. Hess and E. Lindahl, *SoftwareX*, 2015, **1-2**, 19–25.

[7] J. A. Rackers, Z. Wang, C. Lu, M. L. Laury, L. Lagardere, M. Schnieders, J.-P. Piquemal, P. Ren and J. Ponder, *J Chem Theory Comput*, 2018, **14**, 5273–5289.

[8] S. A. Hollingsworth and R. O. Dror, *Neuron*, 2018, **99**, 1129–1143.

[9] F. A. Momany and R. Rone, *J Comput Chem*, 1992, **13**, 888–900.

[10] C. Oostenbrink, A. Villa, A. E. Mark and W. F. Van Gunsteren, *J Comput Chem*, 2004, **25**, 1656–1676.

[11] W. Damm, A. Frontera, J. Tirado–Rives and W. L. Jorgensen, *J Comput Chem*, 1997, **18**, 1955–1970.

[12] J. Wang, R. M. Wolf, J. W. Caldwell, P. A. Kollman and D. A. Case, *J Comput Chem*, 2004, **25**, 1157–1174.

[13] H. Sun, *J Phys Chem B*, 1998, **102**, 7338–7364.

[14] H. Heinz, K. C. Jha, J. Luettmer-Strathmann, B. L. Farmer and R. R. Naik, *J R Soc Interface*, 2011, **8**, 220–232.

[15] S. W. Rick, S. J. Stuart and B. J. Berne, *J Chem Phys*, 1994, **101**, 6141–6156.

[16] G. Lamoureux and B. Roux, *J Chem Phys*, 2003, **119**, 3025–3039.

[17] B. J. Kirby and P. Jungwirth, *J Phys Chem Lett*, 2019, **10**, 7531–7536.

[18] F. Torrens, J. Sánchez-Marín and I. Nebot-Gil, *THEOCHEM*, 1999, **463**, 27–39.

[19] P. Ren and J. W. Ponder, *J Comput Chem*, 2002, **23**, 1497–1506.

[20] B. Thole, *Chem Phys*, 1981, **59**, 341–350.

[21] A. J. Stone, *Chem Phys Lett*, 1981, **83**, 233–239.

[22] J. W. Ponder, C. Wu, P. Ren, V. S. Pande, J. D. Chodera, M. J. Schnieders, I. Haque, D. L. Mobley, D. S. Lambrecht, R. A. DiStasio, M. Head-Gordon, G. N. I. Clark, M. E. Johnson and T. Head-Gordon, *J Phys Chem B*, 2010, **114**, 2549–2564.

[23] H. Heinz, R. A. Vaia, B. L. Farmer and R. R. Naik, *J Phys Chem C*, 2008, **112**, 17281–17290.

[24] I. L. Geada, H. Ramezani-Dakhel, T. Jamil, M. Sulpizi and H. Heinz, *Nat Commun*, 2018, **9**, 716.

[25] F. Iori, R. Di Felice, E. Molinari and S. Corni, *J Comput Chem*, 2009, **30**, 1465–1476.

[26] M. Rosa, S. Corni and R. Di Felice, *J Chem Theory Comput*, 2014, **10**, 1707–1716.

[27] Z. Futera and J. Blumberger, *J Chem Theory Comput*, 2019, 12.

[28] S. N. Steinmann, R. Ferreira De Morais, A. W. Götz, P. Fleurat-Lessard, M. Iannuzzi, P. Sautet and C. Michel, *J Chem Theory Comput*, 2018, **14**, 3238–3251.

[29] P. Clabaut, P. Fleurat-Lessard, C. Michel and S. N. Steinmann, *J Chem Theory Comput*, 2020, **16**, 4565–4578.

[30] D. J. Evans and B. L. Holian, *J Chem Phys*, 1985, **83**, 4069–4074.

[31] R. Tandiana, E. Brun, C. Sicard-Roselli, D. Domin, N.-T. Van-Oanh and C. Clavaguéra, *J Chem Phys*, 2021, **154**, 044706.

[32] D. Biriukov and Z. Futera, *J Phys Chem C*, 2021, **125**, 7856–7867.

[33] T. D. Kühne, M. Iannuzzi, M. Del Ben, V. V. Rybkin, P. Seewald, F. Stein, T. Laino, R. Z. Khaliullin, O. Schütt, F. Schiffmann, D. Golze, J. Wilhelm, S. Chulkov, M. H. Bani-Hashemian, V. Weber, U. Borštnik, M. Taillefumier, A. S. Jakobovits, A. Lazzaro, H. Pabst, T. Müller, R. Schade, M. Guidon, S. Andermatt, N. Holmberg, G. K. Schenter, A. Hehn, A. Bussy, F. Belleflamme, G. Tabacchi, A. Glöß, M. Lass, I. Bethune, C. J. Mundy, C. Plessl, M. Watkins, J. VandeVondele, M. Krack and J. Hutter, *J Chem Phys*, 2020, **152**, 194103.

[34] K. T. Tang and J. P. Toennies, *J Chem Phys*, 1984, **80**, 3726–3741.

[35] R. Nadler and J. F. Sanz, *J Chem Phys*, 2012, **137**, 114709.

[36] F. Calle-Vallejo, J. I. Martínez, J. M. García-Lastra, P. Sautet and D. Loffreda, *Angew Chem - Int Ed*, 2014, **53**, 8316–8319.

[37] L.-P. Wang, T. Head-Gordon, J. W. Ponder, P. Ren, J. D. Chodera, P. K. Eastman, T. J. Martinez and V. S. Pande, *J Phys Chem B*, 2013, **117**, 9956–9972.

[38] P. Clabaut, *PhD thesis*, ENS Lyon - École normale supérieure - Lyon, 2021.

[39] P. Clabaut, R. Staub, J. Galiana, E. Antonetti and S. N. Steinmann, *J Chem Phys*, 2020, **153**, 054703.

[40] L. Lagardère, L.-H. Jolly, F. Lipparini, F. Aviat, B. Stamm, Z. F. Jing, M. Harger, H. Torabifard, G. A. Cisneros, M. J. Schnieders, N. Gresh, Y. Maday, P. Y. Ren, J. W. Ponder and J.-P. Piquemal, *Chem Sci*, 2018, **9**, 956–972.

[41] J. Zhu, V. Q. Vuong, B. G. Sumpter and S. Irle, *MRS Commun*, 2019, **9**, 867–873.

[42] C. L. Gómez-Flores, D. Maag, M. Kansari, V.-Q. Vuong, S. Irle, F. Gräter, T. Kubař and M. Elstner, *J Chem Theory Comput*, 2022, **18**, 1213–1226.

Chapter 3

SIMULATING GNP-LIGAND INTERFACE

Contents

3.1 Introduction

The interaction of ligands on the surface of GNP has significant impacts on the physicochemical behavior of the resulting GNP. The reverse is also true, that in the presence of GNP, large biomolecules might undergo significant structural changes.[1]

Moreover, by exploiting its optical properties, GNP has been increasingly used as the substrate for surface enhanced Raman spectroscopy (SERS), a surface sensitive spectroscopy technique. This technique has been used to study the adsorption of bovine serum albumin,[2] the protein corona formation on GNP,[3] the processes of protein aggregation,[4] and many others. Furthermore, another study has reported changes in the secondary structure of amyloids depending on the curvature of GNP.[5]

Therefore, there is a vast interest in understanding the interacting groups and the orientation of molecules on the surface of GNP, with the objective of assisting the interpretation of experimental spectra and predicting the orientations of large biomolecules on GNP. Gao *et al.* have investigated the adsorption behavior of benzoic acid and phthalic acid on GNP, where the benzoic acid prefers a perpendicular orientation through the interaction with carboxylate group. The phthalic acid, however, prefers a tilted orientation with both carboxylate groups interacting with the surface atoms.[6] In another study, Yao *et al.* reported a combined DFT and SERS methods to discover the preferred interaction sites of cysteine, *i.e.* through both O and S, on the surface of GNP.[7]

The objective of this chapter is, therefore, to systematically study the interaction between small representative organic molecules and a series of GNP with various sizes and shapes. Since the electronic properties are necessary for the investigation, the calculations in this chapter will be performed at DFT level. The complexes are then subjected to topological analysis and energy decomposition approaches to obtain qualitative and quantitative information on the interactions. Lastly, the vibrational frequencies for the complexes are calculated in the harmonic approximation.

3.2 Computational Methodologies

All of the calculations at DFT level have been performed with deMon2k program, and the computational details employed in this chapter will be given in this section.[8] The typical simulation workflow is illustrated in Figure 3.1, where initially the complexes are optimized without constraint, followed by the various topological analyses, energy decomposition approaches, and vibrational analysis. All of the topological analysis described in this chapter and the charge decomposition analyses have been performed with Multiwfn[9], except for the quantification of NCI basins, which has been performed with NCIplot4.[10] The decomposition of the intermolecular interaction has been performed based on SAPT approach and block-localized wavefunctions energy decomposition analysis (BLW-EDA). SAPT has been calculated with Psi4,[11] while BLW-EDA has been calculated with CP2K.[12]

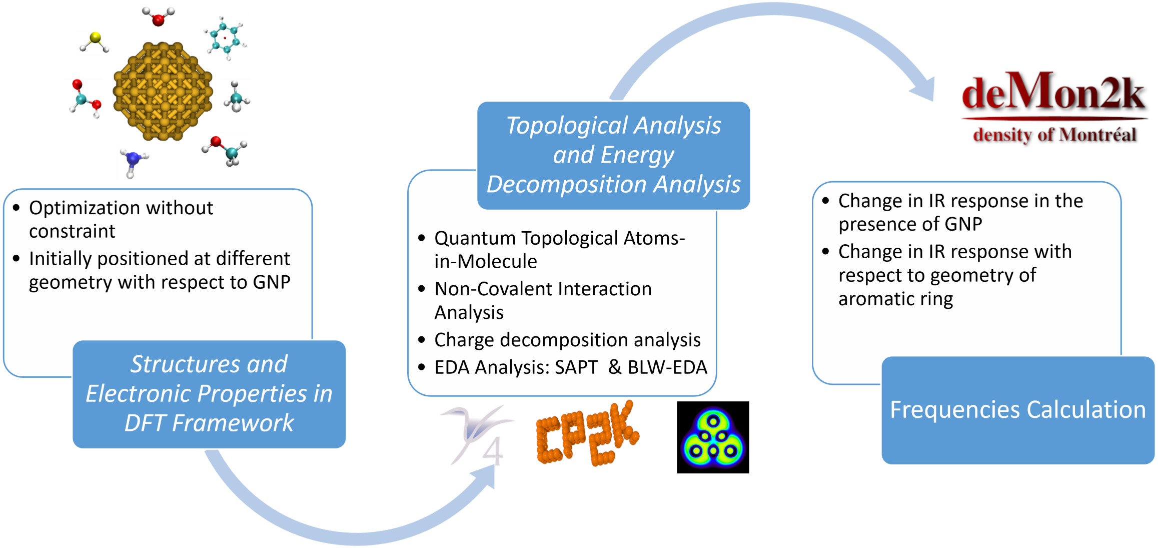

Figure 3.1: The systematic investigation of the interaction between GNP and organic molecules adopted in this chapter.

3.2.1 Quantum Approach

The ground state energy of molecular systems can be calculated by solving the time-independent Schrödinger equation 3.1, with the right hand side of the equation referring to the energy of the particular state of the system and the left hand side of the equation referring to the Hamiltonian of the system.[13] With the adiabatic and Born-Oppenheimer approximations, the exact solution has been successfully obtained for one-electron systems. But, as the number of electron is increasing, a numerical approach has to be applied based on the variational principle, which states that the energy of any approximate wavefunction is either above or equal to the exact function. Taking an approximation of a single Slater determinant, where the electron correlation is neglected and the electron repulsion is taken as an average, the Hartree-Fock method is derived, and an approximate solution can be calculated. Within the self-consistency field framework, the trial wavefunction will be iterated and minimized until a convergence in the energy is achieved.

$$\frac{-\hbar^2}{2m}\nabla^2\Psi(x) + V(x)\Psi(x) = E\Psi(x) \tag{3.1}$$

Afterwards, different methods have been proposed to account for the electron correlation, called post Hartree-Fock methods, such as configuration interaction (CI), multi-configuration self-consistent field (MCSCF), multi-reference configuration interaction (MRCI), many-body perturbation theory, and coupled cluster. Another approach that is based on the electron density, called Density Functional Theory method (DFT), has also been proposed, and it will be the main method employed in this thesis.

3.2.1.1 DFT methods

While the methods mentioned earlier are based on wavefunction approach, Density Functional Theory (DFT) is based on the electron density.[14] The method was first developed by Hohenberg and Kohn and further refined by Kohn and Sham,[15,16] and was based on two important theorems. Firstly, the ground state electronic energy of a system can be represented fully by the electronic density, instead of the wavefunctions, reducing the dimensions of the calculation. Secondly, the kinetic energy of the interacting electrons can be calculated with non-interacting electrons system, assuming the existence of the non-interacting system, and separating the contribution of the interacting parts into the exchange-correlation term. Consequently, the energy calculation can be separated into two parts (see Equation 3.2 and 3.3).

$$E_{DFT}[\rho] = T_S[\rho] + V_{ne}[\rho] + J[\rho] + E_{XC}[\rho] \tag{3.2}$$

$$E_{XC}[\rho] = (T[\rho] - T_S[\rho]) + (E_{ee}[\rho] - J[\rho]) \tag{3.3}$$

The first three terms on the right hand side of Equation 3.2 corresponds to kinetic energy of non-interacting electrons (T_S, potential energy between nuclei and electrons (V_{ne}), and repulsive energy between non-interacting electrons (J, respectively. These three terms can be calculated in an exact manner. The fourth term corresponds to the exchange-correlation term arising from the interacting electrons (E_{XC}). This term is then described by the different types of approximations introduced by functionals that are constantly being developed and proposed over the years.[14]

Perdew and Schmidt introduced the term Jacob's Ladder of density functional approximations to classify the functional according to the "ingredients" used in the definition.[17] The essence of the term is that the functionals characterized into the higher rung give more accurate results, but at the expense of a more complex functional form and sometimes also the computational cost, than the functionals in the lower rung. The first rung of Jacob's ladder depends only on the density of the system, which is called the local spin density approximation (LSDA). Functionals that include the density and its gradient belong to the second rung, called generalized gradient approximations (GGA), to which PBE[18] and PBEsol[19] belong to. The third rung considers also the Laplacian of the density, which is called meta-GGA, for example TPSS[20] and M06-L.[21] The hybrid functional, the fourth rung, includes a certain percentage of nonlocal exact exchange, such as B3LYP[22–24], while the last rung (*i.e.* double-hybrid) includes the contributions from unoccupied orbitals. Eventually, for practical purposes, the choice of functionals will be highly dependent on the system and properties of interest. In the case of metal nanoparticles system, the PBE functional provides a good balance for the accuracy and computational cost. It is important to mention that with the local nature of the functionals of DFT, it does not consider dispersion effects. Therefore, a dispersion correction to the energetic term has to be added to improve the description of the characteristic asymptotic R^{-6} behavior.[25]

3.2.1.2 Basis Sets

Another important aspect in computational chemistry is the choice of basis set, based on which the molecular orbitals are built. The basis function can be described either as atomic orbitals centered on atoms or plane wave, among others. The plane waves are typically used to describe solid state systems, while the atomic basis sets are the typical choice in the molecular quantum chemistry. The atomic basis sets can be further classified as the Gaussian-type orbitals (GTO) or Slater-type orbitals (STO), and the linear combination of these atomic orbitals yields the molecular orbitals. Though STOs are considered as the best physically motivated basis set, the computation of the integrals is proven to be difficult and costly. Therefore, GTOs are by far the most used basis sets in the community of quantum chemistry, and many different families of GTOs basis set have been generated.[26–29]

In a real system, technically infinite basis functions have to be used to build molecular orbitals. However, within computational approach, only finite basis functions can be used. Consequently, two important errors arise, which are basis set incompleteness error (BSIE) and basis set superposition error (BSSE). The BSIE arises due to the difference between the results obtained with small basis set and with (or extrapolated to) complete basis set. On the other hand, the BSSE arises due to the artificial local increase in basis set size within the overlapping regions, and it is important while calculating interaction/binding energy, as it will result in an overestimated energy. Boys and Bernardi proposed a correction method, called Counterpoise (CP), in which the energies of each monomer are corrected by the monomer energies calculated in the presence of the basis functions of the other monomer, but without the atoms.[30]

Equation 3.4 shows the calculation of BSSE correction with CP method, with E_{BSSE} representing the BSSE error, $E_A(AB)$ representing the energy of monomer A in the presence of basis functions of B, and $E_B(AB)$ referring to the energy of monomer B in the presence of basis functions of A, while the $E_A(A)$ and $E_B(B)$ corresponding to the energy of monomer A, and B, respectively. As a rule of thumb, the larger the basis set used to describe a molecule is, the more accurate the calculation would be. However, the computational costs quickly become very expensive for large molecules. As such, a balance between the choice of basis set and the computational cost must be maintained.

$$\begin{aligned} E_{BSSE} =& (E_A(AB) - E_A(A)) + (E_B(AB) - E_B(B)) \\ E_{INT-CORR} =& E_{AB}(AB) - E_A(AB) - E_B(AB) \end{aligned} \tag{3.4}$$

For calculations involving heavy atoms, a basis set that properly considers at least the scalar relativistic effect is important. Different all electron basis set developed using relativistic Hamiltonians, such as ZORA[31] and DKH[32], have been proposed. However, the computational cost associated with large number of electrons can be prohibitive in the calculation of large systems. As such, relativistic effective core potential (RECP) has been proposed as an ideal alternative, where the core electrons are replaced by a potential, and only the valence electrons are treated explicitly.[33,34] For Au atom, different RECPs are available along with their respective associated basis sets, and the ones used in this thesis are the RECP with 19 explicit valence electrons, called as SC-RECP[35] and the RECP with 11 explicit valence electrons, called as LC-RECP[36]. These RECP have been demonstrated to be reliable in both the energetic and geometrical aspects for calculations of gold nanoparticles.

3.2.1.3 DFT in deMon2k

In deMon2k program[8], with which the DFT calculations are performed, the Kohn Sham orbitals are expanded based on the linear combination of Gaussian-type Orbital (LCGTO) approximation. Within the approximation, the computation of the four-centered Coulomb repulsion scales with the fourth power of the size of basis set. Therefore, to reduce the scaling of the calculation by one order, a variational fitting of Coulomb potential, developed by Dunlap,[37] has been implemented. As a result, an auxiliary function has to be introduced, and the density calculated using this auxiliary function is used to calculate the exchange-correlation potential.[38]

This approach is generally known as Auxiliary DFT (ADFT), and the auxiliary density scales linearly with the number of auxiliary functions, as compared to the quadratic scaling of Kohn-Sham density. The auxiliary function set is given by s, spd, and spdfg Hermite Gaussian functions, and the functions adapted to the used basis sets are automatically generated by the program. Subsequently, the converged density projected to the molecular orbitals is obtained with SCF (MinMax) iteration procedure.[39]

In a typical computation setup for a DFT calculation with deMon2k, the convergence criteria for SCF iteration have been set to 1.10E^{-9} a.u. and 5.10E^{-7} a.u, for MinMax SCF and for auxiliary density, respectively. The adaptive grid with tolerance of 1.10E^{-6} a.u. has been used for the numerical integration of exchange-correlation energy and potential. For open-shell complexes, a smearing keyword has been used to allow fractional occupation of the frontier orbitals. The calculation has been performed with dispersion corrected PBE functional.[25] The gold atoms have been described with either SC-RECP or LC-RECP, as described previously. The organic molecules are described with DZVP basis sets. The geometry optimization has been performed with the convergence criteria of at least 1.10E^{-5} a.u.. The frequency analysis for calculation of IR and Raman spectra has been performed analytically within the ADPT framework, as reported by Delgado-Venegas *et al.*.[40]

3.2.1.4 Fukui Function Analysis

To evaluate the reactivity of GNP, Fukui function has been demonstrated to be a good descriptor for organic molecules and GNP, which is based on the frontier molecular orbitals.[41] Fukui function represents the change of electron density with respect to the change in the number of electrons, and they are typically calculated with finite-difference approach. However, the calculation of Fukui function in deMon2k has been implemented with the perturbation theory approach, with comparable results obtained for organic molecules.[42] Equation 3.5 shows the Fukui function associated with the electrophilic attack (f^-) and the nucleophilic attack (f^+). To calculate the Fukui function at atomic center, *i.e.* condensed Fukui function, the evaluation is done in terms of the Mulliken charges, see Equation 3.6. Furthermore, the average of the f_k^- and f_k^+ corresponds to the susceptibility to radical attack. Meanwhile, the $\Delta f(r)$ has been proposed as a dual descriptor,[43] discriminating the atoms to be either nucleophilic (when $\Delta f(r) < 0$) or electrophilic (when $\Delta f(r) > 0$).

$$\begin{aligned} f^-(r) &= \rho(r,N) - \rho(r,N-1) \\ f^+(r) &= \rho(r,N+1) - \rho(r,N) \end{aligned} \tag{3.5}$$

$$\begin{aligned} f_k^-(r) &= q_k(N) - q_k(N-1) \\ f_k^+(r) &= q_k(N+1) - q_k(N) \\ f_k^0(r) &= \frac{f_k^-(r) + f_k^+(r)}{2} \\ \Delta f_k(r) &= f_k^+(r) - f_k^-(r) \end{aligned} \tag{3.6}$$

3.2.2 Topological Analysis

Within the framework of Quantum Theories of Atoms in Molecule (QTAIM),[44,45] information on the molecular bonding can be obtained through the topological analysis of the electron density distribution. This framework has been developed by Richard F.W. Bader and colleagues, and from there onwards, there have been increasing number of topological tools developed with QTAIM as the basis. All these tools are grouped under Quantum Chemical Topology, a term first introduced by Popelier and Aiken.[46] In the QTAIM framework, the molecules are separated into nuclear attractors and basins, based on the gradient vector field of the electron density. An atom is, therefore, defined by the attractor and its associated basins. The interatomic surface, also known as critical point, is the converging point of a set of gradient paths originating from the nuclei. The bond critical points, along with their associated bond paths, refer to the concentrated density that links two atomic centers. The presence of these bond critical points, along with the bond paths, represents the presence of an interaction between the two atoms. On top of the bond critical points, there are also critical points associated to ring (connected to at least three attractors and BCPs) and to cage (connected to four or more non coplanar attractors).

At the bond critical point, the interaction can be characterized based on the local indicators, *i.e.* electron density (ρ_b), the Laplacian of the electron density ($\nabla^2 \rho_b$), and energy density (H_b). Bianchi *et al.* performed a topological analysis on the experimentally obtained electron density distribution of $Mn_2(CO)_{10}$, and they proposed the bonding criteria for metal-ligand bonds, as seen in Table 3.1.[47] There are other characterization criteria proposed for characterization of interaction based on local indicators at BCP, but because of the simplicity and its relevance to our systems of interest, Bianchi's characterization will be applied throughout this chapter.

Another important topological tools is the electron localization function (ELF), proposed and developed by Becke and Edgecombe.[48] ELF, simply put, measures the probability of finding a pair of electrons in a multi-electron system, based on the consideration of the Hartree-Fock pair probability and yet orbital independent. Applying partition based on the gradient dynamical system results in basins that correspond to the core electrons, lone pairs, and bond regions. These basins can be qualitatively compared to the geometry obtained with VSEPR model. The pop-

Table 3.1: The criteria for bond characterization based on local indicators at BCP, as proposed by Bianchi.[47]

Bond type	ρ_b	$\nabla^2\rho_b$	H_b
van der Waals	low	>0	>0
dative	low	>0	<0
covalent	high	<0	«0

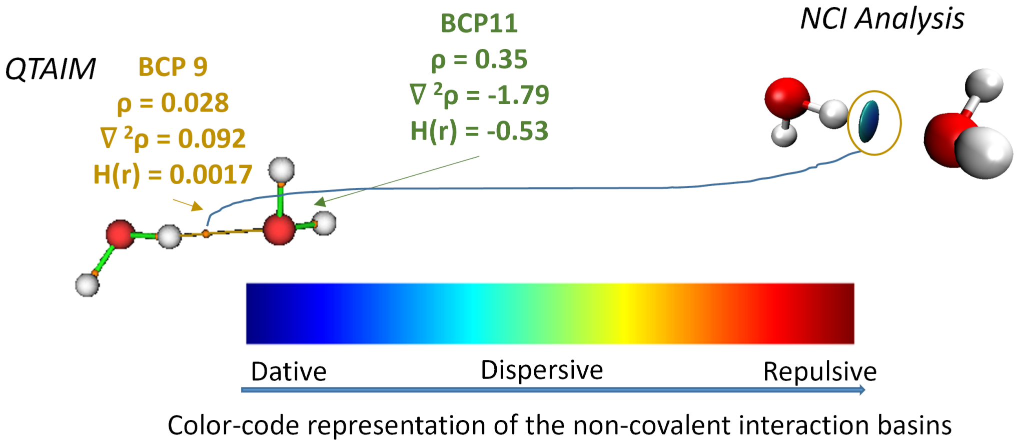

Figure 3.2: Quantum chemical topological analysis of water dimer: (left) QTAIM identifying both the covalent and non-covalent BCP and (right) NCI analysis visualizing the non-covalent interaction basins

ulation analysis performed within these basins could give information on the rearrangement of electrons as molecules interact.[49,50]

Johnson *et al.* proposed Non-Covalent Interaction (NCI) method based on the reduced density gradient (s), to simultaneously identify and visualize non-covalent interactions present in interacting compounds (see Figure 3.2).[51] Calculating the reduced density gradient (s), a dimensionless DFT quantity that describes the deviation from a homogeneous electron distribution, the non-covalent interaction can be easily located. Plotting the s against the electron density (ρ) will feature the non-covalent interactions at low electron density. Furthermore, the interaction can be characterized based on the sign of the second Hessian eigenvalue, where positive sign corresponds to non-bonded non-covalent interaction and negative sign corresponds to the bonded non-covalent interaction. The strength of the interaction is inferred from the electron density. Therefore, the interaction can be characterized into dative type when sign(λ_2)ρ < -0.02, dispersive when -0.02 < sign(λ_2)ρ < 0.02, and repulsive when sign(λ_2)ρ > 0.02. The visualization of the non-covalent interaction is similarly coded into blue (*i.e.* dative), green (*i.e.* dispersive), and red (*i.e.* repulsive). NCI analysis has been extensively used as a qualitative descriptor for various systems. In addition, very recently, quantitative analysis of NCI basins has been demonstrated to evaluate the interaction between DNA base pairs.[10]

Each of the analysis tool mentioned here has been employed to study and visualize the non-covalent interaction between GNP and its ligand, except for the ELF analysis.[52–58] The basis corresponding to the non-covalent interaction has not been detected with ELF analysis, because the likelihood of finding a pair of electrons in a non-covalent interaction is small.

3.2.3 Charge Decomposition Analysis

Proposed by Dapprich and Frenking, charge decomposition analysis allows the investigation of donor-acceptor interactions by partitioning the molecular orbitals into the donor and acceptor fragments.[59] The partitioning is based on the linear combination of the fragment orbitals, from which several terms can be calculated. Firstly, the charge donation (d) is given by mixing the occupied orbitals of donor species and the unoccupied orbitals of acceptor species. Secondly, the back donation (b) is given by mixing the unoccupied orbitals of donor species and occupied orbitals of the acceptor species. Lastly, the mixing of the occupied orbitals of donor and acceptor species give the charge depletion from the overlapping area, or in other words, the charge polarization (r). All these terms are described in Equation 3.7. Furthermore, this decomposition scheme is subjected to basis set superposition error. However, it is the relative term of each of the term, rather than the absolute term that are meaningful. Still, this method has provided a quantitative insight into many donor acceptor complexes, as well as complexes of transition metals.[60,61]

$$\begin{aligned}
d_i &= \sum_k^{occ,A} \sum_n^{vac,B} m_i c_{ki} c_{ni} \langle \Phi_k | \Phi_n \rangle \\
b_i &= \sum_l^{occ,B} \sum_m^{vac,A} m_i c_{li} c_{mi} \langle \Phi_l | \Phi_m \rangle \\
r_i &= \sum_k^{occ,A} \sum_m^{occ,B} m_i c_{ki} c_{mi} \langle \Phi_k | \Phi_m \rangle
\end{aligned} \tag{3.7}$$

3.2.4 Decomposition of Intermolecular Interaction

There are different approaches developed recently to decompose intermolecular interaction into its physically meaningful constituents. These decomposition schemes will provide a great insight into the quantitative understanding of the underlying governing forces contained in the intermolecular interaction energy. In this work, two different approaches have been used to investigate the complexes, *i.e.* Symmetry Adapted Perturbation Theory (SAPT)[62] and Block-Localized Wavefunctions Energy Decomposition Analysis (BLW-EDA).[63] Moreover, these decomposition analysis schemes have been employed to assist in the development of parameters for force fields.[64,65]

3.2.4.1 SAPT

As the name suggests, SAPT is a perturbative approach, where the interaction is treated as a perturbation to the isolated monomers.[62] Within this scheme, the interaction energy is the summation of electrostatic, induction, dispersion, and exchange terms. Each of this contribution is physically meaningful, which helps in understanding the main governing forces of the intermolecular interaction. Electrostatics is defined as the Coulomb interaction between the charge densities of individual monomers. This term includes the charge penetration effects (overlap of electron densities) at short range, and the interaction between permanent multipole moments of the monomers at long range. Induction results from the mutual polarization between the monomers. At long range, the induced dipole moments that depend on static polarizabilities and hyperpolarizabilities are included in this term. Dispersion is defined as the correlated fluctuations of electron density on both molecules, that exhibit attractive effect providing weak intermolecular binding. Lastly, the exchange term comes from the Pauli exclusion principle, which represents the repulsive interaction between the monomers. Depending on the level of treatment of the electron correlation, the interaction energy calculated with SAPT can reach a high accuracy. Furthermore, SAPT based on density constructed from the Kohn-Sham orbitals and orbital energies has also been proposed as an alternative to the Hartree-Fock based, called SAPT(DFT). In this work, only the simplest SAPT method is being used, SAPT0, where the intramonomer correlation is completely neglected. The formulation of SAPT0 can be written as shown in Equation 3.8.

$$E_{int}^{SAPT0} = E_{elst}^{(10)} + E_{exch}^{(10)} + E_{ind,resp}^{(20)} + E_{exch-ind,resp}^{(20)} + E_{disp}^{(20)} + E_{exch-disp}^{(20)} + \delta E_{HF}^{(2)} \quad (3.8)$$

with the $E_{elst}^{(10)}$ corresponds to the electrostatic interaction of the charge densities at HF-level, $E_{exch}^{(10)}$ corresponds to the product of monomer HF determinants, $E_{ind,resp}^{(20)}$ corresponds to the relaxation of monomer in response to the electrostatic potential of the other monomer, $E_{disp}^{(20)}$ corresponds to the electron correlation, and lastly, the $\delta E_{HF}^{(2)}$ term that accounts for the higher order induction and exchange induction effects. The dispersion and induction terms that are quenched by repulsive term has to be included in the equation as well.

3.2.4.2 BLW-EDA

The BLW-EDA has been designed based on the block localized wave function (BLW), that allows a rigorous separation between charge transfer and polarization energy terms.[63] The framework of BLW, which is also known as absolutely localized molecular orbitals (ALMO), defines one block for a molecule by localizing the electrons in terms of atom-centered basis functions, and the expansion of these basis functions is restricted to exclude contributions from other basis functions in the system. The BLW is then variationally optimized, and the mutual polarization interaction between different blocks is also calculated variationally. Meanwhile, the charge transfer energy corresponds to the interactions of bonding orbital between the fragments. The total interaction energy within this framework can be written as Equation 3.9.

$$E_{int}^{BLW-EDA} = E_{frozen} + E_{pol} + E_{CT} \tag{3.9}$$

with E_{frozen} as frozen energy that includes the electrostatic, dispersion, and repulsion, E_{pol} as polarization energy, and E_{CT} as charge transfer energy terms that includes the donor-acceptor interaction, respectively. Each of the term can be further expressed as shown in Equation 3.10

$$\begin{aligned} E_{frozen} =& E_{guess} - E_{frag1} - E_{frag2} \\ E_{pol} =& E_{BLW} - E_{guess} \\ E_{CT} =& E_{system} - E_{BLW} - E_{BSSE} \end{aligned} \tag{3.10}$$

with E_{guess} corresponds to the superposition of the fragment density matrices, E_{BLW} corresponds to the energy obtained by BLW, and E_{BSSE} corresponds to the energy corrected with basis set superposition error. The BSSE has been calculated with CP method, as described in the methodological section. This approach has been employed to understand the charge transfer and polarization behavior of water adlayer on noble metal surfaces.[66]

3.3 Interaction Between Organic Molecules and A Gold Nanoparticle: A Quantum Chemical Topological Analysis

In this section, the interaction between gold nanoparticles and small representative organic molecules has been investigated, with Au_{79} as the model for GNP. The representative small organic molecules consist of methane, methanol, formic acid, ammonia, hydrogen sulfide, and benzene. Each of the organic molecule represents one functional groups, which allows us to investigate the interaction of each functional group in the absence of competitive interaction. With Au_{79} as the model for GNP, there are multiple possible interaction sites, *i.e.* corner, edge, and face sites. The reactivity of these sites has been analyzed with both dual Fukui function and electrostatic potential (ESP). Afterwards, to compare the reactivity of the different sites, each of the molecule has been initially placed at these three interaction sites. Once the optimized geometries have been obtained, the complexes are subjected to various topological analysis to gain more insights into the nature of the interaction. Moreover, the role of the molecular orbitals on the adsorption geometry of the organic molecules has been assessed. The details of the investigation have been published in Theoretical Chemistry Accounts and can be found in the following section.[67]

Theoretical Chemistry Accounts manuscript No.
(will be inserted by the editor)

Interaction between Organic Molecules and a Gold Nanoparticle: a Quantum Chemical Topological Analysis

Rika Tandiana · Nguyen-Thi Van-Oanh · Carine Clavaguéra

Received: date / Accepted: date

Abstract The ligands at the surface of a gold nanoparticle (GNP) have a significant influence on the optical and physical properties, that may render different functionalities to the GNP. Therefore, there is a need in understanding the nature of the interaction at atomic resolution in order to allow rational design of GNPs with desired physico-chemical properties. The interaction between Au_{79} and a series of small organic molecules has been systematically studied at the quantum mechanical level : methane, methanol, formic acid, hydrogen sulfide, benzene, and ammonia. The reactivity of Au_{79} has been first analyzed by performing the condensed Fukui analysis to emphasize that the surface of Au_{79} is dominated by electrophilic sites, with higher reactivity at the corner and edge atoms. The net charge transfer flowing from the organic molecules towards Au_{79}, comes from the electrophilic behaviour of the GNP. Furthermore, the shape of the frontier molecular orbitals of Au_{79} and of the incoming organic molecules has been found to dictate the preferred orientation of the adsorption. Several quantum chemical topological analyses of the electron density have been performed to further classify the interactions to weak dispersive or van der Waals interactions in methane and stronger non-covalent interactions in ammonia, benzene, hydrogen sulfide, methanol, and formic acid. The analysis of the electron localization function (ELF), on the other hand, provides more insight about the charge transfer, as the population of the basins of the organic molecules has decreased after interacting with Au_{79}.

Keywords Quantum Chemical Topology · Gold nanoparticle · Non covalent interactions · DFT

1 Introduction

Gold Nanoparticles (GNPs), due to their versatility and unique optical properties, have largely been applied in many different fields that include catalysis, drug delivery, imaging, molecular recognition, sensors, and biomedical applications. All of these applications require the gold nanoparticles to be surrounded by ligands of an increasing complexity. The tunability of the size and geometrical shape of GNP, along with the variation in surface charge, further adds into the richness of the gold nanoparticles systems. However, we also could not exclude the role of solvent packing at the interface of gold nanoparticles, which have been shown to increase the radiosensitizing properties of gold nanoparticles.[1–3] Therefore, there is an interest in understanding the interaction between GNP and ligands in the presence of solvent at atomic level to allow design of optimal ligands for GNP with desired properties. The pursuit of such understanding has been undertaken by the researchers worldwide. With the development of surface-sensitive spectroscopy techniques, such as Surface Plasmon Resonance (SPR), attenuated total reflection Fourier transform Infrared (ATR-FTIR), Sum Frequency Generation

Rika Tandiana
Université Paris-Saclay
CNRS, Institut de Chimie Physique, UMR8000
91405 Orsay, France E-mail: rika.tandiana@universite-paris-saclay.fr

Van-Oanh Nguyen-Thi
Université Paris-Saclay
CNRS, Institut de Chimie Physique, UMR8000
91405 Orsay, France E-mail: van-oanh.nguyen-thi@universite-paris-saclay.fr

Carine Clavaguéra
Université Paris-Saclay
CNRS, Institut de Chimie Physique, UMR8000
91405 Orsay, France E-mail: carine.clavaguera@universite-paris-saclay.fr

(SFG), Polarization Modulation Infrared Reflectance Absorption Spectroscopy (PM-IRRAS), Time-of-flight Secondary Ion Mass Spectrometry (TOF-SIMS), Surface Enhanced Raman Spectroscopy (SERS), Circular Dichroism (CD), and X-ray Absorption Spectroscopy (XAS), it is possible to probe into the interactions at the interface.[4–13] Computational modelling approaches have also been employed to provide atomistic insight into the nature of the interactions between nanoparticles and biomolecules.[14–28] Yao et al, has reported a combined experimental and theoretical study on the adsorption behavior of l-cystein on gold nanoparticles. The experimentally obtained SERS spectra have been qualitatively compared to calculated spectra for a series of cysteine geometries interacting with gold nanoclusters. They conclude that the S and O sites of cysteine are the binding sites with the nanoclusters.[29]. Shao et al performed a thorough investigation on the interaction of amino acids with gold nanoparticles with classical molecular dynamics simulation. The variables considered during their simulation were the size of GNPs, the preference of either backbone or sidechain, and the influence of the solvation shell, which demonstrated the complexity of the interaction. [30]. Yet, atomic investigation into the interaction with gold nanoparticles is still limited. The precise information on the interaction will present the opportunity to design optimal ligands for desired properties or to predict the bonding orientation of biomolecules.

Therefore, the goal of the current article is to decipher the nature of the interaction between Au_{79} and several small organic molecules, whose functional groups are commonly present in amino acids. The Density Functional Theory (DFT) framework was used and followed by thorough quantum chemical topological analysis to characterize the interaction. The study starts by computing the electronic property and reactivity index of Au_{79}. Then, representative organic molecules, such as methane, ammonia, methanol, hydrogen sulfide, formic acid, and benzene, are adsorbed to the surface of the GNP. The interaction is investigated by electronic structure calculations and quantum chemical topological analysis of the electron density combining several theoretical tools.

2 Methodology

Systems of interest Au_{79} (1.15 nm of diameter) has been selected as the model GNP throughout the article, and representative organic molecules have been selected with commonly available functional groups: methane, ammonia, formic acid, hydrogen sulfide, benzene, and methanol (see Figure 1). The structure of Au_{79} has been taken from the dataset for silver nanoparticles, and re-optimized with gold atoms at the DFT level [31].

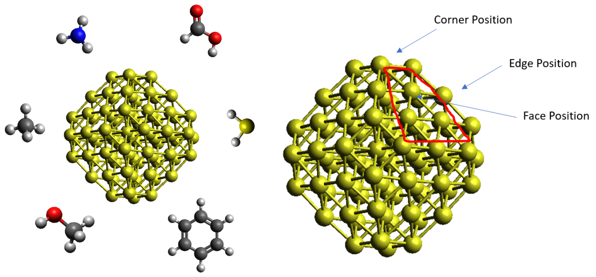

Fig. 1 Left: Schematic representation of Au_{79} interacting with methane, ammonia, formic acid, hydrogen sulfide, benzene, and methanol. Right: Different interaction sites on Au_{79}.

Fukui analysis The reactivity of Au_{79} is analyzed by computing the Fukui function $f(r)$ to identify the electrophilic and nucleophilic sites. Investigations on the Au clusters [32], AuNPs [33], and Au [111] surface [34] based on the Fukui's frontier molecular orbitals theory have demonstrated the effectiveness of the analysis on the prediction of their reactivity. Fukui function analysis at the DFT level is defined as :

$$f(r) = \left[\frac{\delta\mu}{\delta\upsilon(r)}\right]_N = \left[\frac{\delta\rho(r)}{\delta N}\right]_{\upsilon(r)} \tag{1}$$

with μ as the chemical potential, $\upsilon(r)$ as the external potential, $\rho(r)$ as the electron density and N as the total number of electrons. Based on equation (1), Fukui function can be defined as the sensitivity of the chemical potential to a change in the external potential and as the change in the electronic density as the number of electrons change. Therefore, the electrophilic (f^-) and nucleophilic attacks (f^+) can be evaluated using a finite different approach:

$$f^-(r) = \rho(r, N) - \rho(r, N-1) \tag{2}$$

$$f^+(r) = \rho(r, N+1) - \rho(r, N) \tag{3}$$

Yang and Mortier proposed a method that allows evaluating the Fukui function at the atomic center[35], which is also known as condensed Fukui function, in terms of the charges, as follow:

$$f_k^-(r) = q_k(N) - q_k(N-1) \tag{4}$$

$$f_k^+(r) = q_k(N+1) - q_k(N) \tag{5}$$

with k indices representing the atomic centers. With the introduction of dual descriptors, the simultaneous nucleophilic and electrophilic behaviors of the system at point r have been made possible. This dual descriptor, called Δf, is defined as the difference between f^+

and f^-. When $\Delta f > 0$ the atom behaves as electrophilic species and when $\Delta f < 0$, the atom behaves as nucleophilic species.[36,37] In this study, the analytic Fukui function calculation has been performed as implemented in deMon2k,[38,39] which uses auxiliary density perturbation theory (ADPT). ADPT is based on the variational fitting of the coulombic potential and the associated approximation of exchange-correlation energy.

DFT calculations All DFT calculations have been performed with deMon2k code,[40] which generates auxiliary density that are variationally fitted against the Kohn-Sham density, resulting in reduced computational cost that depends on the number of auxiliary functions, instead of the size of the basis set. The electronic properties, such as frontier molecular orbitals were initially calculated for Au_{79}, with unrestricted Kohn-Sham method (convergence criteria: for SCF (self-consistency field convergence) tolerance of $1.0.10^{-9}$ a.u., for CDF (auxiliary density convergence) tolerance of $5.0.10^{-7}$ a.u.). Initially, the organic molecules were placed at the three different positions as shown in Figure 1. Calculations were performed using the PBE functional, with empirical dispersion added[41]. DZVP Gaussian-type basis sets were used for all the organic molecules and relativistic large-core effective core potential (11 valence electrons treated explicitly) with the associated basis set for Au.[42] Local geometry optimizations were performed with the criteria of $1.0.10^{-4}$ a.u. and with $1.0.10^{-7}$ a.u. and $1.0.10^{-5}$ a.u. for SCF and CDF tolerance, respectively. Due to the small electronic gap and degenerated orbitals between the frontier molecular orbitals (MOs), the spin multiplicity was set to 2 at the beginning of the calculation and a smearing process was activated to allow fractional occupation of orbitals with energy difference of 0.01 a.u.. The interaction energy, E_{INT}, was obtained via:

$$E_{INT} = E_{TOT} - E_{GNP} - E_{ORG} \qquad (6)$$

with the E_{TOT} the energy of the system, E_{GNP} the electronic energy of Au_{79}, and E_{ORG} the electronic energy of the respective organic molecule at the geometry of the full system. Basis set superposition error (BSSE) was estimated for several complexes but frequently, the open-shell nature of the systems with different basis sets results to SCF convergence issues. Consequently, BSSE corrections were not included in the interaction energies to simplify the calculations. The provided interaction energies are thus qualitative but the underlying trends are preserved. The charge transfer (CT) was obtained by subtracting the total charge of Au_{79} before and after interacting with organic molecules using different population schemes.

Quantum chemical topology analysis All quantum chemical topological analyses[43,44] were performed with the Multiwfn code,[45] by analyzing the electron density generated from the deMon2k code with tight SCF and CDF criteria of $1.0.10^{-9}$ a.u. and $5.0.10^{-7}$ a.u. respectively. Calculations of bond critical points in the quantum theory of atoms in molecule (QTAIM) framework were performed,[46,47] associated to the computation of several properties, such as the electron density $\rho(r)$, the energy density $H(r)$, and the electron density Laplacian descriptor to characterize the bonding.[48] Then, the electron localization function (ELF) basins of the system were calculated,[49] to observe the change in the population of the basins as the molecule interact with Au_{79}. Lastly, the analysis of Non-Covalent Interactions(NCI) were calculated based on the reduced density gradient (RDG).[50]

3 Results and discussion

3.1 Electronic properties of Au_{79}

We initially calculated the electronic properties of Au_{79}, and the 5 highest occupied and 5 lowest unoccupied molecular orbitals (HOMO and LUMO, respectively) are reported in Figure S1. Considering the degenerated molecular orbitals, the fractional occupation of the orbitals has been allowed during the calculation. Therefore, the 5 HOMOs could act as both electron donor and electron acceptor, while the LUMO can only act as the electron acceptor. The reactivity of Au_{79} was then analyzed by performing both condensed Fukui analysis and the electrostatic potential (ESP) calculation to pinpoint the nucleophilic and electrophilic sites. On the left of Figure 2, the plot of Δf function is shown, with the blue lobes (positive isosurface) corresponding to the electrophilic sites and red lobes (negative isosurface) to the nucleophilic sites (the isosurfaces of f^+, f^- and the average between the two are available in Figure S2, numerical values are provided in Table S1). In this representation, the surface of Au_{79} is more susceptible to the attacks by nucleophile species, while the area sensitive to the electrophile attack is within the core of the GNP. Furthermore, the size of the electrophilic lobes at the corner and edges positions are larger than that of the face positions, which implies an increased reactivity at these sites.[33] As a result, nucleophiles are more likely to adsorb on the corner and edges atoms rather than the face atoms. The electrostatic potential of Au_{79} is shown in Figure 2 right, where the blue isosurface represents the positive potentials (electrophilic sites) and the red isosurface represents the negative potentials (nucleophilic sites). In this analysis, similarly, the surface of GNP has been dominated by the electrophilic sites, while the nucleophilic sites are rather localized at the top and face positions of GNP. Therefore, the ESP also predicts that GNP behaves more as an electrophile and that nucleophile species prefer interacting with the corner and edges atoms rather than the atoms at the surface.

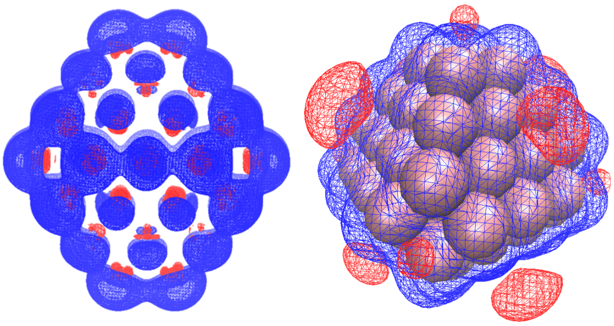

Fig. 2 Left: representation of the condensed Fukui analysis of Au_{79} (isovalue of 0.00025): the blue lobes represent the electrophilic sites and the red lobes the nucleophilic sites. Right: electrostatic potential of Au_{79} with the blue isosurface (+0.005) represents positive potentials and red isosurface (-0.001) represents negative potentials.

3.2 Interaction with small organic molecules

To validate the prediction, geometry optimizations of Au_{79} interacting with the representative organic molecules were performed. The molecules were initially placed at the three different sites (Figure 1). The optimized geometries for different binding sites along with the interaction energy and charge transfer are shown in Figure S3. From the optimization step, several observations can be made. Firstly, the preferred binding sites vary with the ligand, but in most cases they prefer either the corner or edge sites to the face sites, which is consistent with the Fukui analysis. Secondly, the interaction is considered as weak with an interaction energy range between -0.18 and -0.72 eV. The order of interaction strength, considering the most favorable binding site for each system, is found to follow this trend: methane, formic acid, methanol, hydrogen sulfide, benzene, and ammonia, as shown in Figure 3. Methane, considered as weak nucleophile and electrophile, interacts very weakly with Au_{79}, while the other organic molecules form stronger interaction through their functional groups. The availability of lone pairs on these moieties could render them as the anchoring points on the surface of GNP.

Thirdly, CT was calculated using different population schemes, i.e. Mulliken, Hirshfeld, Atomic Dipole Corrected Hirshfeld (ADCH), Voronoi, Becke, and Bader analyses, as the change in the total charge of Au_{79} before and after interacting with the ligand. In most cases, GNP receives electrons which implies that it is acting as electrophile, except in the case of the interaction with methane computed using Hirshfeld and ADCH population schemes. This behavior is consistent with the Fukui analysis. Depending on the population scheme, the calculated CT does not exactly follow the trend for the interaction energy (see Figure S4). Among them, the ADCH scheme provides a good correlation as shown in Figure 3. However, due to the arbitrary nature of the population analysis, and the different reactivity of the molecules investigated, it is less straightforward to draw a direct comparison between the charge transfer and interaction energy. Benzene, owing to the relatively richer π-electron, is more likely to donate more electrons, which has been shown by the different population schemes (Figure S4). Methanol and formic acid, despite having two lone pairs, do not donate more electron than ammonia, with one lone pair on the nitrogen atom. Therefore, further analysis on the interaction would be necessary in order to probe the possibility of other contributing factors to the interaction energy, in addition to the charge transfer.

Lastly, the possible role of the shape of MOs in the orientation of the organic molecules at the surface is investigated. Considering that organic molecules behave as electron donors, the HOMO is expected to interact with empty MOs of GNP (Figure S1). It turns out that the shape of MOs does influence the orientation of the organic molecules (Figure 4). In the example of ammonia and benzene molecules, the HOMO approaches the GNP and re-orientates itself to maximize the overlap with the MOs of Au_{79}. In all of the geometries for ammonia and benzene interacting with GNP (Figure S3), ammonia always adopts the same orientation where the hydrogen atoms are pointing away from the surface while nitrogen atom is pointing towards the surface. Meanwhile, the benzene always adopts a flat configuration and the perpendicular configuration is not stable (back to the flat orientation). The same behaviour is expected for the other organic molecules as well. Therefore, the MOs of the two species are important in determining the orientation of the ligand, which will be helpful in prediction of possible interaction between GNP of any size with other organic molecules.

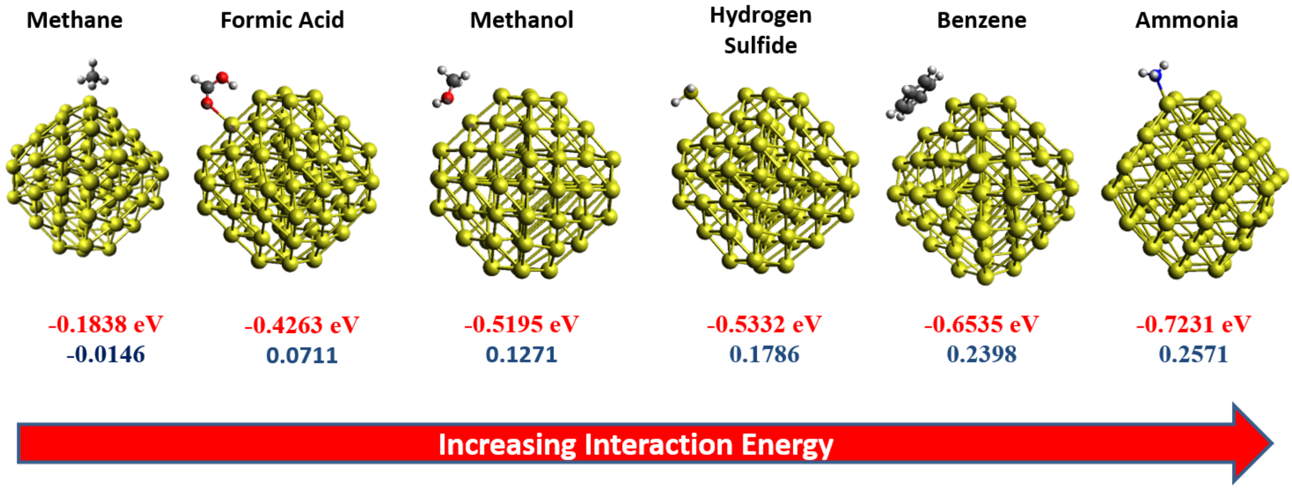

Fig. 3 Trend in interaction energy (ev) and charge transfer (e) using the ADCH[51] population scheme across the different organic molecules.

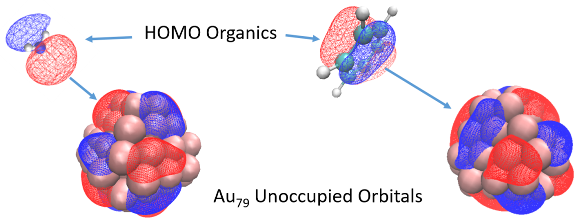

Fig. 4 Approaching HOMO of ammonia (left) and benzene (right) to Au_{79}.

3.3 Quantum chemical topological analysis

To further complement the analysis of the interaction, a thorough quantum chemical topological analysis on each system is presented to gain more insight into the nature of the interaction.

3.3.1 BCP analysis

In the QTAIM framework developed by Bader and coworkers[52], we performed a search for the bond critical points (BCP) and bond paths (BP) with the focus on the interaction sites. BCPs and BPs are present for every system that was analyzed, validating the presence of bonds for the interaction. To characterize the nature of these bonds, several local properties were calculated, i.e. electron density, the Laplacian of the electron density and the energy density, at these BCPs based on the classification proposed by Bianchi and coworkers[48]. The BCPs and properties of the gold-molecule interaction regions are shown in Table 1, in Figure 5 and Figure S5.

The electron density at each BCP is rather small, in contrast to covalent bonds (whose electron density is greater than 0.1 a.u.), which confirms weak interaction. For some of the ligands, i.e. methanol, formic acid, and benzene, there are two BCPs, which indicate the presence of another weak interaction site. Subsequently, the Laplacian for all of the systems is greater than 0, which further clarifies that the interaction is not covalent. The discriminating factor will then be the energy density, whose sign is a good indicator of the stability of the interaction. According to the classification[48], the interaction formed with methane is classified as van der Waals interactions ($H(r) > 0$). Meanwhile, the other organic molecules form at least one interaction, which is classified as dative bonding and characteristic of ligand to metal interactions ($H(r) < 0$). In the case of methanol, two bond critical points are found, one is dative interaction and the other is van der Waals interaction (which forms between the methyl group and the surface). In the case of formic acid, we also found two BCPs between the oxygen of carbonyl group and -OH group with the H pointing to the surface of Au_{79}, respectively. The interaction between the oxygen of carbonyl group is supposedly stronger than that of the -OH, as seen from the electron density. However, it is clear that this interaction contributes to the overall interaction energy. The quantum chemical topological analysis of formic acid oriented differently (see configuration 1 in Figure S6) at the surface reveals that the second interaction point is not favorable, which result in a lower value of the interaction energy. Therefore, the orientation of the ligand at the surface plays a significant role in determining the interaction energy of a system. Lastly, two bond critical points were found for benzene, with the formation of two dative bonds.

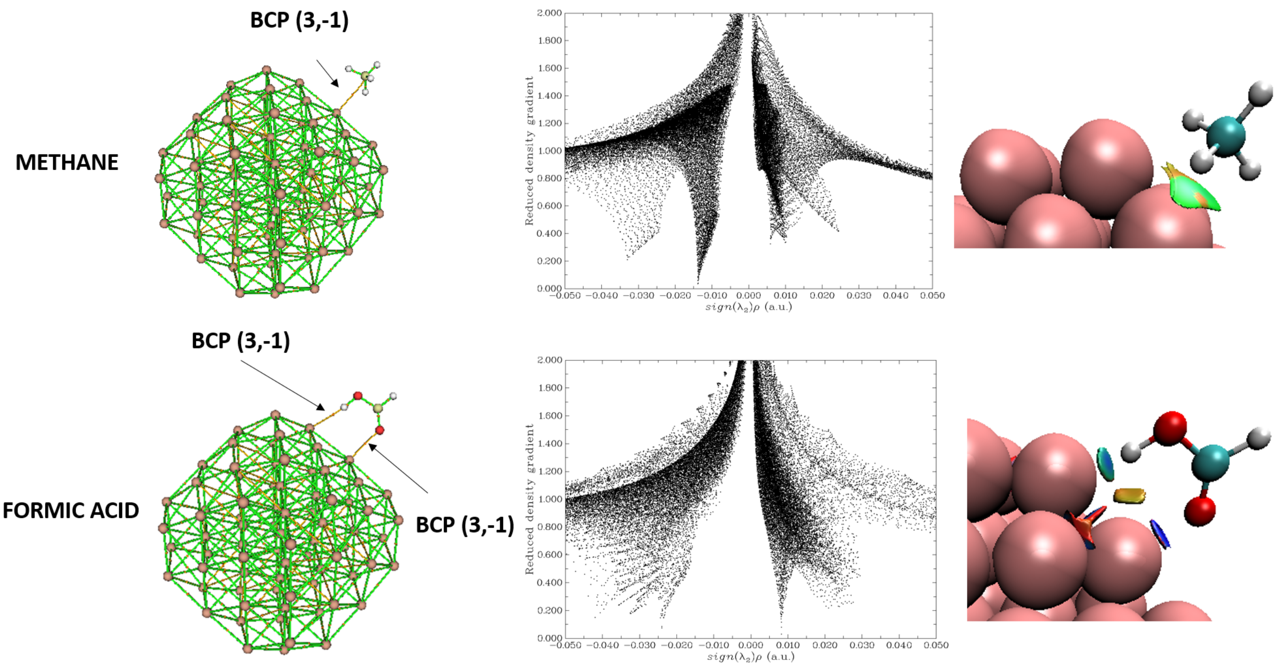

Fig. 5 BCP analysis and the respective RDG and NCI analysis on methane (top) and formic acid (bottom).

Table 1 Distances from the BCP to Au and organic molecule, local AIM electron properties (electron density, energy density and Laplacian of the electron density) calculated at the BCPs for the different ligands interacting with Au_{79}.

System	Au-BCP (Å)	Org-BCP (Å)	$H(r)$ (a.u.)	$\rho(r)$ (a.u.)	Laplacian (a.u.)
Methane	1.625	1.507	0.0016	0.0138	0.0563
NH_3	1.270	1.123	-0.0118	0.0574	0.1992
H_2S	1.367	1.372	-0.0069	0.0430	0.1167
CH_3OH	1.859	1.159	0.0010	0.0065	0.0207
	1.315	1.130	-0.0047	0.0445	0.1960
HCOOH	1.315	1.123	-0.0041	0.0438	0.1997
	1.552	0.736	-0.0018	0.0242	0.0545
Benzene	1.457	1.317	-0.0013	0.0298	0.0974
	1.433	1.284	-0.0023	0.0331	0.1070

3.3.2 ELF analysis

Then, the ELF analysis was performed. As expected for such weak interactions, we do not observe the presence of a valence basin that signifies covalent interaction between the two interacting species. Nevertheless, the population of the detected basins that belong to the ligands was investigated (Table 2). Interestingly, a decrease in the overall population of the ligands interacting with Au_{79}, as compared to the isolated molecule, is highlighted. For CH_4, we observe a very small change in the total population of the basins, which supports the fact that methane forms a very weak interaction with GNP. For ammonia, the population of the lone pair of the nitrogen atom decreases from 2.109 (isolated molecule) to 1.871 upon interaction with GNP. As for H_2S, the population of the lone pairs also decreases and rearranges from 2.127 each to 1.840 and 2.186, respectively. Similarly, the population of the lone pairs of methanol also changes from 2.412 and 2.368 to 2.728 and 1.898. However for formic acid, the population of the lone pairs of both oxygen atoms slightly increases from 4.311 and 5.117 for -OH and C=O respectively, to 4.231 and 5.261, which could probably due to the formation of favorable interaction between Au···H-O. Lastly, the total population of the benzene changes slightly, from 29.293 to 29.228. This analysis demonstrates that the organic ligands form interaction with Au_{79} that involves intermolecular charge transfer. ELF results are consistent with the CT population analysis in section 3.2 and the electrophilic character of GNP.

To check the possibility of back donation from Au_{79} to the ligands, the contribution of gold atoms to the basins of organic ligands was calculated. The results are shown in the last column of Table 2. Though the contribution is small, but it is still non-negligible, and it demonstrates the possibilities of the overlapping of the LUMO of ligands and HOMO of Au_{79}, which results in stronger interactions.[53, 54]

3.3.3 Non-covalent interaction analysis

The NCI analysis, developed by Johnson and coworkers[50], allows the detection and the visualization of weak interactions, such as steric effects, hydrogen bonds, and dispersion interactions. Here, NCI analysis was performed to identify the weak interaction between the Au_{79} and the organic molecules. The plots of the reduced density gradient with respect to the electron density multiplied by the sign of the second eigenvalues of the Hessian matrix [55] restricted to the intermolcular regions are shown in the middle parts of Figure 5 and of Figure S5. Dative interactions are found to overlap with metal-metal interaction, while the dispersion/van der Waals interactions are seen at a very low electron density. The color-coded NCI basins representation [55, 50] on the right parts of Figure 5 clearly reveal non-covalent interactions. The green colored basins between the interacting species represents the weak interactions, i.e. dispersive interactions, as in the case of methane. The color gradually changes to blue as the interaction shifts to the stronger dative interactions as in the case of ammonia. There is a consistent trend observed between this analysis and AIM results in the previous section, where multiple interaction basins have been observed on some of the molecules. There are two interaction points for methanol, with one strong dative interaction and one weak dispersive interaction (NCI basis and RDG plots). Similarly, the formic acid forms one strong dative interaction with one relatively weaker dative interaction. For bezene, two strong dative interactions are identified. Again, this analysis further demonstrates the multiple cooperating weak interactions that eventually contribute to the overall interaction energy.

4 Conclusion

To summarize, we have performed Fukui function and electrostatic potential analysis to identify the reactivity of Au_{79}, based on the electrophilic and nucleophilic sites. These reactivity descriptors predicted that the Au_{79} is more likely to behave as an electrophilic species, with the corner and edges atom identified as the more reactive sites as compared to the surface sites. This prediction has been fulfilled as the geometry optimizated GNP-organic molecules complex indeed demonstrated stronger interaction energy at the corner and edge sites of Au_{79} as compared to the face sites (0.1 to 0.2 eV). Furthermore, the electron rich moieties (O, S, C=O, π electrons) of the organic molecules act as anchor points on the surface of Au_{79}. The subsequent calculation of charge transfer shows that Au_{79} behaves as an electrophile as it accepts electrons from the incoming organic molecules. Among several population analyses, only the dipole-corrected Hirshfeld analysis provides charge transfer which follows the interaction energy trend. Possibly, charge transfer is not the unique contributing factor. Meanwhile, the role of the shapes of frontier molecular orbitals has been proposed to be important in determining the orientation of organic molecules on the surface. Therefore, various quantum chemical topological analyses have been performed to gain deeper insight into the interaction.

The analysis of bond critical points and bond paths in the AIM framework has classified the bond forming between methane to be weak van der Waals interaction, while the other organic molecules form at least one dative interaction. Moreover, the analysis on the different geometries of formic acid has demonstrated the importance of structural orientation in the overall interaction energy. The ELF analysis has helped in following the rearrangement of the electron density, which supports the charge flow from the ligand to GNP. Lastly, NCI analysis highlights weak interactions, which are consistent with the calculation of BCPs in QTAIM. This global quantum chemical topological analysis allows identification of the multiple interaction points for organic molecules, whose contribution to the overall interaction energy could be important.

All in all, this study has investigated thoroughly the interaction between Au_{79} with small organic molecules. The conclusion from this study is a first step in predicting the way larger molecules, with multiple functional groups, would interact with GNPs.

5 Supplementary Information

Valence molecular orbitals of Au_{79}, condensed Fukui analysis, geometries, interaction energies and charge transfers for the different interaction sites, charge transfer from various population analyses, and quantum chemical topological data are provided in Supplementary Information. A set of coordinates for the different complexes is also provided.

Acknowledgements The authors thank Dr. D. Lauvergnat and Dr. J.P. Dognon for a careful reading of the manuscript and helpful discussions. This work was performed using HPC resources from the GENCI (CINES/IDRIS, Grant No. 2020-A0080806830).

Table 2 Population of ELF valence basins (e) of organic molecules before and after interaction with Au_{79}.

Molecule	Isolated (e)	After Interaction (e)	Contribution of GNP (%)
Methane	7.882	7.879	0.20
NH_3	2.109	1.871	2.48
H_2S	4.253	4.025	2.99
CH_3OH	4.780	4.626	0.66
HCOOH	9.428	9.491	0.52
Benzene	29.293	29.228	2.15

References

1. C. Sicard-Roselli, E. Brun, M. Gilles, G. Baldacchino, C. Kelsey, H. McQuaid, C. Polin, N. Wardlow, F. Currell, Small **10**(16), 3338 (2014). DOI 10.1002/smll.201400110
2. G. Baldacchino, E. Brun, I. Denden, S. Bouhadoun, R. Roux, H. Khodja, C. Sicard-Roselli, Cancer Nanotechnology **10**(1), 3 (2019). DOI 10.1186/s12645-019-0047-y
3. M. Gilles, E. Brun, C. Sicard-Roselli, J. Colloid Interface Sci. **525**, 31 (2018). DOI 10.1016/j.jcis.2018.04.017
4. M. Iosin, F. Toderas, P.L. Baldeck, S. Astilean, J. Mol. Struct. **924-926**, 196 (2009). DOI 10.1016/j.molstruc.2009.02.004
5. N. Schwenk, B. Mizaikoff, S. Cárdenas, A.I. Lopez-Lorente, Analyst **143**, 5103 (2018). DOI 10.1039/C8AN00804C
6. C. Carnovale, G. Bryant, R. Shukla, V. Bansal, Phys. Chem. Chem. Phys. **20**(46), 29558 (2018). DOI 10.1039/C8CP05938A
7. G. Brancolini, D.B. Kokh, L. Calzolai, R.C. Wade, S. Corni, ACS Nano **6**(11), 9863 (2012). DOI 10.1021/nn303444b
8. F. Novelli, M. Bernal Lopez, G. Schwaab, B. Roldan Cuenya, M. Havenith, J. Phys. Chem. B (2019). DOI 10.1021/acs.jpcb.9b02358
9. Y.R. Shen, V. Ostroverkhov, Chemical Reviews **106**(4), 1140 (2006). DOI 10.1021/cr040377d
10. J.J. Velasco-Velez, C.H. Wu, T.A. Pascal, L.F. Wan, J. Guo, D. Prendergast, M. Salmeron, Science **346**(6211), 831 (2014). DOI 10.1126/science.1259437
11. M. Hoarau, S. Badieyan, E.N.G. Marsh, Org. Biomol. Chem. **15**(45), 9539 (2017). DOI 10.1039/C7OB01880K
12. J. Gao, Y. Hu, S. Li, Y. Zhang, X. Chen, Spectrochim. Acta A Mol. Biomol. Spectrosc. **104**, 41 (2013). DOI 10.1016/j.saa.2012.11.103
13. T. Petit, H. Yuzawa, M. Nagasaka, R. Yamanoi, E. Osawa, N. Kosugi, E.F. Aziz, J. Phys. Chem. Lett. **6**(15), 2909 (2015). DOI 10.1021/acs.jpclett.5b00820
14. M. Tang, N.S. Gandhi, K. Burrage, Y. Gu, Langmuir **35**(13), 4435 (2019). DOI 10.1021/acs.langmuir.8b03680
15. M. Rosa, R. Di Felice, S. Corni, Langmuir **34**(49), 14749 (2018). DOI 10.1021/acs.langmuir.8b00065
16. J.B. Le, J. Cheng, Curr. Opin. Electrochem. **19**, 129 (2020). DOI 10.1016/j.coelec.2019.11.008
17. F. Ramezani, M. Amanlou, H. Rafii-Tabar, J. Nanoparticle Res. **16**(7), 2512 (2014). DOI 10.1007/s11051-014-2512-1
18. G. Hong, H. Heinz, R.R. Naik, B.L. Farmer, R. Pachter, ACS Appl. Mater. Interfaces **1**(2), 388 (2009). DOI 10.1021/am800099z
19. S.S. Lee, B. Kim, S. Lee, J. Phys. Chem. C **118**(36), 20840 (2014). DOI 10.1021/jp412438f
20. M. Hoefling, F. Iori, S. Corni, K.E. Gottschalk, Langmuir **26**(11), 8347 (2010). DOI 10.1021/la904765u
21. J.G. Wang, A. Selloni, J. Phys. Chem. C **113**(20), 8895 (2009). DOI 10.1021/jp901842p
22. H.R. Abd El-Mageed, M. Taha, J. Mol. Liq. **296**, 111903 (2019). DOI 10.1016/j.molliq.2019.111903
23. Z. Xu, S.L. Yuan, H. Yan, C.B. Liu, Colloid Surf. A-Physicochem. Eng. Asp. **380**(1), 135 (2011). DOI 10.1016/j.colsurfa.2011.02.046
24. J. Feng, J.M. Slocik, M. Sarikaya, R.R. Naik, B.L. Farmer, H. Heinz, Small **8**(7), 1049 (2012). DOI https://doi.org/10.1002/smll.201102066
25. J. Feng, R.B. Pandey, R.J. Berry, B.L. Farmer, R.R. Naik, H. Heinz, Soft Matter **7**(5), 2113 (2011). DOI 10.1039/c0sm01118e
26. M. Hoefling, F. Iori, S. Corni, K.E. Gottschalk, ChemPhysChem **11**(8), 1763 (2010). DOI 10.1002/cphc.200900990
27. A. Domínguez-Castro, D. Hernández, F. Guzmán, Theor. Chem. Acc. **136**(7) (2017). DOI 10.1007/s00214-017-2118-7
28. M. Darvish Ganji, H. Tavassoli Larijani, R. Alamol-hoda, M. Mehdizadeh, Scientific Reports **8**(1), 11400 (2018). DOI 10.1038/s41598-018-29887-5
29. G. Yao, Q. Huang, J. Phys. Chem. C **122**(27), 15241 (2018). DOI 10.1021/acs.jpcc.8b00949
30. Q. Shao, C.K. Hall, Langmuir **32**(31), 7888 (2016). DOI 10.1021/acs.langmuir.6b01693
31. A. Barnard, B. Sun, B. Motevalli Soumehsaraei, G. Opletal (2017). URL https://data.csiro.au/collections/#collection/CIcsiro:23472v3/DItrue. Silver nanoparticle data set
32. H. Sekhar De, S. Krishnamurty, S. Pal, J. Phys. Chem. C **114**(14), 6690 (2010). DOI 10.1021/jp1004852
33. T.C. Allison, Y.J. Tong, Phys. Chem. Chem. Phys. **13**, 12858 (2011). DOI 10.1039/C1CP20376B
34. S. Chrétien, M.S. Gordon, H. Metiu, J. Chem. Phys. **121**(8), 3756 (2004). DOI 10.1063/1.1769366
35. W. Yang, W.J. Mortier, J. Am. Chem. Soc. **108**(19), 5708 (1986). DOI 10.1021/ja00279a008
36. J. Martínez, Chem. Phys. Lett. **478**(4), 310 (2009)
37. C. Morell, A. Grand, A. Toro-Labbé, Chem. Phys. Lett. **425**(4), 342 (2006)
38. R. Flores-Moreno, J. Melin, J.V. Ortiz, G. Merino, J. Chem. Phys. **129**(22), 224105 (2008). DOI 10.1063/1.3036926
39. R. Flores-Moreno, J. Chem. Theory Comput. **6**(1), 48 (2010). DOI 10.1021/ct9002527. Publisher: American Chemical Society
40. G. Geudtner, P. Calaminici, J. Carmona-Espíndola, J.M.d. Campo, V.D. Domínguez-Soria, R.F. Moreno, G.U. Gamboa, A. Goursot, A.M. Köster, J.U. Reveles, T. Mineva, J.M. Vásquez-Pérez, A. Vela, B. Zúñinga-Gutierrez, D.R. Salahub, WIREs Computational Molecular Science **2**(4), 548 (2012). DOI https://doi.org/10.1002/wcms.98
41. A. Goursot, T. Mineva, R. Kevorkyants, D. Talbi, J. Chem. Theory Comput. **3**(3), 755 (2007). DOI 10.1021/ct600373f

42. R.B. Ross, J.M. Powers, T. Atashroo, W.C. Ermler, L.A. LaJohn, P.A. Christiansen, J. Chem. Phys. **93**(9), 6654 (1990). DOI 10.1063/1.458934
43. P.L.A. Popelier, F.M. Aicken, ChemPhysChem **4**(8), 824 (2003). DOI 10.1002/cphc.200300737
44. P.L.A. Popelier, in *The Chemical Bond* (Wiley-VCH Verlag GmbH & Co. KGaA, 2014), pp. 271–308. DOI 10.1002/9783527664696.ch8
45. T. Lu, F. Chen, J. Comput. Chem. **33**(5), 580 (2012). DOI https://doi.org/10.1002/jcc.22885
46. R.F.W. Bader, P.J. MacDougall, C.D.H. Lau, J. Am. Chem. Soc. **106**(6), 1594 (1984). DOI 10.1021/ja00318a009
47. R.F.W. Bader, J. Phys. Chem. A **102**(37), 7314 (1998). DOI 10.1021/jp981794v
48. R. Bianchi, G. Gervasio, D. Marabello, Inorg. Chem. **39**(11), 2360 (2000). DOI 10.1021/ic991316e
49. A.D. Becke, K.E. Edgecombe, J. Chem. Phys. **92**(9), 5397 (1990). DOI 10.1063/1.458517
50. E.R. Johnson, S. Keinan, P. Mori-Sánchez, J. Contreras-García, A.J. Cohen, W. Yang, J. Am. Chem. Soc. **132**(18), 6498 (2010). DOI 10.1021/ja100936w. URL https://doi.org/10.1021/ja100936w
51. T. Lu, F. Chen, J. Theor. Comput. Chem. **11**(01), 163 (2012). DOI 10.1142/s0219633612500113
52. R.F.W. Bader, Acc. Chem. Res. **18**(1), 9 (1985). DOI 10.1021/ar00109a003
53. M. Puyo, E. Lebon, L. Vendier, M.L. Kahn, P. Fau, K. Fajerwerg, C. Lepetit, Inorg. Chem. **59**(7), 4328 (2020). DOI 10.1021/acs.inorgchem.9b03166
54. Y. Bulteau, C. Lepetit, C. Lacaze-Dufaure, Inorg. Chem. **59**(24), 17916 (2020). DOI 10.1021/acs.inorgchem.0c01972
55. R. Laplaza, F. Peccati, R.A. Boto, C. Quan, A. Carbone, J.P. Piquemal, Y. Maday, J. Contreras-García, WIREs Computational Molecular Science **11**(2) (2020). DOI 10.1002/wcms.1497

3.3.1 Conclusion and Perspectives

Our analysis has shown that in the gas phase, ammonia forms the strongest interaction with GNP, and followed by benzene, hydrogen sulfide, methanol, formic acid, and lastly, methane. Non-covalent interactions, that vary between dative-like interaction to dispersive interaction, have subsequently been visualized with NCI analysis. In the relatively larger molecules, *i.e.* methanol, formic acid, and benzene, there are multiple basins of interaction, depending on the orientation of the molecule. This has implication that larger and flexible molecules favor maximized interaction at the interface. Therefore, a larger sampling of the configurational phase of flexible molecules will be necessary to identify the most preferred orientations, which may not be possible with static DFT calculations.

Furthermore, the role of the molecular orbitals on the preferred orientation of the organic molecules has been demonstrated in this work. Due to the donor-acceptor nature of the interaction, a maximized overlap between the highest occupied MO of the donor (organic molecule), and the lowest occupied MO of the acceptor (GNP) is favored. Consequently, benzene has a preference to interact with the aromatic plane flat on the surface of GNP, *i.e.* interacting through the π electrons, and not in a perpendicular way. Considering that aromatic compounds are ubiquitous as possible surface ligands on GNP, it is, therefore, interesting to investigate the substituent effect on the preferred geometry of aromatic compounds, which would be the main focus in the next section.

All in all, our qualitative analysis on the interaction between GNP and a series of organic molecules has provided significant insight into the nature of the interaction. This work could eventually assist in the development of a more accurate semi-empirical tight binding approach or classical force field model. Despite the availability of such parameters currently, a more accurate ones adapted to GNP systems would be highly desirable. With the semi-empirical approaches, an extensive sampling of the configurational phase would be possible with a high accuracy and at a much-reduced computational cost.

3.4 In-depth Theoretical Understanding of the Chemical Interaction of Aromatic Compounds with A Gold Nanoparticle

The focus of this section is the investigation of the substituent effect on the adsorption geometry of aromatic compounds on GNP. Previous section has indicated the preference of benzene to adopt a flat configuration over the perpendicular configuration. Considering that substituted aromatic compounds are ubiquitous in possible surface ligands of GNP, whether or not this preference is maintained is still a question to be answered. Kneipp *et al.* has reported a different preference of phenylalanine and tryptophan despite their closely related structure.[68] Depending on the concentration of the amino acid, the preferred orientation could change as well, due to the balance between surface-ligand and ligand-ligand interactions. Furthermore, they investigated the adsorption geometry of aromatic thiols on GNP, and discovered the pH dependence nature of the interactions at the surface.[69] Therefore, the understanding of the substituent effect on the orientation of aromatic compounds could provide an explanation of the observed experimental finding. Eventually, it could also guide the interpretation of experimental spectra of other aromatic containing molecules.

In this section, the interaction between a series of substituted aromatic compounds, which are toluene, phenol, acetophenone, ethyl benzoate, benzoic acid, thiophenol, and aniline, and Au_{32} is reported. The choice of using Au_{32} instead of Au_{79} is to reduce the degree of freedom, in terms of the possible interaction sites of the GNP, hence allowing the focus on the behavior of substituted aromatic compounds. Furthermore, the computational cost for Au_{32} is lower as compared to Au_{79}. To assess the likelihood of the aromatic compounds to interact with perpendicular configuration, the molecules have initially been placed in either flat or perpendicular configurations. Similarly, the optimized geometries are subjected to various topological analysis. Moreover, a quantitative analysis of the interaction has also been obtained from the energy decomposition approaches and the quantification of NCI basins. Lastly, vibrational analysis of each of the complex is also performed. This work has been submitted for publication, and can be found in the following section.

PCCP

PAPER

View Article Online
View Journal

Cite this: DOI: 10.1039/d2cp02654f

In-depth theoretical understanding of the chemical interaction of aromatic compounds with a gold nanoparticle†

Rika Tandiana,[a] Cécile Sicard-Roselli,[a] Nguyen-Thi Van-Oanh,[a]
Stephan Steinmann[b] and Carine Clavaguéra *[a]

Received 11th June 2022,
Accepted 5th October 2022

DOI: 10.1039/d2cp02654f

rsc.li/pccp

Gold Nanoparticles (GNPs), owing to their unique properties and versatile preparation strategy, have been demonstrated to exhibit promising applications in diverse fields, which include bio-sensors, catalysts, nanomedicines and radiotherapy. Yet, the nature of the interfacial interaction of GNPs with their chemical environment remains elusive. Experimental vibrational spectroscopy can reveal different interactions of aromatic biological molecules absorbed on GNPs, that may result from changes in the orientation of the molecule. However, the presence of multiple functional groups and the aqueous solvent introduces competition, and complexifies the spectral interpretations. Therefore, our objective is to theoretically investigate the adsorption of aromatic molecules containing various functional groups on the surface of GNPs to comparatively study their preferred adsorption modes. The interaction between Au_{32}, as a model of GNPs, and a series of substituted aromatic compounds that includes benzene, aniline, phenol, toluene, benzoic acid, acetophenone, methyl benzoate, and thiophenol, is investigated. Our computed interaction energies highlight the preference of the aromatic ring to lie flat on the surface. The orientations of the molecules can be distinguished using infrared spectroscopy along with strong changes in intensity and significant shifts of some vibrational modes when the molecule interacts with the GNP. The interaction energy and the electron transfer between the nanoparticle and the aromatic molecule are not found to correlate, possibly because of significant back donation of electrons from GNPs to organic molecules as revealed by charge decomposition analysis. A thorough quantum topological analysis identifies multiple non-covalent interactions and assigns the nature of the interaction mostly to dative interactions between the aromatic ring and the GNP as well as dispersive interaction. Finally, energy decomposition analyses point out the role of the charge transfer energy contribution in the subtle balance of the different physical components.

1 Introduction

The interest in understanding the interaction between gold nanoparticles (GNPs) and their surroundings, which includes surface ligands and solvent, has recently increased significantly, owing to their tunability allowing the design and synthesis of materials with desired physical, chemical, and optical properties. These materials have a broad range of application, such as catalysis, nanomedicine, imaging, biosensors, *etc.*[1–6] The different orientation of ligands on the surface, as spectroscopically identified, depends on various factors such as coverage, surface charge, *etc.* and can affect significantly their physical and chemical properties.

With the development of surface sensitive spectroscopy techniques, such as surface enhanced Raman spectroscopy (SERS), Surface Plasmon Resonance (SPR), attenuated total reflection Fourier transform infrared (ATR-FTIR) and sum frequency generation (SFG), it is now possible to obtain structural information of the compounds interacting at the surface of nanoparticles.[7–14] The spectroscopic signatures provide information on the way biomolecules (proteins, lipids, and others) interact with nanoparticles, revealing whether the structural integrity is maintained or disrupted as they interact.[7,15–17] Nevertheless, interpretation of experimental data is often difficult as illustrated with infrared (IR) spectra that exhibit considerable

---

[a] *Institut de Chimie Physique, Université Paris-Saclay – CNRS, UMR 8000, 91405 Orsay, France. E-mail: carine.clavaguera@universite-paris-saclay.fr*
[b] *Laboratoire de Chimie, ENS de Lyon, 69364 Lyon, France*

† Electronic supplementary information (ESI) available: Detailed results for Fukui calculations, BSSE effects, interaction energies, geometries, charge transfer from different populations schemes, CDA and QTAIM analysis, IR calculated spectra, NCI analysis, and SAPT and BLW energy decomposition analysis are provided in Supplementary Information. Separate files for the coordinates of the entire series of compound. See DOI: **https://doi.org/10.1039/d2cp02654f**

vibrations along with band broadening. Also, the presence of solvent molecules can additionally induce an important difference between spectra of isolated or adsorbed molecules, making interpretation uncertain.

Also, there is still limited understanding on the underlying forces governing the interaction energy. Several computational studies investigate the interaction at the interface of nanoparticles with various molecules, such as oxygen, carbon monoxide, amino acids, *etc.*[18–23] However, these efforts have faced several challenges that include the complexity of nanoparticles in terms of size and shape, which result in different reactivity sites.

In this context, computational chemistry can provide insights at the atomistic scale. Within the quantum chemistry framework, there is still a size limitation for the systems under evaluation, despite the rapid development in the computational power. To mitigate this limitation, there are different computational methodologies available to enable the simulation of gold nanoparticles, such as the semi-empirical DFTB method,[24–26] classical force fields[22,27,28] and coarse grained models,[29,30] with increasing level of approximations introduced respectively. Therefore, these methodologies are generally developed relying on more accurate methods acting as a reference to ensure their reliability. Here, an in-depth DFT level investigation is performed to study the interaction between gold nanoparticles with aromatic organic molecules, including the dominant physical origins of the interaction energies. The achieved understanding might help the development of simplified, empirical methods: the strength and physical origin of the interactions are valuable guides for choosing the most appropriate approaches between (polarized) force fields, tight-binding methods and machine-learning potentials.

Our previous work on the interaction with a series of small organic molecules has indicated that benzene prefers to adopt a flat configuration (with the aromatic plane interacting parallel to the surface of GNP).[31] This could be attributed to the optimized interaction between the HOMO of benzene and LUMO of GNP, as well as the maximization of dispersion interactions. However, previous studies of aromatic containing compounds deposited on metal surfaces have indicated that the aromatic plane is not always adsorbed in a parallel configuration.[8,12,13,32] They could adopt either a perpendicular configuration or a tilted orientation with respect to the plane of the surface. Contributing factors include, among others, the presence of functional groups, that either alter the electron density of the aromatic compound, introduce steric effects or lead to stronger "direct" interactions because of high ligand affinity for gold. Considering the extensive presence of aromatic containing systems across diverse fields, *i.e.* materials science, enzyme design, *etc.*, it is important to understand the interactions between GNPs and aromatic compounds, in particular the substituent effect on the preferred adsorption geometries.

In this work, we are systematically investigating the interaction of a series of substituted aromatic compounds, *i.e.* benzene, benzoic acid, acetophenone, ethyl benzoate, toluene, phenol, aniline, and thiophenol, on Au_{32}, which is taken as the GNP model (Fig. 1). As the study is performed in the gas phase, benzoic acid and thiophenol are protonated whereas aniline is not protonated (NH_2 group). These forms are not the ones usually present in experimental conditions in solution. The icosahedral strucutre of Au_{32} has been taken from the literature without further change.[33] Initially, the aromatic compounds are placed in at least two different configurations, called "flat" and "perpendicular" (see Fig. 1). The complexes are then optimized without constraints and subsequently, the IR spectra are computed. The effect of the interaction with GNP is studied in detail by examining the modification of the vibrational modes of the aromatic molecule. Finally, different topological and energy decomposition analyses are performed to probe the nature of the interactions. The comparison between the different approaches leads to a more precise description of the equilibrium of the terms that compose the chemical interaction.

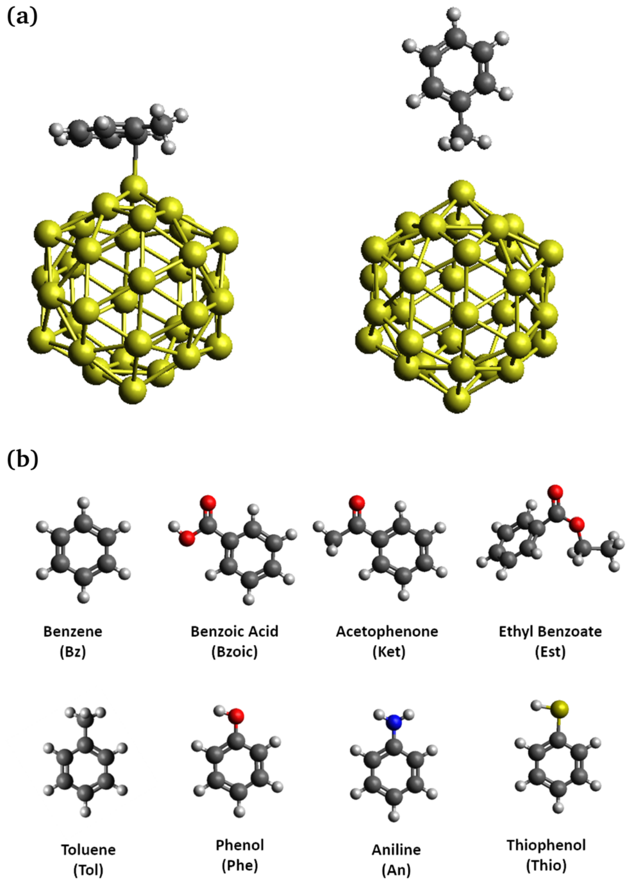

Fig. 1 (a) Schematic representation of aromatic compounds adsorbed on Au_{32} adopting flat configuration "F" (left) or perpendicular configuration "P" (right). (b) Aromatic molecules and their abbreviations.

2 Methodology

2.1 DFT calculations

DFT calculations have been performed with the GGA/PBE functional associated with the D3 dispersion correction[34] using deMon2k,[35,36] unless otherwise mentioned. Gold atoms are described with a relativistic effective core potential (RECP), either with small core (SC), *i.e.* 60 core electrons, or with large core (LC), *i.e.* 68 core electrons, and their associated valence basis sets. The organic atoms are described with DZVP basis set. The deMon2k code, which is based on variational fitting of Coulomb potential, uses an auxiliary density to calculate the exchange-correlation contributions, resulting in significant acceleration in computation time. The criteria for SCF and auxiliary density convergences are set to 1.0×10^{-9} a.u and 1.0×10^{-7} a.u, respectively. The geometry optimizations of each of the complexes have been performed without constraints, with the convergence criterion for RMS gradient set to be 1.0×10^{-5} a.u. Since the LC-RECP optimized geometry of Au_{32} interacting with benzene is similar to the one obtained with SC-RECP, (Au–benzene distance differs by 0.06 Å), the LC-RECP has been used for the optimization of all the other complexes, with a significant reduction in the computational cost.

The interaction energy, E_{int}, was obtained for the optimized geometries *via*:

$$E_{\text{int}} = E_{\text{sys}} - E_{\text{GNP,sys}} - E_{\text{org,sys}} \qquad (1)$$

with E_{sys} the energy of the global system, $E_{\text{GNP,sys}}$ the electronic energy of Au_{32}, and $E_{\text{org,sys}}$ the electronic energy of the respective organic molecule at the geometry of the full system. The adsorption energies of the complexes, which take into account the deformation energy, are provided in ESI† and differ by 3 kcal mol^{-1} in average compared to the interaction energies (GNP contributes to 80% of the deformation energy). The charge transfer (CT) was obtained by subtracting the total charge of Au_{32} with and without the adsorbate using different population schemes. Vibrational frequencies have been computed analytically for each of the optimized complexes with the LC-RECP/DZVP basis sets to obtain the IR spectra, which have been plotted with a Lorentzian line shape and half-width value of 1 cm^{-1}.[37]

Due to convergence issues in deMon2k, the impact of the basis set superposition error (BSSE) has been estimated with the counterpoise method with Orca package.[38] The Au atom is described by the SC-RECP and its associated valence basis set, while the other atoms are described by def2-SVP or def2-TZVP basis set. The calculated BSSE values are reported in Table S2 and Fig. S2 in ESI.† The calculated BSSE using the TZ basis set is small and regular ($\sim$2.5 kcal mol^{-1}), so the interaction energies have not been corrected from here onwards. While the impact of the basis set for the adsorbate geometry and the interaction energy is small (DZVP *vs.* TZVP), the interaction energies computed with LC-RECP are significantly overestimated as compared to SC-RECP, as well as the results from Orca (see Table S2 and Fig. 2).

2.1.1 Condensed Fukui analysis of Au_{32}. Au_{32}, as shown in Fig. S1 (ESI†), is an icosahedral fullerene-like nanostructure, first computationally predicted to be stable by Johansson *et al.*[33] Since then, several works have been done with Au_{32} as the starting model to study the interaction between GNP with amino acids[20] and small molecules (CO, H_2, O_2).[39,40] To assess the reactivity of Au_{32}, the condensed Fukui function has been computed using an analytical approach, as implemented in deMon2k.[36] It allows to localize the electrophilic and nucleophilic sites at the surface, and the results are shown in Table S1 (ESI†).[41,42] Due to the high symmetry, this nanoparticle contains 20 six-coordinated and 12 five-coordinated gold atoms. The condensed Fukui value of all the five-coordinated gold atoms is greater than 0, which means that they are electrophilic sites and susceptible to interact with nucleophilic species. On the other hand, the six-coordinated gold atoms are mostly nucleophilic sites, susceptible to interact with electrophilic species. This assessment agrees with previous molecular electrostatic potential study by Wang *et al.*[43]

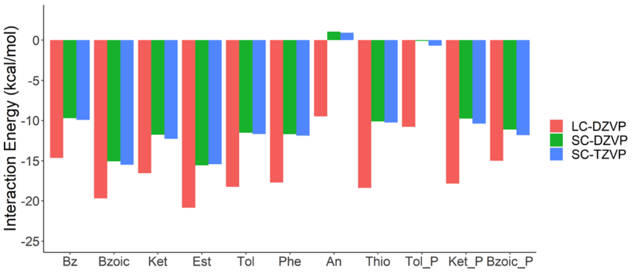

Fig. 2 Uncorrected interaction energy calculated with LC-RECP/DZVP, SC-RECP/DZVP, and SC-RECP/TZVP for the various organic compounds. "P" stands for perpendicular.

2.2 Topological analyses

All of the topological analyses have been carried out within Multiwfn code,[44] except for the quantification of non-covalent interaction (NCI) basins, which has been performed with NCIplot4.[45]

Quantum Theories of Atoms in Molecule (QTAIM). The QTAIM approach, developed by Bader and coworkers,[46,47] provides a robust way to study chemical bonding, based on partitioning of electron density in terms of the basins of attractors of the density gradient field. Within this framework, we can search for bond critical points and their associated bond paths, that are representative of the interaction. The characterization of this interaction is then made possible by calculating the local properties, such as electron density, Laplacian of the electron density, and energy density, according to the classification reported by Bianchi and coworkers.[48]

Non-covalent interaction analysis (NCI). With the NCI analysis, developed by Johnson *et al.*,[49] the intermolecular non-covalent interactions can be identified based on the reduced density gradient, while the strength of the interaction is characterized by the multiplication of the sign of the second eigenvalues of the Hessian matrix with the electron density. This analysis results in qualitative visualization of the interaction basins, color coded based on the strength of the interaction. Furthermore, with the recent implementation in NCIplot4,[45] the interaction basins can be further decomposed into different types of interactions, and they are then integrated to produce quantitative results.

2.3 Energy and charge decomposition analyses

The energy decomposition analysis (EDA) has been performed based on two different approaches, which are the Block-Localized

Wavefunction energy decomposition analysis (BLW-EDA), as implemented in CP2K,[50,51] and Symmetry Adapted Perturbation Theory (SAPT) at HF level with density fitting, as implemented in PSI4 and named SAPT0.[52–54] For the sake of simplicity, the SAPT0 results will be referred to as SAPT in the following text.

BLW-EDA is based on the absolutely localized molecular orbitals (ALMO) and defines molecules in terms of "blocks" of basis functions, inhibiting any exchange or sharing of electrons between blocks. The interaction energy calculated with BLW-EDA is defined in the eqn (2), and it can be decomposed into polarization (pol), charge transfer (CT), and frozen terms. The sum of frozen and polarization terms is called BLW. $E_{\mathrm{GNP,sys}}$ and $E_{\mathrm{org,sys}}$ correspond to the energy of the GNP and organic fragment in their final geometry adopted in the presence of the other fragment. E_{guess} is the systems energy obtained by a superposition of the fragment density matrices. E_{BSSE} corresponds to basis set superposition error estimated in the counterpoise procedure.

$$E_{\mathrm{int}} = E_{\mathrm{frozen}} + E_{\mathrm{pol}} + E_{\mathrm{CT}} = E_{\mathrm{BLW}} + E_{\mathrm{CT}}$$

$$E_{\mathrm{frozen}} = E_{\mathrm{guess}} - E_{\mathrm{GNP,sys}} - E_{\mathrm{org,sys}}$$

$$E_{\mathrm{pol}} = E_{\mathrm{BLW}} - E_{\mathrm{guess}}$$

$$E_{\mathrm{CT}} = E_{\mathrm{sys}} - E_{\mathrm{BLW}} - E_{\mathrm{BSSE}} \qquad (2)$$

Here, we define two blocks, one for the GNP and one for the aromatic adsorbate. Since the polarization of each block in the presence of the other is computed variationally, this method allows rigorous separation between polarization and charge transfer contributions.[50] The frozen term describes the interaction between isolated fragment densities, which encompasses electrostatic, repulsive, and dispersive contributions.[55] For this calculation, we applied PBE-D3 level of theory, using the MOLOPT-DZVP basis set for valence electrons and Goedecker, Teter, and Hutter (GTH) pseudopotentials. For Au atoms, the 11 valence electron potential is used. The electron smearing was approximated at 300 K by Fermi–Dirac distribution. Note that this setup closely follows a previous publication, where it has been shown to yield analogous results to plane-wave basis set computations using VASP.[56]

SAPT, on the other hand, treats the interaction energy as the perturbation introduced to the Hamiltonian of the isolated monomer, as it interacts in a dimer. The simplest SAPT method, is SAPT0, whose interaction energy can be defined as:

$$E_{\mathrm{int}}^{\mathrm{SAPT0}} = E_{\mathrm{elec}}^{(1)} + E_{\mathrm{exch}}^{(1)} + E_{\mathrm{ind}}^{(2)} + E_{\mathrm{disp}}^{(2)} \qquad (3)$$

This interaction can be decomposed into meaningful physical components, which are electrostatic (E_{elec}), exchange (E_{exch}), induction (E_{ind}) and dispersion (E_{disp}). In eqn (3), superscripts (1) and (2) indicate the first and second order terms, respectively. The electrostatic component contains both the interpenetration of the charge clouds and Coulombic interactions. The exchange interaction arises from the overlap of the monomer wave functions and the requirement of a fermionic antisymmetric wave function in the dimer. The induction includes both the polarization response and charge transfer. Dispersion results from the dynamical correlation of electrons between the two monomers. Being the simplest method, SAPT0 has the largest mean absolute error as compared to the other SAPT methods. But, considering the relatively low computational cost, this method has been applied. The SAPT analysis has been performed with density fitting, frozen core, and def2-TZVP basis set. Gold atom has been described with SC-RECP and its associated valence basis set.

Lastly, the charge decomposition analysis (CDA), as developed by Dapprich and Frenking and implemented in Multiwfn,[57] constructs the molecular orbital of complexes by linear combinations of the fragment orbitals. This approach allows the quantification of charge transfer between donor and acceptor (donation, back donation, and polarization term). Furthermore, it also gives insight into which molecular orbitals of the isolated fragments play significant role in the formation of the complex.

3 Results and discussion

3.1 Geometry and electronic structure analysis

3.1.1 Flat configuration. The optimized structures of the complexes adopting flat configurations at the DFT level are shown in Fig. 3 in the order of increasing interaction energy. In overall, there is an increase of the interaction energy with the addition of functional groups on benzene. An increase of the interaction energy in the dimer of substituted benzene has been previously observed and rationalized.[58,59] Thus, the observed increase for the complexes studied here could similarly be attributed to the additional direct dispersive and electrostatic

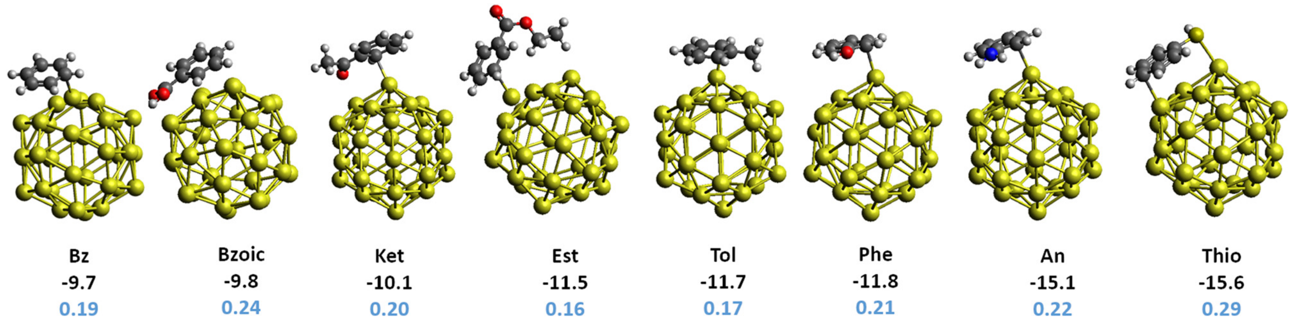

Fig. 3 Interaction of substituted aromatic compounds with Au_{32} adopting a flat configuration of the aromatic ring, along with the interaction energy (in kcal mol^{-1}, black color) and the charge transfer with ADCH scheme (in e^{-}, blue color).

interactions between the substituent groups and Au_{32}. A closer look at the orientation of the aromatic compounds on the surface of Au_{32} reveals quite different orientations depending on the substituent groups (see Fig. S3, ESI†). Benzene, phenol, toluene, and aniline are showed to adopt a slightly tilted orientation. Meanwhile, benzoic acid and thiophenol are revealed to adopt a more flat configuration, where the aromatic plane is almost parallel to the surface of Au_{32}. This could arise due to the stronger interaction between their respective functional groups (–COOH and –SH) with the gold surface atoms. Acetophenone, on the other hand, is tilted away from the surface of GNP, to favor the interaction between carbonyl group with the gold surface atoms. Ethyl benzoate is planar in gas phase but it rearranges itself in favor of interactions with the $–CH_2–CH_3$ group. This rearrangement results in the phenyl group to be tilted away from the surface of GNP. Moreover, other higher-energy conformations have been obtained and are provided in ESI† (see Fig. S4).

The CT has subsequently been obtained from the atomic dipole moment corrected Hirshfeld (ADCH) population scheme and is provided in Fig. 3. In general, there is a net electron transfer from the organic compound to the GNP, which demonstrated the electrophilicity of GNP. However, there seems to be a weak correlation between the interaction energy and CT (R^2 of 0.68, see Fig. S5, ESI†). In particular, the CT calculated for acetophenone and ethyl benzoate are smaller compared to the one for benzoic acid, despite their stronger interaction energy. We have additionally performed population analysis with different schemes for comparison (see Fig. S6 and S7 in ESI†). All schemes produce consistent result in regards to the electrophilicity of GNP, but the different schemes result in different amount of CT, in line with the non-uniqueness of the definition of atomic charges.[60] Reassuringly, regardless of the population schemes a weak correlation is found between the interaction energy and CT.

We have also performed charge decomposition analysis (CDA) to decompose the electron donation and back donation, as well as for the identification of the interacting molecular orbitals (see Table S4 and Fig. 4, Fig. S8–S15 in ESI†). Firstly, the molecular orbitals of the aromatic molecules are in general delocalized throughout the ring and the functional groups. They tend to overlap with the unoccupied molecular orbitals of GNP, leading to a favorable flat orientation (see Fig. S8, ESI†). Secondly, the analysis shows a small contribution of electron back donation the HOMO of GNP to the LUMO of the aromatic molecule. The synergy between donation and back donation eventually results in stronger interaction energy. However, the interpretation of the charge transfer becomes less straightforward.

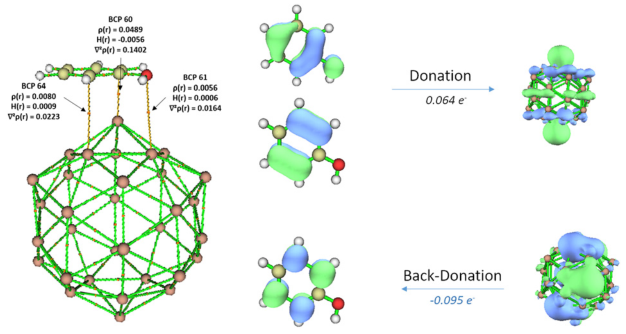

Fig. 4 BCPs calculated within the QTAIM framework, along with the values of local properties, for flat configuration of phenol (left). The interacting molecular orbitals of phenol and GNP, as obtained within CDA framework (right).

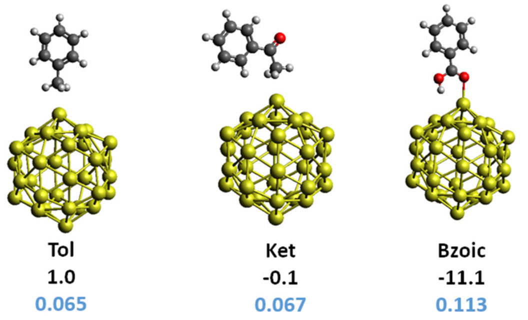

Fig. 5 Interaction of substituted aromatic compounds with Au_{32} adopting perpendicular configuration of the aromatic ring, along with the interaction energy (in kcal mol^{-1}, black color) and the charge transfer with ADCH scheme (in e^-, blue color).

3.1.2 Perpendicular configuration.

The optimized geometries of the complexes adopting perpendicular configuration are shown in Fig. 5. Most of the compounds relaxed back to the flat orientation during the optimization but some of them have a local minimum with perpendicular orientation. In this adsorption mode, the interactions are formed with the substituents, and not with the phenyl ring. The interaction mode through the phenyl ring, with hydrogen pointing towards the GNP surface, also relaxes back to the flat configuration. In the cases of toluene and acetophenone, the perpendicular mode results in a much weaker interaction compared to the flat counterpart. On the other hand, the interaction between GNP and the –COOH functional group is shown to be more favorable compared to the flat counterpart. This implies the stronger interaction between carboxylic functional groups in comparison to benzene. The amount of CT for this interaction mode is also shown in Fig. 5 and is smaller in quantity as compared to that of the flat counterpart, in line with our earlier observation that CT and interaction energy are not correlated.

The charge decomposition analysis shows that the molecular orbital of organic molecule participating in the complex formation is localized on the functional groups (see Fig. S9, S10, and S12 in ESI†). Although electron donation is dominating, back donation also participates to the stabilization of adsorption modes.

3.2 Vibrational analysis

Greenler, *et al.* previously proposed the surface selection rule of molecules adsorbed on small metal particles for IR spectra.[61] Furthermore, Schunke *et al.* investigated the influence of the adsorption orientation of halobenzene on copper surfaces *via* infrared spectroscopy experiments.[32] In this work, frequency calculations have been performed to simulate the vibrational IR spectra of the isolated molecules and the complexes, and to investigate how the interaction with GNP affects the IR spectra. This insight would be helpful to structural identification in experimental IR spectra.

Our general observation is that firstly, some IR inactive vibrational modes for the isolated molecule have become active. This can be seen clearly in the IR spectrum of benzene adsorbed on GNP in Fig. 6. Due to its high symmetry, only few vibrational modes are IR active in the free molecule. Upon interacting with GNP, several modes between 750 cm^{-1} and 1000 cm^{-1}, assigned to C–H aromatic bending modes, have become IR active due to symmetry breaking. Secondly, it is interesting to observe that the intensity of C–H aromatic stretching modes of benzene (at *ca.* 3100 cm^{-1}) have been significantly reduced, as compared to the isolated one (37 km mol^{-1} for isolated benzene *vs.* $<$5 km mol^{-1} for adsorbed benzene). Such observation has consistently been made for all the aromatic compounds adopting flat configurations. Thirdly, the functional groups that interact closely with GNP, or acting as the anchor, undergo quite significant frequency shifts, as can be seen in the case of most of the complexes under study. In the case of toluene, for example, the –CH$_3$ moiety interacts closely with GNP, for both flat and perpendicular configurations. As such, the frequency corresponding to the –CH$_3$ stretching (see Fig. 6) has been considerably red shifted, *i.e.* from 2981 cm^{-1} in isolated toluene to 2942 cm^{-1} in the flat complex and 2936 cm^{-1} in the perpendicular complex. In the case for thiophenol, where –SH interacts strongly with GNP, the frequency corresponding to the –SH stretching mode has red shifted as well, from 2634 cm^{-1} in isolated to 2627 cm^{-1} in the complex (see Fig. 6). Similar observations have been made for acetophenone and benzoic acid (see Fig. S19 and S20 in ESI†), where the C=O stretching mode has considerably shifted due to its relatively strong interaction with GNP, *i.e.* from 1694 cm^{-1} in isolation to 1640 cm^{-1} in flat complex and 1705 cm^{-1} in perpendicular complex in acetophenone, and from 1741 cm^{-1} in isolation to 1678 cm^{-1} in flat complex and to 1664 cm^{-1} in perpendicular complex in benzoic acid.

Moreover, a published FTIR experiment on thiophenol functionalized gold nanoparticles found CH stretching vibration modes (the strongest of which was at 3057 cm^{-1}) in reasonably well agreement with our unscaled calculated frequencies in the region of 3100–3200 cm^{-1}.[62] These peaks were not detectable in thiophenol solutions when the gold nanoparticles were absent, hence demonstrating that thiophenol interacts with gold nanoparticles.

3.3 Topological analysis

3.3.1 Quantum theory of atoms in molecule. Within the QTAIM framework, bond critical points (BCPs) and their associated bond paths have been identified for each of the optimized complexes. The local properties, *i.e.* the electron density, the Laplacian, and the energy density, calculated at the respective BCPs, are shown in Fig. 4, Fig. S16 and S17, and tabulated in Table S5 in ESI.†

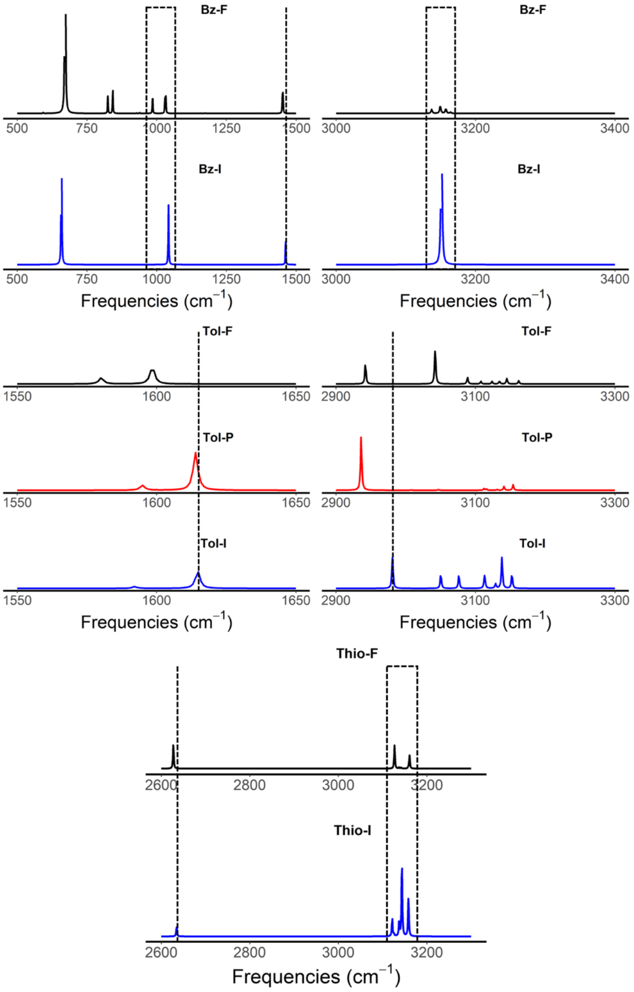

Fig. 6 IR computed spectra of benzene, toluene and thiophenol isolated (I in blue) and adsorbed on Au$_{32}$ (A). "F" (in black) and "P" (in red) stand for flat and perpendicular, respectively.

Flat configuration. When aromatic compounds adopt the flat configuration, multiple BCPs have been found. For benzene, two BCPs are found, one classified as dative and the other as dispersive interactions. The addition of functional groups subsequently results in an increased number of BCPs, associated to stronger interaction energies. This observation is in agreement with general observations of substituent effects on interaction energies and for adsorption energies on metal surfaces, and can be rationalized by the direct interaction between the functional groups and the GNP surface.[58,63] In the cases of toluene, phenol, and aniline, one BCP is found in between the –CH$_3$, –OH, and –NH$_2$, respectively, and the interaction is classified as dispersion. In the cases of benzoic acid and thiophenol, the –COOH and –SH functional groups both form strong dative interactions with GNP. Meanwhile, in the cases of both acetophenone and ethyl benzoate, as discussed earlier, the aromatic ring does not lie flat on the surface of GNP and only one BCP corresponding to the interaction between aromatic moiety and GNP has been found. The functional groups, on the other hand, form rather strong interaction with the surface, according to the local properties of the BCP. Furthermore, it can be deduced from this analysis that the carbonyl and thiol functional groups form stronger interaction with the surface, as compared to the hydroxyl and amine functional groups.

Perpendicular configuration. For the molecules adsorbed in a perpendicular configuration, only a few BCPs exist. In the cases of toluene and acetophenone, only one BCP has been found, between GNP and $-CH_3$ and $-COCH_3$, respectively. Based on the essentially zero interaction energy and basic chemical principles, they correspond to a very weak dispersion interaction between the adsorbate and the GNP. As for benzoic acid, two BCPs have been found for both C=O and O–H, with the interaction classified as dative with the one formed with C=O being stronger than O–H, an expected result based on the availability of oxygen electron lone-pairs to interact with the GNP.

3.3.2 Non-covalent interaction analysis. Since QTAIM analysis has indicated the non-covalent nature of the interactions, NCI analysis[49] is used to obtain a visualization and spatial understanding of these non-covalent interactions. Fig. 7 and 8 show the intermolecular NCI results of the optimized complexes, with the basins color-coded to represent the strength and the nature of the interaction (red representing repulsive interactions, green representing dispersion interactions, and blue representing dative interactions). By construction, the position of the basins found in NCI corresponds the calculated BCPs.

Flat configuration. For the complexes adopting a flat configuration, multiple delocalized interaction basins have been found. For benzene, there are two delocalized basins, with one stronger dative interaction and the other a dispersive interaction. Similarly, by adding substituents, these two delocalized basins are still generally present in the flat configuration. In addition to these two delocalized basins, there are additional interactions formed between the functional groups and the GNP. The –OH, $-NH_2$, $-CH_3$ in phenol, aniline and toluene form dispersive interaction with GNP. On the other hand, the –COOH and –SH functional groups in benzoic acid and thiolbenzene form a rather strong dative interaction. As for ethyl benzoate and acetophenone, ester and ketone functional groups form multiple non-covalent interactions that caused the phenyl ring to form only one interaction with the GNP.

Perpendicular configuration. For the perpendicular configuration, and similar to QTAIM analysis, lesser number of interaction basins have been found (see Fig. 8). The non-covalent basins are present for the CH_3 moiety for both toluene and acetophenone. For benzoic acid, two interaction basins are found between the carboxylic acid functional groups and the GNP, *i.e.* one for the C=O and one for –OH.

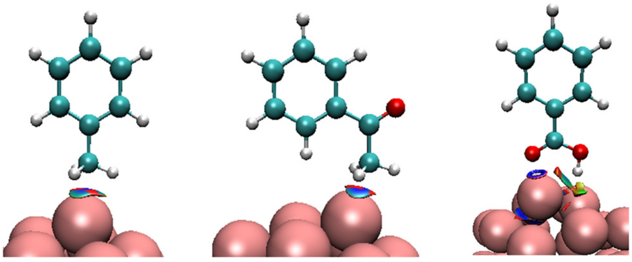

Fig. 8 NCI analysis of the aromatic molecules adsorbed on Au_{32} in a perpendicular configuration, see Fig. 7 for the color code: toluene, acetophenone, and benzoic acid.

Quantification of NCI basins. The NCI basins have been integrated for quantitative analysis and tabulated in Table S6 in (ESI†). Fig. 9 shows the integrated volumes based on the decomposition terms: dative interaction (in blue), dispersive interaction (in green), and repulsive interaction (in red) for each system. Based on this analysis, the total interaction is a subtle interplay between the three terms. Since Fig. 9 shows largest volume integral for the dispersive basins, the interaction between aromatic system and Au_{32} is driven by dispersive interactions. Additionally, the dative interaction is increasing for all of the substituted benzene, as compared to that of benzene. In some cases, it can be attributed to the additional blue basins formed by the functional groups (*i.e.* –C=O of benzoic acid, –C=O of acetophenone, $-CH_3$ of ethylbenzoate, and –SH of thiophenol) as seen in Fig. 7. In the cases of toluene, phenol, and aniline, however, the dative interaction is only observed for the interaction with the phenyl ring. This can then be related to the electron donating nature of these functional groups, that results in increased electron density of the phenyl ring, leading to an increase of dative interaction.

The integrated total volume of NCI basins (summation of the volumes of all constituting basins), which could represent the strength of the interaction energy, is found to be moderately correlated with the interaction energy calculated above (see Fig. S23, $R^2 = 0.60$). In particular, the total volumes of NCI basins for benzoic acid in flat and perpendicular configurations (102.70 and 24.78, respectively) clearly do not reflect the change in the interaction energy (−9.8 *vs.* −11.1 kcal mol^{-1}). This qualitative disagreement might be due to an inaccurate

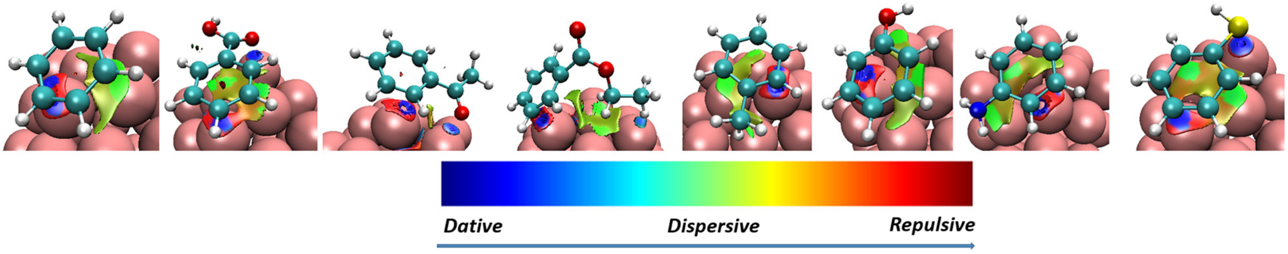

Fig. 7 NCI analysis of the aromatic molecules adsorbed on Au_{32} in a flat configuration, and the associated color code: from left to right, benzene, benzoic acid, acetophenone, ethylbenzoate, toluene, phenol, aniline, and thiophenol.

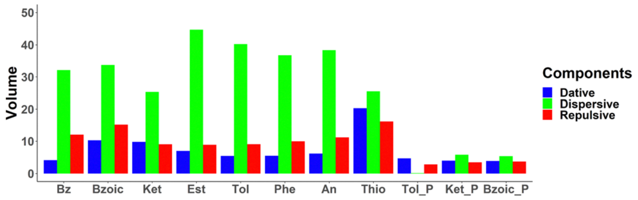

Fig. 9 Integrated volumes of the NCI basins for the aromatic molecules for flat and perpendicular geometries adsorbed on Au_{32}.

description of the electrostatic interactions by the NCI basins. Interestingly, a strong correlation is, however, found between the volumes of the NCI basins and the CT (obtained with the ADCH scheme, see Fig. S23 in ESI,† $R^2 = 0.91$). This can be rationalized by the general observation of the distance dependence of charge transfer: the more contact there is between the two fragments at the equilibrium distance, the higher the charge transfer is expected to be, with the volumes of the NCI basins being a convenient measure for the contact volume. This is further corroborated by the correlation between the repulsive NCI basin volumes with the total NCI basin volumes ($R^2 > 0.9$, see Fig. S24), even though it is the smallest component (the volume corresponding to dispersion interactions are about twice as large).

3.4 Energy decomposition analysis (EDA)

To further understand the underlying contributing factors to the interaction from an energetic point of view, EDA has also been performed using two different approaches, *i.e.* BLW-EDA and SAPT. The total energies from BLW-EDA and SAPT correlate well with the interaction energy obtained previously (R^2 = 0.96 and 0.81, see Fig. 10).

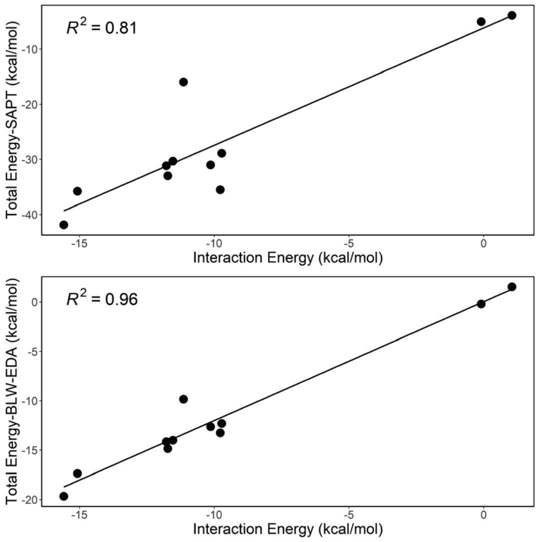

Fig. 10 The correlation between the total interaction energy obtained with SAPT (top), BLW-EDA (bottom) with the interaction energy obtained with molecular approach.

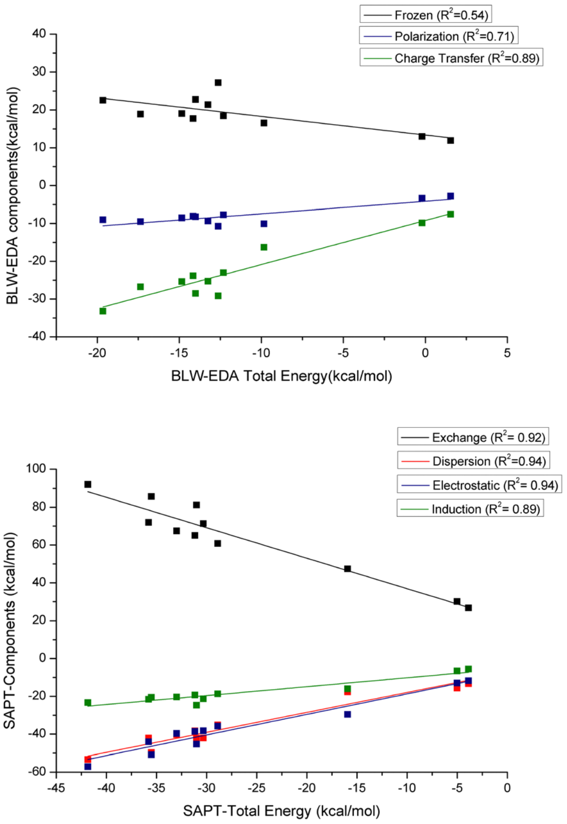

Fig. 11 The correlation of the respective energy decomposition terms with respect to the total energy for the various complexes: (top) BLW-EDA, and (bottom) SAPT.

BLW-EDA. Fig. 11 shows the contributing energy terms calculated with the BLW-EDA approach, *i.e.* frozen, polarization, and charge transfer, for each system. The frozen term is positive highlighting the dominant role of the Pauli repulsion contribution compared to electrostatic and dispersion contributions. This term is nearly constant across the series and, therefore, uncorrelated to the total interaction energy (see Fig. 11, R^2 = 0.54). This repulsive energy is only partially compensated by the favorable polarization and it is the charge transfer term that provides the actual stabilization. The functional groups generally increase the weight of polarization in the interaction, with –CO functional groups leading to the highest polarization as shown in the case of acetophenone and benzoic acid in a perpendicular configuration (see Fig. S26, ESI†). Similarly, the functional groups also affect the charge transfer energy, taking benzene as the reference. Except for –SH functional group, the effect is similar to that observed for polarization energy. Sulfur has a high tendency to form bonds with Au,[64] which rationalizes that the charge transfer contribution of the interaction between thiophenol and GNP is found to be the strongest.

According to Fig. 11 and Fig. S28 (ESI†), and in contrast to our observations for water add-layers,[56] the polarization energy is neither sufficiently strong to off-set the Pauli repulsion, nor to induce a significant correlation between FRZ + POL (called BLW interaction energy) and the total interaction energy (R^2 = 0.14). For the GNP-aromatics interaction, it is the correlation between the charge transfer energy and the BLW-EDA energy that is found to be strong (R^2 = 0.89, see Fig. 11). This demonstrates the relative importance of charge transfer energy term as compared to polarization term for these systems. This is reminiscent of the correlation between the interaction energy and the ADCH analysis and indeed the two completely independent measures for CT are well correlated (R^2 = 0.80, see Fig. S27). In contrast, the correlation between CT and the dative NCI basins, which should describe a similar physics, is weak (R^2 = 0.41, see Fig. S29).

SAPT. Fig. 11 shows the energy terms calculated with SAPT approach, *i.e.* exchange energy, electrostatic energy, dispersion energy, and induction energy. As compared to DFT, the interaction energy obtained with SAPT is significantly (factor 2.85) more stabilizing. Our hypothesis is that the perturbative treatment of the dispersion energy is to blame for this overestimation: for metallic systems (small band-gap) low-order perturbation theory can be expected to lead to overestimations. The exchange energy represents the repulsion contribution, which is necessarily positive. According to SAPT both electrostatic and dispersion energies give a significant contribution to the total interaction energy, while induction energy is smaller in magnitude. As could have been expected, the sum of electrostatic and exchange energies from SAPT is well correlated with the frozen term of BLW-EDA (R^2 = 0.87, see Fig. S29, ESI†), even though the later also includes the dispersion-correction components of the DFT interaction energy. Given that all SAPT components correlate well (R^2 > 0.8) with the total interaction energy, it is difficult to distinguish which physical effects lead to increased interaction energy. Based on the above analysis (ADCH, BLW), one could have expected induction to be dominating, but according to the slopes with respect to the total interaction energy, dispersion is found to be much more significant. However, this has to be taken with caution, as the total interaction energy obtained with SAPT is significantly overestimated compared to the DFT results. This later originates probably in the perturbative treatment of dispersion. Note that in contrast to dispersion, the induction energy contains an ''infinite order'' correction terms, δ_{HF}, which leads to a near perfect (R^2 = 0.98) correlation with the sum of polarization and charge-transfer interactions as obtained by BLW-EDA. According to Fig. S29 in ESI,† the correlation between the repulsion energy from SAPT and the corresponding NCI basins is strong (R^2 = 0.80), while the agreement for the dispersive interaction energies is significantly lower (R^2 = 0.66). This highlights the difficulty to capture dispersion interactions solely based on the (reduced) density (gradient).

4 Conclusion

We have systematically and quantitatively investigated the chemical interaction between substituted aromatic compounds and Au_{32} as a model of gold nanoparticles. These interactions mainly consist of multiple non-covalent interactions, with dative, dispersive, and repulsive nature. In general, the substituted aromatic compounds prefer to adopt a relatively flat configuration, where the aromatic ring lies almost parallel to the surface of Au_{32}, except for benzoic acid, where the interaction with the –COOH group is stronger than the interaction with the phenyl ring, resulting in a favorable perpendicular orientation. These flat and perpendicular orientations can be distinguished using vibrational spectroscopy, where the CH aromatic stretching modes are less IR active for the flat configuration. The interactions have further been quantitatively decomposed using NCI, BLW-EDA and SAPT analyses. Though these three methods adopt different approaches in the energy decomposition, we found strong agreement among them, and the results of this analysis could help in designing accurate force fields for gold nanoparticles based materials. In particular, our analysis has evidenced the importance of charge transfer, both in terms of interaction energy and in terms of transferred electrons, which impacts the medium-range electrostatic interactions with the environment (*e.g.*, solvent).

Conflicts of interest

There are no conflicts to declare.

Acknowledgements

We thank Dr Dominik Domin for his valuable technical assistance. This collaborative work was supported by GDR 2035 SolvATE, funded by CNRS. This work was performed using HPC resources from the GENCI (CINES/IDRIS, Grant no. 2021-A0100806830).

Notes and references

1 G. Li and R. Jin, *Nanotechnol. Rev.*, 2013, **2**, 529–545.
2 G. Han, P. Ghosh and V. M. Rotello, *Nanomedicine*, 2007, **2**, 113–123.
3 S. Her, D. A. Jaffray and C. Allen, *Adv. Drug Delivery Rev.*, 2017, **109**, 84–101.
4 A. Corma and H. Garcia, *Chem. Soc. Rev.*, 2008, **37**, 2096–2126.
5 X. Hu, Y. Zhang, T. Ding, J. Liu and H. Zhao, *Front. Bioeng. Biotechnol.*, 2020, **8**, 1–17.
6 L. Pasquato, P. Pengo and P. Scrimin, *J. Mater. Chem.*, 2004, **14**, 3481–3487.
7 M. Iosin, F. Toderas, P. L. Baldeck and S. Astilean, *J. Mol. Struct.*, 2009, **924-926**, 196–200.
8 J. Gao, Y. Hu, S. Li, Y. Zhang and X. Chen, *Spectrochim. Acta, Part A*, 2013, **104**, 41–47.
9 S. Hussain and Y. Pang, *J. Mol. Struct.*, 2015, **1096**, 121–128.
10 G. P. Szekeres and J. Kneipp, *Analyst*, 2018, **143**, 6061–6068.
11 G. P. Szekeres and J. Kneipp, *Front. Chem.*, 2019, **7**, 30.
12 F. Madzharova, Z. Heiner and J. Kneipp, *J. Phys. Chem. C*, 2020, **124**, 6233–6241.
13 F. Madzharova, Z. Heiner and J. Kneipp, *J. Phys. Chem. C*, 2017, **121**, 1235–1242.
14 M. Moskovits, *J. Chem. Phys.*, 1982, **77**, 4408–4416.
15 I. Lynch and K. A. Dawson, *Nano Today*, 2008, **3**, 40–47.
16 X. Toledo-Fuentes, D. Lis and F. Cecchet, *J. Phys. Chem. C*, 2016, **120**, 21399–21409.

17 A. M. Engstrom, R. A. Faase, G. W. Marquart, J. E. Baio, M. R. Mackiewicz and S. L. Harper, *Int. J. Nanomed.*, 2020, **15**, 4091–4104.

18 X. Cheng, F. Li and C. Wang, *Comput. Theor. Chem.*, 2016, **1097**, 1–7.

19 G.-J. Kang, Z.-X. Chen and Z. Li, *J. Chem. Phys.*, 2009, **131**, 034710.

20 M. Darvish Ganji, H. Tavassoli Larijani, R. Alamol-hoda and M. Mehdizadeh, *Sci. Rep.*, 2018, **8**, 11400.

21 H. R. Abd El-Mageed and M. Taha, *J. Mol. Liq.*, 2019, **296**, 111903.

22 Q. Shao and C. K. Hall, *Langmuir*, 2016, **32**, 7888–7896.

23 G. Yao and Q. Huang, *J. Phys. Chem. C*, 2018, **122**, 15241–15251.

24 A. Fihey, C. Hettich, J. Touzeau, F. Maurel, A. Perrier, C. Köhler, B. Aradi and T. Frauenheim, *J. Comput. Chem.*, 2015, **36**, 2075–2087.

25 A. Domnguez-Castro, D. Hernández and F. Guzmán, *Theor. Chem. Acc.*, 2017, **136**, 84.

26 G. Fazio, G. Seifert, M. Rapacioli, N. Tarrat and J.-O. Joswig, *Z. Phys. Chem.*, 2018, **232**, 1583–1592.

27 O. A. Perfilieva, D. V. Pyshnyi and A. A. Lomzov, *J. Chem. Theory Comput.*, 2019, **15**, 1278–1292.

28 H. Heinz, K. C. Jha, J. Luettmer-Strathmann, B. L. Farmer and R. R. Naik, *J. R. Soc., Interface*, 2011, **8**, 220–232.

29 M. S. Jahan Sajib, P. Sarker, Y. Wei, X. Tao and T. Wei, *Langmuir*, 2020, **36**, 13356–13363.

30 F. Tavanti and M. C. Menziani, *Int. J. Mol. Sci.*, 2021, **22**, 8722.

31 R. Tandiana, N.-T. Van-Oanh and C. Clavaguéra, *Theor. Chem. Acc.*, 2021, **140**, 118.

32 C. Schunke, D. P. Miller, E. Zurek and K. Morgenstern, *Phys. Chem. Chem. Phys.*, 2022, **24**, 4485–4492.

33 M. P. Johansson, D. Sundholm and J. Vaara, *Angew. Chem., Int. Ed.*, 2004, **116**, 2732–2735.

34 S. Grimme, J. Antony, S. Ehrlich and H. Krieg, *J. Chem. Phys.*, 2010, **132**, 154104.

35 G. Geudtner, P. Calaminici, J. Carmona-Espndola, J. M. d Campo, V. D. Domnguez-Soria, R. F. Moreno, G. U. Gamboa, A. Goursot, A. M. Köster, J. U. Reveles, T. Mineva, J. M. Vásquez-Pérez, A. Vela, B. Zúñinga-Gutierrez and D. R. Salahub, *Wiley Interdiscip. Rev.: Comput. Mol. Sci.*, 2012, **2**, 548–555.

36 R. Flores-Moreno, J. Melin, J. V. Ortiz and G. Merino, *J. Chem. Phys.*, 2008, **129**, 224105.

37 R. I. Delgado-Venegas, D. Meja-Rodrguez, R. Flores-Moreno, P. Calaminici and A. M. Köster, *J. Chem. Phys.*, 2016, **145**, 224103.

38 F. Neese, F. Wennmohs, U. Becker and C. Riplinger, *J. Chem. Phys.*, 2020, **152**, 224108.

39 Y. Wang and X. G. Gong, *J. Chem. Phys.*, 2006, **125**, 124703.

40 L. Fang, T. Chen, Y. Meng, Y. Wang, J. Xue, Z. Ni and S. Xia, *Mol. Catal.*, 2020, **483**, 110757.

41 C. Morell, A. Grand and A. Toro-Labbé, *Chem. Phys. Lett.*, 2006, **425**, 342–346.

42 T. C. Allison and Y. J. Tong, *Phys. Chem. Chem. Phys.*, 2011, **13**, 12858–12864.

43 D.-L. Wang, X.-P. Sun, H.-T. Shen, D.-Y. Hou and Y.-C. Zhai, *Chem. Phys. Lett.*, 2008, **457**, 366–370.

44 T. Lu and F. Chen, *J. Comput. Chem.*, 2012, **33**, 580–592.

45 R. A. Boto, F. Peccati, R. Laplaza, C. Quan, A. Carbone, J.-P. Piquemal, Y. Maday and J. Contreras-Garcia, *J. Chem. Theory Comput.*, 2020, **16**, 4150–4158.

46 R. F. W. Bader, P. J. MacDougall and C. D. H. Lau, *J. Am. Chem. Soc.*, 1984, **106**, 1594–1605.

47 R. F. W. Bader, *J. Phys. Chem. A*, 1998, **102**, 7314–7323.

48 R. Bianchi, G. Gervasio and D. Marabello, *Inorg. Chem.*, 2000, **39**, 2360–2366.

49 E. R. Johnson, S. Keinan, P. Mori-Sánchez, J. Contreras-Garcia, A. J. Cohen and W. Yang, *J. Am. Chem. Soc.*, 2010, **132**, 6498–6506.

50 R. Staub, M. Iannuzzi, R. Z. Khaliullin and S. N. Steinmann, *J. Chem. Theory Comput.*, 2019, **15**, 265–275.

51 T. D. Kühne, M. Iannuzzi, M. Del Ben, V. V. Rybkin, P. Seewald, F. Stein, T. Laino, R. Z. Khaliullin, O. Schütt, F. Schiffmann, D. Golze, J. Wilhelm, S. Chulkov, M. H. Bani-Hashemian, V. Weber, U. Borštnik, M. Taillefumier, A. S. Jakobovits, A. Lazzaro, H. Pabst, T. Müller, R. Schade, M. Guidon, S. Andermatt, N. Holmberg, G. K. Schenter, A. Hehn, A. Bussy, F. Belleflamme, G. Tabacchi, A. Glöß, M. Lass, I. Bethune, C. J. Mundy, C. Plessl, M. Watkins, J. VandeVondele, M. Krack and J. Hutter, *J. Chem. Phys.*, 2020, **152**, 194103.

52 D. G. A. Smith, L. A. Burns, A. C. Simmonett, R. M. Parrish, M. C. Schieber, R. Galvelis, P. Kraus, H. Kruse, R. Di Remigio, A. Alenaizan, A. M. James, S. Lehtola, J. P. Misiewicz, M. Scheurer, R. A. Shaw, J. B. Schriber, Y. Xie, Z. L. Glick, D. A. Sirianni, J. S. O'Brien, J. M. Waldrop, A. Kumar, E. G. Hohenstein, B. P. Pritchard, B. R. Brooks, H. F. Schaefer, A. Y. Sokolov, K. Patkowski, A. E. DePrince, U. Bozkaya, R. A. King, F. A. Evangelista, J. M. Turney, T. D. Crawford and C. D. Sherrill, *J. Chem. Phys.*, 2020, **152**, 184108.

53 B. Jeziorski, R. Moszynski and K. Szalewicz, *Chem. Rev.*, 1994, **94**, 1887–1930.

54 E. G. Hohenstein and C. D. Sherrill, *J. Chem. Phys.*, 2010, **132**, 184111.

55 S. N. Steinmann, C. Corminboeuf, W. Wu and Y. Mo, *J. Phys. Chem. A*, 2011, **115**, 5467–5477.

56 P. Clabaut, R. Staub, J. Galiana, E. Antonetti and S. N. Steinmann, *J. Chem. Phys.*, 2020, **153**, 054703.

57 S. Dapprich and G. Frenking, *J. Phys. Chem.*, 1995, **99**, 9352–9362.

58 S. E. Wheeler and K. N. Houk, *J. Am. Chem. Soc.*, 2008, **130**, 10854–10855.

59 M. O. Sinnokrot and C. D. Sherrill, *J. Am. Chem. Soc.*, 2004, **126**, 7690–7697.

60 J. F. Gonthier, S. N. Steinmann, M. D. Wodrich and C. Corminboeuf, *Chem. Soc. Rev.*, 2012, **41**, 4671–4687.

61 R. G. Greenler, D. R. Snider, D. Witt and R. S. Sorbello, *Surf. Sci.*, 1982, **118**, 415–428.

62 C. Humbert, O. Pluchery, E. Lacaze, A. Tadjeddine and B. Busson, *Gold Bull.*, 2013, **46**, 299–309.

63 R. Réocreux, M. Huynh, C. Michel and P. Sautet, *J. Phys. Chem. Lett.*, 2016, **7**, 2074–2079.

64 H. Hakkinen, *Nat. Chem.*, 2012, **4**, 443–455.

3.4.1 Conclusion and Perspectives

Our work has shown that the substituted aromatic compounds still prefer the flat configuration, except for benzoic acid, that forms stronger interaction through the -COOH. Moreover, it is indeed true that large flexible molecules tend to re-orient themselves to maximize the interaction with the surface, as demonstrated by ethyl benzoate. In isolation, the ester functional group lies at the same plane as the aromatic plane, but, the interaction with Au_{32} leads to the rotation of the ester group to allow interaction between the -CH_2CH_3 and GNP. However, an extensive sampling would be necessary to further locate the global minimum of the system.

The quantitative analysis of the interaction has been investigated systematically in this work. The SAPT and BLW-EDA schemes have been demonstrated to agree with each other, while the NCI analysis has been shown to capture the repulsive interactions very well, but not as much for the other interactions. This could be caused by the rather crude classification of the type of the interactions, while it is good for organic molecules, it may not reflect the GNP-organic interactions well.

The general observations derived from the analysis of the calculated IR spectra of the complexes are, firstly, due to symmetry breaking, some IR-inactive modes of the molecules have become IR-active modes upon adsorption on GNP. Secondly, the interaction with GNP has induced both shifts in the frequency and also changes in the intensity of the vibrational mode. Particularly interesting observation is the significantly reduced intensity of peaks associated to the C-H aromatic stretching modes for the flat configuration, as compared to the perpendicular configuration, due to the selection rule for IR spectra on metal surfaces.[70] Therefore, the objective of the next section would be to validate this observation, by qualitative comparison with the experimental IR spectra.

3.5 Vibrational Analysis of Small Organic Molecules Interacting At the Surface of Gold Nanoparticles

Our analysis in the previous section has demonstrated that IR spectra could reveal important information regarding the adsorption geometry of ligands at the surface of GNP. Indeed, Schunke *et al.* has reported a study on the investigation of the orientation of halogenated benzene by exploiting the surface selection rule in reflection-absorption IR spectroscopy.[71] However, before directly comparing with the experimental spectra, there are several considerations that we have to take. Firstly, experimentally synthesized GNP typically are much larger than the ones considered here, *i.e.* between 5 to 30 nm in diameter. Secondly, experimental IR spectrum is an average of all the different possible orientations adopted by the molecules and interaction sites on the GNP. Thirdly, the protonation state of the molecules has to be considered, as sample preparation is usually done in a solution. Lastly, the effect of environment is crucial in the conformations and orientations adopted by the surface ligands, either in a vacuum or dried sample or in solution. Previously reported articles have suggested that gold cluster models are sufficient to represent the metal surfaces.[7,58] However, in this section, our objective is to bridge the theoretical models and the experimental observation, by systematically investigating the size and interaction effects of intermediate sized GNP on the calculated IR spectra.

The analysis will begin with the investigation of the nature of the interaction between GNP and a series of small representative organic molecules. Then, the effect of size and the interaction sites on the interaction will be discussed. Subsequently, the calculated vibrational spectra will be analyzed. For the purpose of qualitative comparison with the experimentally obtained spectra, benzoic acid has been chosen as the model compound, because of the availability of reference data, and also because it is the relatively easier compound to work with experimentally.

3.5.1 Systems of Interest

The GNP considered in this study are Au_{32} and Au_{55}, with their respective diameter of 0.9 nm and 1.1 nm. Meanwhile, the organic molecules studied are methane, methanol, formic acid, hydrogen sulfide, and ammonia, and at the subsequent section, the interaction with benzoic acid is investigated as the model system for qualitative comparison with experimental data. The typical simulation setup will follow the scheme shown in Figure 3.1.

The reactivity descriptors have been firstly calculated, which are electrostatic potential (ESP) and Fukui function, to identify the reactive sites of the two GNP. These two properties have been calculated with deMon2k code, with gold atoms described with large relativistic effective core potential (RECP), and its associated valence basis set (11 e$^-$).[36] The results are plotted as isosurface, and shown in Figure 3.3. The blue isosurface in ESP represents the electrophilic sites, while the red isosurface represents the nucleophilic sites. Electrophilic and nucleophilic sites are alternating for Au$_{32}$, while the surface of Au$_{55}$ is fully electrophilic.

Likewise for the Δf function, the blue isosurfaces represent the electrophilic sites, while the red isosurfaces represent the nucleophilic sites. The blue isosurfaces on Au$_{32}$ vary in size depending on the coordination number of the respective atom. The gold atoms connected to 5 neighbors are all electrophilic, while most of the atoms connected to 6 neighbors are nucleophilic. In the case of Au$_{55}$, 13 of the atoms make up the core of the GNP, and 32 atoms are located at the surface and exposed for interactions with the surroundings (see Figure 3.3). According to isosurface of Δf functions, the nucleophilic interacting sites are buried within the GNP, and the surface is covered with electrophilic isosurfaces, agreeing with the ESP calculation. However, according to the values of Δ Fukui functions, the majority of the surface and core atoms of GNP are electrophilic in nature, to a varying degree. Still, there are atoms exhibiting nucleophilic nature scattered around the surface atoms as well.

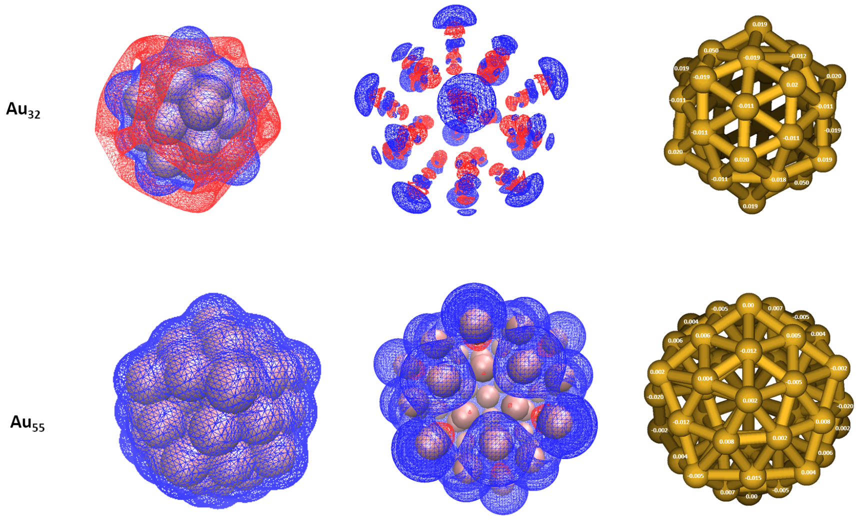

Figure 3.3: The reactivity descriptors: ESP (left) and Δf (middle and right) of Au$_{32}$ (top) and Au$_{55}$ (bottom)

Subsequently, geometry optimization has been performed on the series of organic molecule interacting on Au$_{32}$, and interacting on Au$_{55}$ at the corner sites and at the edge sites (see figure 3.4). The optimization has been done without any constraint on any of the atoms, and large RECP (LC-RECP) and its associated valence basis set (11 e$^-$) has been used to describe gold atoms, while DZVP have been used to describe the rest of the atoms. Once the optimized geometry has been obtained, the calculation of interaction energy has been performed with the small RECP (SC-RECP) and its associated valence basis set (19 e^-) to describe gold atoms,[35] and the same for the rest of the atoms. In the previous section, the BSSE is shown to be minimal when the interaction energy is calculated with SC-RECP describing gold atoms, and DZVP describing the organic molecules. Therefore, the interaction energies reported here are not going to be corrected.

We have subsequently performed topological analysis with Multiwfn[9] on each of the optimized complexes, *i.e.* QTAIM and NCI analysis, to obtain insight on the nature of the interactions, and followed by energy decomposition approaches to further understand the main contributing factor to the interaction energy. There are two schemes of energy decomposition approaches that have been carried out, which are SAPT, performed in psi4,[11], and BLW-EDA, performed in CP2K.[12] The IR spectra of the complexes have also been computed for the optimized geometries in the harmonic approximation.[40] Currently, the scaling factor is not yet added because the comparison is done among the calculated spectra, where the same basis sets and functionals are used.

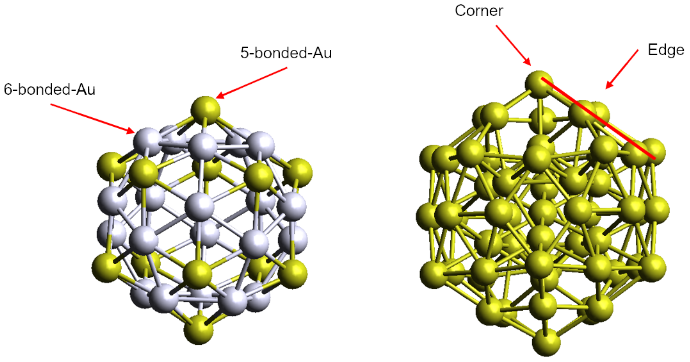

Figure 3.4: The possible interaction sites of Au_{32} (left) with the silver balls representing the six-bonded Au atoms, and the yellow balls representing the five-bonded Au atoms, and Au_{55} (right)

3.5.2 Structural and Electronic Properties of the Complexes

The optimized geometries for organic molecules adsorbed on Au_{32} are shown in Figure 3.5 in the order of increasing interaction energy. Methane forms the weakest interaction energy, which is followed by formic acid, where the -COOH functional group is interacting with the surface of Au_{32}. Methanol forms interaction through the oxygen atom of -OH functional group. The hydrogen sulfide interacts through the S atom, with the molecular plane lying flat on the surface. Ammonia forms the strongest interaction with all the hydrogen pointing away from the surface of

GNP, as the lone pair interacts with the GNP. Consistent with the previous section, the directionality of the HOMO and LUMO of both the GNP and organic molecules also plays a role in this set of complexes. Similarly, GNP has acted as an electron acceptor, while the organic molecule has acted as an electron donor. Additionally, the organic molecules are indeed interacting with the atoms having 5 neighbors, instead of the ones having 6 neighbors, which highlighted the relatively higher reactivity of the 5-neighbors atoms as compared to the 6-neighbors atoms.

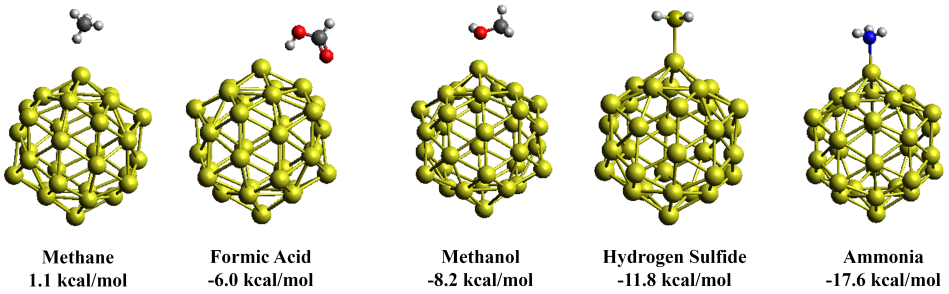

Figure 3.5: The optimized geometries of organic molecules interacting with Au_{32} along with the interaction energies

The optimized geometries of those adsorbed on the corner and edge sites of Au_{55} are shown in Figure 3.6 in the order of increasing interaction energy. In general, they adopt the same orientation as when they interact with Au_{32}, and the observed trend in the interaction energy is the same, except for formic acids and methanol. Formic acid forms stronger interaction than methanol on the surface of Au_{55}. In the cases for the complexes interacting at the edge sites, the trend in the interaction energy, and the orientation of the molecules are the same as those interacting at the corner sites. The only difference is that the interaction at the corner sites of Au_{55} is stronger than that at the edge sites, highlighting that the edge atoms have a lower reactivity than the corner atoms. Allison *et al.* have similarly identified the higher reactivity for atoms at the vertex and edge.[41] However, comparing the reactivity between different sizes of GNP, based on condensed Fukui function, cannot be done, due to the normalization of the function. In any case, there does not seem to be a significant difference in terms of interaction energies, when either Au_{32} or Au_{55} is interacting with the organic molecules. More significant and consistent differences are shown rather when the interaction occurs at the vertex or at the edge sites.

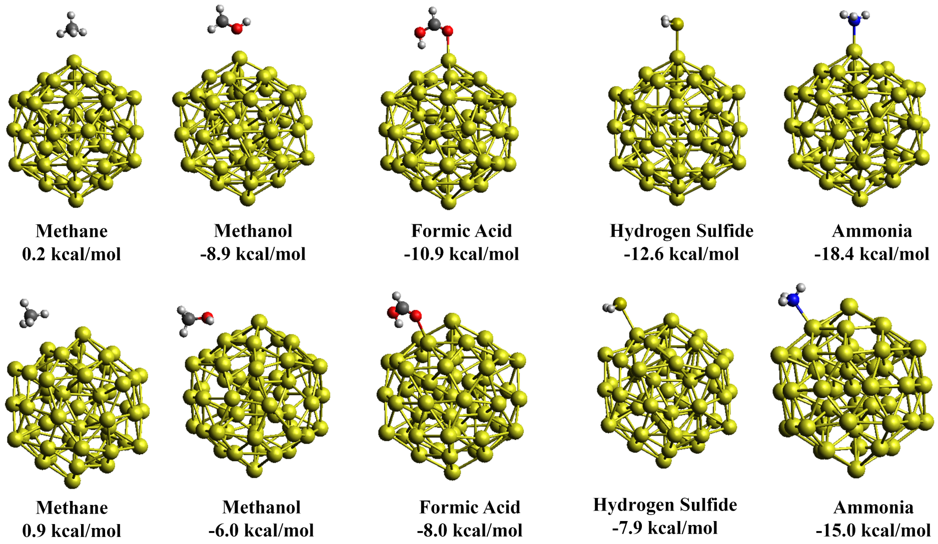

Figure 3.6: The optimized geometries of complexes of Au_{55} at corner positions (top) and at edge positions (bottom), along with their respective interaction energies

3.5.3 Decomposition of Intermolecular Interaction Analysis

The decomposition of intermolecular interaction analysis is then performed to further investigate the nature of the interaction. Both SAPT and BLW-EDA have been carried out for Au_{32}. Due to the associated computational cost of SAPT, only BLW-EDA has been carried out for Au_{55}. These energies are plot in Figure 3.7 for Au_{32} complexes and Figure 3.8 for Au_{55} complexes. The tabulated values of these energies are shown in the Appendix.

SAPT, which defines the interaction energy as the summation of electrostatic, exchange, dispersion, and induction energies, provides interesting energetic insight into the interaction. For Au_{32} complexes, (see Figure 3.7 (bottom)), the electrostatic contribution increases from methane, formic acid, methanol, hydrogen sulfide, and ammonia. The exchange term, which is the repulsive term, is smallest for methane, as the interaction occurs with the hydrogen atom. As the molecule gets bulkier, the repulsive contribution increases as well. As for the dispersion term, the variation across the organic series is not as large, *i.e.* only difference of 4 kcal/mol, with methane having the smallest dispersive contribution, and formic acid and hydrogen sulfide having the largest contribution. Lastly, the induction term, in general, follows the trend as in the electrostatic contribution, except for formic acid and methanol, where formic acid is found to be more polarizing as compared to methanol. All in all, according to SAPT, the interaction is dominated by the electrostatic contribution, whose magnitudes are larger than both the dispersion and induction contributions. Additionally, the ratio between electrostatic and dispersion increases as the interaction energy increases, *i.e.* 1.07, 1.18, 1.99, 1.77, and 2.71. Furthermore, the correlation between each of the energy term with the total SAPT energy yields R^2 of 0.96, 0.67, 0.09, and 0.76, respectively. Therefore, the electrostatic could be an excellent descriptor for the interaction between Au_{32} and these molecules. Yet, before generalizing to the other GNP, more calculations would need to be done.

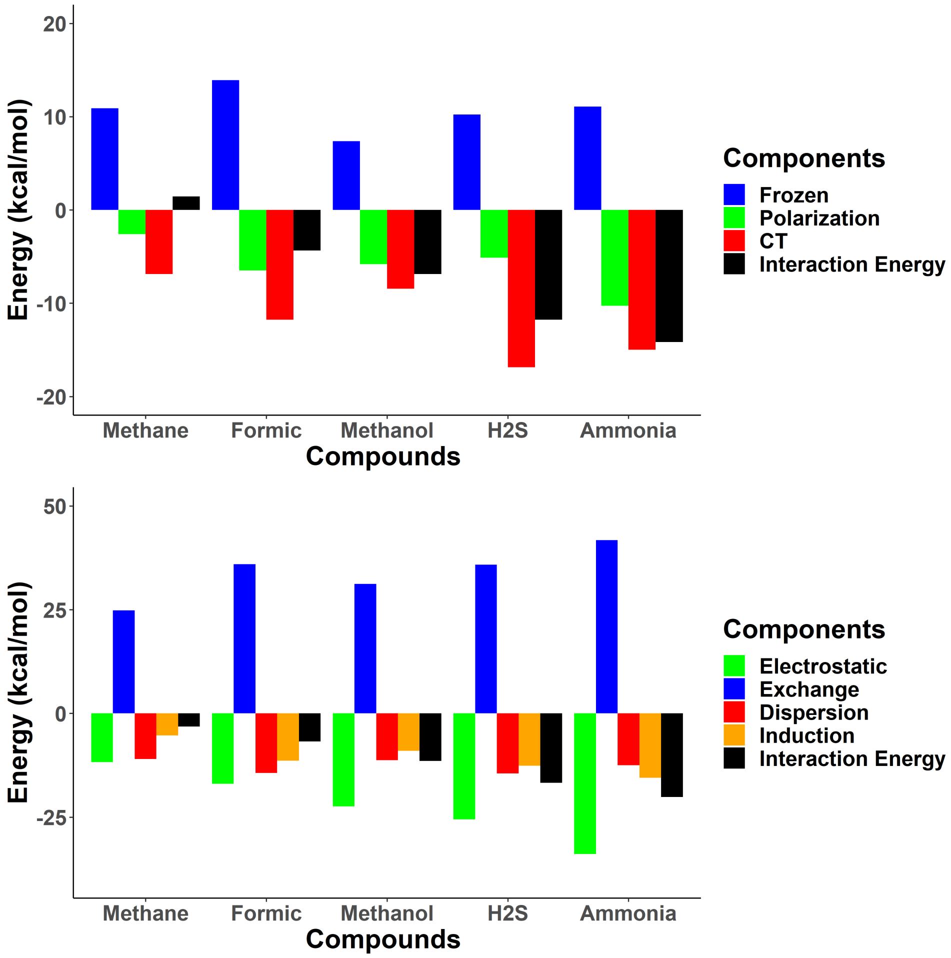

Figure 3.7: The decomposition of intermolecular interaction analysis performed for Au_{32} complexes based on (top) BLW-EDA approach and (bottom) SAPT approach

The BLW-EDA is subsequently performed on Au_{32} complexes (see Figure 3.7 (top)), which decomposes the interaction into frozen (inclusive of dispersion, electrostatic, and repulsion terms), polarization and charge transfer energies. The frozen terms for all of the complexes are consistently positive, which implies that the repulsion terms are more dominant than the dispersion and electrostatic contributions. As such, the stabilizing energy contributions are coming from both the polarization and charge transfer contributions. The polarization contribution increases from methane, hydrogen sulfide, methanol, formic acid, and ammonia. This indicates the difference in polarizing effect of each molecule. However, the trend observed in charge transfer contribution is different, and it increases from methane, methanol, formic acid, ammonia, and hydrogen sulfide. In addition, the data indicates that the charge transfer energy terms has moderately stronger contribution for formic acid, methanol and ammonia, and very strong contribution for methane and hydrogen sulfide. Comparatively, the contribution of charge transfer is generally larger than the polarization term, in average twice as large. Furthermore, the correlation between the energy term with the total BLW-EDA energy yields R^2 of 0.03, 0.62, and 0.73, respectively. As such, charge transfer plays a significant role in the complex formation, according to BLW-EDA.

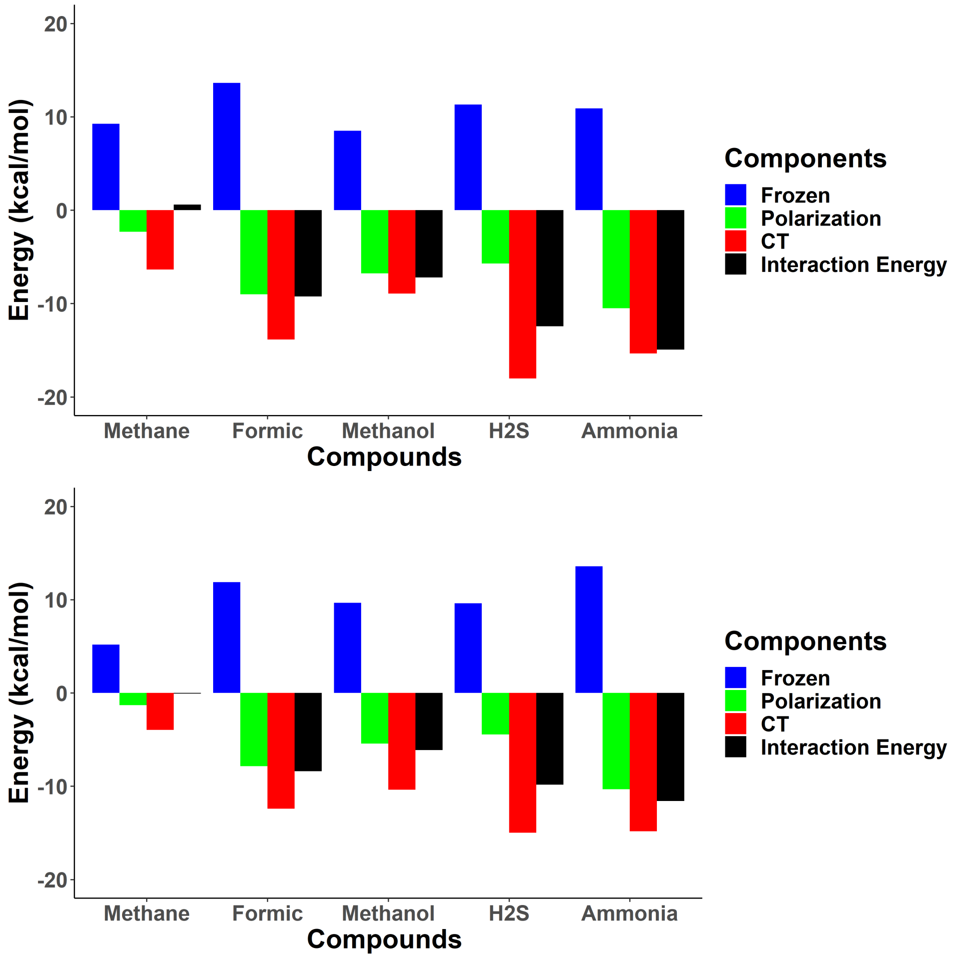

Figure 3.8: The BLW-EDA analysis performed for Au$_{55}$ complexes interacting at the corner sites (top) and sites (edge)

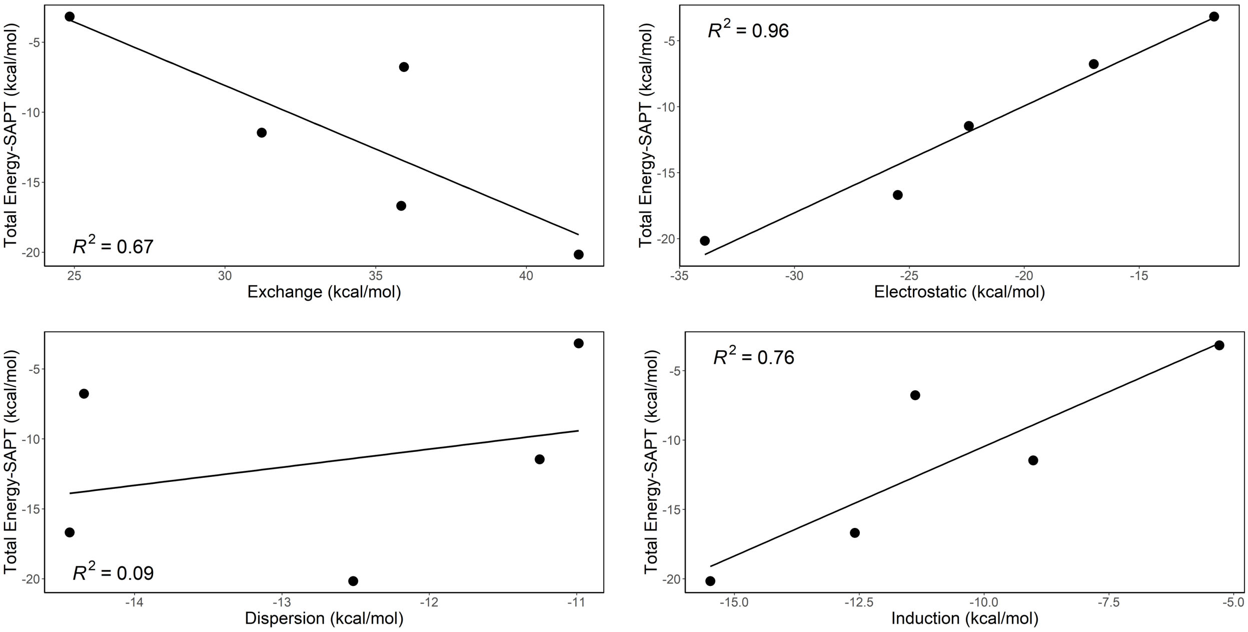

Figure 3.9: The correlation between the energy components of SAPT and the respective interaction energy for Au$_{32}$ complexes

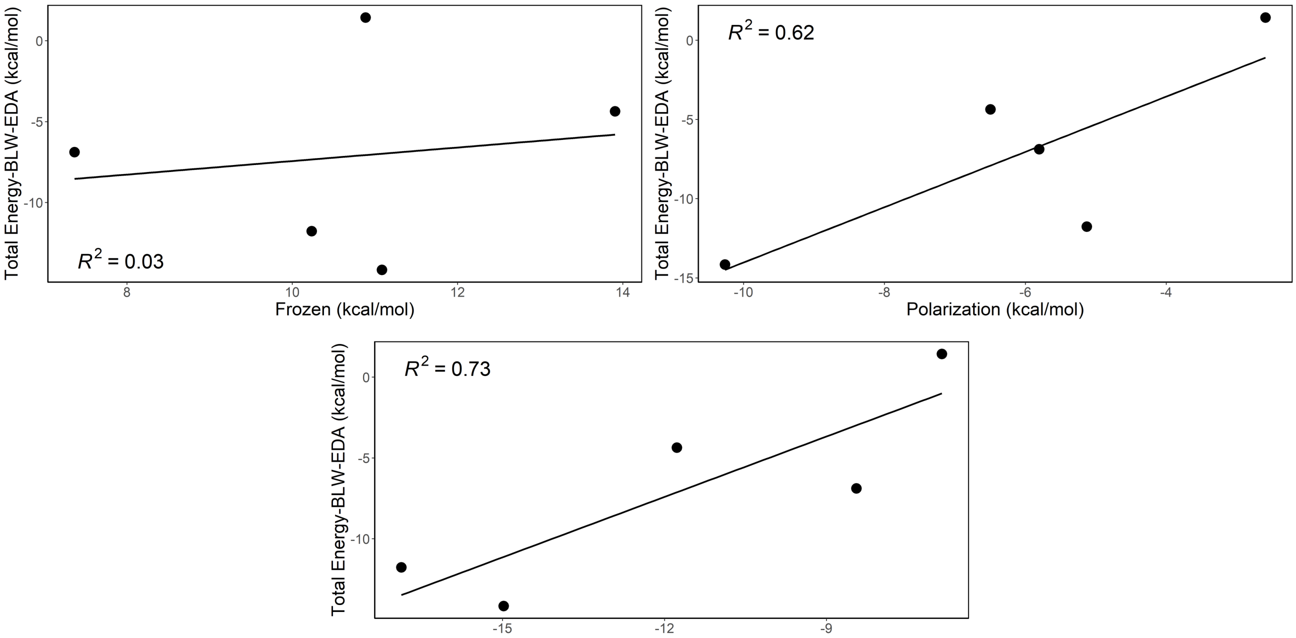

Figure 3.10: The correlation between the energy components of EDA-BLW and the respective interaction energy for Au$_{32}$ complexes

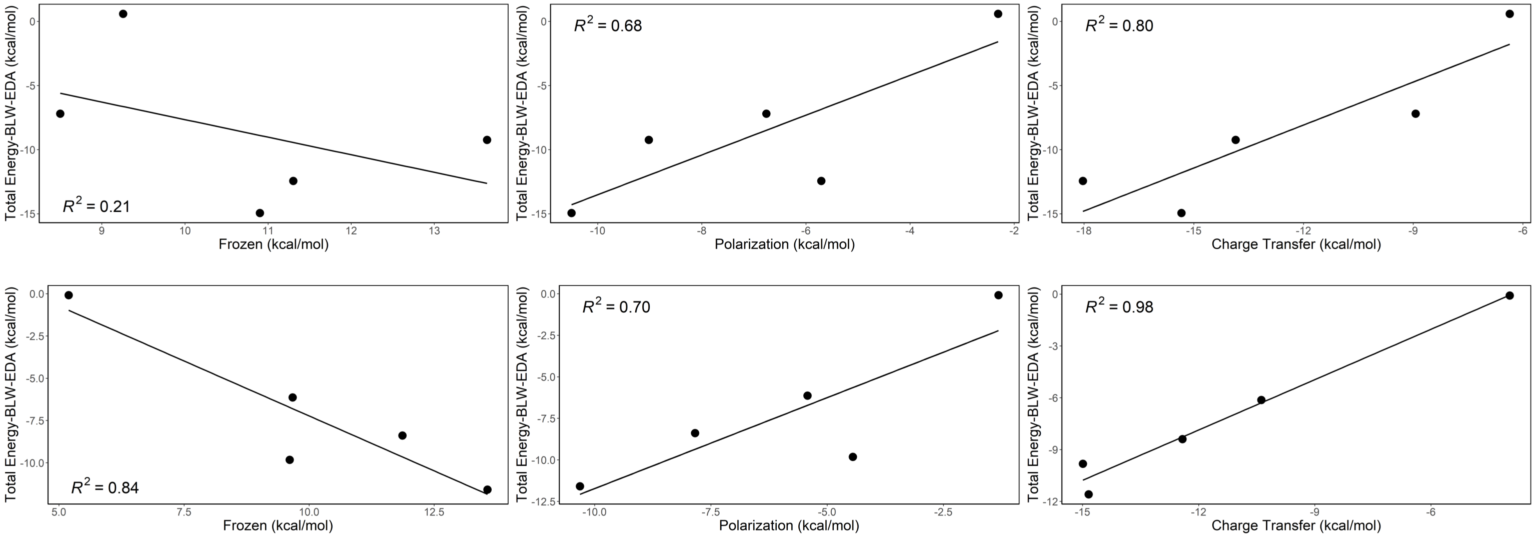

Figure 3.11: The correlation between the energy components of EDA-BLW and the respective interaction energy for Au$_{55}$ complexes at corner (top) and edge (bottom) interactions sites.

Moving on to the larger GNP, Au_{55}, the energy decomposition for complexes interacting at the corner and edge sites is shown in Figure 3.8 (top) and (bottom) respectively. Consistent with the trend observed above, the interaction energy obtained by BLW-EDA scheme increases from methane, methanol, formic, hydrogen sulfide, and ammonia. Additionally, the trend is the same for the complexes interacting at the two sites, though with a smaller magnitude for the complexes interacting at the edge site. The frozen component for all the complexes is likewise positive, so the stabilizing energy contributions are from both the polarization and charge transfer, with charge transfer has in average larger magnitude as compared to the polarization. Interestingly, the trend for the polarization and charge transfer energy terms is the same for both the complexes interacting at the corner and at the edge sites, despite the edge sites having smaller magnitude. The energy terms are then correlated with the total BLW-EDA energy to give R^2 of 0.21, 0.68, and 0.80, respectively for complexes at the corner, and 0.84, 0.70, and 0.98, respectively for complexes at the edge. As such, charge transfer terms correlate the best with the interaction energy, consistent with Au_{32} complexes.

While comparing the interaction energy between the two sizes of GNP, it does not seem to imply significant difference in the reactivity of Au_{32} and Au_{55}. There is a larger difference in the interaction energy between the interaction sites in Au_{55}, again, highlighting the difference in reactivity of the corner and the edge sites.

3.5.4 Topological Analysis

All of the complexes are then subjected to various topological analysis to characterize and visualize the nature of the interactions. The QTAIM and NCI analyses are shown in Figure 3.12 and 3.13, for Au_{32} and Au_{55}, respectively. Table 3.2 shows the local properties at the identified BCP, and based on which, the nature of interactions can be characterized. The ρ calculated at all of the BCP is found to be quite low, $\rho < 0.1$ a.u.. Furthermore, the Laplacian of the electron density of all the BCPs is calculated to be positive, therefore, the interactions do not have a covalent character. The discriminating property will then be the energy density. According to Bianchi's classification, the interaction is characterized as dispersive when $H(\rho(r)) > 0$, and dative when $H(\rho(r)) < 0$.[47]

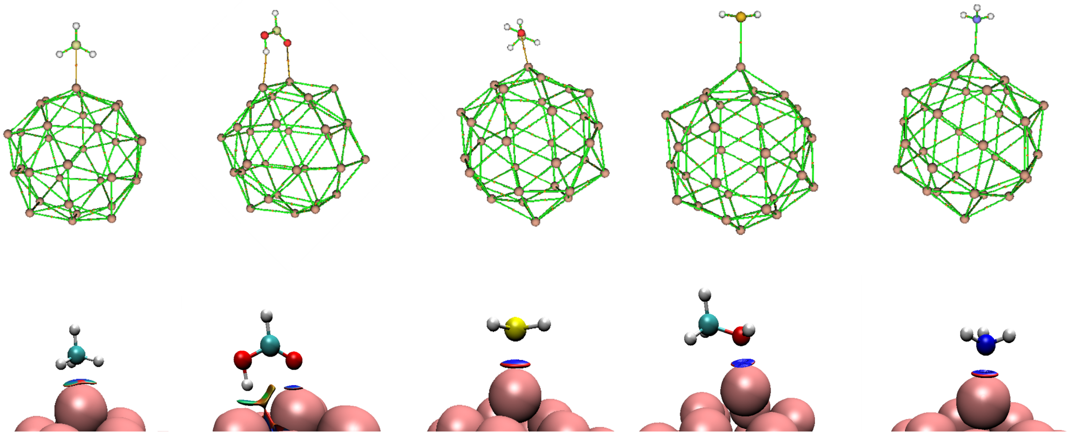

Figure 3.12: The bond critical points (top) and NCI analysis (bottom) calculated for complexes of Au_{32}

In the cases for Au_{32}, all the complexes interact through the dative like interaction with GNP, though the ρ is very low. Additionally, there are two BCP found for formic acid, one for the O atom of C=O, and the other one for H of -OH. The two interactions are characterized as the dative like interaction. Since the characterization in BCP coincides by definition with NCI analysis, the interactions can then be visualized, with color coded basins representing the non-covalent interactions, with red as repulsive interaction, blue as dative interaction, and green as dispersive interactions (see Figure 3.12 (bottom)).

The interactions in Au_{55} are likewise non-covalent in nature, according to the properties at BCP. Moreover, the values of ρ for the BCP at the corner sites seems to be higher than those at the edge sites, again supporting the higher reactivity of the corner sites. Particularly in the case for methane, the interaction at the corner site is dative like, and it becomes dispersive like at the edge site. In other cases, there are multiple BCP found, such as in the cases of formic acid at the corner site, and methanol at the edge sites. These additional BCP correspond to the interaction with -OH of formic acid, and with $-CH_3$ of methanol, which have comparatively lower ρ values, and are dispersive in nature. These interactions are then visualized with the NCI analysis (see Figure 3.13).

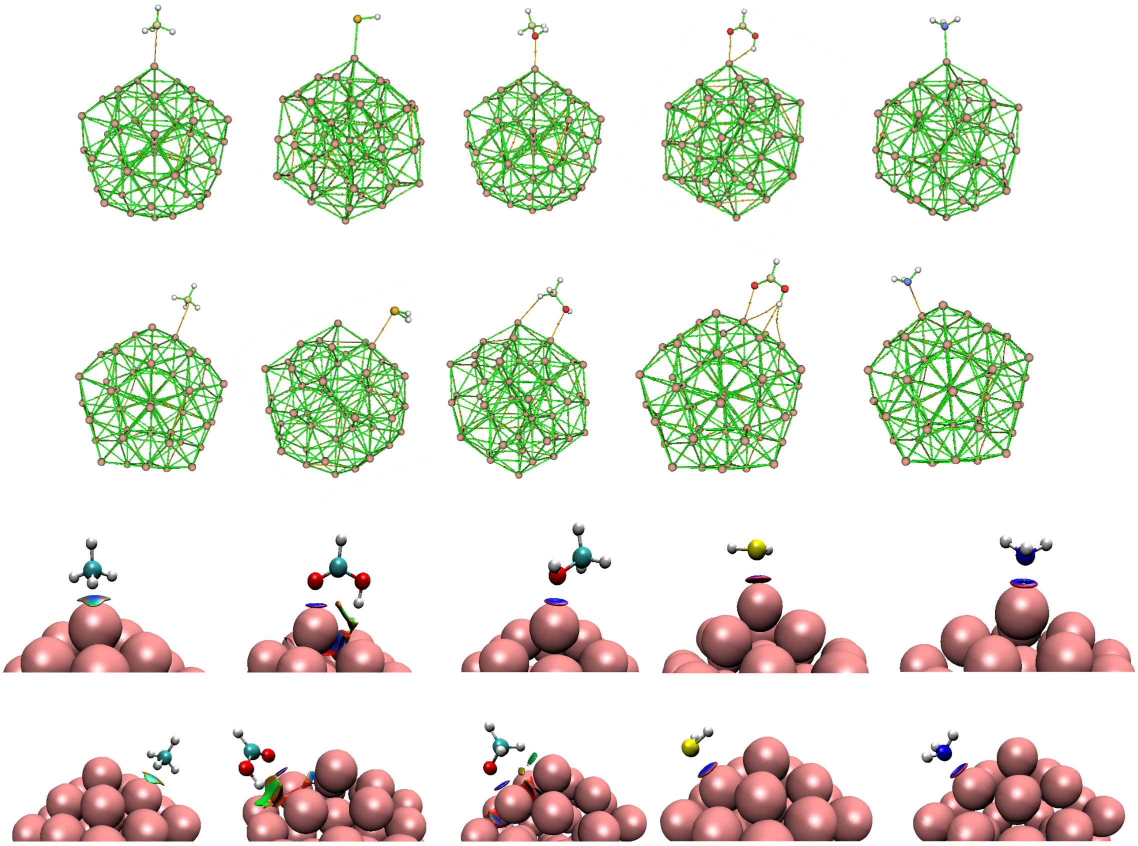

Figure 3.13: The bond critical points (row 1 and 2) and NCI analysis (row 3 and 4) calculated for complexes of Au_{55} interacting at the corner (row 1 and 3) and edge sites (row 2 and 4)

Table 3.2: The local properties calculated at the respective BCP of each complexes

GNP	Organic	Position	BCP	ρ (a.u.)	$\nabla\rho$ (a.u.)	$H(r)$ (a.u.)
Au_{32}	CH_4	-	Au-C	0.030	0.116	-0.001
	HCOOH	-	Au-O	0.038	0.168	-0.002
			Au-H	0.021	0.052	-0.001
	H_2S	-	Au-S	0.046	0.128	-0.008
	CH_3OH	-	Au-O	0.048	0.215	-0.006
	NH_3	-	Au-N	0.060	0.212	-0.013
Au_{55}	CH_4	Corner	Au-C	0.027	0.106	-0.0004
		Edge	Au-C	0.019	0.078	0.001
	HCOOH	Corner	Au-O	0.052	0.235	-0.007
			Au-H	0.014	0.039	0.001
		Edge	Au-O	0.039	0.173	-0.003
	H_2S	Corner	Au-S	0.048	0.130	-0.009
		Edge	Au-S	0.040	0.109	-0.006
	CH_3OH	Corner	Au-O	0.051	0.232	-0.069
		Edge	Au-O	0.041	0.178	-0.004
			Au-C	0.016	0.049	0.001
	NH_3	Corner	Au-N	0.059	0.208	-0.012
		Edge	Au-N	0.057	0.199	-0.012

3.5.5 Vibrational Analysis

The vibrational analysis were subsequently performed to investigate the change in vibrational spectra of the organic molecules, as they interact with the GNP. Therefore, the computed IR spectra of the complexes with Au_{32} and Au_{55} are systematically compared with the isolated organic molecules (see Figure 3.14, 3.15, 3.16, 3.17, and 3.18). In the case of methane, in its isolated state, it is a highly symmetrical compound, with tetrahedral geometry, and only 2 peaks that correspond to CH bending and CH stretching modes are observed in the spectrum. Upon adsorption on GNP, however, more vibrational modes become IR active due to symmetry breaking, at 1230, 1513 and 2962 cm^{-1} . The vibrational mode at 1230 cm^{-1} corresponds to an umbrella like bending mode of CH_3 moiety while the vibrational mode at 2962 cm^{-1} corresponds to the stretching mode of this moiety. In addition, the adsorption induces slight red shift in the frequencies of both the bending (*i.e.* 1288 to 1281 cm^{-1}) and stretching vibrational modes (*i.e.* 3115 to 3103 cm^{-1}). Comparing the IR spectra of complexes interacting on the Au_{32} and Au_{55} does not show significant differences, neither are the spectra sensitive to the corner or edge sites of Au_{55} (see dotted line in Figure 3.14).

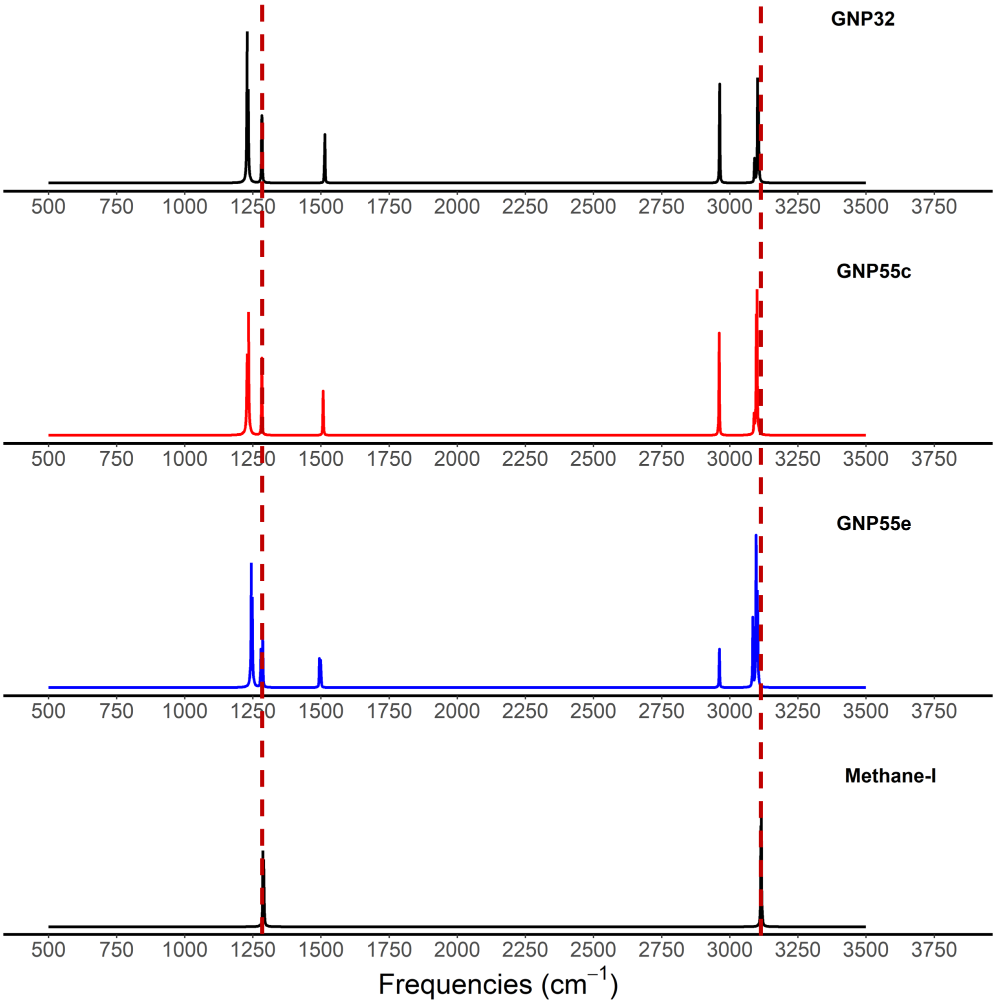

Figure 3.14: The calculated IR spectra for Methane adsorbed on Au$_{32}$, Au$_{55}$ corner and edge sites, in comparison to the isolated molecule (-I)

In the case of formic acid, upon adsorption, the IR spectrum change rather significantly (see Figure 3.15). As the interactions are formed by both the C=O and OH, the whole structure of formic acid seems to have changed. The peaks corresponding to the-OH and -CH stretching modes have shifted quite significantly, *i.e.* red shift (3684 to 3306 cm^{-1}) and blue shift (2912 to 3007 cm^{-1}), respectively. The hydrogen bond like interaction between Au – H-O has led to the red shift of the OH stretching mode. Owing to the electron donation from the C=O to the GNP, it has led to the strengthening of C-H bond, which results in the significant blue shift of the C-H stretch mode. The C=O stretching mode has red shifted from 1813 to 1718 cm^{-1}. Similar trends are observed across the sizes and interaction sites of GNP, since the formic acid interacts in the same geometry. Likewise, the IR spectra is sensitive to the environment of the molecule, but not as much to the properties of GNP itself.

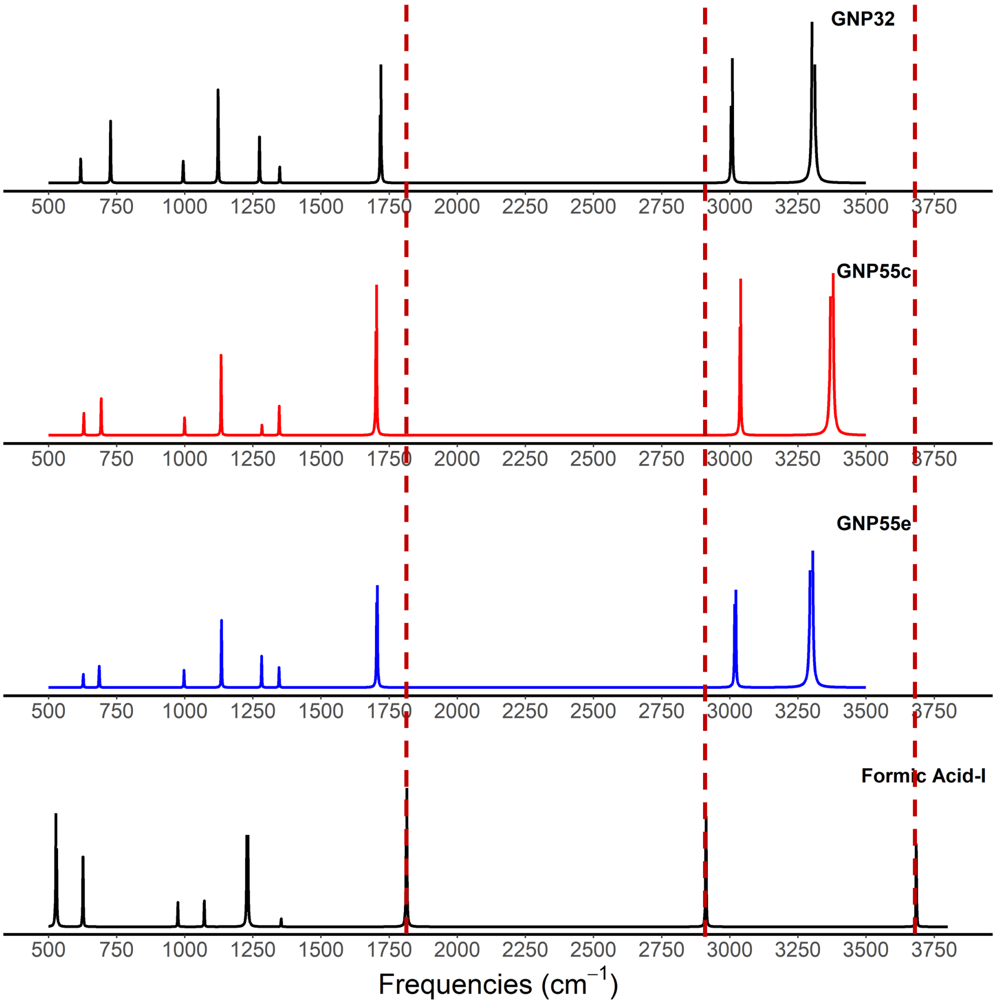

Figure 3.15: The calculated IR spectra for Formic acid adsorbed on Au$_{32}$, Au$_{55}$ corner and edge sites, in comparison to the isolated molecule (-I)

As for hydrogen sulfide, a slight red shift of the vibrational modes has been observed upon adsorption on GNP (1169 to 1164 cm^{-1} for SH bending mode, and 2656 to 2651 cm^{-1} for SH stretching mode). The interaction with GNP does not seem to induce significant changes, despite the relatively strong interaction between the two (see Figure 3.16).

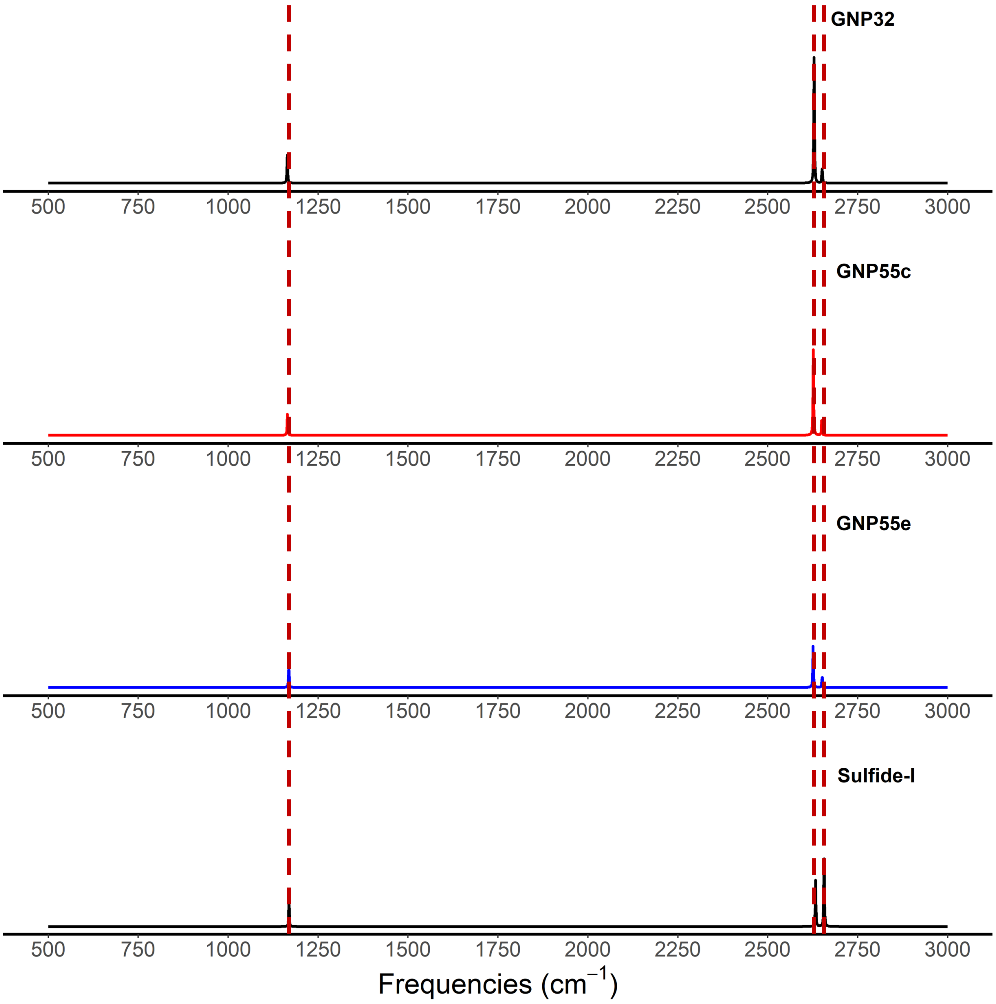

Figure 3.16: The calculated IR spectra for H_2S adsorbed on Au_{32}, Au_{55} corner and edge sites, in comparison to the isolated molecule (-I)

In the case of methanol (see Figure 3.17), the interactions are formed by the -OH functional group. Therefore, the -OH stretching mode is slightly red shifted upon adsorption on all the GNP, *i.e.* 3748 to 3731 cm^{-1} for adsorption on Au$_{32}$. Though, the red shift for the methanol adsorbed on the edge sites of Au$_{55}$ is reported to be higher than the rest. This highlights the difference in the configuration of methanol on the edge of Au$_{55}$ (see Figure 3.6). The stretching mode of -CH$_3$ moieties seems to have blue shifted slightly upon adsorption, except for one of the CH stretching mode that is red shifted for methanol on the edge of Au$_{55}$. This red shift is caused by the dispersive interaction between C-H – Au, as seen in the topological analysis above. The C-O stretching mode has red shifted due to the interaction, *i.e.* 1458 to 1435 cm^{-1} for adsorption on Au$_{32}$. This analysis has demonstrated that the IR spectra is sensitive to the adsorption configuration of the molecule.

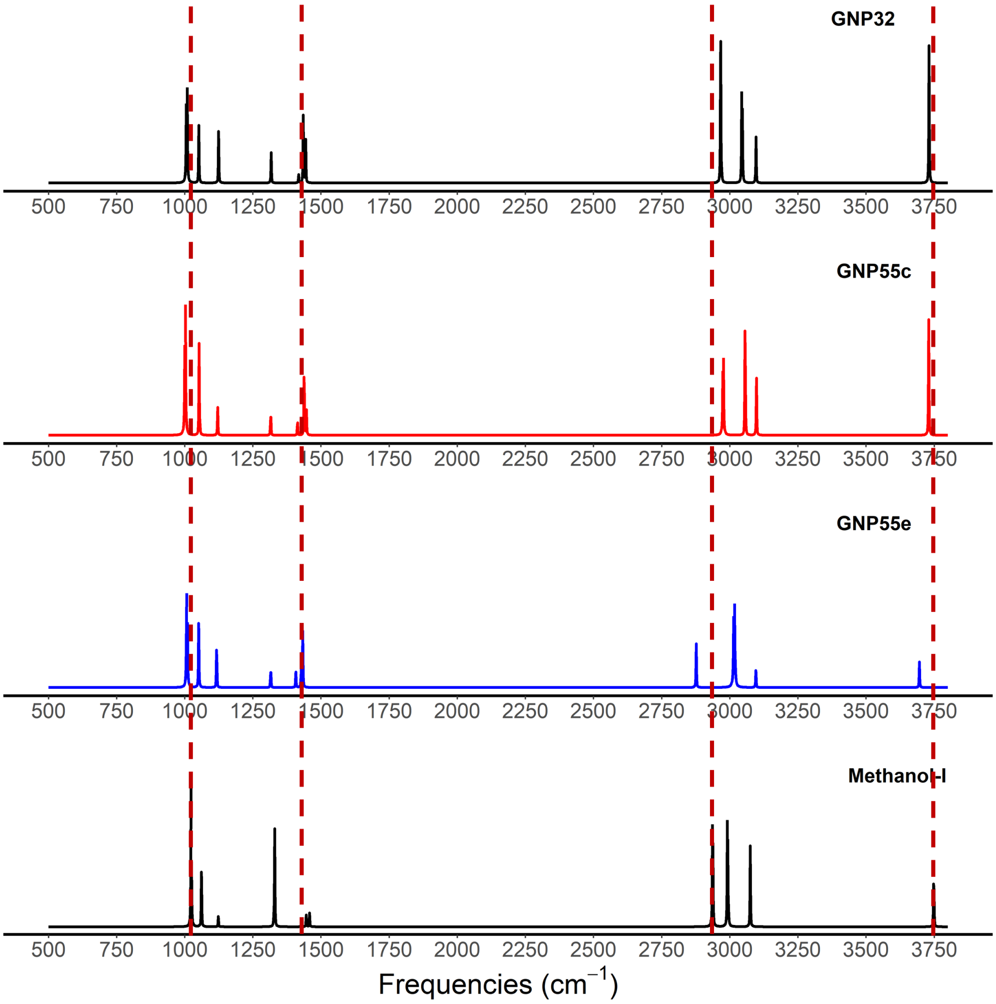

Figure 3.17: The calculated IR spectra for Methanol adsorbed on Au$_{32}$, Au$_{55}$ corner and sites, in comparison to the isolated molecule (-I)

Lastly, in the case of ammonia (see Figure 3.18), there is a significant increase in the intensity of NH asymmetric stretching mode upon adsorption on GNP, as the change in the dipole seems to be enhanced by the GNP. In addition, the umbrella-like bending mode has undergone a blue shift upon adsorption (1029 to 1108 cm^{-1}), as the umbrella bending mode is now confined in the presence of the GNP. The IR spectra of ammonia have likewise changed in the same manner across the sizes and interaction sites of GNP.

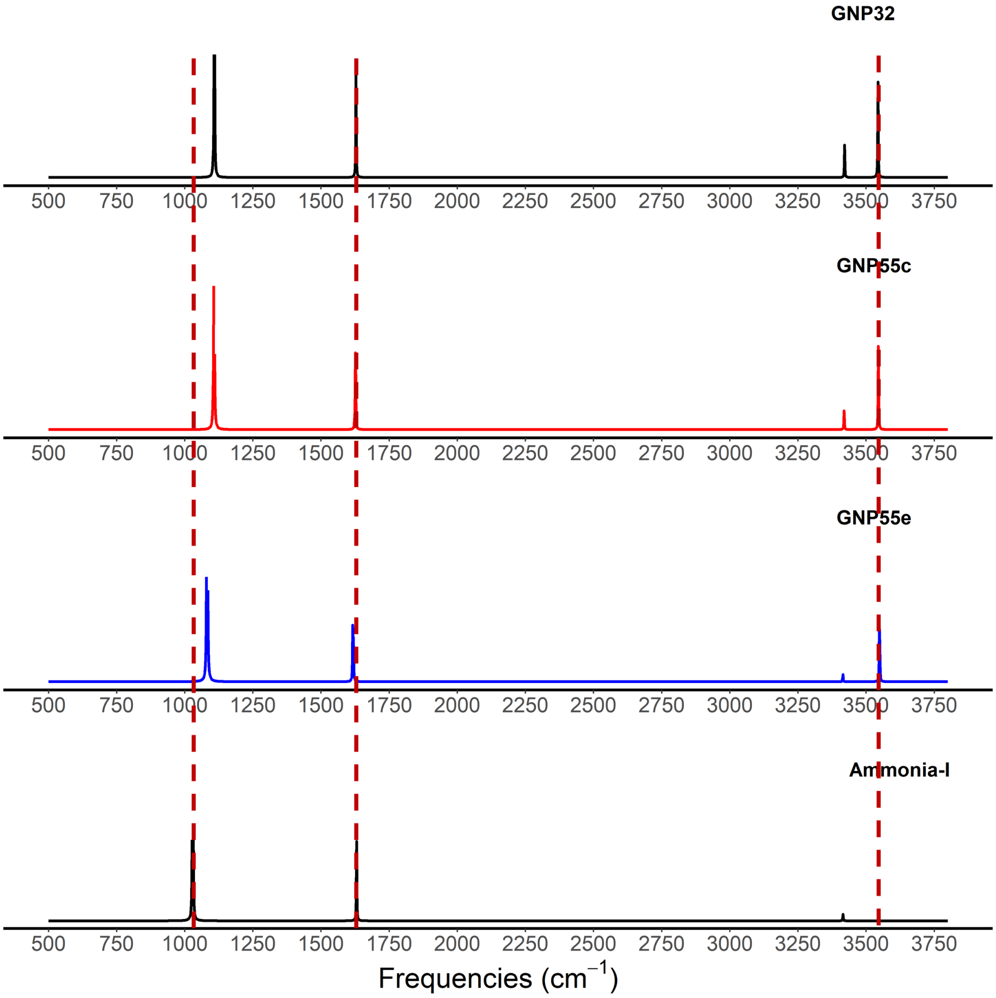

Figure 3.18: The calculated IR spectra for Ammonia adsorbed on Au$_{32}$, Au$_{55}$ corner and edge sites, in comparison to the isolated molecule (-I)

In summary, the IR spectra of the molecules are affected in the same way across the different sizes and interaction sites of GNP studied here, as long as the configuration adopted by the molecules remains constant. Therefore, the change in the vibrational spectra depends rather on the configuration of the molecules, than the properties of GNP itself.

3.5.6 The Case for Benzoic Acid

To further explore the effect of size and shape of GNP on changes in vibrational spectra, benzoic acid has been selected as the model compound for the organic compound. With the goal of validating theoretical insights on experimental observation, either a collaborative work with experimentalists or the availability of the reported experimental spectra is indispensable. As such, this work has been carried out in close collaboration with C. Sicard-Roselli (ICP, Paris-Saclay Univ.). Because of the constraints in the experimental setup, out of all the compounds investigated here, only benzoic acid is adsorbed well and long enough for IR spectra to be recorded. Additionally, reference data of isolated and adsorbed benzoic acid on different metal surfaces are available in the literature.[72,73] In terms of computational approach, benzoic acid is small enough, and it is able to adopt 2 different configurations, which are the flat and perpendicular configurations. Moreover, we have also observed a noticeable change in the IR spectra for the two interaction configurations, thanks to the IR selection rule on surfaces. Therefore, benzoic acid is an ideal model for a further study, and for a qualitative comparison with the experimental spectra.

Our investigation in the previous section has highlighted the sensitivity of IR spectra on the configuration of the molecules upon adsorption and the indifference of the size and interaction sites on GNP. However, the GNP investigated is limited to Au_{32} and Au_{55}. Therefore, additional studies are performed for larger series of GNP: Au_{55}, Au_{79}, and Au_{105}. The same simulation workflow has been followed, which is geometry optimization and followed by calculation of IR spectra in harmonic approach. The optimized geometries and their respective IR spectra of benzoic acid adsorbed on Au_{55}, Au_{79}, and Au_{105} are shown in Figure 3.19, 3.20, and 3.21, respectively. The scaling factor is still not yet included, because the comparison is still being done among the calculated spectra. The computed vibrational frequencies of isolated benzoic acid are shown in Table 3.3, for comparison.

Table 3.3: The selected calculated frequencies of isolated benzoic acid, along with their assignment.

Frequency (cm^{-1})	Assignment
412.8	C=C aromatic bend out-of-plane
606.9	COOH scissoring bend
675.2	C-H aromatic symm bend out-of-plane
695.2	C-H aromatic symm bend out-of-plane
752.5	C=C aromatic bend in-plane
781.3	C-H aromatic bend out-of-plane + C-COOH bend out-of-plane
913.3	C-H aromatic bend out-of-plane
1022.2	CH aromatic bend + C=C aromatic stretch
1065.7	CH aromatic bend
1154.5	CH aromatic bend + OH bend
1178.9	CH aromatic bend + OH bend
1337.7	C-OH stretch
1376.1	C=C aromatic stretch
1434.6	C=C aromatic stretch + CH aromatic bend
1474.2	C=C aromatic stretch + CH aromatic bend
1590.9	C=C aromatic stretch
1610.9	C=C aromatic stretch
1740.2	C=O stretch
3139.8	CH aromatic stretch
3150.1	CH aromatic stretch
3159.2	CH aromatic stretch
3165.6	CH aromatic stretch
3658.5	-OH stretch

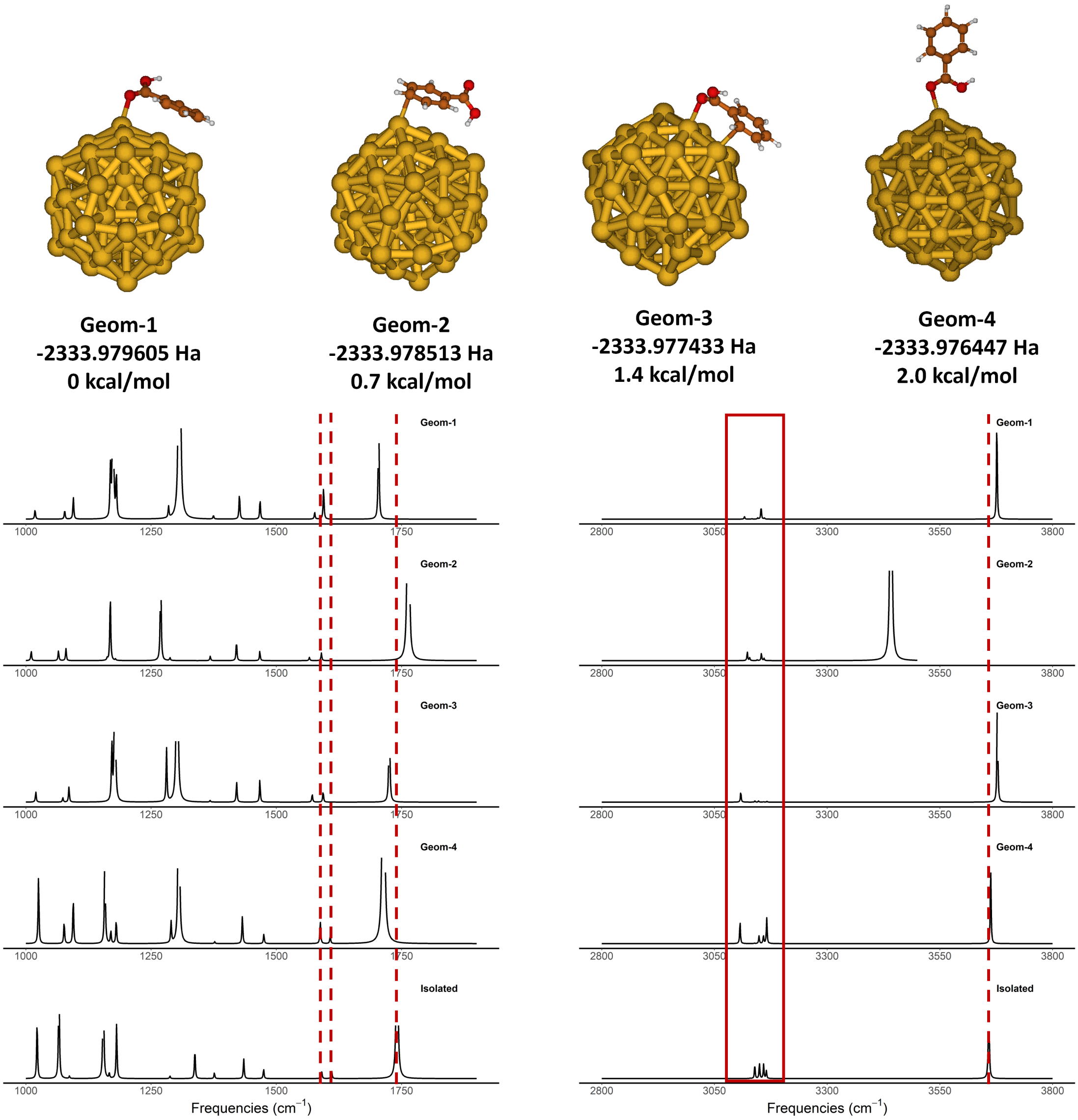

Figure 3.19: The optimized geometries of benzoic acid adsorbed on Au$_{55}$ along with their relative energy with respect to the most stable configuration, and their respective calculated IR spectra

The geometry optimizations of benzoic acid complexes with Au$_{55}$ result in several geometries as local minima of the potential energy surface (see Figure 3.19 top). Three out of the four complexes are considered as flat configurations, where the plane of the aromatic ring lies flat on the surface. The carboxylic acid in these three structures is tilted out of the aromatic plane either towards the surface, or away from the surface. These tilted geometries, usually not observed for isolated benzoic acid, are the result of interaction between either the C=O or O-H groups with Au surface. The last geometry shows the perpendicular configuration, where the C=O group forms a favorable interaction with the surface, and stabilizes the overall structure. The flat configuration, *i.e.* geom-1, is found to be the most stable complex out of the four complexes.

These interactions with GNP have led to shifts in the simulated IR spectra, (see Figure 3.19 bottom), especially on the vibrational modes corresponding to the carboxylic acid. The C=O stretching mode, observed at 1741 cm^{-1} in vacuum, has shifted to 1704 cm^{-1}, 1763 cm^{-1}, and 1725 cm^{-1}, respectively for the first 3 flat complexes. This difference in shift is due to the different degree of interaction formed by the C=O. The first complex adopting flat configuration seems to result in strong interaction with the surface, leading to almost 40 cm^{-1} shift in the CO frequency. The second complex, however, forms interaction through the -OH group, resulting in a blue shift of the CO stretching mode. The third complex also forms interaction through the -C=O functional group, while the -OH is pointing slightly away from the surface.

The modes associated to the phenyl ring have undergone changes as well, as a result of the interaction, in particular the CH aromatic stretching mode. Firstly, there is a red shift observed on the stretching mode, and secondly, the intensity of the modes decreased significantly, as compared to the isolated benzoic acid. Additionally, the peaks associated to C=C aromatic stretching modes, at 1610 and 1590 cm^{-1} for isolated molecule, have undergone a red shift for these three complexes, for example to 1594 and 1577 cm^{-1}, respectively for geom-1. At the lower frequency range, which are associated to the in plane and out-of-plane bending modes of C=C and C-H aromatic, the modes are also considerably impacted due to the metal-surface selection rule of IR spectroscopy. For example, the peak at 1022 cm^{-1} is associated to the CH aromatic bending mode, and the intensity is likewise reduced significantly.

For the last structure, which is in perpendicular configuration, the CO stretching mode is not only red shifted to 1714 cm^{-1}, but also increased in intensity to 694 km/mol from 296.8 km/mol in isolation. Additionally, the C=C aromatic stretching modes are less red shifted as compared to the flat counterparts, implying the relatively unperturbed phenyl structure by the adsorption in perpendicular configuration.

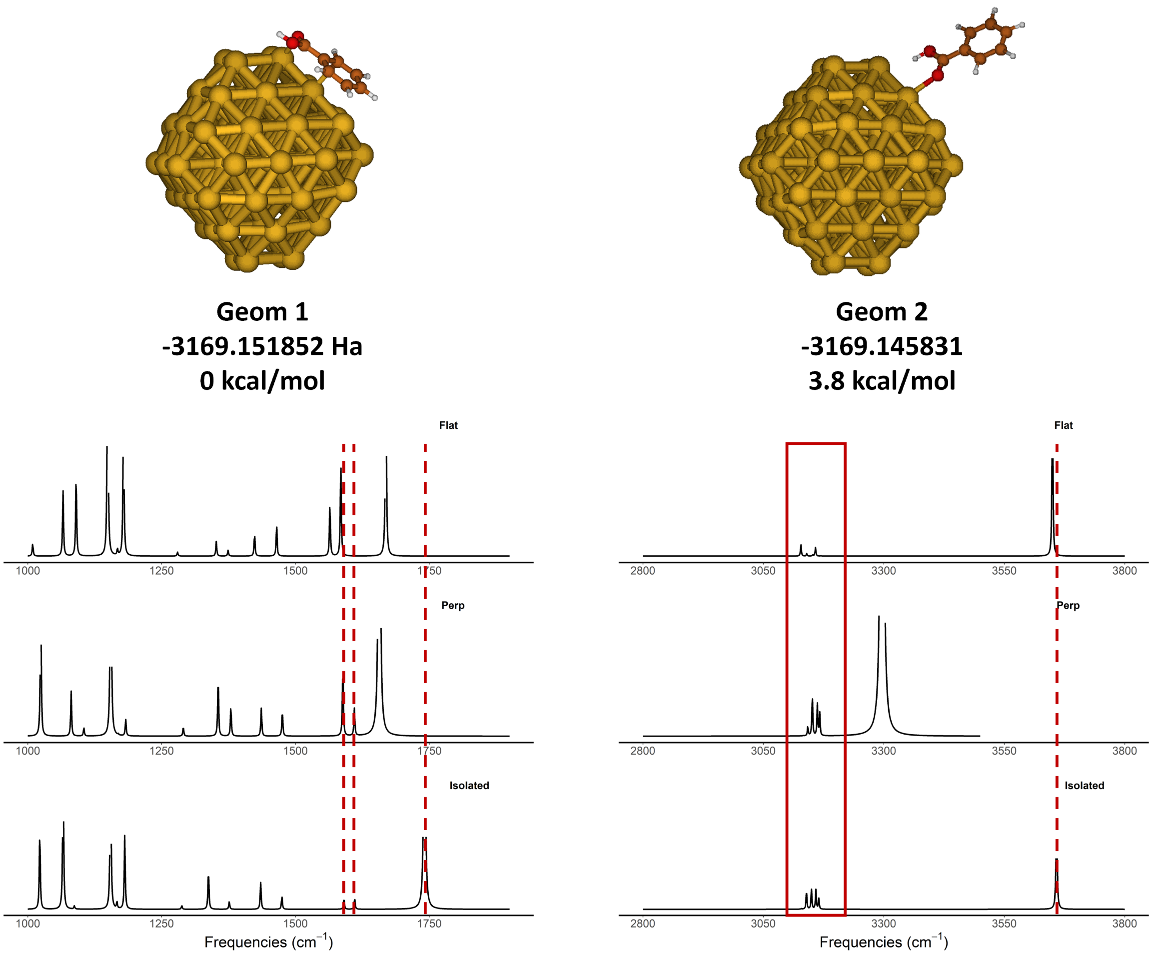

Figure 3.20: The optimized geometries of benzoic acid adsorbed on Au$_{79}$ along with their relative energy with respect to the most stable configuration in the series, and their respective calculated IR spectra.

For the adsorption of benzoic acid on Au$_{79}$, only two geometry optimizations have been performed with initial flat and perpendicular configurations of benzoic acid, which resulted in two minima for which the spectra are shown in Figure 3.20. The flat configuration is found to be more stable by 3.8 kcal/mol as compared to the perpendicular configuration. As for the calculated IR spectra, the peak associated to the C=O stretching mode has similarly been red shifted for both the configurations, to 1668 cm^{-1} for flat and to 1656 cm^{-1} for perpendicular, respectively. Additionally, the peaks associated with the phenyl CC stretching modes are quite significantly red shifted in the flat configuration (1564 cm^{-1} and 1584 cm^{-1}), but not in the perpendicular configuration (1588 cm^{-1} and 1610 cm^{-1}). Considering the rather isolated positions of these peaks, they could also be a suitable indicator for benzoic acid in either the perpendicular or flat configuration. Similarly, the phenyl CH stretching mode has also considerably shifted, with significantly reduced intensity in flat configuration, as compared to the perpendicular configuration. Lastly, the -OH stretching mode has been significantly shifted because of the direct interaction in the perpendicular configuration, but not in the flat configuration.

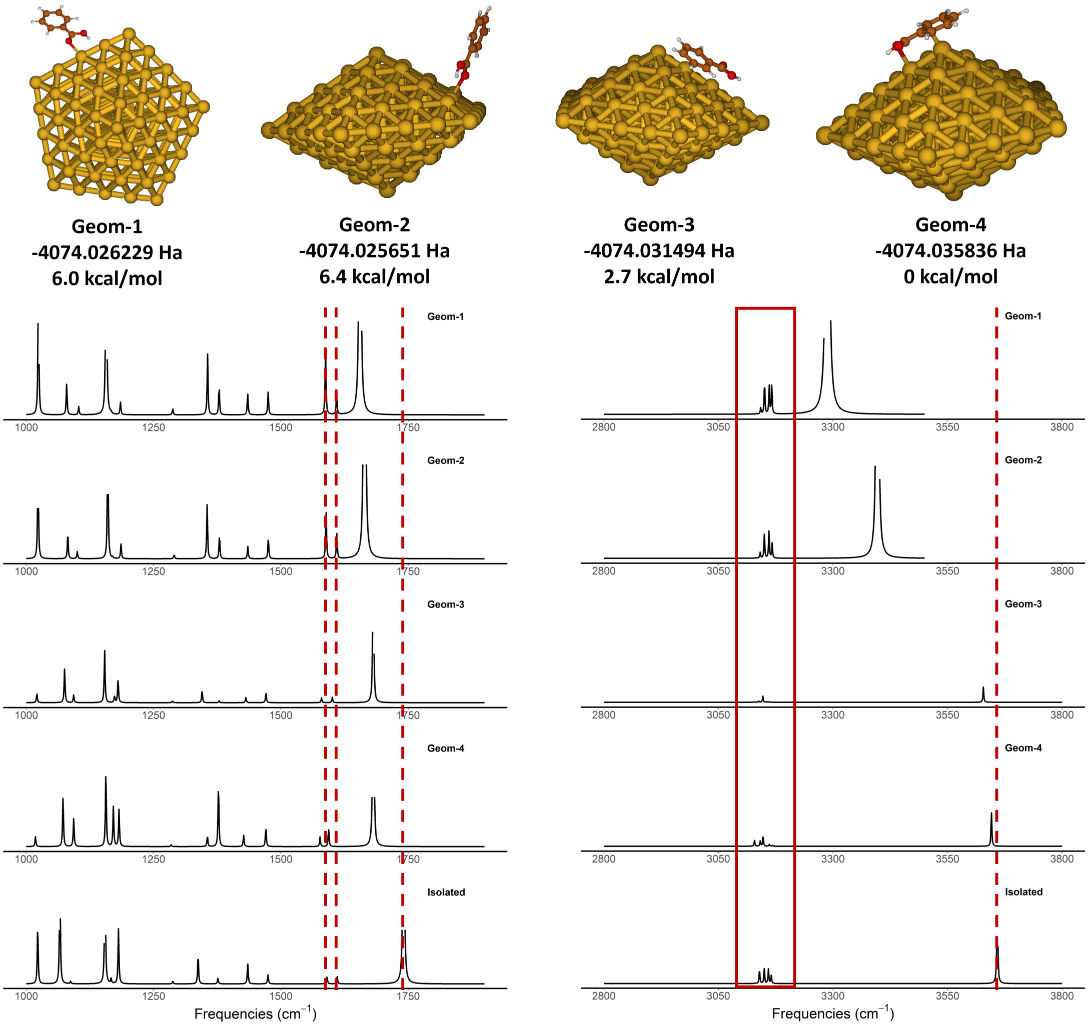

Figure 3.21: The optimized geometries of benzoic acid adsorbed on Au$_{105}$ along with their relative energy with respect to the most stable configuration in the series, and their respective calculated IR spectra.

In the case of adsorption on Au$_{105}$, multiple local minima with the benzoic acid interacting at different interaction sites have been obtained (see Figure 3.21). Likewise, the flat configurations (last 2 complexes) are found to be more stable as compared to the perpendicular configurations (the first two complexes). Comparing the calculated spectra, there is no significant difference in the considered range of frequencies observed for the geom-1 and geom-2, as they both are in perpendicular configuration. Similarly, there is no significant difference observed for geom-3

and geom-4, as they both are in flat configuration. These observations support our initial investigation for Au$_{55}$, which implies the observation could also be extrapolated to the other larger GNP.
Since the C=O group interacts with the GNP in all the complexes, the C=O stretching mode is red shifted. Again, comparing between the flat and perpendicular configurations, an increase in the intensity of the C=O stretching mode is observed for the perpendicular and not for the flat complexes. The modes associated to C=C aromatic stretching are similarly unperturbed for the perpendicular complexes, and red shifted for the flat complexes.

All in all, a consistent observation in the IR spectra for the adsorption of benzoic acid across different sizes and interaction sites has been shown (see Figure 3.22 and Figure 3.23). Firstly, the C=O stretching mode is always red shifted upon interaction with the Au surface, except in one of the complex with Au$_{55}$, where it has blue shifted, because of the interaction between the -OH with the surface. Secondly, the intensity of some of the phenyl CH stretching modes and C-H aromatic in-plane bending modes is significantly reduced for the flat configuration, in contrast to the perpendicular configuration. And thirdly, the phenyl C=C stretching modes are more impacted by the adsorption for the flat configuration, as compared to the perpendicular configuration.

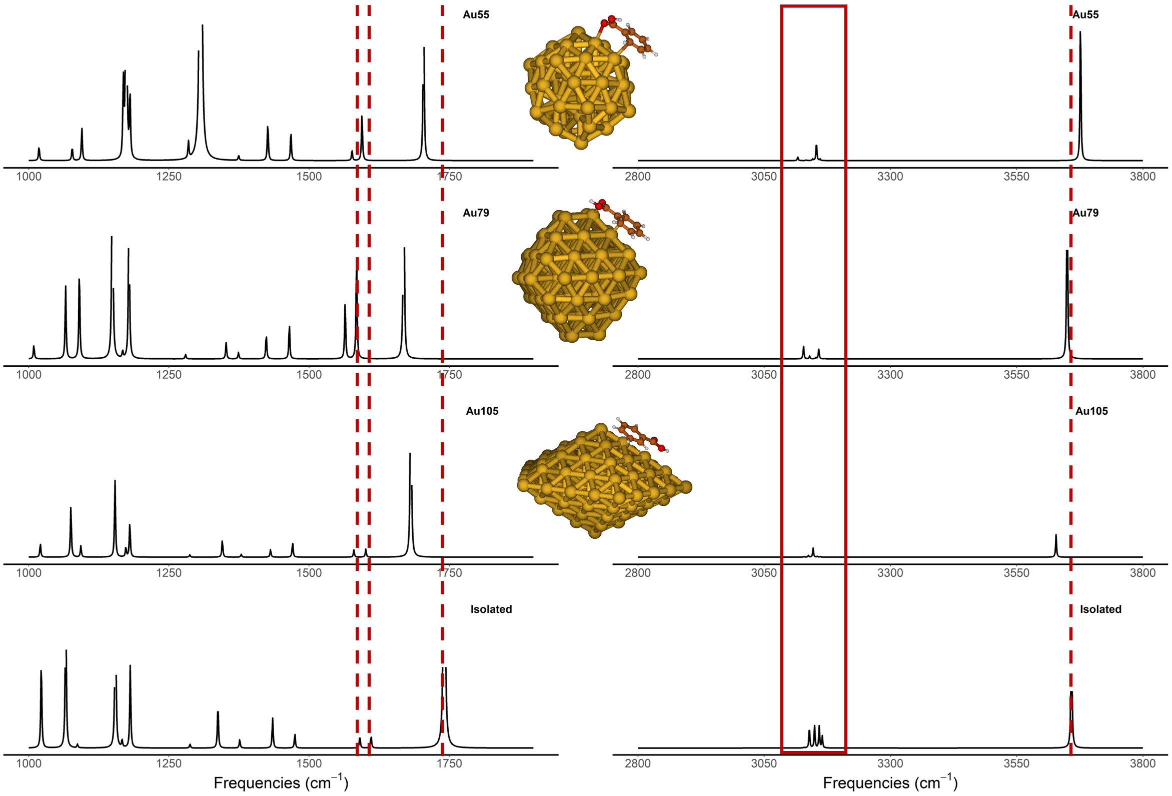

Figure 3.22: The simulated IR spectra of benzoic acid adopting flat configuration across different sizes of GNP

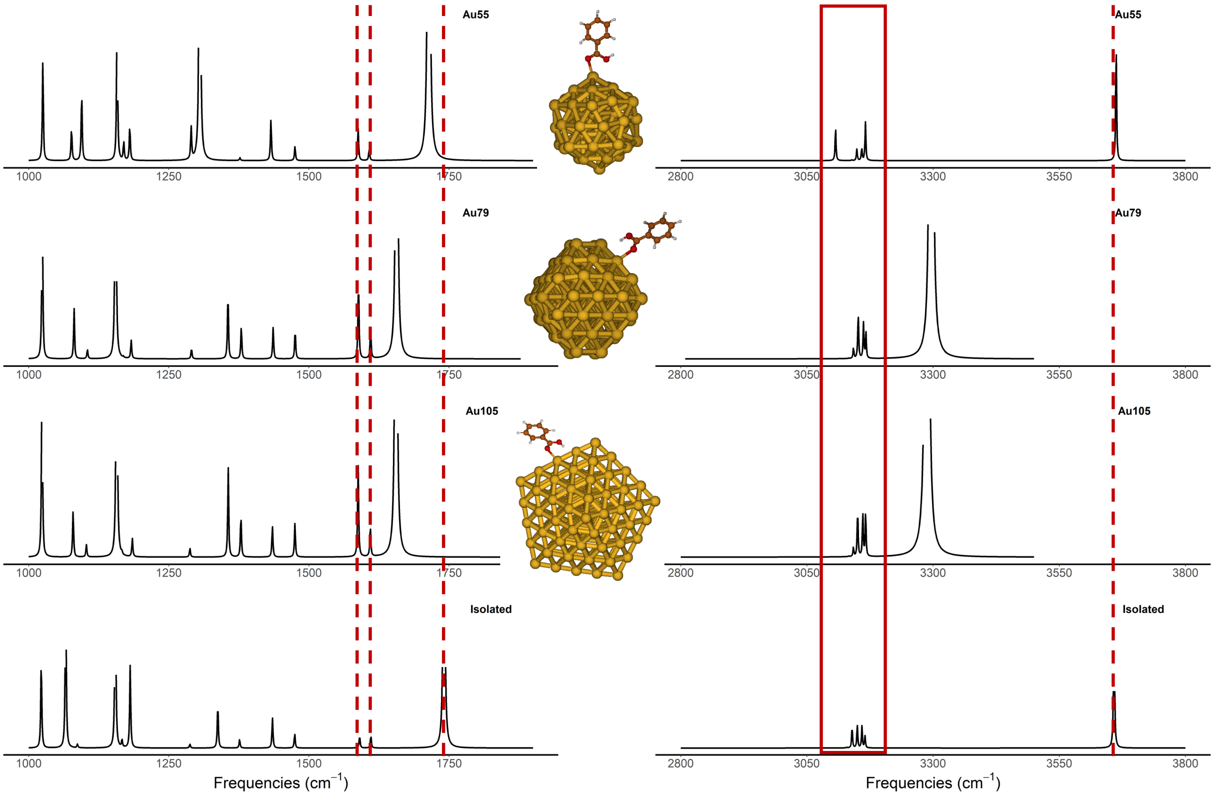

Figure 3.23: The simulated IR spectra of benzoic acid adopting perpendicular configuration across different sizes of GNP

While all the simulated IR spectra here are obtained from optimized geometries, it may not reflect directly the experimental condition yet, which is an average of multiple configurations at the surface. Therefore, additional calculations of the IR spectra have been carried out for benzoic acid at several tilt angles with respect to the surface of Au$_{32}$. The objective of such calculation is to capture the transition of the spectra from the flat configuration to the perpendicular configuration. As shown in Figure 3.24, the first tilted geometry and its simulated IR spectrum, labelled as Tilt-1, still resembles the flat adsorption mode. As the phenyl ring moves away from the surface, at Tilt-2 and Tilt-3, the simulated spectra resemble the perpendicular spectra observed above. The C=O stretching mode is largely unchanged in the three geometries, as C=O is the interacting moiety in all configurations. As for the peaks associated to the phenyl stretching mode, the peaks in Tilt-1 are largely red shifted and reduced in intensity, reflecting flat configuration, as compared to the other tilted geometries. Therefore, the vibrational mode associated to the phenyl ring seems to provide more discriminating observation between flat or perpendicular interaction configurations, than that associated with C=O stretch mode, as CO group almost always interacts at the surface.

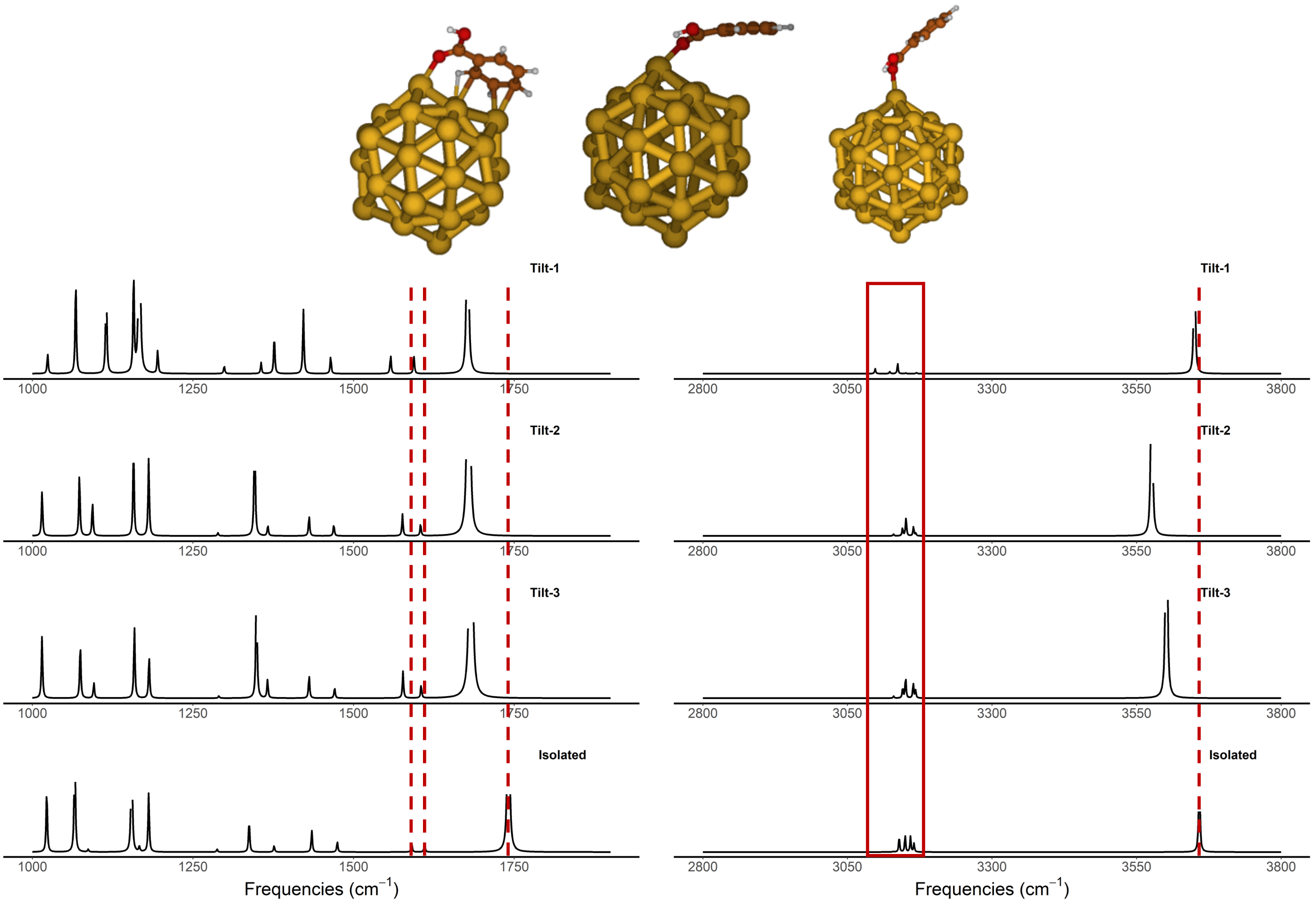

Figure 3.24: The geometry of benzoic acid adsorbed at different tilt angles on Au_{32}, and their respective calculated IR spectra

Considering that benzoic acid in solution is almost always deprotonated to Ph-COO^-, additional calculations with the deprotonated benzoic acid have been performed. The deprotonated benzoic acid is found to be more stable adopting perpendicular configuration than the flat configuration by 7.4 kcal/mol. Meanwhile, the simulated spectra are considerably different from the protonated one (see Figure 3.25). The difference between the flat and perpendicular interaction configurations is even more pronounced in the deprotonated case. Firstly, both the symmetrical and asymmetrical -COO^- vibrational modes are quite intense and broad. In particular, the peak associated to the asymmetrical stretch has red shifted significantly in the perpendicular configuration, as compared to the flat configuration. It has now appeared on the lower frequency range as compared to the phenyl -CH bending mode. Therefore, the relative position of this peak can be a good indicator for deciphering experimental spectrum. In terms of the phenyl -CH stretching mode, the intensity is significantly smaller in flat configuration, as compared to the one in perpendicular configuration, consistent to what we observed previously.

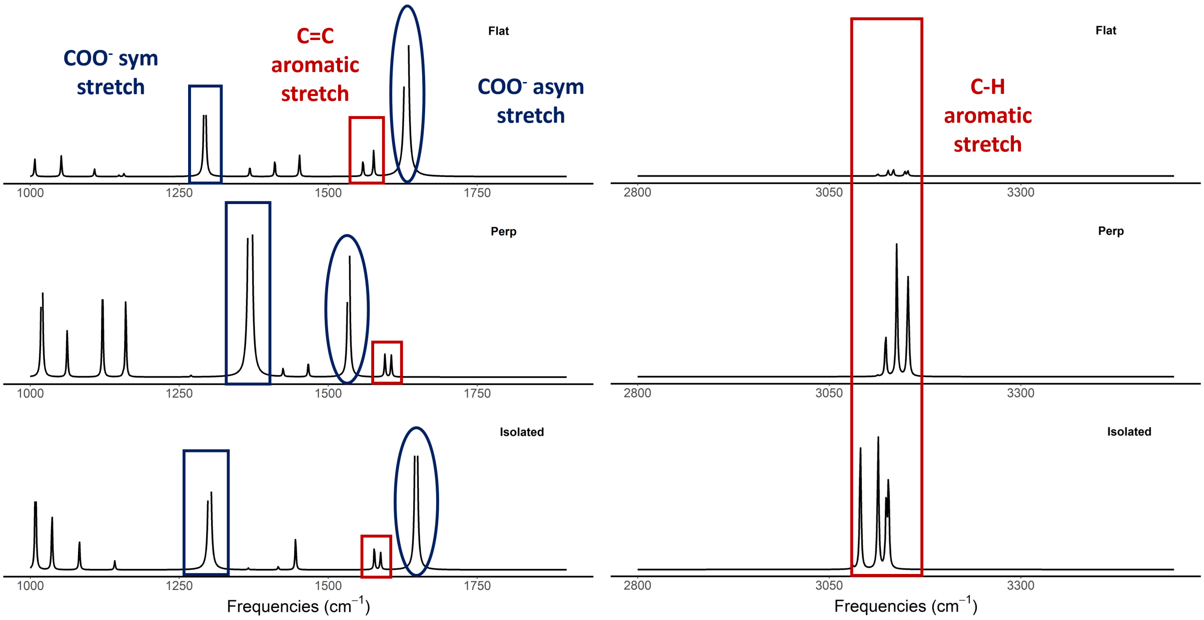

Figure 3.25: The simulated IR spectra of deprotonated benzoic acid adopting flat and perpendicular configuration on Au_{32}

3.5.7 Conclusion and Perspectives

All in all, our systematic investigation of the interaction of small organic molecules across a series of GNP has unveiled that the interaction is largely determined by the nature of the organic molecules itself. The interactions are quite independent on the size of the GNP, at least for the sizes considered in this section, as well as for the Au_{79} complexes investigated in the previous section. The interaction energies calculated for Au_{79} are quite close to those for Au_{32} and Au_{55}, while the reactivity of the corner is also found to be higher, and followed by the edge and face sites, which is consistent with the observation for Au_{55}. This can be good news in the development of the force field for systems of GNP. As long as the force field could describe well the reactivity index across different interaction sites, *i.e.* corner sites are more reactive than the edge sites, their transferability across different sizes and shapes of GNP could be excellent, as shown in Chapter 2.

In addition, our results also indicate that the shifts in vibrational modes are also less dependent on the size and interaction sites on GNP. This has significant implication for prediction of interaction configurations of various organic molecules on GNP. A model based on GNP as small as Au_{32} would be able to provide reliable prediction on the orientation of organic molecules, without the needs to go for large GNP, hence saving significant amount of computational cost. However, larger GNP would still be required when more surface ligands are present.

The qualitative comparison between the calculated and experimentally collected IR spectra is currently ongoing (see Figure 3.26). The experimental spectra of benzoic acid, carried out by C. Sicard-Roselli) adsorbed on GNP have been collected with dried sample, where the solvent and surface ligand have presumably been removed completely. As such, benzoic acid has direct contact with the surface of GNP. However, different experimental conditions are still needed to be explored to study the orientation of benzoic acid on GNP, such as pH, concentrations of benzoic acid, and the size of GNP.

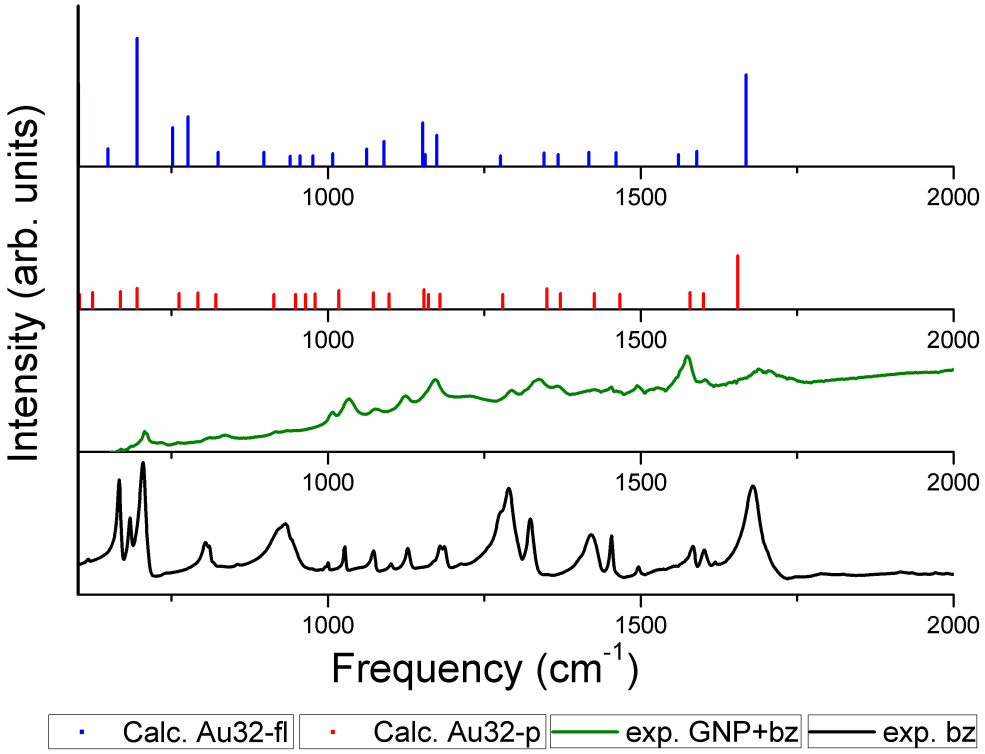

Figure 3.26: The comparison between calculated IR spectra of benzoic acid interacting with Au_{32} in flat and perpendicular configurations with 0.994 as scaling factor; and the experimental spectra for benzoic acid and benzoic acid adsorbed on GNP performed by C. Sicard-Roselli.

3.6 General Conclusion and Perspectives

In this chapter, the focus has been on the electronic structure of GNP-ligand interactions by employing DFT-level calculations. The nature of the interactions between the GNP and the organic ligands has also been qualitatively and quantitatively assessed, to find that the interaction has been dependent on the nature of the ligands, rather than the electronic properties of GNP. The quantitative analysis can eventually be used as a guide for physically motivated force field development for GNP. Additionally, the vibrational properties of the organic ligands are not quite sensitive to the size and shape of GNP, but rather they are dependent on the configuration and the interaction sites of the organic ligand. This has important implication on the simulation approach on the investigation adsorption geometry of biomolecules on GNP, as small GNP can be sufficient as the model for gold.

We have only considered a series of small organic ligands in this chapter, and going further, there are various directions that can be taken. Firstly, the study of amino acids and nucleobases will be of interest, because they are important building blocks of proteins, and DNA. Additionally, there are multiple functional groups present in the molecules, that can lead to multiple possible configurations on the surface of GNP. For this purpose, multiple optimization procedures will be necessary, and can be followed by the quantitative analysis of the nature of the interaction to investigate the preferred interaction sites. The study reported here can guide in preparing the initial configurations that are close to different local minima and also predicting the favored configuration, based on the interacting functional groups.

Secondly, the interaction of multiple ligands on the surface of GNP will be of interest as well. The ligand-ligand interactions eventually will have important effect on the adopted configurations, since both GNP-ligand and ligand-ligand interactions have to be maximized. Such model is more likely to represent experimental observation, especially at high concentration of ligands. Lastly, the inclusion of either explicit or implicit solvent will be important to investigate the competitive interaction between GNP-ligand, GNP-solvent, and ligand-solvent.

Bibliography

[1] X. Toledo-Fuentes, D. Lis and F. Cecchet, *J Phys Chem C*, 2016, **120**, 21399–21409.

[2] G. P. Szekeres and J. Kneipp, *Analyst*, 2018, **143**, 6061–6068.

[3] G. P. Szekeres and J. Kneipp, *Front Chem*, 2019, **7**, 2019.

[4] N. Schwenk, B. Mizaikoff, S. Cárdenas and A. I. Lṕpez-Lorente, *Analyst*, 2018, **143**, 5103–5111.

[5] C. P. Shaw, D. A. Middleton, M. Volk and R. Lévy, *ACS Nano*, 2012, **6**, 1416–1426.

[6] J. Gao, Y. Hu, S. Li, Y. Zhang and X. Chen, *Spectrochim Acta, Part A*, 2013, **104**, 41–47.

[7] G. Yao and Q. Huang, *J Phys Chem C*, 2018, **122**, 15241–15251.

[8] G. Geudtner, P. Calaminici, J. Carmona-Espíndola, J. M. d. Campo, V. D. Domínguez-Soria, R. F. Moreno, G. U. Gamboa, A. Goursot, A. M. Köster, J. U. Reveles, T. Mineva, J. M. Vásquez-Pérez, A. Vela, B. Zúñinga-Gutierrez and D. R. Salahub, *WIREs Comput. Mol. Sci.*, 2012, **2**, 548–555.

[9] T. Lu and F. Chen, *J Comput Chem*, 2012, **33**, 580–592.

[10] R. A. Boto, F. Peccati, R. Laplaza, C. Quan, A. Carbone, J.-P. Piquemal, Y. Maday and J. Contreras-García, *J Chem Theory Comput*, 2020, **16**, 4150–4158.

[11] D. G. A. Smith, L. A. Burns, A. C. Simmonett, R. M. Parrish, M. C. Schieber, R. Galvelis, P. Kraus, H. Kruse, R. Di Remigio, A. Alenaizan, A. M. James, S. Lehtola, J. P. Misiewicz, M. Scheurer, R. A. Shaw, J. B. Schriber, Y. Xie, Z. L. Glick, D. A. Sirianni, J. S. O'Brien, J. M. Waldrop, A. Kumar, E. G. Hohenstein, B. P. Pritchard, B. R. Brooks, H. F. Schaefer, A. Y. Sokolov, K. Patkowski, A. E. DePrince, U. Bozkaya, R. A. King, F. A. Evangelista, J. M. Turney, T. D. Crawford and C. D. Sherrill, *J Chem Phys*, 2020, **152**, 184108.

[12] T. D. Kühne, M. Iannuzzi, M. Del Ben, V. V. Rybkin, P. Seewald, F. Stein, T. Laino, R. Z. Khaliullin, O. Schütt, F. Schiffmann, D. Golze, J. Wilhelm, S. Chulkov, M. H. Bani-Hashemian, V. Weber, U. Borštnik, M. Taillefumier, A. S. Jakobovits, A. Lazzaro, H. Pabst, T. Müller, R. Schade, M. Guidon, S. Andermatt, N. Holmberg, G. K. Schenter, A. Hehn, A. Bussy, F. Belleflamme, G. Tabacchi, A. Glöß, M. Lass, I. Bethune, C. J. Mundy, C. Plessl, M. Watkins, J. VandeVondele, M. Krack and J. Hutter, *J Chem Phys*, 2020, **152**, 194103.

[13] F. Jensen, *Introduction to Computational Chemistry*, John Wiley & Sons, 2nd edn, 1999.

[14] P. Morgante and R. Peverati, *Int J Quantum Chem*, 2020, **120**, e26332.

[15] P. Hohenberg and W. Kohn, *Phys Rev*, 1964, **136**, B864–B871.

[16] W. Kohn and L. J. Sham, *Phys Rev*, 1965, **140**, A1133–A1138.

[17] J. P. Perdew and K. Schmidt, *AIP Conf Proc*, 2001, **577**, 1–20.

[18] J. P. Perdew, K. Burke and M. Ernzerhof, *Phys Rev Lett*, 1996, **77**, 3865–3868.

[19] J. P. Perdew, A. Ruzsinszky, G. I. Csonka, O. A. Vydrov, G. E. Scuseria, L. A. Constantin, X. Zhou and K. Burke, *Phys Rev Lett*, 2008, **100**, 136406.

[20] J. Tao, J. P. Perdew, V. N. Staroverov and G. E. Scuseria, *Phys Rev Lett*, 2003, **91**, 146401.

[21] Y. Zhao and D. G. Truhlar, *J Chem Phys*, 2006, **125**, 194101.

[22] A. D. Becke, *Phys Rev A*, 1988, **38**, 3098–3100.

[23] A. D. Becke, *J Chem Phys*, 1993, **98**, 5648–5652.

[24] C. Lee, W. Yang and R. G. Parr, *Phys Rev B*, 1988, **37**, 785–789.

[25] A. Goursot, T. Mineva, R. Kevorkyants and D. Talbi, *J Chem Theory Comput*, 2007, **3**, 755–763.

[26] T. H. Dunning, *J Chem Phys*, 1989, **90**, 1007–1023.

[27] R. Ditchfield, W. J. Hehre and J. A. Pople, *J Chem Phys*, 1971, **54**, 724–728.

[28] F. Weigend and R. Ahlrichs, *Phys Chem Chem Phys*, 2005, **7**, 3297–3305.

[29] P.-O. Widmark, P.-Å. Malmqvist and B. O. Roos, *Theor Chim Acta*, 1990, **77**, 291–306.

[30] S. Boys and F. Bernardi, *Mol Phys*, 1970, **19**, 553–566.

[31] E. v. Lenthe, E. J. Baerends and J. G. Snijders, *J Chem Phys*, 1993, **99**, 4597–4610.

[32] M. Douglas and N. M. Kroll, *Ann Phys-new York*, 1974, **82**, 89–155.

[33] G. Frenking, I. Antes, M. Böhme, S. Dapprich, A. W. Ehlers, V. Jonas, A. Neuhaus, M. Otto, R. Stegmann, A. Veldkamp and S. F. Vyboishchikov, *Rev Comp Ch*, 1996, 63–144.

[34] T. R. Cundari, M. T. Benson, M. L. Lutz and S. O. Sommerer, *Rev Comp Ch*, 1996, 145–202.

[35] P. Schwerdtfeger, M. Dolg, W. H. E. Schwarz, G. A. Bowmaker and P. D. W. Boyd, *J Chem Phys*, 1989, **91**, 1762–1774.

[36] R. B. Ross, J. M. Powers, T. Atashroo, W. C. Ermler, L. A. LaJohn and P. A. Christiansen, *J Chem Phys*, 1990, **93**, 6654–6670.

[37] J. W. Mintmire and B. I. Dunlap, *Phys Rev A*, 1982, **25**, 88–95.

[38] A. M. Köster, J. U. Reveles and J. M. del Campo, *J Chem Phys*, 2004, **121**, 3417–3424.

[39] A. M. Köster, J. M. del Campo, F. Janetzko and B. Zuniga-Gutierrez, *J Chem Phys*, 2009, **130**, 114106.

[40] R. I. Delgado-Venegas, D. Mejía-Rodríguez, R. Flores-Moreno, P. Calaminici and A. M. Köster, *J Chem Phys*, 2016, **145**, 224103.

[41] T. C. Allison and Y. J. Tong, *Phys Chem Chem Phys*, 2011, **13**, 12858–12864.

[42] R. Flores-Moreno, J. Melin, J. V. Ortiz and G. Merino, *J Chem Phys*, 2008, **129**, 224105.

[43] C. Morell, A. Grand and A. Toro-Labbé, *Chem Phys Lett*, 2006, **425**, 342 – 346.

[44] R. F. W. Bader, P. J. MacDougall and C. D. H. Lau, *J Am Chem Soc*, 1984, **106**, 1594–1605.

[45] R. F. W. Bader, *J Phys Chem A*, 1998, **102**, 7314–7323.

[46] P. L. A. Popelier and F. M. Aicken, *ChemPhysChem*, 2003, **4**, 824–829.

[47] R. Bianchi, G. Gervasio and D. Marabello, *Inorg Chem*, 2000, **39**, 2360–2366.

[48] A. D. Becke and K. E. Edgecombe, *J Chem Phys*, 1990, **92**, 5397–5403.

[49] Y. Bulteau, C. Lepetit and C. Lacaze-Dufaure, *Inorg Chem*, 2020, 13.

[50] M. Puyo, E. Lebon, L. Vendier, M. L. Kahn, P. Fau, K. Fajerwerg and C. Lepetit, *Inorg Chem*, 2020, **59**, 4328–4339.

[51] E. R. Johnson, S. Keinan, P. Mori-Sánchez, J. Contreras-García, A. J. Cohen and W. Yang, *J Am Chem Soc*, 2010, **132**, 6498–6506.

[52] Q. Zhao, *J Mol Model*, 2021, **27**, 132.

[53] Q. Zhao, *J Mol Model*, 2021, **27**, 328.

[54] R. Barzaga, M. P. Hernández, F. Aguilar-Galindo and S. Díaz-Tendero, *J Phys Chem C*, 2020, **124**, 9924–9939.

[55] Y. Lu, S. Zhang, C. Peng and H. Liu, *J Phys Chem C*, 2017, **121**, 24707–24720.

[56] M. Darvish Ganji, H. Tavassoli Larijani, R. Alamol-hoda and M. Mehdizadeh, *Sci Rep*, 2018, **8**, 11400.

[57] H. R. Abd El-Mageed and M. Taha, *J Mol Liq*, 2019, **296**, 111903.

[58] M. Prakash, G. Chambaud, M. M. Al-Mogren and M. Hochlaf, *J Mol Model*, 2014, **20**, 2534.

[59] S. Dapprich and G. Frenking, *J Phys Chem*, 1995, **99**, 9352–9362.

[60] M. García Hernández, A. Beste, G. Frenking and F. Illas, *Chem Phys Lett*, 2000, **320**, 222–228.

[61] U. Pidun and G. Frenking, *Organometallics*, 1995, **14**, 5325–5336.

[62] B. Jeziorski, R. Moszynski and K. Szalewicz, *Chem Rev*, 1994, **94**, 1887–1930.

[63] R. Staub, M. Iannuzzi, R. Khaliullin and S. N. Steinmann, *J Chem Theory Comput*, 2018, **15**, 265–275.

[64] S. Naseem-Khan, N. Gresh, A. J. Misquitta and J.-P. Piquemal, *J Chem Theory Comput*, 2021, **17**, 2759–2774.

[65] J. G. McDaniel and J. Schmidt, *J Phys Chem A*, 2013, **117**, 2053–2066.

[66] P. Clabaut, R. Staub, J. Galiana, E. Antonetti and S. N. Steinmann, *J Chem Phys*, 2020, **153**, 054703.

[67] R. Tandiana, N.-T. Van-Oanh and C. Clavaguéra, *Theor Chem Acc*, 2021, **140**, 118.

[68] F. Madzharova, Z. Heiner and J. Kneipp, *J Phys Chem C*, 2017, **121**, 1235–1242.

[69] F. Madzharova, Z. Heiner and J. Kneipp, *J Phys Chem C*, 2020, **124**, 6233–6241.

[70] R. G. Greenler, D. R. Snider, D. Witt and R. S. Sorbello, *Surf Sci*, 1982, **118**, 415–428.

[71] C. Schunke, D. P. Miller, E. Zurek and K. Morgenstern, *Phys Chem Chem Phys*, 2022, **24**, 4485–4492.

[72] M. Boczar, K. Szczeponek, M. J. Wójcik and C. Paluszkiewicz, *J Mol Struct*, 2004, **700**, 39–48.

[73] Y. J. Kwon, D. H. Son, S. J. Ahn, M. S. Kim and K. Kim, *J Phys Chem*, 1994, **98**, 8481–8487.

Chapter 4

SIMULATING SYSTEMS UNDER IRRADIATION

Contents

4.1 Introduction

The optical and radiosensitizing properties of GNP have led to their broad and promising applications in the medical field, in bioimaging, nanomedicine, and radiotherapy for cancer treatments.[1–6] Additionally, their plasmonic properties have been proposed to exhibit catalytic properties as well.[7] Despite the numerous research efforts dedicated to investigate these properties, the understanding of the relationship between the structure and properties in the context of optical properties is still limited. With various morphologies of GNP having been successfully synthesized experimentally so far, such as nanocages, nanorods, nanostars, nanoclusters, nanopyramids, nanoshells, etc.,[8] and the surface ligands having significant impact,[9] the challenge for a rational design of GNP with desired optical and physical properties is multi-dimensional and complex.

Meanwhile in the context of radiotherapy, the mechanisms behind the increase in the observed damage in DNAs in the presence of GNP are still under debate. While the interaction between ionizing radiation and GNP can result in ejection of electrons through physical processes such as photoelectric effect and Compton scattering, different contributions can be at play as well. Sicard-Roselli *et al.*, has developed a protocol to quantify the production of hydroxyl radical and secondary electrons, with the objective to investigate the relative increase in the production of reactive species under irradiation.[10] They have observed a four-fold increase in the presence of GNP, to which they propose that the unique water structure at the interface of GNP has significant contribution on top of the photoelectric effect. Verkhovtsev *et al.* has also proposed that the excitation of plasmons contributes to the radiosensitizing enhancement.[11] Additionally, there is a recently proposed explanation where the GNP could act as a catalyst in the production of hydroxyl radical instead.[12]

Therefore, molecular simulations can be a powerful tool to provide important atomistic insights into both the structure-property relationship and the mechanism behind the radiosensitizing properties of GNP. The development of real-time time-dependent DFT (RT-TD-DFT) has given us access into the dynamics of electrons in the presence of external perturbation at a very short time scale (attosecond domain).[13] This work has been conducted in collaboration with Aurélien de la Lande (ICP, Paris-Saclay Univ.), who has implemented the method in deMon2k program.[14] With RT-TD-DFT, his group has calculated and compared the absorption spectra of coumarine in gas phase and in solvent (in QM/MM framework). They have also simulated the collision of high energy charged particle with water and DNA, and followed the electronic response after the collision.[15–17] In this chapter, we are looking into the application of RT-TD-DFT in calculation of absorption spectra and simulation of radiosensitizing properties of GNP and water clusters.

4.2 Computational Methodologies

This chapter focuses on the simulation of systems in their excited state, which requires solving the time-dependent Schrödinger equation, or TD-KS within DFT framework, in contrast to what we have seen in previous chapters. All the calculations performed in this chapter have been done with RT-TD-DFT method, implemented in deMon2k program.[14]

4.2.1 Fundamentals of Time-Dependent DFT

The formulation of Time-Dependent DFT (TD-DFT) was first proposed by Runge and Gross, where they have rigorously proven that at any time, the information of the external potential can be obtained from the density.[18] The time-dependent Kohn-Sham formulation for TD-DFT is shown in Equation 4.1, with $\psi(t)$ corresponds to the wavefunction at time t, and $\rho(t)$ corresponds to the electron density at time t. The Hamiltonian can be further written as Equation 4.2, with the $v_{ext}(t)$ corresponds to the external potential felt by the electrons, that includes the nuclear potentials, and additional potentials from perturbation introduced by electromagnetic field or projectiles. The second and third terms correspond to the kinetic operators of the electrons, and the last term corresponds to the exchange correlation potential, which is independent of time (adiabatic approximation). The KS density of the system is shown in Equation 4.3.

$$i\frac{\partial \psi_i(r,t)}{\partial t} = \hat{H}(r,t)\psi_i(r,t) \tag{4.1}$$

$$\hat{H}(r,t) = v_{ext}(r,t) - \frac{1}{2}\nabla^2 + \int \frac{\rho(r',t)}{|r-r'|}dr' + v_{xc}[\rho(r,t)] \tag{4.2}$$

$$\begin{aligned} \rho(r,t) =& \sum_i^{all} n_i \psi_i^*(r,t)\psi_i(r,t) \\ E[\rho(r,t)] =& \int v_{ext}(r,t)\rho(r,t)dr + \sum_i^{all}\int n_i\psi_i^*(r,t)(-\frac{1}{2}\nabla^2)\psi_i(r,t)dr \\ &+ \frac{1}{2}\int\int\frac{\rho(r,t)\rho(r',t)}{|r-r'|}drdr' + E_{xc}[\rho(r,t)] \end{aligned} \tag{4.3}$$

4.2.2 Real-Time Propagation

The Real Time (RT) framework of TD-DFT numerically propagates in time the electron density based on Liouville-von Neumann equation of motion.[19] . It gives access to electron dynamics on the order of atto to femtoseconds, hence allowing simulation of ultrafast processes. The formal solution for TD-DFT is shown in Equation 4.4. With discrete time steps, the propagation of the electron densities through a product of time-evolution operators are shown in Equation 4.5, with $U(t, t_0)$ refers to the time evolution operator and T refers to the time-ordering operator, ensuring the operators for later times always come before the operators for the earlier time, and P corresponds to the density matrix.

$$i\frac{\partial P(t)}{\partial t} = [H(t), P(t)] \tag{4.4}$$

$$\begin{aligned} P(t) =& U(t,t_0)P(t_0)U^{\dagger}(t_0,t) \\ U(t,t_0) =& \prod_{i=0}^{N-1} U(t_i+\Delta t, t_i) \\ U(t_i+\Delta t, t_i) =& Texp{-}i\int_{t_i}^{t_i+\Delta t} H'(\tau)d\tau \end{aligned} \tag{4.5}$$

Different algorithms have been proposed for the propagators, such as the Euler and the Magnus propagators. The Euler propagator is based on Lagrange's mean value theorem, and is shown in Equation 4.6. However, the norm preservation is not guaranteed throughout the propagation.

$$P(t_i+\Delta t) = P(t_i) - i[H(t_i, P(t_i)] * \Delta t \tag{4.6}$$

Alternatively, Magnus propagator expresses time-unordered exponential by a series of nested commutators (see Equation 4.7). Inclusion of the second order in the series (Ω_1), generally called second order Magnus propagator (SOMP), requires the knowledge of the KS potential at time $t + \Delta t/2$. Inclusion of additional series is possible, but it comes at the expense of much higher computational cost (up to 3 times), because it will require addition knowledge of KS potential at $t + [(1/2) - \sqrt{3}/6]\Delta t$, and at $t + [(1/2) + \sqrt{3}/6]\Delta t$. But, inclusion of this additional series allows larger time step as compared to the SOMP. Since previous study by Cheng *et al.* have demonstrated that SOMP offers a good balance between performance and stability, SOMP will be applied in this chapter.[20]

$$\begin{aligned} Texp(-i\int_{t_i}^{t_i+\Delta t} H'(\tau)d\tau) =& e^{W} = e^{\Omega_1+\Omega_2+\Omega_3\dots} \\ \Omega_1(t+\Delta t, t) =& -i\int_{t}^{t+\Delta t} H'(\tau)d\tau \\ =& -iH'(t+\frac{\Delta t}{2})\Delta t \end{aligned} \tag{4.7}$$

As seen in Equation 4.7, SOMP propagator requires the information on the KS potential at $H'(t + \Delta t/2)$, which is unknown. To compute that, either iterative or propagator corrector methods, illustrated in Figure 4.1 and Figure 4.2 respectively, have been proposed.

For each step of time propagation, the iterative method starts with extrapolation of $H(t_n)$ and $H(t_{n-1})$ to obtain $H^0(t_n + \Delta t/2)$ (*i.e.* iteration 0). From this midpoint potential, the density is then propagated by SOMP from t_n to $t_n + \Delta$ t. Then the KS potential of $H^0(t_n + \Delta t)$ can be built. The midpoint potential $H^1(t_n + \Delta t/2)$ can then be calculated again from $H(t_n)$ and $H^0(t_n + \Delta t)$ (*i.e.* iteration 1), based on which the $P(t_n)$ is propagated again to $P^1(t_n + \Delta t)$ to obtain KS potential at ($t_n + \Delta t$). Then, the H^i at $(t_n + \Delta t/2)$ can be interpolated again from $H(t_n)$ and $H^i(t_n + \Delta t)$. These steps are iterated until the convergence criterion is reached. Then, upon convergence, this whole iterative step is repeated again until the desired number of steps has been reached. This scheme can potentially be computationally demanding, due to the multiple calculations of KS potential and the SOMP potential.

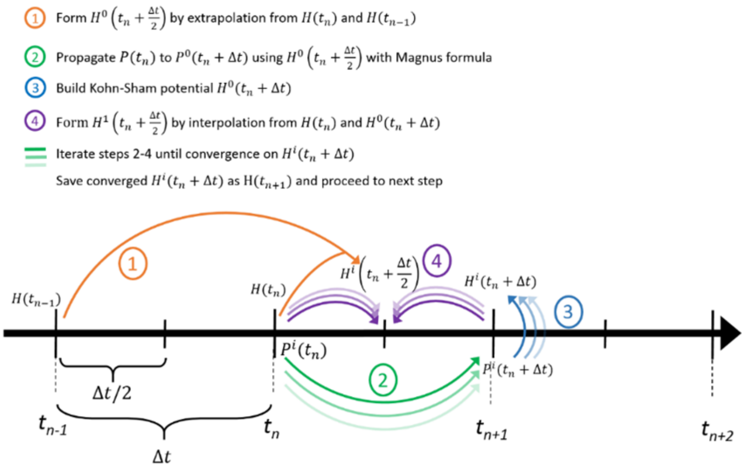

Figure 4.1: The schematic diagram of iterative methods of SOMP, adapted from reference.[21]

Meanwhile, the propagator-corrector scheme, proposed by Van Voorhis *et al.*, begins with the predictor steps and followed by the corrector steps.[20] In the predictor step, the $H(t_n + \frac{\Delta t}{4})$ is extrapolated from $H(t_{n-1} + \frac{\Delta t}{2})$ and $H(t_{n-2} + \frac{\Delta t}{2})$. The density is then propagated by SOMP to $P(t_n + \frac{\Delta t}{2})$ with the now known $H(t_n + \frac{\Delta t}{4})$. Next, the corrector step kicks in, with building the KS potential at $t_n + \frac{\Delta t}{2}$ from the density and followed by propagation of the density from t_n to $t_n + \frac{\Delta t}{2}$ using the now known $H(t_n + \frac{\Delta t}{2})$. And the steps are repeated until the desired time has been achieved. This scheme involves less evaluation of the KS and SOMP potential, which demands less computational effort as compared to the iterative method. Additionally, the performance of PC algorithm generally leads to stable propagation.

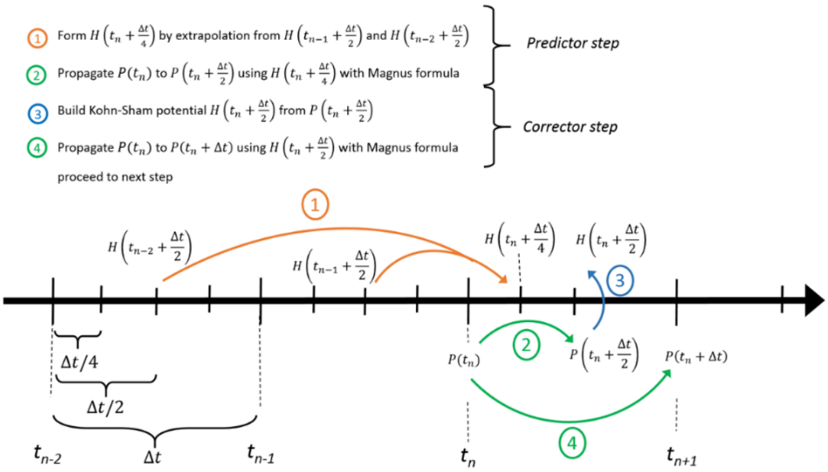

Figure 4.2: The schematic diagram of propagator-corrector methods of SOMP, adapted from reference.[21]

As for the evaluation of the exponential term in SOMP equation, which can be time consuming, different solutions, such as diagonalization, polynomial expansions, Krylov subspace projection, splitting projection, have been proposed.[22] Polynomial expansions typically offers an advantage in terms of the scaling problem, and one such example is the Taylor expansion (Equation 4.8). The number of the terms, n, doesn't need to reach infinity, but it has to be sufficiently large to achieve convergence.

$$e^W = \sum_{n=0}^{\infty} \frac{1}{n!} W^n \tag{4.8}$$

4.2.3 Imaginary Time Propagation

Within the RT-TD-DFT framework, the propagation with imaginary time has been proposed as an alternative and robust method to obtain convergence of electronic states into its lowest energy state, called IT-TD-DFT.[23,24] At any time t, the Hamiltonian contains the information of the electronic ground state, and propagating in imaginary time results in amplification of the low energy eigenstates of the Hamiltonian. The propagation eventually leads to the continuous decrease of the energy of the system until it reaches a convergence to the electronic ground state. This imaginary propagation can be achieved by substituting the t in Equation 4.5 with $-i\tau$, where τ is real. However, the imaginary-time propagation causes the norm of the wave function to change over time. Therefore, the orthonormalization of the orbitals has to be performed at each propagation step to maintain the orthonormality.

4.2.4 Simulation Setup in deMon2k

Both RT-TD-DFT and IT-TD-DFT have been implemented in deMon2k code,[14] which utilizes linear combination of atomic orbitals (LCAO) and auxiliary DFT (ADFT) framework. The details of the two frameworks have been given in detail in the methodology section of Chapter 3. The simulations in this chapter have been performed with PBE functional, with relativistic ECP and its associated basis sets for 11 valence electrons describing the gold atoms, unless otherwise mentioned.

The practical consideration for running both RT-TD-DFT and IT-TD-DFT will include the choice of time step for the propagation, the choice of propagator, the exponential term for the Taylor expansion, on top of the other typical parameters for DFT calculation. To ensure stable propagation, the starting density is preferably the ground state, and the convergence criteria for the SCF step are set to 1.10^{-10} Hartree and the auxiliary density to 1.10^{-7} Hartree. A tight grid of 1.10^{-7} is sufficient to ensure the stability of the propagation. Time step of 1 attosecond is generally small enough for stable propagation with SOMP-PC scheme and with Taylor expansion ($N = 60$) to solve the exponential term of SOMP.

In RT-TD-DFT, depending on properties of interest, different external perturbations can be added, such as a classical charged projectile or electric field. The properties of the charged projectile can be defined at the beginning of the simulation. The mass of the projectile can be set as desired (1 for proton), and the kinetic energy of the projectile can be varied in the range of keV to MeV. The position and direction of the projectile can also be set, either along the x, or y, or z axis, or even diagonally to the center of mass of the system. The position of the projectile has to initially be sufficiently far away (50 Å away, for example) from the system to minimize the interaction between the projectile and the target at the beginning of the simulation. The external potential of the projectile can be calculated with Equation 4.9, with Φ_{proj} corresponds to the potential created by the projectile with charge, q_{proj} and velocity, v_{proj}, and R corresponds to the distance between the projectile and the electron density of the target.[21]

$$
\begin{aligned}
E^{proj} &= -\int \rho(r,t)\Phi_{proj}(r,t)dr + \sum_{A} Z_A R_A \Phi_{proj}(r,t) \\
\Phi_{proj}(r) &= \frac{q_{proj}}{R[1 - \frac{v_{proj}^2 sin^2\Theta}{c^2}^{1/2}} = \frac{\gamma q_{proj}}{R}
\end{aligned}
\tag{4.9}
$$

To introduce electric field as the external perturbation to the system, four different shapes of electromagnetic wave have been implemented, which are Gaussian pulses (squared sinusoidal pulse), Dirac pulses (infinitely narrow pulse), squared sinusoidal pulses, and linear ramp. Gaussian and Dirac pulses bring the systems to low lying excited states, while the linear ramp corresponds to strong ionizing laser field. The external potential of the electric field can be calculated based on the interaction between electron cloud and the electric field, which is described in Equation 4.10, with μ representing the dipole moment of the system, and $\mathbf{F(t)}$ representing the electric field. The external potential is, then, the first derivative of the interaction energy with respect to the electron density, as shown in Equation 4.10. The electric field can be further expressed as Equation 4.10, with $\mathbf{F_{max}}$ representing the maximum field strength, X representing the enveloped of the pulse, d corresponding to the direction of the field, and ω representing the frequency of the light.

$$\begin{aligned} E^{efield} &= -\mu(t)F(t) \\ \frac{\delta E^{efield}}{\delta P_{\mu\nu}} &= F(t)D_{\mu\nu} \\ F(t) &= F_{max}X(t)cos\omega td \end{aligned} \tag{4.10}$$

4.2.5 Calculation of Electronic Stopping Power

When charged particles penetrate matters, energy transfer occurs as a result of their collision with nuclei and electrons of the matters. This energy transfer, measured relative to the distance travelled by the projectile is referred to the stopping power. At low kinetic energy of the projectile, below keV energy, the collision with the projectile leads to nuclear stopping (increased energy of the target nuclear). When high kinetic energy projectile interacts with matter (between keV to MeV range), however, it will lead to excitation at the electronic level at a very short timescale, *i.e.* electronic stopping. The RT-TD-DFT method, within the adiabatic and frozen nuclei framework, allows the simulation of this process. The frozen nuclei framework can be justified by the assumption that at a very short timescale (a few femtoseconds), the nuclear motion, as a result of collision, is not yet induced. However, there are ongoing works to simulate the nuclear movement in response to the collision, *i.e.* with Ehrenfest dynamics.[25]

There are different ways of calculating the electronic stopping power, and in this chapter, our calculation is based on the instantaneous method.[26] By definition, the electronic stopping power is the average of the change in energy, with respect to the distance travelled by the projectile in the matter. Considering that in a typical simulation setup, the projectile is initially placed at a 50 Å away from the center of mass of the target matter, and that the projectile is leaving the matter eventually. The enter and exit distances of the projectile considered as the start and ending for the calculation of stopping power have been set to 1 Å. The average of the deposited energy over the distance travelled by the projectile is considered as the electronic stopping power. Several trajectories have to be calculated to obtain a convergence in the electronic stopping power at a particular energy of the projectile.

4.2.6 Calculation of Absorption Spectra

The absorption spectra can be calculated by performing Fourier transformation on the time-dependent dipole moments to obtain dipole strength function (S), shown in Equation 4.11.

$$\begin{aligned} \mu(t) &= Tr[DP(t)] \\ S(\omega) &= \frac{4\pi\omega Tr[Im\alpha(\omega)]}{3c} \\ \mu_i(\omega) &= \alpha_{ii}E_i(\omega) \end{aligned} \tag{4.11}$$

with $\mu(t)$ corresponding to time-dependent dipole moment, D as dipole matrix, and P as density matrix, α (ω) corresponding to the polarizability in frequency domain that can be obtained by the relation between electric field (E_i) and dipole moment (μ_i) as shown in Equation 4.11.

4.3 Validating the RT-TD-ADFT Framework

We start our investigation by first validating the ADFT framework in RT-TD-DFT simulation of collision of high kinetic energy projectile (proton) with lithium clusters. This work has been published as a part of a more thorough evaluation in Theor. Chem. Acc.[27] The properties of interest are the energy deposition and the electronic stopping power. The geometry of lithium cluster, consisting of 62 atoms, has been taken from Maliyov *et al.*, and used without further optimization.[28] Their work has demonstrated that electronic stopping power is sensitive to the choice of basis set describing atoms that are close to the path of the projectile. Therefore, the lithium atoms close to projectile path, *i.e.* 18 atoms, are described with cc-pVTZ basis set, and the rest is described with cc-pVDZ to reduce the computational costs. A series of increasingly more complex auxiliary functions, *i.e.* GenA2, GenA2*, GenA3, and GenA3*, has been tested for both RT-TD-DFT and RT-TD-ADFT frameworks. Out of the series, GenA3* will be considered as the most accurate and hence, the reference calculation. The criteria for the grid has been set to 1.10^{-8} a.u. to ensure stability during the dynamics. The SCF and CDF criteria have been set to 1.10^{-9} a.u. and 5.10^{-7} a.u., respectively. The SOMP-PC has been used as propagator, with the number of Taylor expansion set to be 65, and time step of 1 attosecond. The electronic stopping power has been calculated from one trajectory as a function of the kinetic energy of proton (0.005, 0.025, 0.05, 0.1, 0.5, and 1.0 MeV) for each of the auxiliary function.

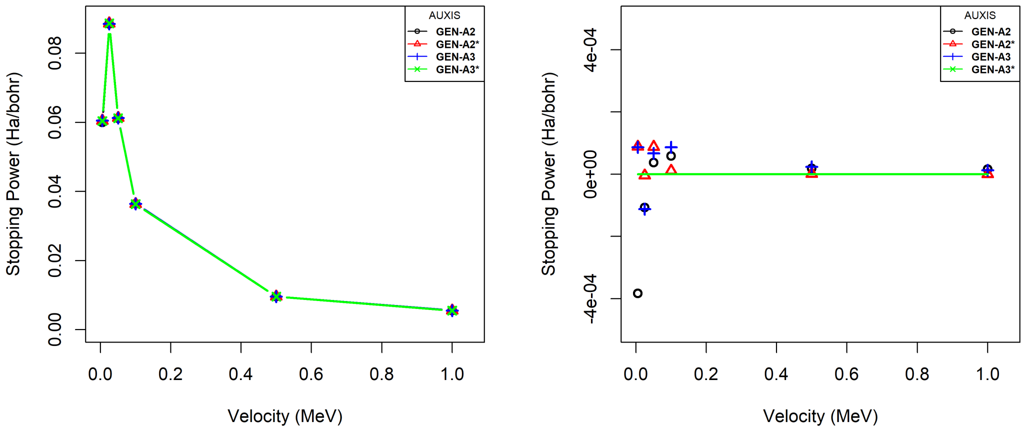

Figure 4.3: (left) The electronic stopping power of proton in lithium as a function of the kinetic energy of the projectile calculated with RT-TD-ADFT; (right) The difference between the stopping power obtained with the GenA2, GenA2*, and GenA3 with GenA3* as the reference

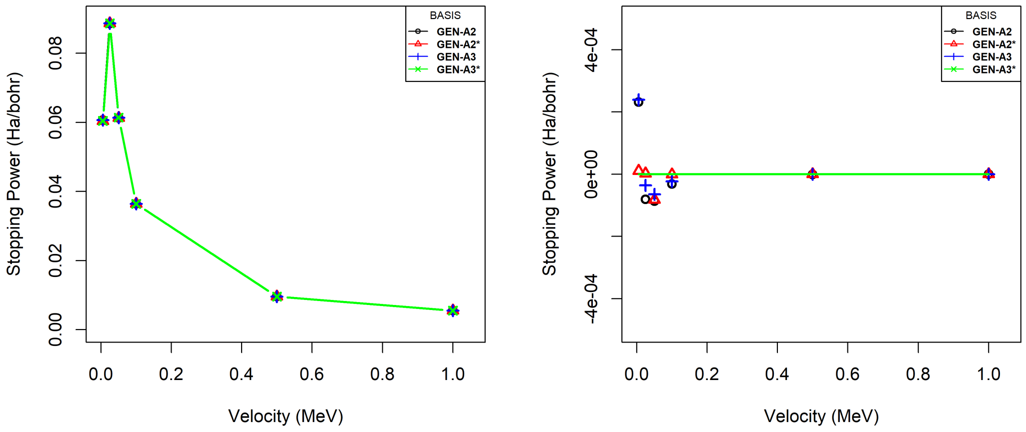

Figure 4.4: (left) The electronic stopping power of proton in lithium as a function of the kinetic energy of the projectile calculated with RT-TD-DFT; (right) The difference between the stopping power obtained with the GenA2, GenA2s, and GenA3 with GenA3s as the reference

The electronic stopping power curves calculated with RT-TD-ADFT for each of the auxiliary functions are shown to be overlapping with one another, as seen in Figure 4.3 (left). Figure 4.3 (right) shows the energy difference between the stopping power curves of each set with respect to the GenA3* function. The difference is in the scale of 10-4 Ha/bohr, which illustrates the insensitivity of the electronic stopping power to the auxiliary functions used. This has also been shown in terms of the energy deposition (dE/dt) in Figure 4.5 (left). Similarly, the electronic stopping power curves calculated with RT-TD-DFT framework for each of the auxiliary functions are overlapping, as seen in Figure 4.4 (left), with the difference with GENA3* function is also in the range of 10-4 Ha/bohr (Figure 4.4 right). Moreover, it is worth mentioning that the RT-TD-DFT framework takes around 3 to 4 times as long for the calculation. Therefore, the performance of RT-TD-ADFT has significantly cut the computational cost, giving access to calculation for larger systems. From here onwards, we are performing the simulations with the RT-TD-ADFT framework.

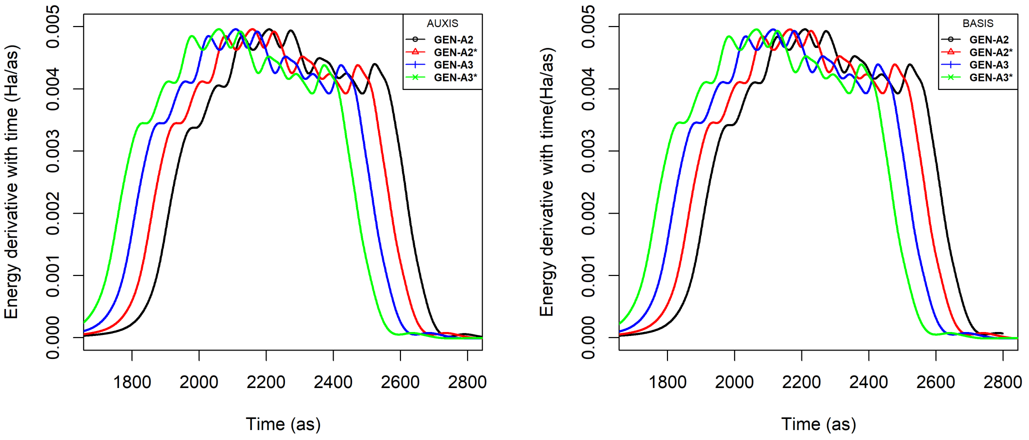

Figure 4.5: The dE/dt calculated with the series of auxiliary functions at RT-TD-ADFT (left) and RT-TD-DFT (right) as the projectile of 0.025 MeV travel through the Lithium cluster, the plots are slightly shifted in the x-axis for clarity purposes.

4.4 Investigating the Dependence of Water Electronic Stopping Power on Basis Set

We have mentioned earlier that the calculation of electronic stopping power is sensitive to the choice of basis set, for which Maliyov *et al.* has proposed an algorithm for basis set optimization that is targeted to maximize the electronic stopping power.[28] Meanwhile, Coccia *et al.* proposed that basis sets capable of describing the oscillating function in continuum are crucial in the calculation of systems in excited state.[29] They have employed such basis set to obtain an accurate computation of high-harmonic generation spectra. A recent report on the fitting of continuum wavefunctions with complex Gaussians has demonstrated its superiority in calculating (photo)ionization of hydrogen.[30] Still another study reported that basis sets augmented with truncated GTOs generated by completeness-optimization scheme, result in an improved accuracy in plasmonic calculations of nanoparticles.[31] In the context of electronic stopping power calculation with RT-TD-DFT, mostly plane wave approach has been used. Therefore, in this section, our objectives are two fold, which are the generation of continuum basis sets for Gaussian type orbitals (GTO) suggested by Coccia's work, and followed by the evaluation of these basis sets for the calculation of electronic stopping power. Within the context of this thesis, our choice of model system is water, before extending our investigation to GNP systems.

4.4.1 Optimization of Continuum Basis Sets

The universal Gaussian continuum basis set has firstly been proposed by Kaufmann *et al.* based on L^2 approximation of the Slater-type functions.[32] The motivation of generating such basis sets was the fact that despite the suitability of Gaussian basis sets on describing the bound states, they do not describe the essential nodal structure and large spatial domain of continuum orbitals. Subsequently, Faure *et al.* proposed GTOBAS program to fit Gaussian-type orbitals to Bessel and Coulomb functions over a finite range, using the method of Nestmann and Peyerimhoff.[33] The generated basis sets have been applied for calculations of bound and continuum states of charged molecules, such as C_nH^- and N_2^+.[34] In this chapter, the GTOBAS program is used to generated continuum GTOs.[33]

The optimization of the exponents of Gaussian functions (α_i) to fit continuum functions ($u_{hl}(r_k)$) is done by minimizing the Equation 4.12, with N as the number of continuum functions and n being the number of Gaussian exponents, and the coefficients c_{hi} determined by a least-squared fit. The D term has been added to avoid two different α_i converging towards the same value, and calculated with Equation 4.12. The g corresponds to the boundary radius. The variable input parameters for the optimization includes the upper bound for the eigenvalues and the boundary radius. A series of continuum basis sets for hydrogen and oxygen atoms has been generated, varying the boundary radius, between 3, 4, 8, and 12 Bohrs, while keeping the upper bound eigenvalues to 5 Rydberg. Gaussian exponents up to $l = 2$ are generated.

$$\begin{aligned} F_{l,N} &= \sum_{h=1}^{N} \frac{\sum_k [\sum_{i=1}^{n} c_{hi} r_k^l exp(-\alpha_i r_k^2) - u_{hl}(r_k)]^2}{\sum_k [u_{hl}(r_k)]^2} + D(\alpha_1, .., \alpha_n) \\ D(\alpha_1, ..., \alpha_n) &= \sum_{i=2}^{n} \sum_{j=1}^{i-1} exp(-gx|\frac{\alpha_i}{\alpha_j} - \frac{\alpha_j}{\alpha_i}|) \end{aligned} \tag{4.12}$$

4.4.2 Evaluation of the Continuum Basis Set on Water

Following the work of Maliyov *et al.*, we have taken the Dunning basis sets family as the reference basis sets.[28,35] Our model system for the evaluation of the continuum basis set is an isolated water molecule and a water cluster. The optimized Gaussian functions are then augmented to the basis sets of water, and the corresponding energy and density of states of the system are computed and compared in Table 4.1. For comparison purposes, the basis set for hydrogen has always been kept constant, *i.e.* cc-pVDZ for the no-GTO system, and cc-pVDZ-R3-L2-5 for the GTO augmented systems, while varying the basis set of oxygen atom.

Without augmentation with the GTO basis sets, the number of orbitals for water molecule has increased as we go across the series of the Dunning's family (see Figure 4.6). The density of states between 0 - 10 Ha, has been plotted, and the virtual orbitals at this range are discretely distributed for the cc-pVDZ. Going up the series of the basis set, there are increasingly more orbitals within this energy range, though they are still quite discretized.

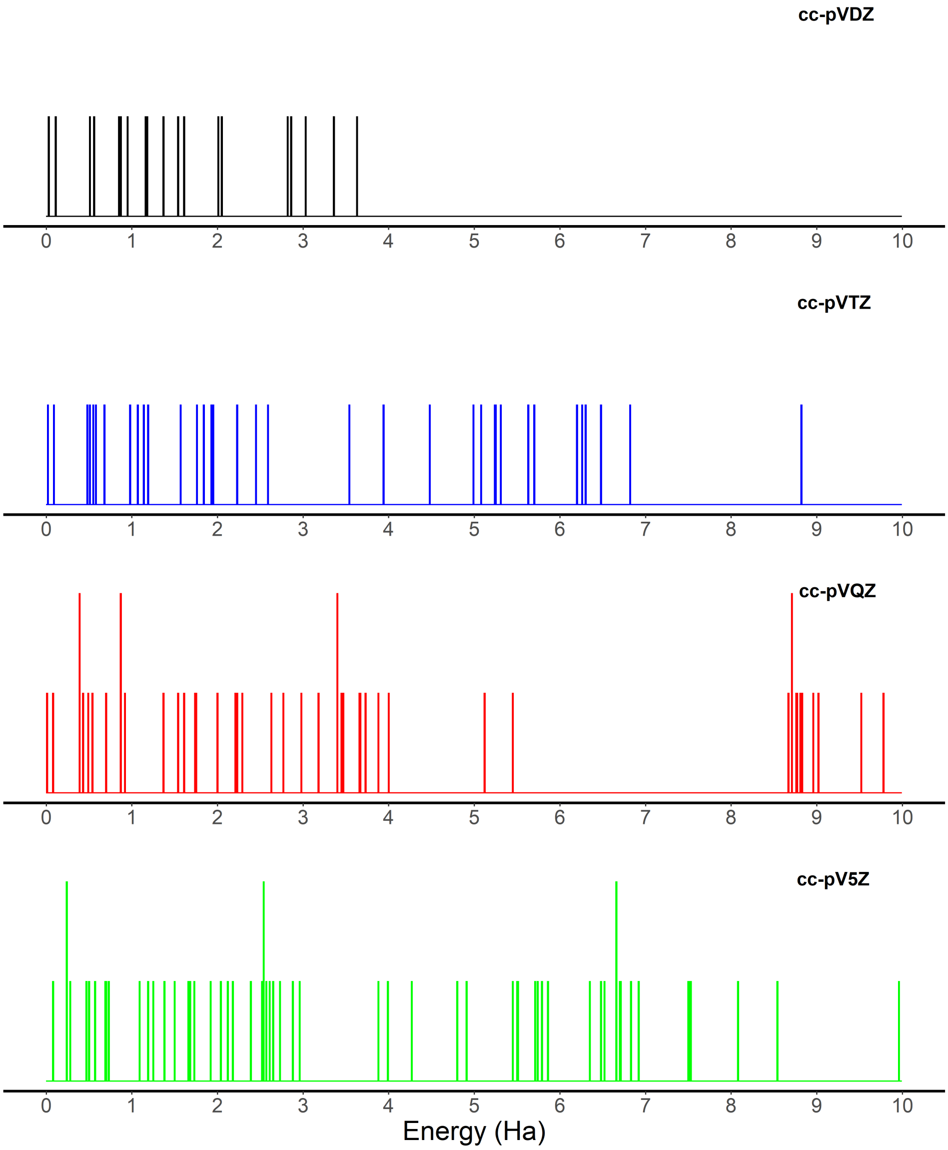

Figure 4.6: The density of states of water molecule described with the family of Dunning basis set, cc-pVXZ, with X=D, T, Q, and 5.

We subsequently augment the GTO basis set onto cc-pVQZ, and observe a significant increase in the number of orbitals, from 80 to 154 (see Table 4.1). We then evaluate the variation of the number of orbitals with respect to the boundary of the GTO-RX, with X = 3, 4, 8, 12, and 15 Bohr respectively. An increase in the number of orbitals has been observed, with the increase in the boundary of the GTO (see Figure 4.7). With the augmentation of GTO-R3, there is a significant increase in the number of virtual orbitals, in particular below 5 Ha, as compared to standard cc-pVQZ. Moreover, these orbitals are close in energies, resulting in a more continuous orbitals within this range. As the increasingly larger GTO-RX is augmented to cc-pVQZ, more orbitals are packed into the energy range below 5 Ha.

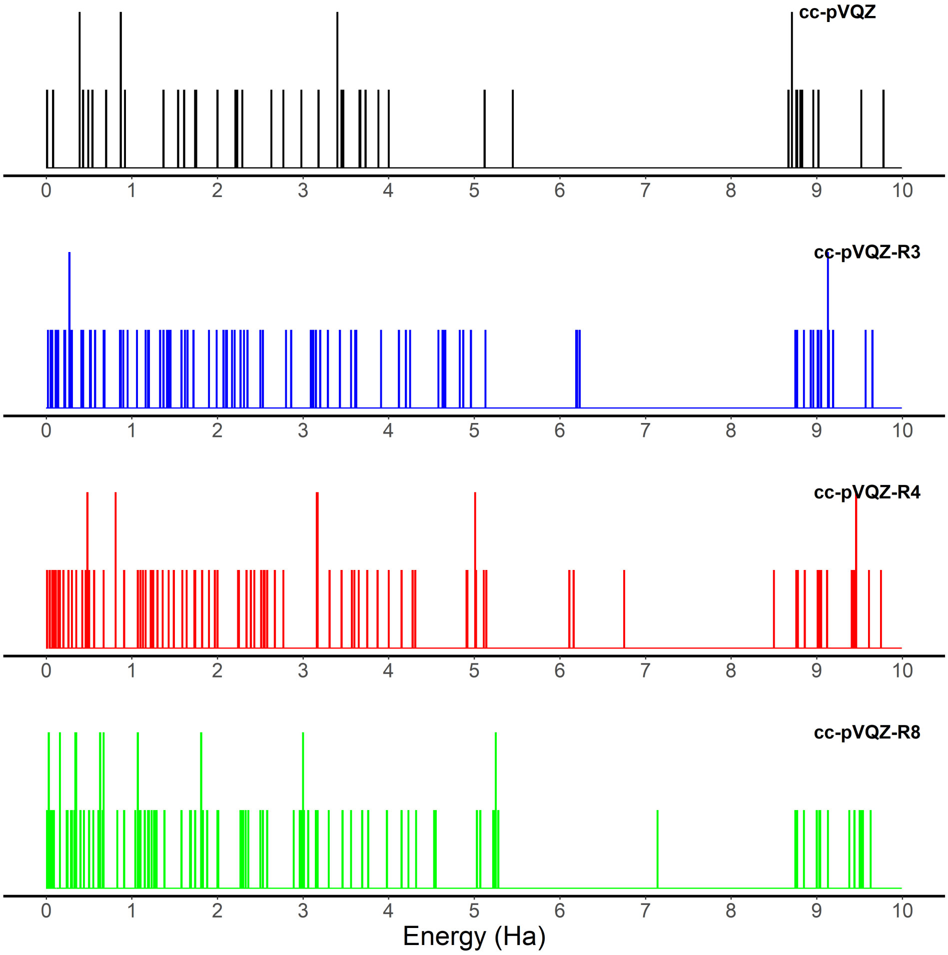

Figure 4.7: The density of states of water molecule described with the family of Dunning basis set, cc-pVQZ augmented with GTO-Rn, n=3, 4, and 8.

When diffuse basis sets augmented with GTO-R3 are used, however, the increase in the number of orbitals introduced by the diffuse functions is not significant, from 154 with cc-pVQZ-R3 to 157 with aug-cc-pVQZ-R3. Since the accuracy of stopping power is sensitive also on the incompleteness of basis sets, therefore, the basis sets with largest number of orbitals should be ideal. However, this comes

Table 4.1: The total energy and number of orbitals calculated for water molecule with the series of basis sets.

System	Basis Set	Total Energy (Hartree)	No. of Orbitals
Water			
No-GTO	cc-pVDZ	-76.336643	25
	cc-pVTZ	-76.366559	45
	cc-pVQZ	-76.377303	80
	cc-pV5Z	-76.385402	136
GTO-RX	cc-pVQZ-R3-L2-5	-76.386829	154
	cc-pVQZ-R4-L2-5	-76.394595	164
	cc-pVQZ-R8-L2-5	-76.403804	192
	cc-pVQZ-R12-L2-5	-76.39932	237
	cc-pVQZ-R15-L2-5	-76.38921	240
GTO-R3	aug-cc-pVDZ-R3-L2-5	-76.369272	100
	aug-cc-pVTZ-R3-L2-5	-76.382909	123
	aug-cc-pVQZ-R3-L2-5	-76.387543	157
	aug-cc-pV5Z-R3-L2-5	-76.389465	204
Water Cluster			
No-GTO	cc-pVDZ	-3720.009834	3700
	cc-pV5Z	-3720.160524	4144
GTO-RX	cc-pVDZ-R3-L2-5	-3720.120918	3996
	cc-pVDZ-R8-L2-5	-3720.176061	4148

with a significant increase in the computational cost as well. At this stage, the best choice of basis sets is not yet straightforward.

4.4.3 Evaluation of the Continuum Basis Set on Water Cluster

Considering that the electronic stopping power is the properties of interest, the evaluation of the performance of these basis sets needs to be carried out with respect to that calculation. A cluster of water, consisting of 49 molecules, has been selected as the model system. The geometry of the water cluster has been taken from an equilibrated water box in force field-based molecular dynamics simulation. Considering the high computational cost of describing all 49 water molecules with augmented GTOs, only 4 water molecules are augmented with GTOs. Maliyov *et al.* have, after all, concluded that the atoms closest to the path of the projectile need to be described with the largest basis set.[28] These four water molecules are found to be closest to the path of the projectile, and are represented by yellow balls in Figure 4.8. At all cases, the rest of the water molecules will be described with cc-pVQZ for oxygen, and cc-pVDZ for hydrogen. Only the basis sets of the 4 water molecules are varied for the testing purposes.

Similarly, the density of states of the water cluster has been calculated, and only selected basis sets are reported in Table 4.1 and Figure 4.9. When the four water molecules highlighted before are described with cc-pVDZ, there is a large number of virtual orbitals within the range of 0 - 10 Ha. These virtual orbitals are the result of linear combination of the atomic orbitals of all 49 water molecules. A significant increment within this range is observed when cc-pV5Z has been used to describe the four water molecules. As GTO-R3 is augmented on the standard cc-pVDZ basis set, the total number of orbitals is approaching the system described with cc-pV5Z, and the plot of density of states is also quite similar to cc-pV5Z. Therefore, in all these cases, there is a dense distribution of low lying virtual orbitals within the range of 0 - 10 Ha.

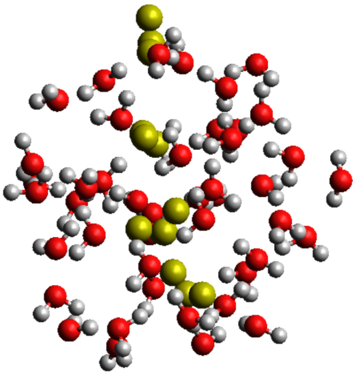

Figure 4.8: The schematic representation of water cluster with the yellow balls corresponding to the water molecules augmented with GTO basis sets

Subsequently, the electronic stopping power of water cluster is calculated, while varying the basis set of the four water molecules. The simulation has been performed by introducing a proton projectile (mass = 1), placed at 50 Å away from the center of mass of water cluster. The energy of the projectile is set to either 0.075 MeV or 1 MeV. The electron dynamics has been propagated with time step of 1.0 attosecond with SOMP-PC, and number of Taylor expansion set as 65. The calculation has been performed with LDA functional and GEN-A2* auxiliary function. To ensure the stability of the propagation, a tight grid has been used, *i.e.* 1.10^{-7} a.u..

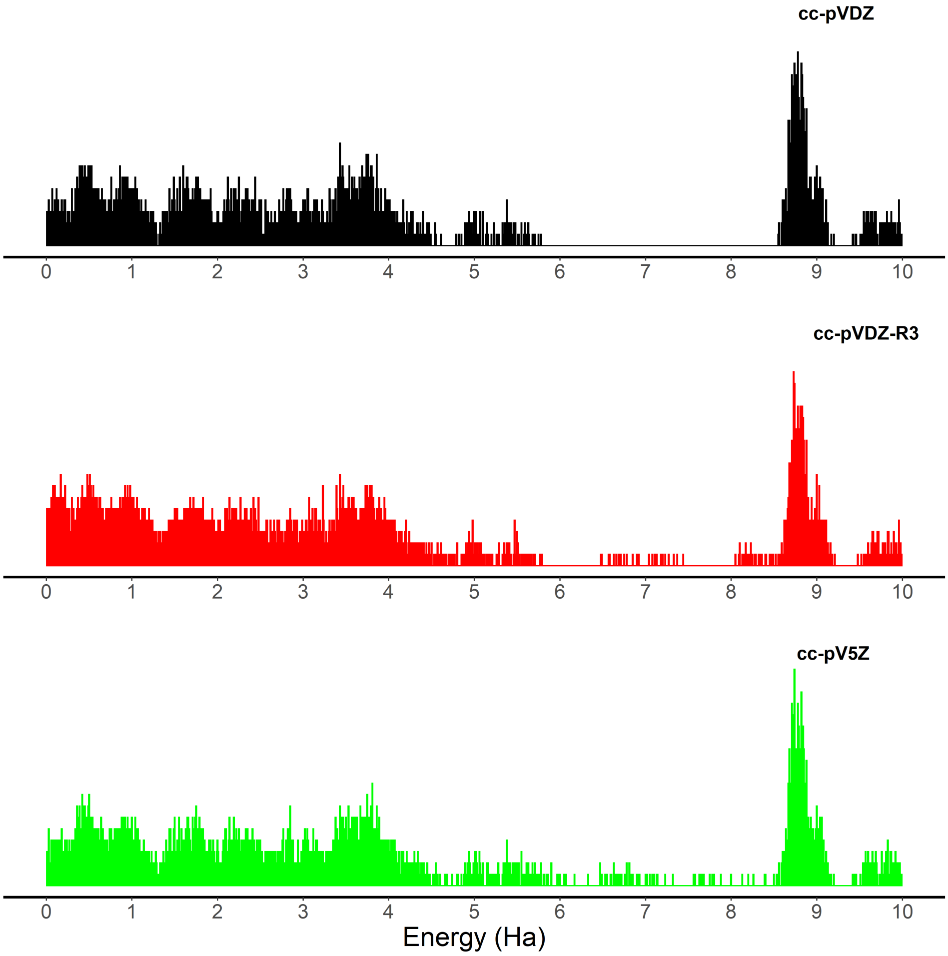

Figure 4.9: The density of states of water cluster described with cc-pVDZ, cc-pVDZ-R3, and cc-pV5Z.

Firstly, the electronic stopping power calculated with the Dunning's series of basis set, cc-pVXZ, X= D, T, Q, and 5, is compared. Figure 4.10 shows the stopping power at 0.075 MeV and 1 MeV. In this set of simulation, the oxygen atom of the four water molecules is described with cc-pVXZ, while the hydrogen atom is described with cc-pVDZ at all time. The calculated electronic stopping power has progressively increased across the series for both velocities. However, a convergence has not yet been reached.

We subsequently calculate the stopping power of the cluster with GTO-R3 augmented basis sets on cc-pVXZ of O, and keeping the H atom described by cc-pVDZ-GTO-R3. There is a significant increase in the calculated stopping power with the addition of GTO for 0.075 MeV, and a modest increase for 1 MeV. Additionally, the calculated stopping power seems to be converging better for GTO augmented basis set compared to the standard one. The addition of diffuse functions to the Dunning basis sets, aug-cc-pVXZ, X=D, T, Q, 5, further adds a bit more energy, as compared to the non-diffuse sets. Hence, the result shows that adding GTO on the Dunning's basis set results in higher electronic stopping power, while further addition of diffuse functions does not have significant effect. The increase in stopping power is presumably owing to not just the additional number of virtual orbitals, but also better description of the continuum orbitals. From these comparisons, cc-pVDZ + GTO-R3 seems to be a good compromise between computational cost and accuracy of the stopping power.

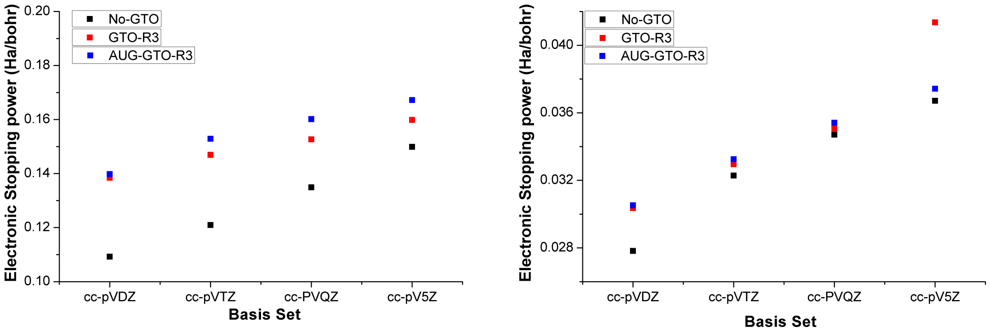

Figure 4.10: The stopping power of water cluster described with varying basis sets calculated at 0.075MeV (left) and 1.0 MeV (right) with one trajectory

Afterwards, the full electronic stopping power profile was calculated for different energies of projectile, *i.e.* 0.01, 0.05, 0.075, 0.1, 0.5, and 1 MeV. The shape of the electronic stopping power profile agrees well with previous calculations with plane wave approach and empirical approach, in which the highest energy is deposited when water is irradiated by proton with kinetic energy of approximately 0.075 MeV.[36] The comparison of the curve obtained for cc-pVDZ, cc-pV5Z, cc-pVDZ+GTO-R3, and cc-pVDZ+GTO-R8 is shown in Figure 4.11 Since GTO-R8 adds more virtual orbitals than GTO-R3, the augmentation of GTO-R8, however, does not give advantage over GTO-R3 to the calculation of stopping power. This comparison further validates that cc-pVDZ+GTO3 is a good choice of basis sets. Lastly, we calculate the averaged electronic stopping power of the cluster with 8 trajectories for the cc-pVDZ and cc-pVDZ+GTO-R3 as comparison (see Figure 4.11), and indeed we have observed a significant increase in the stopping power with addition of GTO-R3.

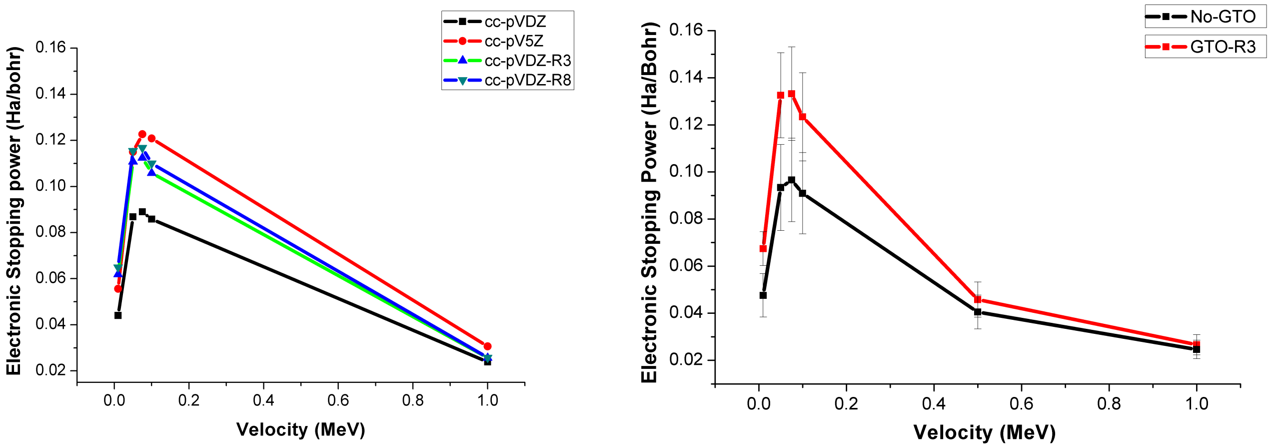

Figure 4.11: (left) The stopping power calculated based on one trajectory for each velocity of projectiles with different basis sets, (right) The averaged stopping power calculated based on 8 trajectories for each velocity of projectiles with and without the GTO basis sets

4.4.4 Conclusion and Perspectives

All in all, our work has demonstrated that the addition of GTO designed for describing continuum function, is indeed important for the calculation of electronic stopping power. cc-pVDZ augmented with GTO-R3 seems to provide a good balance between the size and the accuracy of the calculation, and also the stability of the propagation.

Now that the choice of basis set has been set, the question of whether water cluster is a good model for the calculation of electronic stopping power, which is an averaged property, is still unclear. Kanai *et al.* has calculated the electronic stopping power of water slab with PBC based on plane wave approach, and the resulting curve of stopping power is higher in energy than that obtained in this work. Therefore, further works to investigate the sensitivity of electronic stopping power on the model are needed to explain the discrepancy in the calculated electronic stopping power reported here, as compared to that reported by Kanai *et al.*.[36] Additionally, the path taken by the projectile strongly affects the deposited energy as well. Therefore, careful consideration of the trajectories of projectile should be taken, or more trajectories should be performed to obtain the averaged electronic stopping power.

4.5 Optical Absorption of GNP

The optical properties of GNP, in particular the plasmonic properties, have been the subject of interest, in particular for imaging and sensors. As such, research efforts have been directed to the understanding and designing materials with desired optical properties. RT-TD-DFT has recently been used to simulate the longitudinal and transversal absorption spectra of a linear gold nanowire, between 4, 6, 8, 10, and 12 gold atoms.[37] They observed the red shift in the absorption spectra in the longitudinal as the length of the nanowire increases, while the transversal spectra remain unchanged.

In this chapter, we calculated the absorption spectra of a series of increasing size of GNP with RT-TD-DFT. The starting electron density of GNP has been initially obtained with the IT-TD-DFT to ensure that the GNP are in their ground state.[23,24] The imaginary propagations of Au$_{55}$ and Au$_{147}$ are shown in Figure 4.12. The electric field has been introduced with Dirac pulse of 0.06 a.u. at each of x-, y-, and z-axis. The electric field has been applied only at the beginning of the simulation, and the electron dynamics is propagated during 9 fs, using a time step of 1 as.

The absorption spectra of Au$_{55}$, Au$_{79}$, and Au$_{147}$ are shown in Figure 4.12 (top). A red shift in the absorption spectra has been observed as the size of the GNP increases, consistent with the previously reported computational studies on bare GNP.[38] Similarly, the absorption spectra of Au$_{39}$ and Au$_{54}$ are shown in Figure 4.12. These two GNP have a different shape as compared to Au$_{55}$, Au$_{79}$, and Au$_{147}$. Therefore, the shape of the absorption spectra is also observed to be quite different, as Au$_{39}$ and Au$_{54}$ have two absorption peaks at < 5.0 eV. This could arise due to asymmetrical transversal and longitudinal lengths. However, as the number of GNP increases, these peaks are consistently shifted to lower energy. The shape dependent of the absorption spectra has previously been reported in the literature.[37–39]

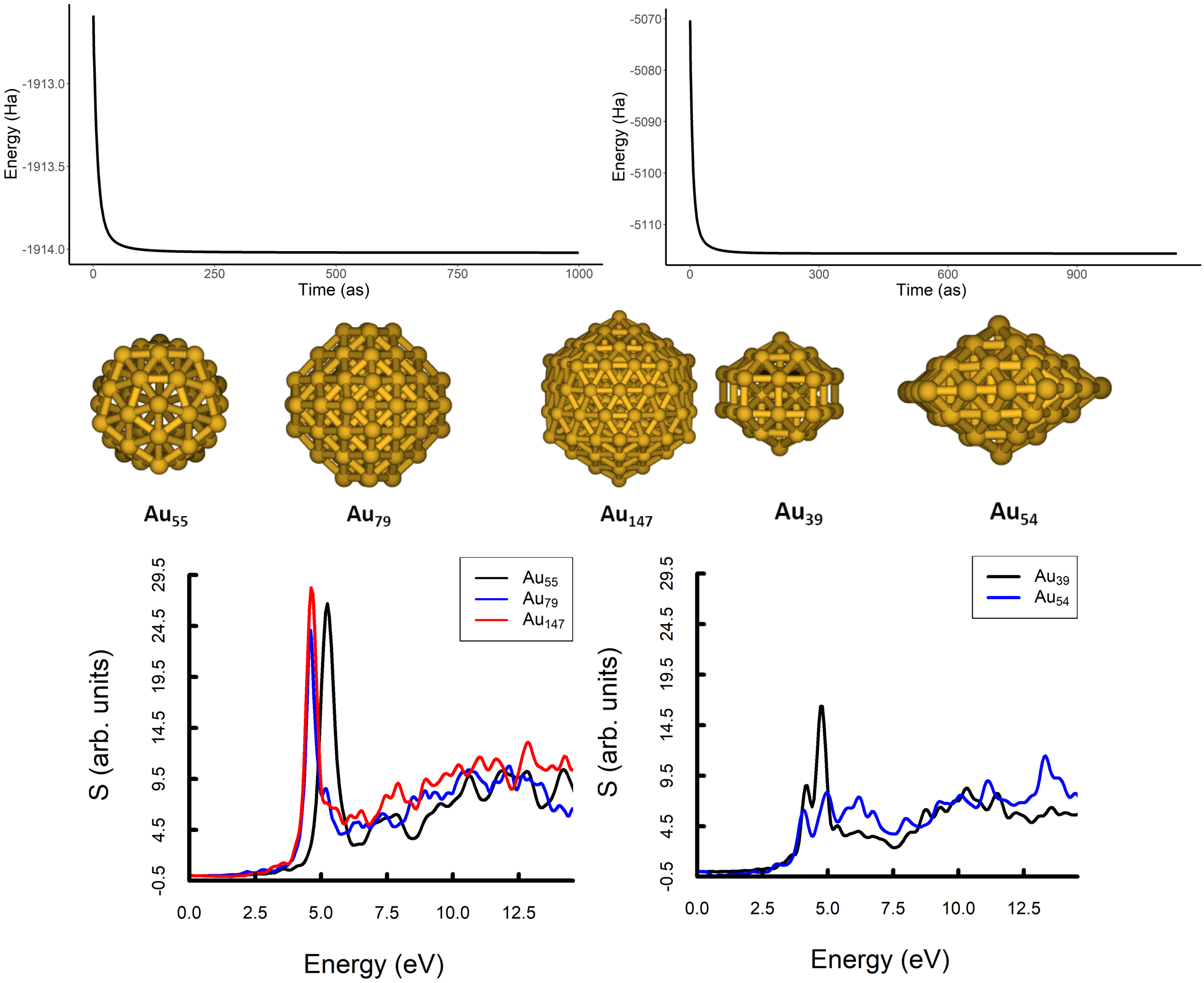

Figure 4.12: (top) The schematic representation of the series of GNP studied in this section; (middle) The imaginary time propagation of Au_{55} (left) and Au_{147} (right) to obtain the lowest energy state as starting density of optical absorption analysis; (bottom) The absorption spectra of Au_{55}, Au_{79}, and Au_{147} (left) and Au_{39} and Au_{54} (right) computed using RT-TD-DFT

4.5.1 Conclusion and Perspectives

In this section, the application of imaginary time propagation in achieving lowest electronic ground state of GNP has been shown, and from which, their respective absorption spectra have been calculated in the presence of Dirac pulse as the external perturbation. The absorption peaks have been shown to red shift as the size of GNP increases. Additionally, the absorption spectra is dependent on the shape of GNP.

The advantage of the RT-TD-DFT method is that the excitation profile at high energy range can be calculated (strong perturbation). This allows the simulation of systems under strongly ionizing radiation, that could result in the excitation of core electrons, along with ionization. The dynamics of the electron can then be followed as they are either excited or ionized. K. Omar (ICP, Paris-Saclay Univ.) has tested the application of RECP in calculation of absorption spectra. Therefore, the excitation profile at high energy range can be investigated, and eventually compared with X-ray based Spectroscopy techniques.

It has been previously reported that the plasmonic properties of GNP usually start appearing for thiolated $Au_{279}(SR)_{84}$, while in the cases of AgNPs, the plasmonic properties start to appear for nanoparticles containing more than 400 atoms. There have been debates on the critical number of atoms for bare GNP to start exhibiting the plasmonic properties. However, with the computational cost associated with calculations for larger nanoparticles, there have been limited amount of computational studies. With the implementation of GPU architect, however, it might be possible to simulate larger GNP with reasonable computational time, which is currently ongoing. Alternatively, the TD-DFT with tight-binding approximation could offer a significant reduction in computational costs, with which the calculation of the absorption spectra of a series of GNP and AgNP up to 165 atoms has been reported.[40]

4.6 General Conclusion and Perspectives

In this chapter, the investigation of systems, *i.e.* water cluster and GNP, under external perturbation has been performed by employing RT-TD-DFT method. This work has demonstrated that cc-pVDZ augmented with GTO designed to describe continuum functions offers a good balance of computational cost and accuracy in the calculation of electronic stopping power of water cluster. Furthermore, with the same method, the absorption spectra of various GNP has been calculated to show the dependence of the spectra on the shape of GNP, as well as the red shift of absorption peak as the size of GNP increases.

With our motivation in investigating the effect of water shell on the radiosensitizing properties of GNP, it will be crucial to include GNP in the system. The application of RECP has been investigated for the calculation of absorption spectra with the conclusion that the basis set does not need to be augmented with the continuum GTO. Therefore, the simulation can be performed for hydrated GNP, with RECP describing GNP, and cc-pVDZ-GTO-R3 describing the hydration shell. A schematic representation of hydrated GNP is shown in Figure 4.13. The charges of the system can be computed with Hirshfeld's population analysis scheme to follow the electron dynamics. Upon collision, the GNP initially accepts electrons from the surrounding water molecule before the electrons are ejected back to the surrounding water molecules. Afterwards, the electron remains delocalized among the water molecules, while GNP remains slightly positive. A careful analysis of the electron dynamics, for example by employing topological analysis, will eventually be needed for further understanding of this irradiation process.[15]

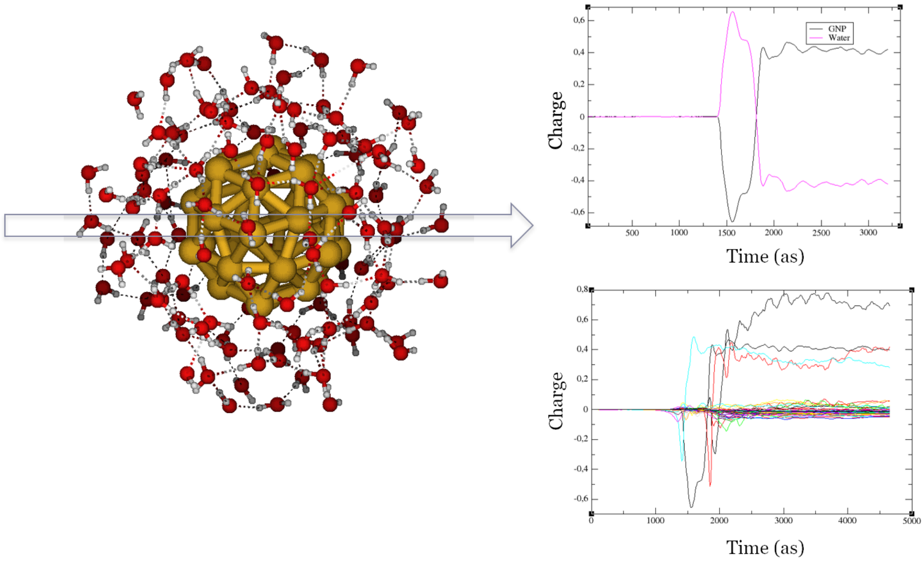

Figure 4.13: The schematic representation of solvated GNP as collided with proton with high kinetic energy (left), and the resulting dynamics of the charge of GNP and the surrounding water molecules (right).

Bibliography

[1] G. Han, P. Ghosh and V. M. Rotello, *Nanomedicine-uk*, 2007, **2**, 113–123.

[2] D. R. Cooper, D. Bekah and J. L. Nadeau, *Front Chem*, 2014, **2**, 2014.

[3] Fen-Ying Kong, Jin-Wei Zhang, Rong-Fang Li, Zhong-Xia Wang, Wen-Juan Wang and Wei Wang, *Molecules*, 2017, **22**, 1445.

[4] S. Her, D. A. Jaffray and C. Allen, *Adv Drug Deliver Rev*, 2017, **109**, 84–101.

[5] X. Hu, Y. Zhang, T. Ding, J. Liu and H. Zhao, *Front Bioeng Biotechnol*, 2020, **8**, 2020.

[6] Z. Kuncic and S. Lacombe, *Phys Med Biol*, 2018, **63**, 02TR01.

[7] S. Mukherjee, F. Libisch, N. Large, O. Neumann, L. V. Brown, J. Cheng, J. B. Lassiter, E. A. Carter, P. Nordlander and N. J. Halas, *Nano Lett.*, 2013, **13**, 240–247.

[8] P. Singh and I. Mijakovic, *Expert Rev Mol Diagn*, 2021, **21**, 627–630.

[9] L. Sementa, G. Barcaro, A. Dass, M. Stener and A. Fortunelli, *Chem Commun*, 2015, **51**, 7935–7938.

[10] M. Gilles, E. Brun and C. Sicard-Roselli, *J Colloid Interface Sci*, 2018, **525**, 31–38.

[11] A. V. Verkhovtsev, A. V. Korol and A. V. Solov'yov, *Phys Rev Lett*, 2015, **114**, 063401.

[12] V. Shcherbakov, S. A. Denisov and M. Mostafavi, *Nanomaterials*, 2020, **10**, 2020.

[13] K. Lopata and N. Govind, *J Chem Theory Comput*, 2011, **7**, 1344–1355.

[14] X. Wu, J.-M. Teuler, F. Cailliez, C. Clavaguéra, D. R. Salahub and A. de la Lande, *J Chem Theory Comput*, 2017, **13**, 3985–4002.

[15] A. Parise, A. Alvarez-Ibarra, X. Wu, X. Zhao, J. Pilmé and A. de la Lande, *J Phys Chem Lett*, 2018, **9**, 844–850.

[16] A. Alvarez-Ibarra, A. Parise, K. Hasnaoui and A. de la Lande, *Phys Chem Chem Phys*, 2020, **22**, 7747–7758.

[17] K. A. Omar, K. Hasnaoui and A. de la Lande, *Annu Rev Phys Chem*, 2021, **72**, 445–465.

[18] E. Runge and E. K. U. Gross, *Phys Rev Lett*, 1984, **52**, 997–1000.

[19] J. Jakowski and K. Morokuma, *J Chem Phys*, 2009, **130**, 224106.

[20] C.-L. Cheng, J. S. Evans and T. Van Voorhis, *Phys Rev B*, 2006, **74**, 155112.

[21] X. Wu, A. Alvarez-Ibarra, D. R. Salahub and A. de la Lande, *Eur Phys J D*, 2018, **72**, 206.

[22] A. Castro, M. A. L. Marques and A. Rubio, *J Chem Phys*, 2004, **121**, 3425–3433.

[23] C. Flamant, G. Kolesov, E. Manousakis and E. Kaxiras, *J Chem Theory Comput*, 2019, **15**, 6036–6045.

[24] J. McFarland and E. Manousakis, *J Phys : Condens Matter*, 2021, **33**, 055903.

[25] L. Lacombe and N. T. Maitra, *J Phys Chem Lett*, 2021, **12**, 8554–8559.

[26] A. Schleife, Y. Kanai and A. A. Correa, *Phys Rev B*, 2015, **91**, 014306.

[27] R. Tandiana, C. Clavaguéra, K. Hasnaoui, J. N. Pedroza-Montero and A. de la Lande, *Theor Chem Acc*, 2021, **140**, 126.

[28] I. Maliyov, J.-P. Crocombette and F. Bruneval, *Phys Rev B*, 2020, **101**, 035136.

[29] E. Coccia, B. Mussard, M. Labeye, J. Caillat, R. Taïeb, J. Toulouse and E. Luppi, *Int J Quantum Chem*, 2016, **116**, 1120–1131.

[30] A. Ammar, A. Leclerc and L. U. Ancarani, *J Comput Chem*, 2020, **41**, 2365–2377.

[31] T. P. Rossi, S. Lehtola, A. Sakko, M. J. Puska and R. M. Nieminen, *J. Chem. Phys.*, 2015, **142**, 094114.

[32] K. Kaufmann, W. Baumeister and M. Jungen, *J Phys B: At , Mol Opt Phys*, 1989, **22**, 2223–2240.

[33] A. Faure, J. D. Gorfinkiel, L. A. Morgan and J. Tennyson, *Comput Phys Commun*, 2002, **144**, 224–241.

[34] S. Harrison and J. Tennyson, *J Phys B: At Mol Opt Phys*, 2011, **44**, 045206.

[35] T. H. Dunning, *J Chem Phys*, 1989, **90**, 1007–1023.

[36] K. G. Reeves, Y. Yao and Y. Kanai, *Phys Rev B*, 2016, **94**, 041108.

[37] R. D. Senanayake, D. B. Lingerfelt, G. U. Kuda-Singappulige, X. Li and C. M. Aikens, *J Phys Chem C*, 2019, **123**, 14734–14745.

[38] R. W. Burgess and V. J. Keast, *J Phys Chem C*, 2014, **118**, 3194–3201.

[39] O. Baseggio, M. De Vetta, G. Fronzoni, M. Stener, L. Sementa, A. Fortunelli and A. Calzolari, *J Phys Chem C*, 2016, **120**, 12773–12782.

[40] N. Asadi-Aghbolaghi, R. Rüger, Z. Jamshidi and L. Visscher, *J Phys Chem C*, 2020, **124**, 7946–7955.

Chapter 5

Conclusion

In this thesis, various levels of computational methods have been employed to model GNP in various environments, depending on the properties of interest. In the second chapter, the dynamical interaction of a series of increasing size of hydrated GNP has been systematically studied by employing the force field, proposed by Heinz *et al.*. Based on the structural, dynamical, and vibrational properties, the water at the first solvation shell has been observed to undergo re-orientation of the solvation shell to form 2D hydrogen bond network in large GNP. The distribution of water's orientation has also indicated an increase in the proportion of water molecule adopting the dangling configuration, which is the characteristic configuration of water molecule at the interface of gold surfaces. Despite the satisfactory results obtained, the force field employed still neglects the important contribution of the polarization term, and the reactivity of the different facet present at the surface of GNP. This has led us to propose an accurate force field describing the Au-water interaction, which is derived from GAL21. The proposed force field accounts for the local environment of the GNP surface, and explicitly treats the polarization term within the AMOEBA framework. Our work has shown that the new force field performs excellently in describing the many body interactions, when multiple water molecules are adsorbed on GNP surfaces. Additionally, the transferability of the force field has been shown to be exceptional for the series of GNP studied in this chapter.

Going further, the force field still needs to be tested on various sizes and shapes of GNP, to evaluate further its transferability. Additionally, the force field will be evaluated further for its application in studying the interaction with ions and other surface ligands, either charged or neutral ligands. With the inclusion of polarization, the environmental response of charged species should be described better than with the traditional force field. Moreover, the charge transfer term could also be introduced into the force field as a pairwise term that decays exponentially with distance. Finally, a larger and increasingly more complex molecules, for example peptides or proteins, can be included in the system to study their preferred orientation and to perform extensive sampling. Vibrational spectra can be computed from the trajectory in MD simulations as well, which may be directly comparable to experimental spectra.

With the accurate force field available for GNP-water interaction, it is important to re-evaluate the parameters currently available for organic molecules as well.

With that objective in mind, in the third chapter, we have systematically studied the interaction of a series of GNP with small organic molecules at DFT level. The qualitative and quantitative studies of the nature of the interaction have been studied by employing various topological analyses, and energy decomposition approaches. Additionally, the size and interaction sites effects of Au$_{32}$, Au$_{55}$, and Au$_{79}$ on the interaction energy have been investigated. It was observed that interactions with corner are the most favored ones, and followed by the edge positions, and lastly the face positions. The reactivity of these different interaction sites has additionally been computed with Fukui function, and it is highly related with the coordination number of the respective atoms. However, minimal energy difference has been observed across the three GNP studied here. The energy decomposition approaches employed in this chapter have also given significant insight into the physically meaningful energy terms that contribute the most to the interaction, and it was found to be the molecule dependent, rather than GNP dependent. This has strong implication in force field development of GNP systems. Lastly, the vibrational spectra of adsorbed organic molecules have been systematically studied to highlight the main changes that occurred due to the interaction. Similarly, the effect of the size of GNP seems to be minimal on the calculated vibrational spectra, with benzoic acid as the model compound.

Since the descriptors in the calculated vibrational spectra associated to two possible orientations of benzoic acid on GNP have been proposed in the study, a qualitative comparison with the experimental data would be necessary for the validation. By following similar procedure as proposed in this study, studies of increasingly more complex molecules can be performed, such as amino acid. This work is currently ongoing, the competitive interaction between GNP-ligand, and ligand-ligand is particularly being assessed. Furthermore, experimental SERS data have indicated a different preference on the adsorption geometry between phenylalanine and tyrosine, which are structurally very similar, except for the hydroxyl functional group substituent on the phenyl ring of tyrosine. This observation has been one of the motivations of the study reported in this thesis, and works are currently ongoing to explain this preference. With the force field proposed in this thesis, the environmental effect of the solvent on the adsorption of these molecules can be studied with MD simulations.

With the vast interest in the plasmonic and radiosensitizing properties of GNP, the fourth chapter focuses on the simulation of systems in excited state. With the Real-Time TD-DFT method, in which the electrons are propagated over time, the dynamics of electrons can be studied at a very short time scale, *i.e.* attosecond. The chapter has started with the evaluation of auxiliary density framework on the calculation electronic stopping power, an important descriptor to assess radiosensitizing property. We subsequently proposed a basis set for water molecule, that is fitted to describe the oscillating characteristics of continuum function. The performance of the basis set has been studied for the application in calculation of electronic stopping power. Lastly, the imaginary time propagation, within RT-TD-DFT framework, has been employed to obtain the electronic ground state of a series of GNP, before subjecting them to an electric pulse. The absorption spectra have subsequently been calculated based on the time-dependent dipole moment. A red shift has been observed for the larger size of GNP studied in this thesis, which is consistent with the previously reported observation.

Going forward, the electronic stopping power of hydrated GNP will be calculated, to study the increment of energy deposition with respect to the water droplet. Our work has demonstrated the importance of the continuum basis set in the calculation of electronic stopping power. Furthermore, our collaborator has evaluated the use of effective core potentials in simulations under strong electric field. On top of the electronic stopping power, it will be interesting to follow the electron dynamics through topological analysis currently implemented for excited states. This study will provide insight into the underlying mechanism of radiosensitizing properties of GNP, and its implication on the production of hydroxyl radical and secondary electrons. Since this method is computationally expensive, there is currently ongoing work that is devoted to the implementation of this method in semi-empirical approach, such as DFTB. This approximation eventually will allow the introduction of surface ligands into the system, which can provide insight on the possible effect of surface ligands in trapping of the secondary electrons ejected by GNP. Additionally, the surface ligands effect on the optical properties of GNP can also be evaluated.

All in all, the works reported in this thesis have demonstrated the multi-dimensional problems in simulating GNP systems. Nevertheless, with different methods currently available in the computational chemist’s toolbox, a complete understanding of GNP systems can be achieved. Especially with the increase in the applications of machine learning in computational methods, especially in improving the accuracy of the approximated approaches, methods that balance the computational cost and size of the system will be available in the near future. One such example is the currently ongoing project done by N. Bhatia in collaboration with M. Elstner’s group, which employs the artificial neural network to predict energy corrections for Au-water interactions.

Appendices

Appendix A

Appendix

A.1 Simulating GNP-Water interface

A.1.1 Probing the Structural Properties of the Water Solvation Shell Around Gold Nanoparticles: A Computational Study

Probing the structural properties of the water solvation shell around gold nanoparticles: a computational study

Supplementary Material

Rika Tandiana,[1] Emilie Brun,[1] Cécile Sicard-Roselli,[1] Dominik Domin,[1] Nguyen-Thi Van-Oanh†,[1, a)] and Carine Clavaguéra†[1, b)]

Université Paris-Saclay, CNRS, Institut de Chimie Physique, UMR8000, 91405 Orsay, France

(Dated: December 24, 2020)

[a)] Electronic mail: van-oanh.nguyen-thi@universite-paris-saclay.fr

[b)] Electronic mail: carine.clavaguera@universite-paris-saclay.fr

†These authors contributed equally to this work.

COMPUTATIONAL DETAILS

Classical Molecular Dynamics

The system of GNP in water was initially set up in GROMACS,[1–7] by forming a cubic box with additional 1.2 nm at each of the three dimensions and extended infinitely using periodic boundary conditions. As for Au_{887}, 2.0 nm were added at each of the three dimensions, to ensure that the box was large enough. Then, water molecules were added to fill the box using the rigid SPC/E model.[8–12] Svishchev et. al. have previously performed MD simulation of 256 water molecules with periodic boundary system at 25°C to reproduce the self-diffusion coefficient and the dielectric constant within 2% of accuracy.[13] The system was then equilibrated in both NVT and NPT ensembles for 1 ns each using a time of 1 fs. The electrostatic and van der Waals cutoff were set to 1.2 nm each. The long-range electrostatics was accounted by particle mesh Ewald scheme.[14,15] The temperature coupling was done with V-rescale[16] (modified Berendsen thermostat), with a time constant of 0.1 ps and a temperature of 300 K, for the NVT ensemble. The pressure coupling was set with isotropic Parrinello-Rahman,[17] with a time constant of 1.0 ps and a reference pressure of 1.0 bar. The density and temperature of the system were found to reach equilibrium at the end of these steps. Then, the production phase of dynamics was collected over 20 ns in the NVT ensemble, after 1 ns of simulation in the NPT ensemble, with a time step of 2 fs.

The force field parameters for GNP were taken from a previous study in which the parameters were optimized for water-gold interactions on a gold surface (see Table S2).[18] Rigid Au-Au bonds have been imposed to preserve the structure during the molecular dynamics simulations. The radial distribution functions (RDF) of Au-Au has been examined to remain constant across the different equilibrium and production steps. The relevant properties of the systems have been analyzed by tools available in the GROMACS software, such as energetic properties, radial distribution function, and self-diffusion coefficient of solvent. For salt systems, several solvent molecules were replaced by the desired number of sodium and chloride ions, while maintaining the neutrality of the system. Then, both the equilibrium and production phases were performed with the parameters mentioned above. However, the production time for salt containing system has been extended up to 30 ns for the Au_{32} with increasing salt content, and up to 5 times 30 ns for increasing size of GNP at salt content of 1:10, to ensure the thorough exploration of configurational space for the ions.

To ensure the reliability of the simulations, the potential energy, average pressure, average temperature, average density and average total energy of the system were computed at each simulation's ensemble. Several examples of such properties are provided in Figure S1 to show the stability of the simulations. In addition, the trajectories have also been visualized with VMD software[19] to follow realistic evolution of the systems.

Quantum chemical calculations

DFT

Calculations at the DFT level have been performed with deMon2k code[20] which builds an auxiliary density, that is variationally fitted to the Kohn-Sham density. This approach reduces the scaling of the calculation of Coulomb interactions and the numerical integration of exchange correlation energies to the number of generated auxiliary functions instead of the size of the system. As a result, this process accelerates the computational time significantly. The self-consistency field energy and the auxiliary density convergence criteria were set to 1.0×10^{-9} a. u. and 1.0×10^{-7} a. u., respectively, to ensure high accuracy.

The PBE functional was used associated to the DZVP basis set for O and H, and a relativistic effective core potential (60 core electrons) with 19 valence electrons explicitly treated in combination with its basis set for Au.[21] Empirical dispersion corrections were included in the calculations.[22] The geometry of the systems was optimized without any constraint with the tolerance of 1.0×10^{-6} a. u. with a SCF convergence criterion of 1.0×10^{-9} a. u. and 1.0×10^{-7} a.u. for the auxiliary density fitting.

DFTB

All DFTB calculations were performed with DFTB+ code.[23,24] The geometry optimization of the systems was done with the conjugate gradient algorithm without any constraint. The tolerance was set to 1.0×10^{-6} a. u., while the self charge consistency tolerance was set to 1.0×10^{-10} a. u.. The Fermi temperature of the system was set to 100 K to allow fractional occupancy of the HOMO. Dispersion corrections were systematically introduced using the DFTB3 framework[25] along with hydrogen bond corrections, as proposed in previous publications.[26] The angle analysis has been done with the procedure mentioned in the main article for the optimized structures of solvated

GNPs. Normal mode analysis was performed by Hessian calculations. The resulting vibrational density of states (VDOS) spectrum was then plot in the form of histogram because the infrared intensities are not provided by DFTB+.

Table S1. Structural and electronic properties of the GNP studied.

Properties	Au_{32}	Au_{54}	Au_{55}	Au_{72}	Au_{79}	Au_{105}	Au_{147}	Au_{201}	Au_{344}	Au_{887}
Diameter (Å)	8.51	12.85	8.60	12.17	11.50	16.97	15.85	15.47	26.57	27.86
d_{Au-Au} (Å)	2.630-2.767	2.615-2.829	2.581-2.849	2.630-2.750	2.671-2.842	2.578-3.072	2.593-2.881	2.632-2.839	2.625-2.844	
$N_{electrons}$	352	594	605	792	869	1155	1617	2211	3784	9757
HOMO (eV)	-5.935	-5.005	-5.349	-5.548	-5.417	-4.953	-4.987	-5.087	-5.129	-5.186
LUMO (eV)	-4.279	-4.873	-4.32	-5.085	-5.214	-4.91	-4.749	-4.947	-4.991	-5.051
Band gap (eV)	1.656	0.132	1.020	0.463	0.203	0.043	0.138	0.140	0.138	0.135
$N_{surf-atom}$	32	47	42	72	60	82	92	122	198	358

Table S2. Atomic and pair van der Waals force field parameters.

Atom (i)	Atom (j)	C_6 (kJ mol^{-}1 nm^{6})	C_{12} (kJ mol^{-}1 nm^{12})
Au	Au	0.05842	3.85029E-05
O_w		0.0026188	2.4351E-06
H_w		0	0
Au	O_w	0.0124152	0.000010148

Table S3. Au-O distance (Å) and interaction energy (eV) for Au_{54}, Au_{79}, and Au_{105} interacting with one water molecule using different DFTB parameter sets as compared to DFT calculations.

System	DFT		Auorg		Auwater	
	dAu-O	E_{int}	dAu-O	E_{int}	dAu-O	E_{int}
Au_{54}	2.416	-0.545	3.176	-0.158	3.068	-0.182
Au_{79}	2.468	-0.392	3.273	-0.163	3.075	-0.177
Au_{105}	2.439	-0.476	3.195	-0.144	3.074	-0.160

Table S4. Interaction energies (eV), deformation energies (eV) and charge transfer (e) of Au_{54} with one solvation shell using different sets of DFTB parameters.

Properties	Auorg (Hbond)	Auwater	Auwater (Hbond)
E_{int}	-10.906	-8.208	-11.363
E_{int} / water	-0.114	-0.086	-0.118
E_{def}	0.039	-0.006	0.033
Charge transfer	-1.188	-1.427	-1.465

Table S5. Bulk properties of the water box and the solvated GNP calculated from classical MD simulations.

System	Box (nm)	Water molecules	Density (kg/m^3)	Diffusion ($1E^{-5}$ cm^{2}s^{-1})	$T_{orient.}$ (ps)
Water box	3.56	1504	998.5	2.79	4.95
Au_{32}	3.28	1163	1286.4	2.43	5.17
Au_{54}	3.62	1566	1360.0	2.42	5.18
Au_{55}	3.39	1288	1444.8	2.38	5.20
Au_{72}	3.67	1636	1451.4	2.34	5.33
Au_{79}	3.53	1446	1565.9	2.43	5.30
Au_{105}	4.07	2225	1489.9	2.43	5.21
Au_{147}	3.98	2042	1737.9	2.36	5.41
Au_{201}	4.06	2170	1940.8	2.31	5.38
Au_{344}	4.96	3978	1877.9	2.42	5.31
Au_{887}	6.92	10240	2862.6	2.55	5.19

Table S6. Interaction energies (eV) and charge transfer (e) for Au_{32} interacting with one water molecule with flat configuration at different distances (Å) calculated at the DFT and DFTB levels.

Distance	$E_{int/DFT}$	CT_{DFT}	$E_{int/DFTB}$	CT_{DFTB}
2.057	6.925	0.151	21.443	0.341
2.248	-3.972	0.154	8.867	0.286
2.440	-8.070	0.149	2.419	0.230
2.634	-9.055	0.138	-1.527	0.176
2.828	-8.677	0.133	-4.042	0.128
3.023	-7.815	0.122	-4.709	0.087
3.219	-6.774	0.112	-3.978	0.054
3.415	-5.768	0.102	-2.915	0.031
3.612	-4.860	0.094	-1.972	0.016
3.809	-4.135	0.086	-1.301	0.007
4.006	-3.575	0.078	-0.879	0.003

Table S7. Interaction energies (eV) of Au_{32} with one solvation shell at DFT and DFTB levels.

Geometry	$E_{int/DFT}$	$E_{int/DFT}$/water	$E_{int/DFTB}$	$E_{int/DFTB}$/water
1	-7.286	-0.110	-7.363	-0.112
2	-7.337	-0.108	-7.534	-0.111
3	-7.062	-0.107	-7.115	-0.108
4	-6.103	-0.097	-6.227	-0.099
5	-6.755	-0.111	-6.775	-0.111
6	-6.335	-0.109	-6.562	-0.113
7	-7.343	-0.120	-6.909	-0.113
8	-8.068	-0.134	-7.600	-0.127
9	-7.713	-0.129	-7.365	-0.123
10	-6.744	-0.112	-6.659	-0.111
11	-7.594	-0.131	-7.082	-0.122

Table S8. Interaction energies (eV) and charge transfer (e) for a series of GNP interacting with one water in various configurations calculated at the DFTB level.

System	Configuration of water	Adsorption site	E_{int}	Charge Transfer
Au_{54}	Flat	Top corner	-0.182	0.08
Au_{54}	Flat	Edge	-0.190	0.058
Au_{54}	Flat	Face	-0.204	0.061
Au_{54}	Flat	Side Corner	-0.209	0.094
Au_{55}	Flat	Top corner	-0.196	0.088
Au_{79}	Flat	Corner	-0.177	0.075
Au_{79}	Flat	Edge	-0.211	0.079
Au_{105}	Flat	Top corner	-0.160	0.075
Au_{105}	Up	Face	-0.187	0.043
Au_{105}	Flat	Side corner	-0.173	0.083
Au_{105}	Flat	Edge	-0.175	0.042
Au_{147}	Up	Edge	-0.186	0.056
Au_{147}	Flat	Corner	-0.164	0.059
Au_{147}	Flat	Face	-0.186	0.069
Au_{201}	Flat	Face	-0.185	0.067
Au_{201}	Up	Corner	-0.179	0.075

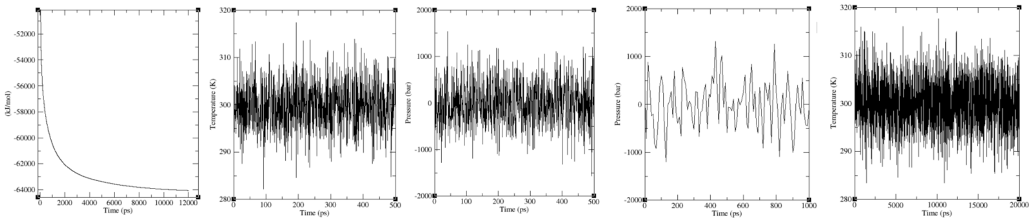

Figure S1. Au_{32} solvated system. From left to right: potential energy at energy minimization step, temperature at NVT equilibration step, pressure at NPT equilibration step, pressure at NPT production phase, temperature at NVT production phase, as a function of the simulation time.

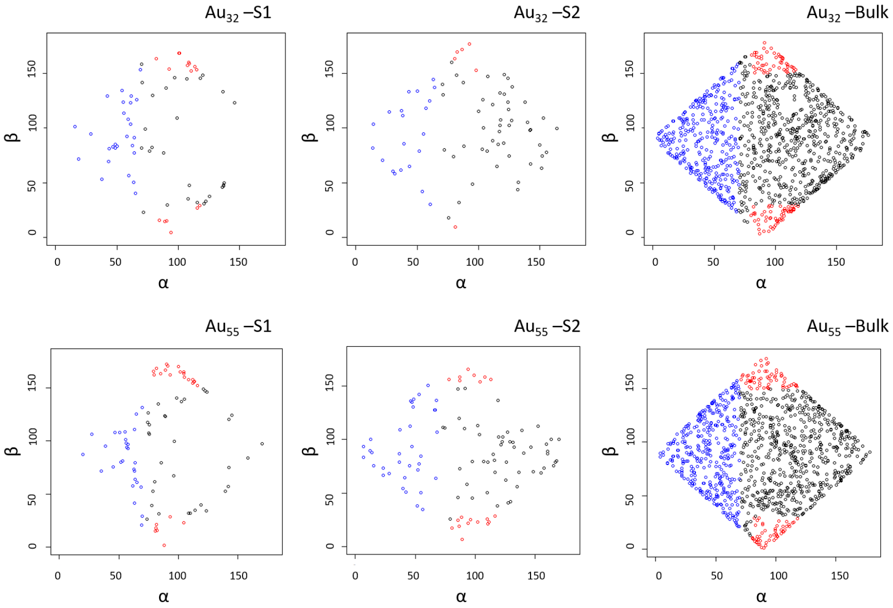

Figure S2. Angle distribution of water molecules from the first and second solvation shells and from the bulk for Au_{32} and Au_{55} systems. Blue circles represent up configuration, red circles represent flat configuration, and black circles represent other configurations.

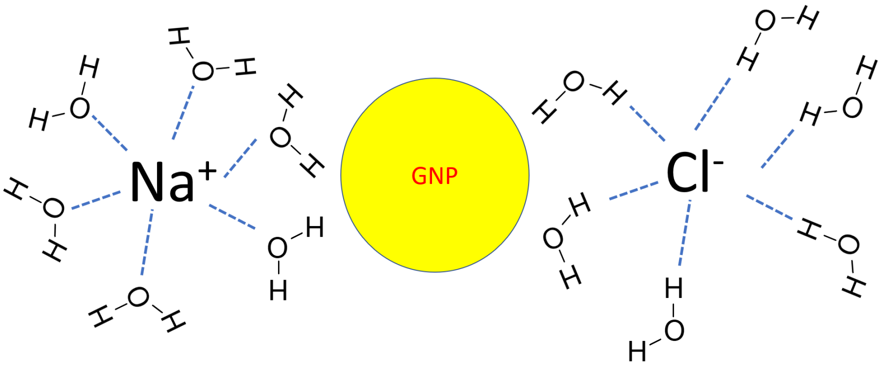

Figure S3. Schematic representation of the solvation shell of ions in interaction with GNP.

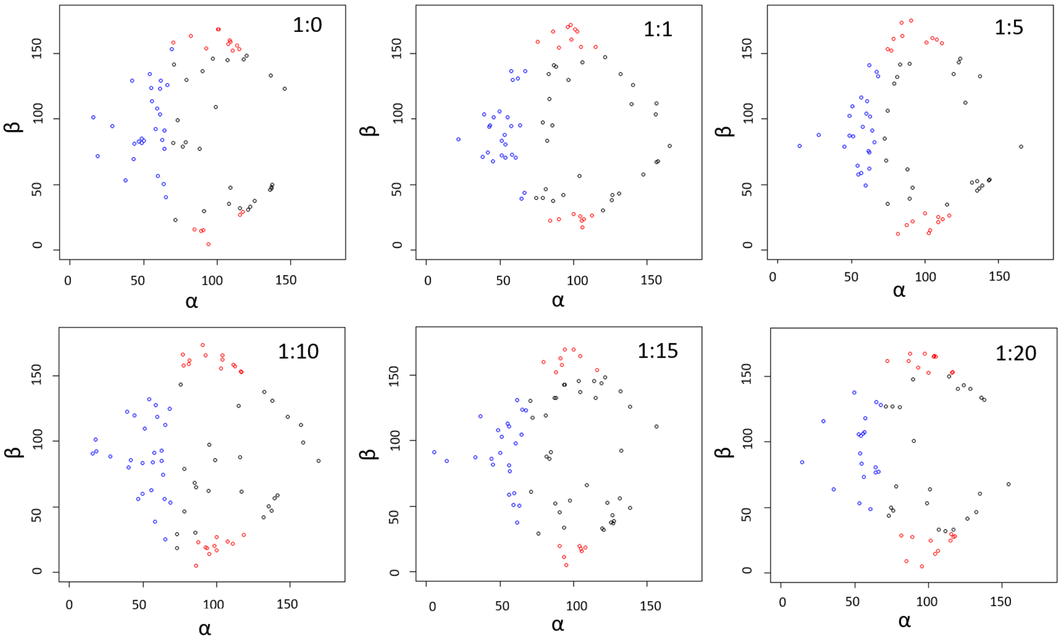

Figure S4. Angle distribution of water molecules at the surface of Au_{32} with increasing number of ions (0, 1, 5, 10, 15, and 20 ions, respectively). Blue circles represent up configuration, red circles represent flat configuration, and black circles represent other configurations.

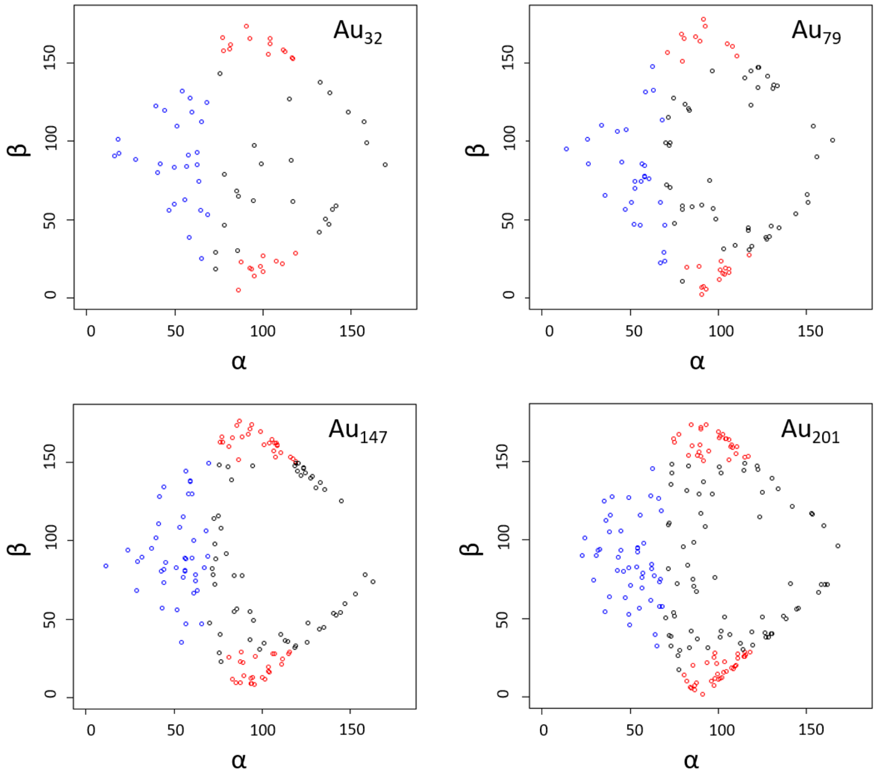

Figure S5. Angle distribution of water molecules at the surface of Au_{32}, Au_{79}, Au_{147} and Au_{201} in the presence of 10 chloride ions and 10 sodium ions. Blue circles represent up configuration, red circles represent flat configuration, and black circles represent other configurations.

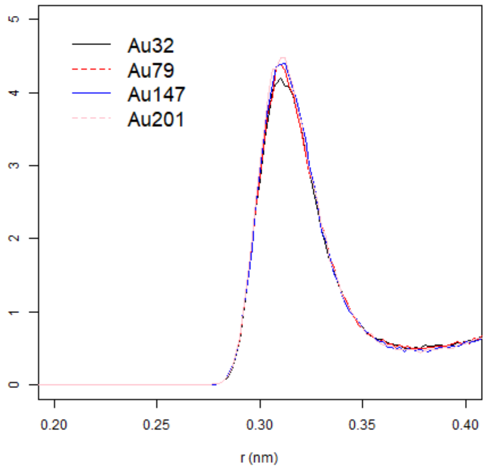

Figure S6. Radial distribution function of water molecules with respect to chloride ions for different GNP.

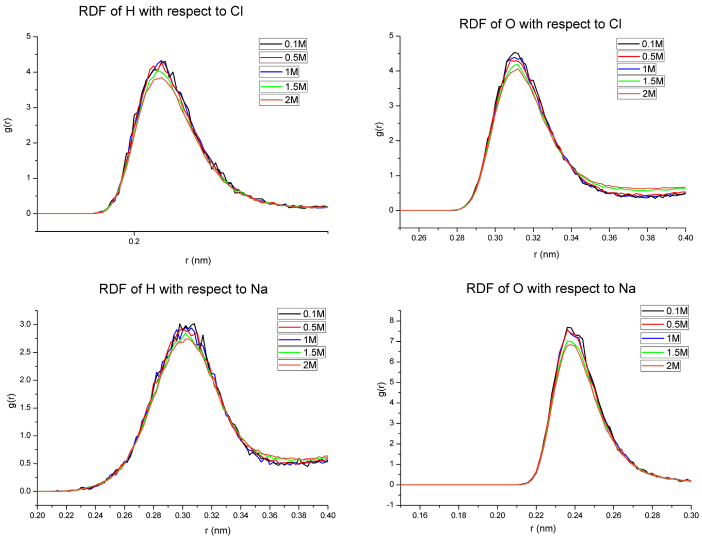

Figure S7. Radial distribution function of O and H of water molecules with respect to chloride and sodium ions for Au_{32} and various ion concentrations.

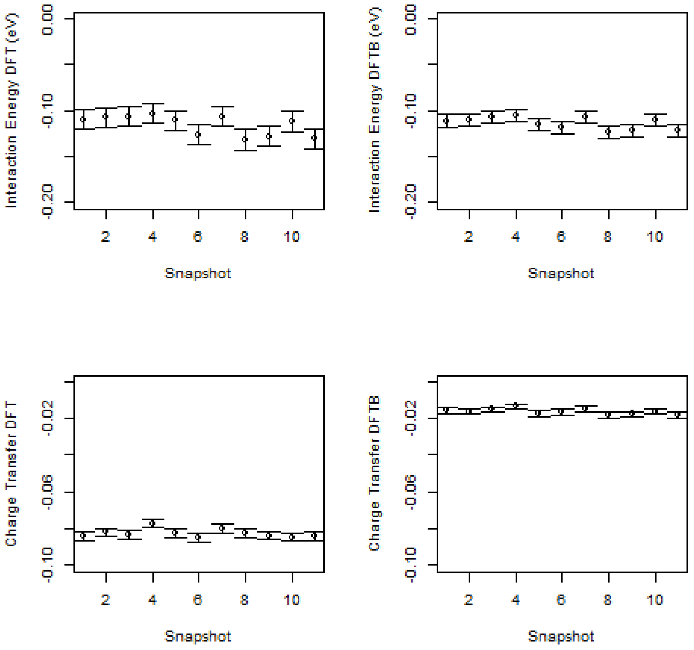

Figure S8. Interaction energy and charge transfer per water molecule with error bars at the DFT and DFTB levels for solvated Au_{32} system.

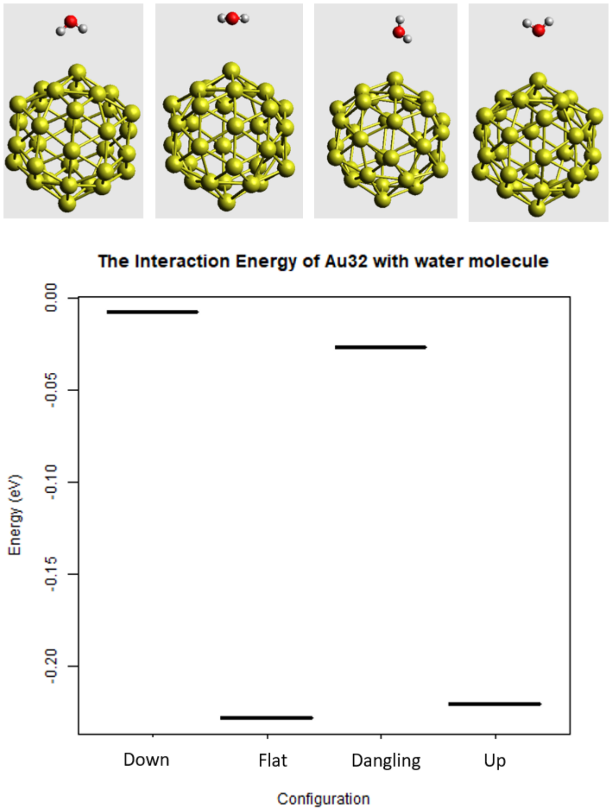

Figure S9. Different configurations of Au_{32} interacting with one water molecule and their respective DFT interaction energy.

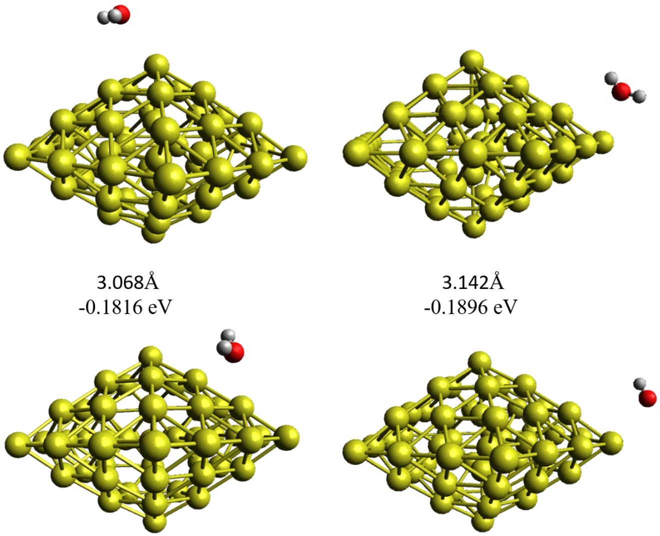

3.068Å
-0.1816 eV

3.142Å
-0.1896 eV

3.099Å
-0.2038 eV

2.988Å
-0.2085 eV

Figure S10. Four configurations of Au_{54} with one water molecule with their respective Au-O distance and interaction energy.

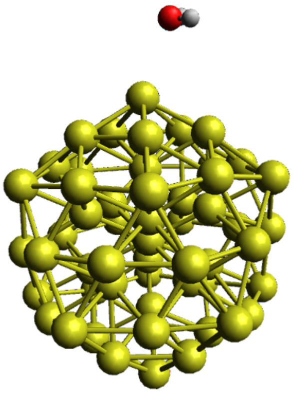

3.024Å
-0.196 eV

Figure S11. The configuration of Au_{55} with one water molecule with its Au-O distance and interaction energy.

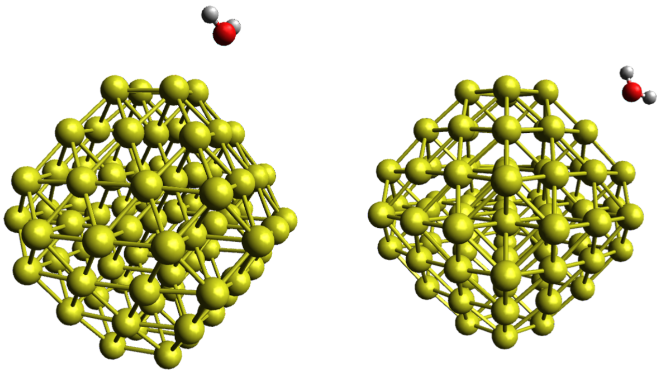

3.075Å
-0.1769 eV

3.053Å
-0.2113 eV

Figure S12. Two configurations of Au$_{79}$ with one water molecule with their respective Au-O distance and interaction energy.

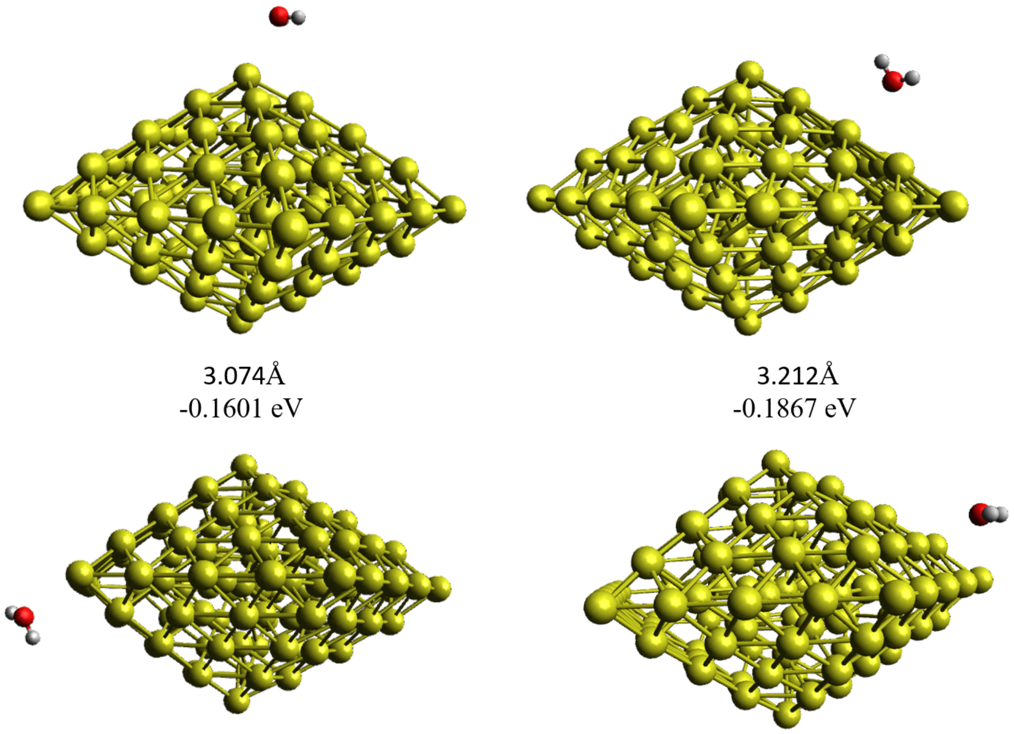

3.074Å
-0.1601 eV

3.212Å
-0.1867 eV

3.031Å
-0.1726 eV

3.226Å
-0.1753 eV

Figure S13. Four configurations of Au$_{105}$ with one water molecule with their respective Au-O distance and interaction energy.

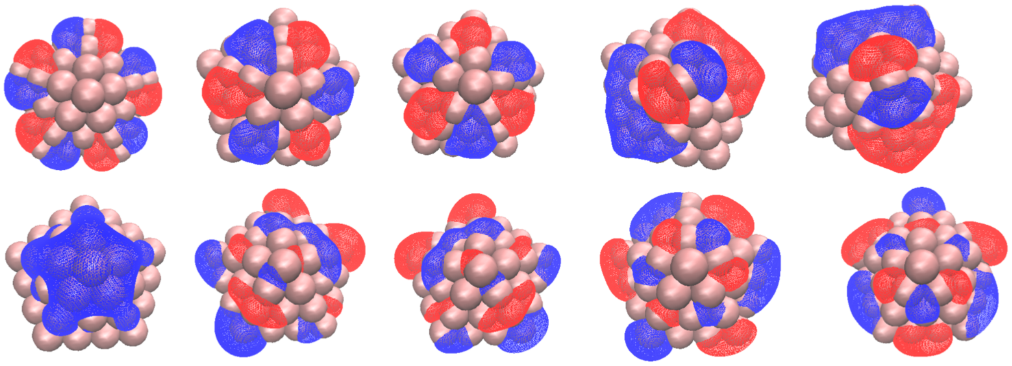

Figure S14. The 5 HOMO and LUMO of Au_{54}.

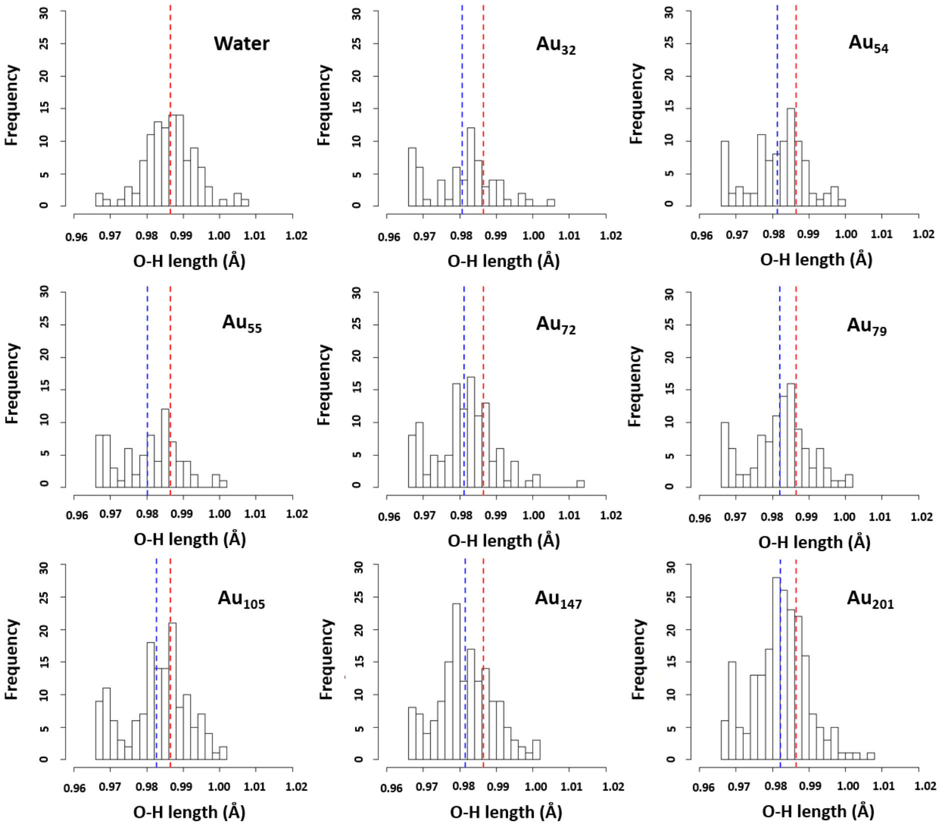

Figure S15. Distribution of O-H bond length of water molecules for: water droplet, Au_{32}, Au_{54}, Au_{55} Au_{72} Au_{79}, Au_{105}, Au_{147}, Au_{201}, respectively. The blue dash line corresponds to the average value of the respective system, while the red dash line corresponds to the average value of water droplet.

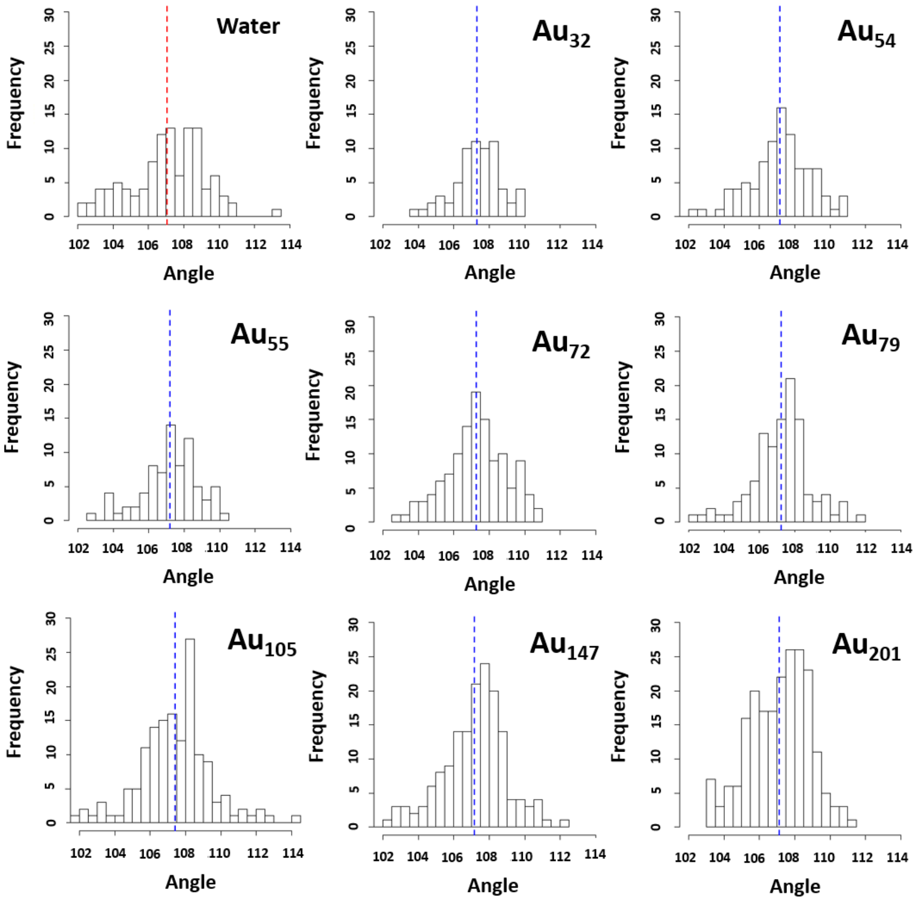

Figure S16. Distribution of H-O-H angle of water molecules for: water droplet, Au$_{32}$ Au$_{54}$, Au$_{55}$, Au$_{72}$ Au$_{79}$, Au$_{105}$, Au$_{147}$, Au$_{201}$, respectively.

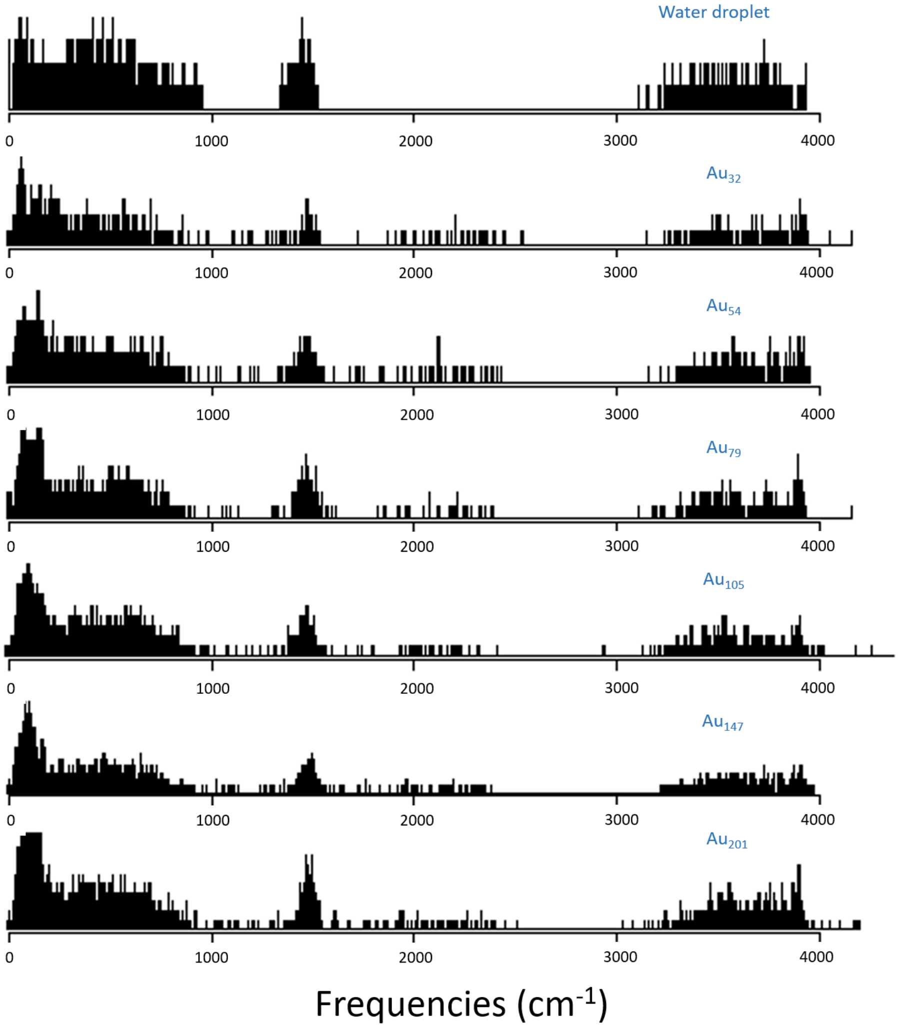

Figure S17. Vibrational density of states of water molecules in water droplet, solvated Au_{32}, Au_{54}, Au_{79}, Au_{105}, Au_{147}, Au_{201}, respectively.

REFERENCES

[1] M. J. Abraham, T. Murtola, R. Schulz, S. Páll, J. C. Smith, B. Hess, and E. Lindahl, SoftwareX **1-2**, 19 (2015).

[2] H. Berendsen, D. van der Spoel, and R. van Drunen, Computer Physics Communications **91**, 43 (1995).

[3] E. Lindahl, B. Hess, and D. van der Spoel, Molecular Modeling Annual **7**, 306 (2001).

[4] D. Van Der Spoel, E. Lindahl, B. Hess, G. Groenhof, A. E. Mark, and H. J. C. Berendsen, J. Comput. Chem. **26**, 1701 (2005).

[5] S. Páll, M. Abraham, C. Kutzner, B. Hess, and E. Lindahl, *Lecture Notes in Computer Science*, Vol. 8759 (Springer,Cham, 2015).

[6] S. Pronk, S. Páll, R. Schulz, P. Larsson, P. Bjelkmar, R. Apostolov, M. R. Shirts, J. C. Smith, P. M. Kasson, D. van der Spoel, B. Hess, and E. Lindahl, Bioinformatics **29**, 845 (2013).

[7] B. Hess, C. Kutzner, D. van der Spoel, and E. Lindahl, J. Chem. Theory Comput. **4**, 435 (2008).

[8] H. J. C. Berendsen, J. R. Grigera, and T. P. Straatsma, J. Phys. Chem **91**, 6269 (1987).

[9] P. Mark and L. Nilsson, J. Phys. Chem. A **105**, 9954 (2001).

[10] J. Zielkiewicz, J. Chem. Phys. **123**, 104501 (2005).

[11] M. W. Mahoney and W. L. Jorgensen, J. Chem. Phys. **114**, 363 (2001).

[12] L. A. Báez and P. Clancy, J. Chem. Phys. **101**, 9837 (1994).

[13] I. M. Svishchev and P. G. Kusalik, J. Phys. Chem. **98**, 728 (1994).

[14] C. L. Wennberg, T. Murtola, S. Pall, M. J. Abraham, B. Hess, and E. Lindahl, J. Chem. Theory Comput. **11**, 5737 (2015).

[15] C. L. Wennberg, T. Murtola, B. Hess, and E. Lindahl, J. Chem. Theory Comput. **9**, 3527 (2013).

[16] S. Páll and B. Hess, Computer Physics Communications **184**, 2641 (2013).

[17] M. Parrinello and A. Rahman, Journal of Applied Physics **52**, 7182 (1981).

[18] A. Berg, C. Peter, and K. Johnston, J. Chem. Theory Comput. **13**, 5610 (2017).

[19] W. Humphrey, A. Dalke, and K. Schulten, J. Mol. Graph. **14**, 33 (1996).

[20] G. Geudtner, P. Calaminici, J. Carmona-Espíndola, J. M. del Campo, V. D. Domínguez-Soria, R. F. Moreno, G. U. Gamboa, A. Goursot, A. M. Köster, J. U. Reveles, T. Mineva, J. M. Vásquez-Pérez, A. Vela, B. Zúñinga-Gutierrez, and D. R. Salahub, WIREs Computational Molecular Science **2**, 548 (2012).

[21] P. Schwerdtfeger, M. Dolg, W. H. E. Schwarz, G. A. Bowmaker, and P. D. W. Boyd, J. Chem. Phys. **91**, 1762 (1989).

[22] A. Goursot, T. Mineva, R. Kevorkyants, and D. Talbi, J. Chem. Theory Comput. **3**, 755 (2007).

[23] B. Aradi, B. Hourahine, and T. Frauenheim, J. Phys. Chem. A **111**, 5678 (2007).

[24] B. Hourahine, B. Aradi, V. Blum, F. Bonafé, A. Buccheri, C. Camacho, C. Cevallos, M. Y. Deshaye, T. Dumitrică, A. Dominguez, S. Ehlert, M. Elstner, T. van der Heide, J. Hermann, S. Irle, J. J. Kranz, C. Köhler, T. Kowalczyk, T. Kubař, I. S. Lee, V. Lutsker, R. J. Maurer, S. K. Min, I. Mitchell, C. Negre, T. A. Niehaus, A. M. N. Niklasson, A. J. Page, A. Pecchia, G. Penazzi, M. P. Persson, J. Řezáč, C. G. Sánchez, M. Sternberg, M. Stöhr, F. Stuckenberg, A. Tkatchenko, V. W.-z. Yu, and T. Frauenheim, J. Chem. Phys. **152**, 124101 (2020).

[25] M. Gaus, Q. Cui, and M. Elstner, J. Chem. Theory Comput. **7**, 931 (2011).

[26] J. Řezáč, J. Chem. Theory Comput. **13**, 4804 (2017).

Table A.1: The fitted GAL19 parameters for Au [100] and Au [111] surfaces, and for the different fitting procedures of GAL19, with the texts in red correspond to parameters that are not optimized.

Parameters	Au [100]	Au [111]	AuNP-fmix	AuNP-f79	AuNP-fall
R_O (Å)	2.03	2.10	2.03	2.03	2.03
R_H (Å)	0.34	0.33	0.34	0.34	0.34
$b_\perp$ ($Å^{-2}$)	0.52	0.70	0.397	0.405	0.377
$b_\parallel$($Å^{-2}$)	0.13	0.09	0.310	0.175	0.234
B ($Å^{-1}$)	25890	273900	13890.2	14251	14150.1
a_1 (kcal/mol)	22.42	18.51	14.55	13.35	10.93
a_2 (kcal/mol)	11.56	9.74	-3.94	7.65	-2.29
a_3 (kcal/mol)	-5.79	-4.26	1.45	-4.92	4.18
a_4 (kcal/mol)	4.72	4.07	-19.11	5.10	-12.41
ε_s (kcal/mol)	14.73	7.95	137.66	32.42	5.47
A (kcal/mol)	3.48	4.42	2.82	3.15	3.05
A_H (kcal/mol)	3305	3313	3304	3301	3301
C ($Å^6$ kcal/mol)	918	918	918	918	918

A.1.2 Development of an Accurate Force Field for the Au-Water Interaction

Table A.2: The fitted GAL21 parameters for reported Au surface, and for AuNP systems fitted in this work.

Parameters	Au	AuNP21-fmix	AuNP21-f79
$b_{\perp,0}$ ($Å^{-2}$)	0.43	0.42	0.25
$b_{\perp,1}$ ($Å^{-2}$)	0.00	-0.00	0.01
$b_{\parallel,0}$ ($Å^{-2}$)	0.09	0.19	0.21
$b_{\parallel,1}$ ($Å^{-2}$)	0.00	0.02	0.00
B_0 ($Å^{-1}$)	3.49	3.32	3.45
B_1 ($Å^{-1}$)	-0.09	-0.09	-0.01
$B_{H,0}$ ($Å^{-1}$)	4.69	3.19	3.57
$B_{H,1}$ ($Å^{-1}$)	-0.18	0.00	-0.10
$a_{1,0}$ (kcal/mol)	-122.35	-69.93	51.15
$a_{1,1}$ (kcal/mol)	43.43	30.29	-19.75
$a_{1,2}$ (kcal/mol)	-3.20	-2.86	2.06
$a_{2,0}$ (kcal/mol)	10.64	2.87	10.36
$a_{2,1}$ (kcal/mol)	-1.50	-0.66	-1.75
$a_{2,2}$ (kcal/mol)	0.07	0.08	-0.00
$a_{3,0}$ (kcal/mol)	-13.00	-0.82	-23.13
$a_{3,1}$ (kcal/mol)	-0.26	-0.39	-0.26
$a_{3,2}$ (kcal/mol)	0.26	-0.12	0.68
$a_{4,0}$ (kcal/mol)	0.58	0.43	0.56
$a_{4,1}$ (kcal/mol)	0.00	-0.76	-0.51
$a_{4,2}$ (kcal/mol)	-0.01	-0.01	-0.01
$\varepsilon_{a,0}$ (kcal/mol)	0.54	-0.22	-1.77
$\varepsilon_{a,1}$ (kcal/mol)	3.47	24.16	17.68
$\varepsilon_{a,2}$ (kcal/mol)	-0.28	-0.22	-0.29
A_0 (kcal/mol)	7553.69	19464.38	31858.89
A_1 (kcal/mol)	-175.69	-654.52	-235.42
$A_{H,0}$ (kcal/mol)	32286.66	4533.44	6336.65
$A_{H,1}$ (kcal/mol)	-3619.43	16.08	-495.70
C ($Å^6$.kcal/mol)	918	918	918

Table A.3: The fitted GAL21 parameters for polarizable force field.

Parameters	Pol-2T-fmix	Pol-2T-f79	Pol-fmix	Pol-f79
$b_{\perp,0}$ (Å^{-2})	0.39	0.28	0.50	0.18
$b_{\perp,1}$ (Å^{-2})	0.005	0.002	-0.02	0.02
$b_{\parallel,0}$ (Å^{-2})	0.17	0.18	0.13	0.14
$b_{\parallel,1}$ (Å^{-2})	0.02	-0.005	0.03	0.00
B_0 (Å^{-1})	3.54	4.70	3.45	4.65
B_1 (Å^{-1})	-0.07	-0.01	-0.08	-0.01
$B_{H,0}$ (Å^{-1})	2.997	3.03	2.69	3.05
$B_{H,1}$ (Å^{-1})	-0.008	-0.04	0.04	-0.05
$a_{1,0}$ (kcal/mol)	-1.24	-6.28	27.72	19.85
$a_{1,1}$ (kcal/mol)	2.93	1.83	1.26	1.89
$a_{1,2}$ (kcal/mol)	-0.17	0.21	0.12	0.33
$a_{2,0}$ (kcal/mol)	0.14	-1.27	-2.75	-1.92
$a_{2,1}$ (kcal/mol)	0.37	-0.40	0.07	-0.59
$a_{2,2}$ (kcal/mol)	-0.004	-0.004	-0.00	-0.00
$a_{3,0}$ (kcal/mol)	-3.69	-1.26	-0.70	-0.41
$a_{3,1}$ (kcal/mol)	-0.26	-0.18	-0.20	-0.11
$a_{3,2}$ (kcal/mol)	-0.03	-0.03	-0.04	-0.02
$a_{4,0}$ (kcal/mol)	0.39	0.42	0.37	0.41
$a_{4,1}$ (kcal/mol)	-0.28	-1.61	-4.53	-2.90
$a_{4,2}$ (kcal/mol)	-0.01	-0.01	-0.01	-0.01
$\varepsilon_{a,0}$ (kcal/mol)	-0.19	-0.81	1.06	-0.65
$\varepsilon_{a,1}$ (kcal/mol)	17.48	7.62	15.60	6.65
$\varepsilon_{a,2}$ (kcal/mol)	-0.26	-0.29	-0.26	-0.28
A_0 (kcal/mol)	27478.00	353921.8	21868.23	304737.97
A_1 (kcal/mol)	-405.62	-276.48	-294.66	-277.94
$A_{H,0}$ (kcal/mol)	2681.43	2190.00	2193.13	2339.22
$A_{H,1}$ (kcal/mol)	17.44	3.99	55.47	14.57
C (Å^6.kcal/mol)	918	918	918	

Table A.4: The RMSD (in kcal/mol) calculated for the dataset with the fitted parameters for GAL19. The values in italic correspond to geometries included in the training data set.

Parameters	Au_{39}	Au_{55}				Au_{79}				Au_{147}	Au_{201}
	Monomer	Monomer	Dimer	Trimer	Tetramer	Monomer	Dimer	Trimer	Tetramer	Monomer	Monomer
AuNP-fmix	*1.59*	*0.77*	1.12	2.80	3.25	*1.43*	2.62	3.06	4.06	2.91	1.62
AuNP-f79	3.06	1.78	2.04	1.58	1.62	*1.40*	2.06	3.05	3.06	1.38	0.96
AuNP-fall	*2.25*	*1.24*	*1.17*	*1.94*	*2.26*	*1.19*	*1.69*	*2.50*	*3.04*	2.04	1.18

Table A.5: The RMSD (in kcal/mol) calculated for the dataset with the fitted parameters for GAL21. The values in italic correspond to geometries included in the training data set.

Parameters	Au_{39}	Au_{55}				Au_{79}				Au_{147}	Au_{201}
	Monomer	Monomer	Dimer	Trimer	Tetramer	Monomer	Dimer	Trimer	Tetramer	Monomer	Monomer
AuNP21-fmix	*1.29*	*0.86*	1.34	3.20	3.44	*0.97*	1.88	2.66	4.11	2.27	1.10
AuNP21-f79	2.29	1.51	1.52	5.32	6.64	*0.64*	3.11	5.04	7.21	1.67	0.88
Polarizable FF											
P1T-fmix	*1.31*	*0.80*	1.01	2.32	2.96	*1.09*	1.98	2.80	3.09	3.00	1.49
P1T-f79	1.89	1.15	0.91	2.86	3.46	*0.52*	1.73	2.48	3.79	2.36	1.57
P2T-fmix	*1.29*	*0.78*	1.14	2.79	2.77	*0.86*	1.87	2.42	3.75	2.32	0.94
P2T-f79	1.91	1.13	3.29	3.29	3.33	*0.41*	1.76	2.39	3.69	2.09	1.06

Configuration	Frozen Energy	Polarization	Charge Transfer	Interaction Energy
CHF-1	63.6765	-19.6988	-25.1531	18.8247
CHF-2	35.1863	-11.9246	-17.2684	5.9933
CHF-3	13.7876	-5.7053	-10.4392	-2.3569
CHF-4	5.4744	-3.0729	-7.0036	-4.6022
CHF-5	1.3002	-1.6642	-4.6473	-5.0113
CHF-6	-0.8791	-0.8214	-2.8037	-4.5043
CHF-7	-1.5506	-0.4669	-1.8148	-3.8322
CHF-8	-1.7213	-0.3069	-1.2845	-3.3126
CHF-9	-1.7006	-0.1354	-0.8549	-2.6908
CHF-10	-1.5506	-0.0904	-0.5353	-2.1762
CHF-11	-1.3171	-0.0420	-0.3131	-1.6723
CHU-1	40.6744	-17.4317	-17.0778	6.1650
CHU-2	20.4035	-10.7856	-11.0946	-1.4767
CHU-3	7.6515	-5.9963	-6.6692	-5.0140
CHU-4	1.7994	-3.3770	-4.0780	-5.6556
CHU-5	-0.7850	-1.9328	-2.5268	-5.2446
CHU-6	-1.7897	-1.1641	-1.5420	-4.4958
CHU-7	-2.0121	-0.8308	-1.0204	-3.8633
CHU-8	-2.0036	-0.5512	-0.6028	-3.1576
CHU-9	-1.8686	-0.3778	-0.4057	-2.6520
CHU-10	-1.6376	-0.2679	-0.2514	-2.1569
CHU-11	-1.4336	-0.2065	-0.1573	-1.7973
CHDown-1	156.0360	-29.1846	-50.8830	75.9684
CHDown-2	68.3484	-11.3827	-27.1564	29.8093
CHDown-3	35.2256	-5.6109	-16.5282	13.0865
CHDown-4	17.7122	-2.8265	-10.1257	4.7600
CHDown-5	8.4725	-1.5145	-6.2060	0.7521
CHDown-6	3.5835	-0.8735	-3.7437	-1.0338
CHDown-7	1.0626	-0.5478	-2.2268	-1.7120
CHDown-8	-0.1534	-0.3345	-1.3339	-1.8219
CHDown-9	-0.6004	-0.2663	-0.9077	-1.7744
CHDown-10	-0.8748	-0.2016	-0.5059	-1.5823
CHDown-11	-0.9090	-0.1274	-0.3175	-1.3540
CHDang-1	128.2720	-24.7779	-40.9320	62.5621
CHDang-2	57.4568	-10.3594	-21.7689	25.3285
CHDang-3	33.1193	-5.8213	-14.2300	13.0680
CHDang-4	16.1886	-2.9228	-8.3280	4.9379
CHDang-5	7.1432	-1.5077	-4.7479	0.8877
CHDang-6	2.3315	-0.7664	-2.5580	-0.9929
CHDang-7	0.8053	-0.5050	-1.7366	-1.4363
CHDang-8	-0.1523	-0.3367	-1.0979	-1.5869
CHDang-9	-0.6262	-0.2479	-0.6934	-1.5674

CHDang-10	-0.8817	-0.1079	-0.4700	-1.4596
CHDang-11	-0.9115	-0.0735	-0.2293	-1.2143
EHF-1	67.7408	-23.0148	-25.0314	19.6947
EHF-2	33.8756	-12.6841	-15.8726	5.3189
EHF-3	13.9667	-5.9524	-9.6330	-1.6187
EHF-4	4.9846	-2.7832	-5.8777	-3.6763
EHF-5	1.5230	-1.4729	-3.9667	-3.9166
EHF-6	-0.4666	-0.7286	-2.3254	-3.5207
EHF-7	-1.0144	-0.4963	-1.6681	-3.1788
EHF-8	-1.3199	-0.3116	-1.0738	-2.7053
EHF-9	-1.3624	-0.1471	-0.6488	-2.1583
EHF-10	-1.2972	-0.1141	-0.4352	-1.8464
EHF-11	-1.1634	-0.0654	-0.2973	-1.5260
EHU-1	55.3725	-22.1711	-20.5925	12.6088
EHU-2	22.9265	-11.3225	-11.1907	0.4133
EHU-3	10.6838	-6.6356	-7.0258	-2.9776
EHU-4	4.3474	-3.9307	-4.4371	-4.0205
EHU-5	0.6966	-2.1035	-2.5092	-3.9161
EHU-6	-0.6052	-1.3310	-1.5625	-3.4986
EHU-7	-1.1834	-0.8037	-1.0334	-3.0205
EHU-8	-1.3704	-0.5567	-0.6367	-2.5638
EHU-9	-1.3613	-0.3699	-0.3339	-2.0651
EHU-10	-1.2889	-0.2582	-0.2784	-1.8255
EHU-11	-1.1623	-0.1944	-0.1623	-1.5191
EHDown-1	137.9475	-26.1487	-46.9771	64.8216
EHDown-2	78.0846	-13.5028	-30.4743	34.1075
EHDown-3	38.2096	-5.9127	-17.8639	14.4330
EHDown-4	18.2443	-2.7586	-10.3912	5.0946
EHDown-5	9.6230	-1.5921	-6.6682	1.3628
EHDown-6	3.1250	-0.7415	-3.4944	-1.1109
EHDown-7	1.4350	-0.5591	-2.4617	-1.5858
EHDown-8	0.1165	-0.4089	-1.5391	-1.8315
EHDown-9	-0.6490	-0.2978	-0.8615	-1.8083
EHDown-10	-0.8927	-0.2170	-0.5723	-1.6820
EHDown-11	-0.9615	-0.1730	-0.3742	-1.5088
EHDang-1	158.5935	-29.6876	-49.9980	78.9080
EHDang-2	79.0338	-13.9157	-29.0324	36.0857
EHDang-3	40.9164	-6.7625	-17.5419	16.6120
EHDang-4	16.9849	-2.7689	-9.0617	5.1542
EHDang-5	7.5528	-1.4304	-5.0694	1.0530
EHDang-6	3.8044	-0.9219	-3.3128	-0.4304
EHDang-7	1.2348	-0.5737	-1.9770	-1.3159
EHDang-8	-0.0629	-0.3035	-1.2470	-1.6134

EHDang-9	-0.6812	-0.2161	-0.7455	-1.6428
EHDang-10	-0.9167	-0.1565	-0.4385	-1.5117
EHDang-11	-0.9482	-0.1060	-0.2340	-1.2882
FHF-1	100.2948	-25.1456	-28.1441	47.0050
FHF-2	26.3100	-7.7400	-10.2112	8.3588
FHF-3	9.3920	-3.7924	-5.6512	-0.0516
FHF-4	2.9285	-2.1883	-3.5013	-2.7611
FHF-5	-0.1264	-1.3944	-2.3588	-3.8796
FHF-6	-1.2877	-0.9985	-1.7120	-3.9982
FHU-1	167.5413	-42.0558	-38.5817	86.9038
FHU-2	79.2455	-20.1728	-19.9292	39.1435
FHU-3	41.4903	-11.0140	-12.0050	18.4712
FHU-4	26.0203	-7.3312	-8.5971	10.0920
FHU-5	16.6374	-5.0674	-6.4159	5.1541
FHU-6	4.7523	-2.3086	-3.3408	-0.8971
FHU-7	-0.5122	-0.9276	-1.3931	-2.8329
FHDown-1	431.2389	-80.6283	-112.1732	238.4375
FHDown-2	141.2238	-23.8516	-51.6912	65.6810
FHDown-3	70.6446	-11.6272	-30.9021	28.1154
FHDown-4	27.7640	-4.9673	-15.3823	7.4144
FHDown-5	9.4086	-2.3280	-7.6314	-0.5508
FHDown-6	4.0265	-1.5660	-5.0311	-2.5706
FHDown-7	-0.6071	-0.7371	-2.2809	-3.6251
FHDang-1	254.8542	-58.5126	-72.4186	123.9231
FHDang-2	59.0588	-12.8640	-22.7926	23.4022
FHDang-3	28.7096	-6.9997	-13.7652	7.9447
FHDang-4	15.5263	-4.5142	-9.2856	1.7264
FHDang-5	6.8144	-2.6980	-5.8744	-1.7580
FHDang-6	1.2563	-1.5119	-3.2594	-3.5150
FHDang-7	-1.2073	-0.8537	-1.7128	-3.7739

Table A.6: The energy decomposition analysis of water adsorbed on Au$_{39}$

Configuration	Frozen Energy	Polarization	Charge Transfer	Interaction Energy
THF-1	63.3249	-21.3598	-23.0869	18.8782
THF-2	29.4055	-10.9274	-13.7932	4.6850
THF-3	13.0895	-5.4698	-8.6220	-1.0023
THF-4	5.3076	-2.7640	-5.3640	-2.8204
THF-5	1.2603	-1.4309	-3.1539	-3.3244
THF-6	-0.2129	-0.8421	-2.1135	-3.1685
THF-7	-1.1448	-0.4802	-1.1188	-2.7438
THF-8	-1.8297	-0.2411	-0.6727	-2.7435

THF-9	-1.5152	-0.1312	-0.2096	-1.8560
THF-10	-1.4566	-0.1024	-0.0307	-1.5897
THF-11	-1.3037	-0.0137	0.1224	-1.1950
THU-1	59.5800	-23.0302	-20.9011	15.6487
THU-2	25.9019	-11.9369	-11.2895	2.6755
THU-3	10.2445	-6.1058	-6.2845	-2.1458
THU-4	4.2923	-3.6519	-3.9315	-3.2911
THU-5	0.6935	-2.0338	-2.1023	-3.4426
THU-6	-0.6832	-1.3249	-1.1582	-3.1663
THU-7	–1.4259	-0.7776	-0.5282	-2.7317
THU-8	–1.6086	-0.5583	-0.1627	-2.3296
THU-9	–1.5788	-0.3398	0.0508	-1.8679
THU-10	-1.4448	-0.1815	0.1161	-1.5102
THU-11	-1.2847	-0.1433	0.2288	-1.1992
THDown-1	142.6336	-27.5527	-47.1674	67.9136
THDown-2	78.2228	-13.6929	-29.6762	34.8538
THDown-3	37.3756	-5.8652	-16.9741	14.5363
THDown-4	19.4359	-2.9800	-10.4782	5.9777
THDown-5	9.4277	-1.6165	-6.2833	1.5280
THDown-6	4.1064	-0.9431	-3.6791	-0.5158
THDown-7	1.2180	-0.5522	-2.1404	-1.4746
THDown-8	-0.2567	-0.3445	-1.1258	-1.7269
THDown-9	-0.9470	-0.2624	-0.5145	-1.7239
THDown-10	-1.1929	-0.1412	-0.1914	-1.5255
THDown-11	-1.2224	-0.1155	0.0370	-1.3008
THDang-1	161.5567	-30.1361	-48.4249	82.9957
THDang-2	81.6120	-13.8090	-28.1771	39.6259
THDang-3	40.9561	-6.4000	-16.4050	18.1512
THDang-4	20.3214	-3.1344	-9.5256	7.6614
THDang-5	10.7610	-1.7608	-5.9526	3.0477
THDang-6	3.6537	-0.8839	-2.8370	-0.0672
THDang-7	1.3623	-0.5685	-1.6905	-0.8967
THDang-8	0.0734	-0.4160	-0.9457	-1.2883
THDang-9	-0.7398	-0.2417	-0.3870	-1.3686
THDang-10	-1.0254	-0.1870	-0.0753	-1.2876
THDang-11	-1.1193	-0.0427	-0.0163	-1.1783
EHF-1	72.2063	-22.2791	-26.8380	23.0892
EHF-2	38.6690	-13.0396	-17.6751	7.9543
EHF-3	16.3265	-6.3347	-10.6068	-0.6150
EHF-4	7.4285	-3.6621	-7.1480	-3.3816
EHF-5	1.9029	-1.8204	-4.2438	-4.1613
EHF-6	-0.3922	-1.0159	-2.5577	-3.9659
EHF-7	-1.3661	-0.6401	-1.5744	-3.5806

EHF-8	-1.7984	-0.3665	-0.8603	-3.0252
EHF-9	-1.8637	-0.1443	-0.4876	-2.4956
EHF-10	-1.7652	-0.1079	-0.1732	-2.0463
EHF-11	-1.6008	-0.0797	0.0872	-1.5932
EHU-1	59.7551	-22.8575	-21.3212	15.5764
EHU-2	23.5276	-11.1852	-10.8659	1.4766
EHU-3	11.0866	-6.5073	-6.8569	-2.2776
EHU-4	3.8511	-3.5646	-4.1026	-3.8161
EHU-5	0.3909	-2.0237	-2.2678	-3.9006
EHU-6	-1.1365	-1.2222	-1.1504	-3.5090
EHU-7	-1.6173	-0.8880	-0.6728	-3.1781
EHU-8	-1.8404	-0.6406	-0.2714	-2.7524
EHU-9	-1.8323	-0.3825	-0.0803	-2.2950
EHU-10	-1.6985	-0.2868	0.1744	-1.8109
EHU-11	-1.5250	-0.2250	0.2523	-1.4977
EHDown-1	140.1175	-26.3626	-45.3453	68.4095
EHDown-2	74.0014	-12.7799	-27.5991	33.6224
EHDown-3	39.1382	-6.4029	-17.0891	15.6461
EHDown-4	17.6985	-2.8876	-9.6670	5.1439
EHDown-5	8.9451	-1.6788	-6.1038	1.1625
EHDown-6	3.0177	-0.9249	-3.2752	-1.1824
EHDown-7	0.6554	-0.6331	-1.9526	-1.9302
EHDown-8	-0.6190	-0.4250	-1.1142	-2.1582
EHDown-9	-1.2688	-0.2864	-0.5611	-2.1163
EHDown-10	-1.5273	-0.2212	-0.1583	-1.9068
EHDown-11	-1.5627	-0.0703	-0.0469	-1.6799
EHDang-1	212.1473	-38.1592	-59.7448	114.2432
EHDang-2	100.4194	-16.6992	-33.4856	50.2346
EHDang-3	49.4238	-7.8373	-19.2696	22.3169
EHDang-4	23.8500	-3.8149	-10.9016	9.1335
EHDang-5	10.7585	-1.9067	-6.0876	2.7642
EHDang-6	4.2845	-1.0543	-3.2675	-0.0372
EHDang-7	1.0582	-0.5820	-1.7045	-1.2283
EHDang-8	-0.3297	-0.3244	-0.9557	-1.6098
EHDang-9	-1.0768	-0.2158	-0.3530	-1.6457
EHDang-10	-1.2800	-0.1657	-0.0851	-1.5307
EHDang-11	-1.3350	-0.1221	0.1089	-1.3481
FHF-1	109.8209	-32.8498	-39.1739	37.7973
FHF-2	51.7797	-17.2604	-21.7859	12.7334
FHF-3	23.3617	-8.7256	-12.6373	1.9988
FHF-4	10.7052	-4.6751	-7.9284	-1.8983
FHF-5	4.3773	-2.6385	-5.0457	-3.3068
FHF-6	0.3758	-1.4136	-2.8232	-3.8611

FHF-7	-1.0287	-0.9376	-1.7968	-3.7631
FHF-8	-1.7809	-0.5723	-1.0788	-3.4320
FHF-9	-2.1331	-0.3221	-0.6060	-3.0612
FHF-10	-2.1646	-0.2372	-0.2743	-2.6761
FHF-11	-2.0912	-0.1818	-0.0650	-2.3379
FHU-1	51.8698	-19.3978	-18.4930	13.9790
FHU-2	30.8161	-12.6674	-12.4856	5.6630
FHU-3	12.8119	-6.5168	-6.9124	-0.6173
FHU-4	4.8836	-3.5605	-4.1436	-2.8206
FHU-5	0.9783	-2.0779	-2.3754	-3.4750
FHU-6	-0.9218	-1.2688	-1.2517	-3.4423
FHU-7	-1.7422	-0.8212	-0.5862	-3.1496
FHU-8	-1.9734	-0.5510	-0.2508	-2.7751
FHU-9	-1.9752	-0.3703	-0.0407	-2.3862
FHU-10	-1.8381	-0.2822	0.1458	-1.9744
FHU-11	-1.6571	-0.1170	0.1407	-1.6333
FHDown-1	168.2964	-31.7758	-52.3043	84.2163
FHDown-2	93.4929	-16.2694	-33.1235	44.1000
FHDown-3	48.2824	-7.9171	-20.0528	20.3125
FHDown-4	23.6415	-3.9654	-11.9830	7.6931
FHDown-5	10.4474	-2.0947	-7.0129	1.3398
FHDown-6	3.1650	-1.1703	-3.7311	-1.7365
FHDown-7	0.5146	-0.7607	-2.4126	-2.6587
FHDown-8	-1.3487	-0.5206	-1.2222	-3.0915
FHDown-9	-2.0710	-0.3231	-0.6561	-3.0502
FHDown-10	-2.2826	-0.2610	-0.3127	-2.8564
FHDown-11	-2.2826	-0.2061	-0.0329	-2.5217
FHDang-1	123.3189	-24.7692	-36.8321	61.7176
FHDang-2	62.3890	-12.0398	-21.3730	28.9762
FHDang-3	36.8923	-7.2334	-14.2799	15.3789
FHDang-4	17.6108	-3.8640	-8.6081	5.1386
FHDang-5	7.5044	-2.0975	-5.0741	0.3328
FHDang-6	2.4898	-1.3308	-3.1309	-1.9719
FHDang-7	-0.2089	-0.8935	-1.8689	-2.9713
FHDang-8	-1.3533	-0.6171	-1.2926	-3.2629
FHDang-9	-2.0545	-0.4613	-0.7324	-3.2482
FHDang-10	-2.3101	-0.2852	-0.4265	-3.0219
FHDang-11	-2.3488	-0.2298	-0.1687	-2.7473

Table A.7: The energy decomposition analysis of water adsorbed on Au_{79}

A.2 Simulating GNP-ligand interface

A.2.1 Interaction Between Organic Molecules and A Gold Nanoparticle: A Quantum Chemical Topological Analysis

Theoretical Chemistry Accounts manuscript No.
(will be inserted by the editor)

Supplementary Information
Interaction between Organic Molecules and a Gold Nanoparticle: a Quantum Chemical Topological Analysis

Rika Tandiana · Nguyen-Thi Van-Oanh ·
Carine Clavaguéra

Received: date / Accepted: date

Rika Tandiana
Université Paris-Saclay
CNRS, Institut de Chimie Physique, UMR8000
91405 Orsay, France E-mail: rika.tandiana@universite-paris-saclay.fr

Van-Oanh Nguyen-Thi
Université Paris-Saclay
CNRS, Institut de Chimie Physique, UMR8000
91405 Orsay, France E-mail: van-oanh.nguyen-thi@universite-paris-saclay.fr

Carine Clavaguéra
Université Paris-Saclay
CNRS, Institut de Chimie Physique, UMR8000
91405 Orsay, France E-mail: carine.clavaguera@universite-paris-saclay.fr

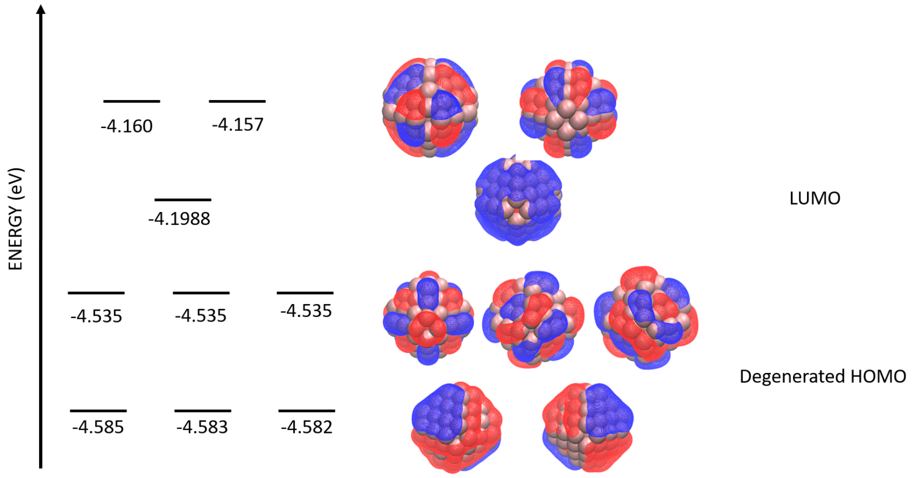

Fig. S1 The 5 highest occupied and 3 lowest unoccupied molecular orbitals of Au_{79}.

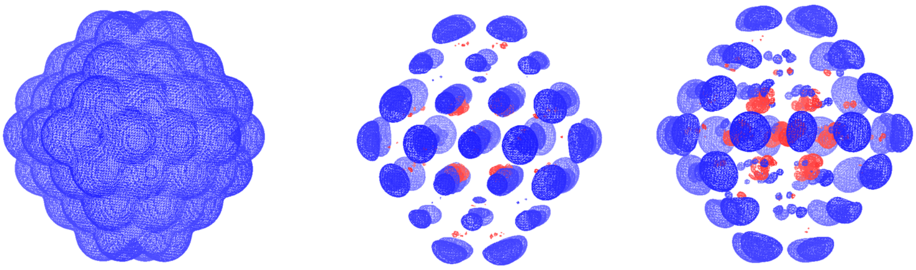

Fig. S2 Condensed Fukui analysis of Au_{79}: $f^{-}(r)$ (isosurface: 0.01) (left), $f^{+}(r)$ (isosurface: 0.0002) (middle), and $f^{0}(r)$ (average of f^{-} and f^{+}, isosurface: 0.0002) (right).

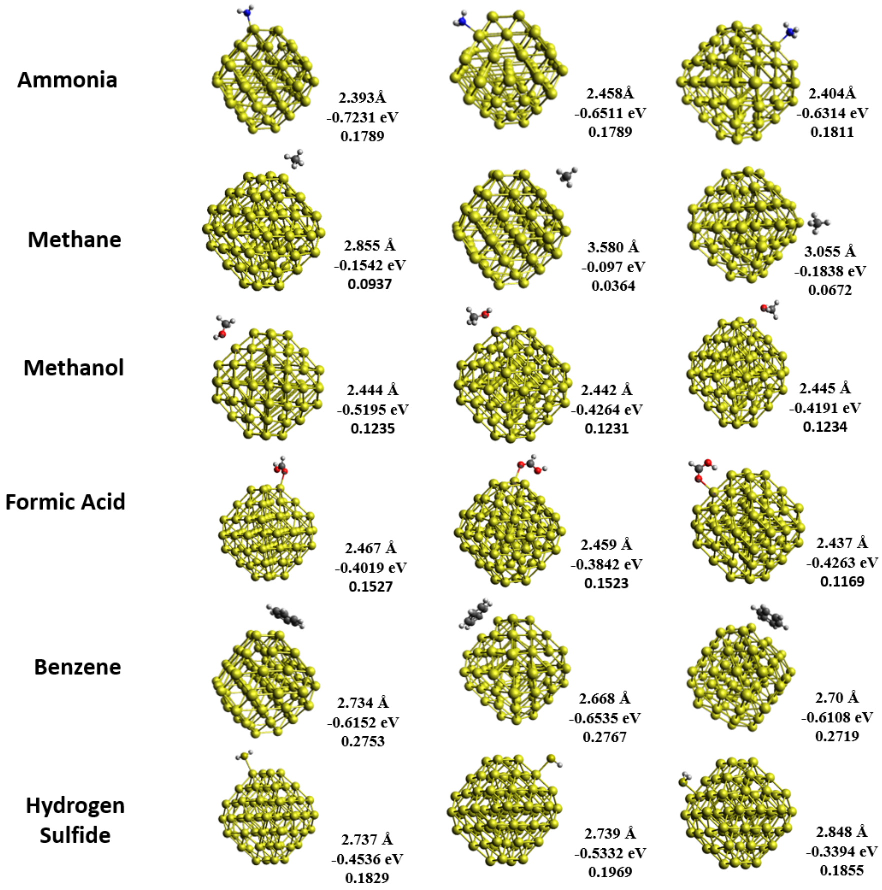

Fig. S3 The optimized geometry of Au_{79} interacting with the various organic molecules along with the interaction energy (eV) and the charge transfer (e) using Mulliken population scheme.

Table S1 The condensed Fukui analysis of Au_{79}.

Atom	$f^{-}(r)$	$f^{+}(r)$	$f^{0}(r)$	$\Delta f(r)$
Au	-0.010	-0.013	-0.012	-0.003
Au	0.010	-0.013	-0.002	-0.023
Au	0.010	-0.013	-0.002	-0.023
Au	0.014	0.018	0.016	0.004
Au	0.015	0.017	0.016	0.002
Au	0.025	0.024	0.024	-0.001
Au	-0.000	-0.003	-0.002	-0.003
Au	0.024	0.026	0.025	0.002
Au	0.025	0.024	0.024	-0.001
Au	0.024	0.025	0.025	0.001
Au	0.006	0.016	0.011	0.010
Au	0.007	0.015	0.011	0.008
Au	0.007	0.013	0.010	0.006
Au	0.011	0.002	0.007	-0.009
Au	0.015	0.016	0.015	0.001
Au	0.010	-0.012	-0.001	-0.022
Au	0.013	0.021	0.017	0.008
Au	0.006	-0.004	0.001	-0.010
Au	0.025	0.022	0.024	-0.003
Au	-0.001	-0.003	-0.002	-0.002
Au	0.025	0.024	0.024	-0.001
Au	0.024	0.026	0.025	0.001
Au	0.024	0.025	0.025	0.001
Au	0.007	0.013	0.010	0.005
Au	0.006	0.015	0.011	0.009
Au	0.011	0.004	0.007	-0.007
Au	0.006	0.017	0.011	0.011
Au	0.013	0.020	0.017	0.007
Au	0.005	-0.002	0.001	-0.007
Au	0.012	0.022	0.017	0.010
Au	0.006	-0.005	0.001	-0.011
Au	0.025	0.024	0.024	-0.001
Au	-0.004	0.002	-0.001	0.006
Au	0.025	0.025	0.025	0.000
Au	0.025	0.024	0.024	-0.000
Au	0.025	0.025	0.025	0.000
Au	0.007	0.013	0.010	0.005
Au	0.006	0.017	0.011	0.011
Au	0.007	0.014	0.010	0.007
Au	0.011	0.003	0.007	-0.008
Au	0.025	0.024	0.024	-0.001
Au	-0.000	-0.004	-0.002	-0.004
Au	0.025	0.022	0.024	-0.003
Au	0.024	0.025	0.024	0.000
Au	0.024	0.026	0.025	0.001
Au	0.007	0.014	0.011	0.007
Au	0.006	0.016	0.011	0.010
Au	0.011	0.004	0.008	-0.007
Au	0.007	0.014	0.010	0.007
Au	0.015	0.017	0.016	0.002
Au	0.010	-0.013	-0.001	-0.023
Au	0.025	0.024	0.024	-0.001
Au	-0.001	-0.002	-0.002	-0.001
Au	0.025	0.024	0.024	-0.001
Au	0.025	0.025	0.025	0.000
Au	0.024	0.026	0.025	0.001
Au	0.006	0.016	0.011	0.010
Au	0.006	0.016	0.011	0.010
Au	0.012	0.002	0.007	-0.010
Au	0.008	0.011	0.010	0.003
Au	0.013	0.021	0.017	0.008
Au	0.006	-0.004	0.001	-0.010
Au	0.013	0.020	0.017	0.006
Au	0.005	-0.003	0.001	-0.008
Au	0.013	0.020	0.016	0.007
Au	0.005	-0.002	0.001	-0.006
Au	0.024	0.026	0.025	0.001
Au	-0.003	0.004	0.000	0.007
Au	0.025	0.025	0.025	0.001
Au	0.024	0.025	0.025	0.001
Au	0.025	0.025	0.025	0.000
Au	0.007	0.011	0.009	0.004
Au	0.005	0.018	0.011	0.014
Au	0.007	0.013	0.010	0.006
Au	0.011	0.001	0.006	-0.010
Au	0.013	0.021	0.017	0.008
Au	0.006	-0.005	0.001	-0.011

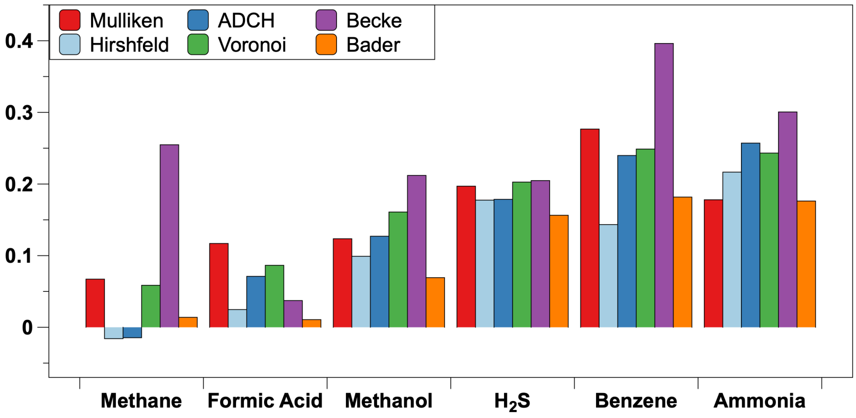

Fig. S4 Values of charge transfer (e) calculated with various population schemes at the DFT level.

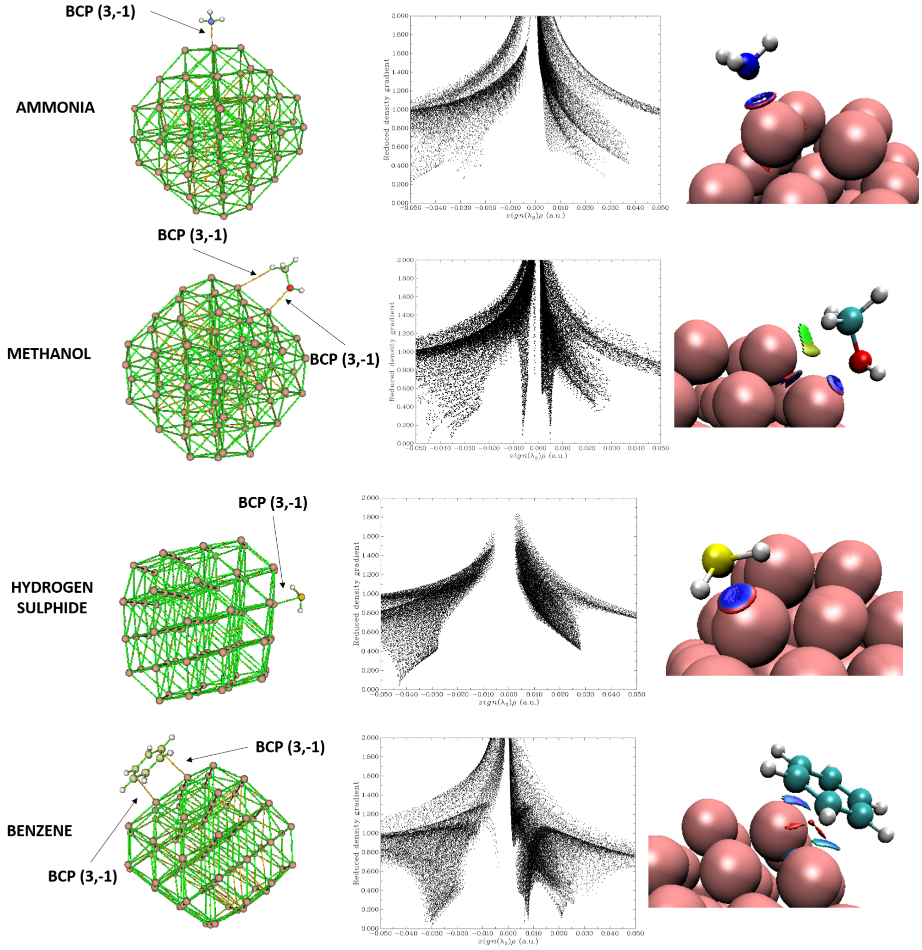

Fig. S5 BCPs from the QTAIM analysis and the respective RDG and NCI analysis.

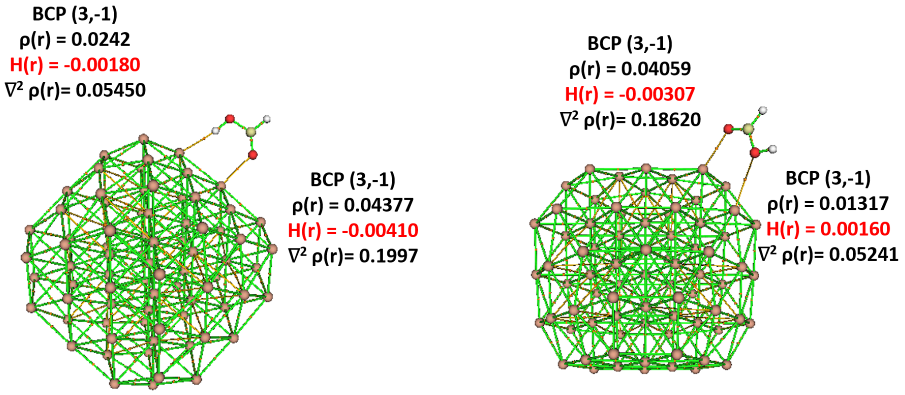

BCP (3,-1)
$\rho(r)$ = 0.0242
H(r) = -0.00180
$\nabla^2 \rho(r)$= 0.05450

BCP (3,-1)
$\rho(r)$ = 0.04377
H(r) = -0.00410
$\nabla^2 \rho(r)$= 0.1997

BCP (3,-1)
$\rho(r)$ = 0.04059
H(r) = -0.00307
$\nabla^2 \rho(r)$= 0.18620

BCP (3,-1)
$\rho(r)$ = 0.01317
H(r) = 0.00160
$\nabla^2 \rho(r)$= 0.05241

Fig. S6 BCPs from the QTAIM analysis of two configurations of formic acid, highlighting the different nature of the interaction as the geometry changes.

A.2.2 In-depth Theoretical Understanding of the Chemical Interaction of Aromatic Compounds with A Gold Nanoparticle

Electronic Supplementary Material (ESI) for Physical Chemistry Chemical Physics.

Supplementary Information: In-depth theoretical understanding of the chemical interaction of aromatic compounds with a gold nanoparticle

Rika Tandiana[a], Cécile Sicard-Roselli[a], Nguyen-Thi Van-Oanh[a], Stephan Steinmann[b], Carine Clavaguéra,*[a]

---

[a] *Institut de Chimie Physique, Université Paris-Saclay - CNRS, UMR 8000, 91405 Orsay, France; E-mail: carine.clavaguera@universite-paris-saclay.fr*

[b] *Laboratoire de Chimie, ENS de Lyon, 69364 Lyon, France*

Table S1 The Condensed Fukui Analysis of Au$_{32}$. The gold atoms are labeled as 5- and 6-coordinated.

Atom	f^-	f^+	f^0	Δf
Au(5)	0.028	0.047	0.037	0.020
Au(5)	0.028	0.047	0.038	0.019
Au(5)	0.028	0.047	0.037	0.019
Au(5)	0.028	0.047	0.037	0.019
Au(5)	0.027	0.047	0.037	0.020
Au(5)	0.027	0.047	0.037	0.020
Au(5)	0.028	0.047	0.038	0.019
Au(5)	0.028	0.047	0.037	0.019
Au(5)	0.028	0.047	0.038	0.019
Au(5)	0.028	0.047	0.037	0.020
Au(5)	0.027	0.047	0.037	0.020
Au(5)	0.028	0.047	0.037	0.020
Au(6)	0.034	0.022	0.028	-0.011
Au(6)	0.017	0.023	0.020	0.005
Au(6)	0.033	0.022	0.028	-0.011
Au(6)	0.033	0.022	0.027	-0.012
Au(6)	0.033	0.022	0.028	-0.011
Au(6)	0.017	0.023	0.020	0.005
Au(6)	0.033	0.022	0.028	-0.011
Au(6)	0.034	0.022	0.028	-0.011
Au(6)	0.033	0.022	0.027	-0.011
Au(6)	0.040	0.021	0.031	-0.019
Au(6)	0.033	0.022	0.027	-0.011
Au(6)	0.032	0.021	0.027	-0.011
Au(6)	0.040	0.021	0.031	-0.019
Au(6)	0.032	0.021	0.027	-0.011
Au(6)	0.032	0.021	0.027	-0.011
Au(6)	0.040	0.021	0.031	-0.019
Au(6)	0.032	0.021	0.027	-0.011
Au(6)	0.040	0.021	0.030	-0.019
Au(6)	0.040	0.021	0.030	-0.019
Au(6)	0.039	0.021	0.030	-0.018

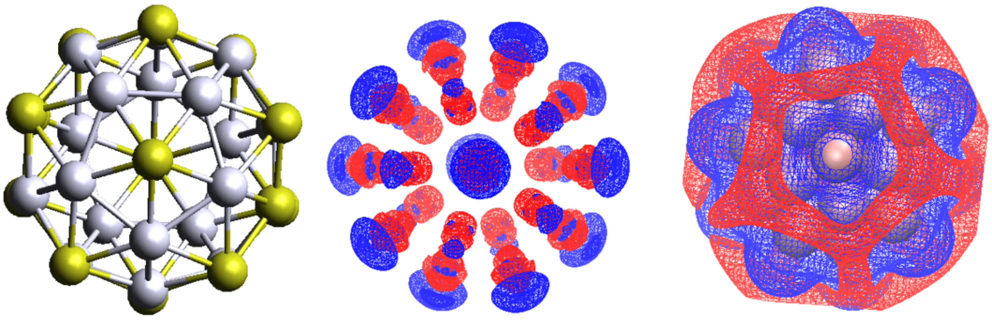

Fig. S1 The reactivity descriptors of Au$_{32}$:(left) geometry of Au$_{32}$ with the yellow balls representing the five-coordinated gold atoms and the silver balls representing the six-coordinated gold atoms, (middle) dual descriptor $\Delta f(r)$ Fukui function and (right) molecular electrostatic potential, with blue lobes corresponding to electrophilic sites and red lobes corresponding to nucleophilic sites.

Table S2 Evaluation of the dependence of basis set superposition error (BSSE) in kcal/mol calculated with Counterpoise method on choice of basis set and the uncorrected interaction energies, in kcal/mol, of the complexes calculated with either the LC-RECP and SC-RECP.

Complexes	SC-def2-SVP		SC-def2-TZVP		LC-DZVP	SC-DZVP	SC-TZVP
	E_{int}	BSSE	E_{int}	BSSE	Uncorrected E_{int}	Uncorrected E_{int}	Uncorrected E_{int}
Flat							
Benzene	-9.1	-3.9	-9.3	-2.3	-14.7	-9.7	-9.9
Benzoic Acid	-10.3	-7.3	-8.0	-3.6	-17.8	-9.8	-10.4
Acetophenone	-11.4	-6.8	-9.1	-3.0	-18.4	-10.1	-10.23
Ethyl Benzoate	-10.6	-5.5	-9.9	-3.0	-18.3	-11.5	-11.7
Toluene	-10.8	-4.5	-10.5	-2.6	-17.7	-11.7	-11.9
Phenol	-12.2	-6.1	-10.6	-2.9	-16.6	-11.8	-12.3
Aniline	-15.2	-6.2	-13.6	-3.0	-19.7	-15.1	-15.5
Thiophenol	-16.2	-6.9	-14.9	-3.3	-20.9	-15.6	-15.4
Perpendicular							
Toluene	1.4	-1.8	1.4	-1.0	-9.5	1.0	0.9
Acetophenone	0.3	-2.2	0.3	-1.4	-10.8	-0.1	-0.7
Benzoic Acid	-13.9	-6.1	-10.7	-1.9	-15.0	-11.1	-11.8

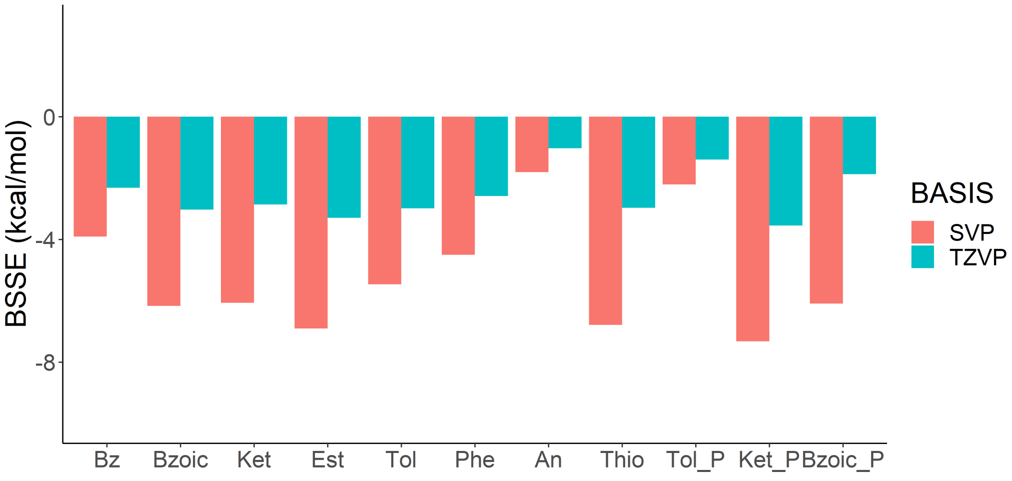

Fig. S2 BSSE estimates for SC-RECP associated with SVP or TZVP basis set.

Table S3 Energies of the complexes and fragments using SC-RECP and DZVP basis sets, along with the interaction energies and adsorption energies. "fr" stands for a frozen geometry of the fragments in the geometry of the complex. "opt" stands for an optimized geometry of the fragments.

Complexes	Total Energy (Ha)	E_{Au-fr} (Ha)	E_{Au-opt} (Ha)	E_{Org-fr} (Ha)	$E_{Org-opt}$ (Ha)	E_{Int} (kcal/mol)	E_{Ads} (kcal/mol)
Flat							
Benzene	-4582.8874	-4350.9346	-4350.9383	-231.9372	-231.9378	-9.8	-7.1
Benzoic Acid	-4771.3002	-4350.9333	-4350.9383	-420.3513	-420.3538	-9.8	-5.1
Acetophenone	-4735.3721	-4350.9333	-4350.9383	-384.4226	-384.4246	-10.2	-5.8
Ethyl Benzoate	-4849.7974	-4350.9343	-4350.9383	-498.8447	-498.8455	-11.6	-8.5
Toluene	-4622.1534	-4350.9348	-4350.9383	-271.2000	-271.2007	-11.8	-9.1
Phenol	-4658.0564	-4350.9348	-4350.9383	-307.1028	-307.1038	-11.9	-9.0
Aniline	-4638.2020	-4350.9345	-4350.9383	-287.2434	-287.2447	-15.2	-12.0
Thiophenol	-4980.7903	-4350.9329	-4350.9383	-629.8323	-629.8333	-15.8	-11.8
Perpendicular							
Toluene	-4622.1342	-4350.9355	-4350.9383	-271.2003	-271.2007	1.1	3.0
Acetophenone	-4735.3596	-4350.9355	-4350.9383	-384.4240	-384.4246	-0.1	2.0
Benzoic Acid	-4771.3047	-4350.9343	-4350.9383	-420.3526	-420.3538	-11.2	-7.9

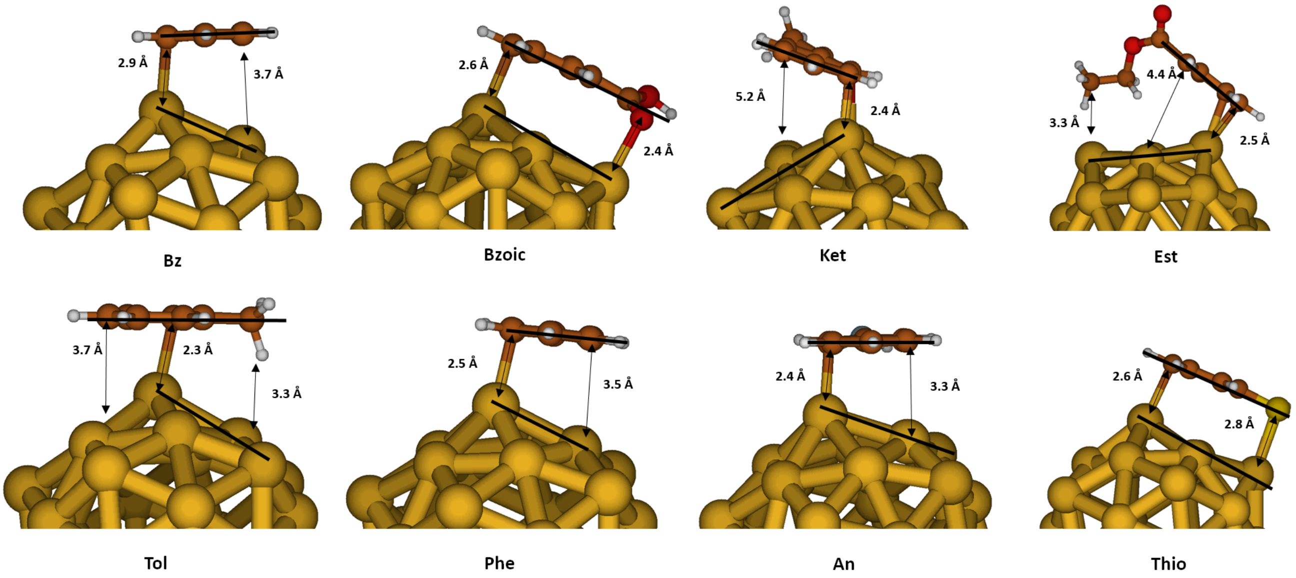

Fig. S3 A closer look at the geometry of the aromatic compounds on the surface of GNP: benzene, benzoic acid, acetophenone, ethyl benzoate, toluene, phenol, aniline, and thiophenol, with their respective distances of Au-C or Au-H, respectively. The black lines are guide for the eyes to highlight the planar region.

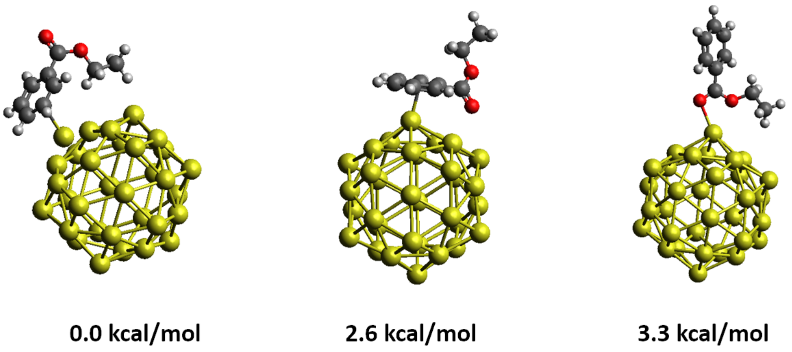

Fig. S4 Optimized configurations of ethyl benzoate and their relative electronic energy.

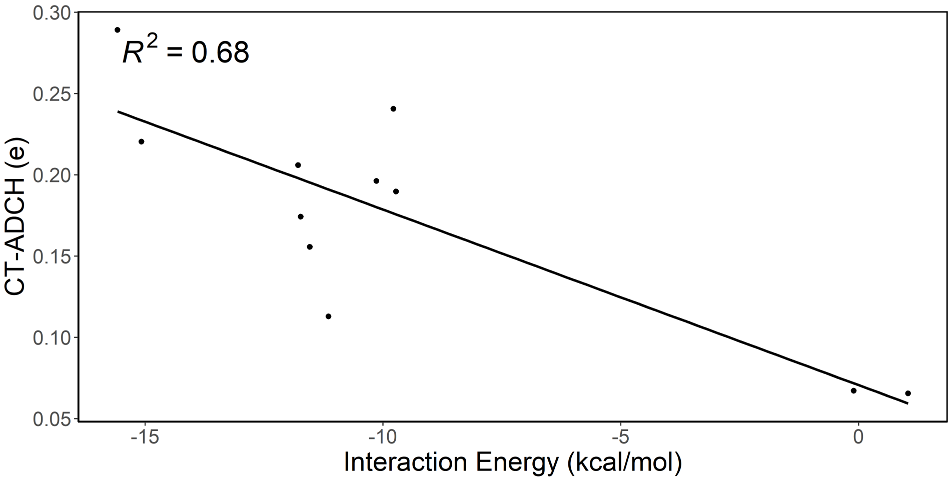

Fig. S5 Correlation of interaction energy and charge transfer as calculated using the ADCH scheme.

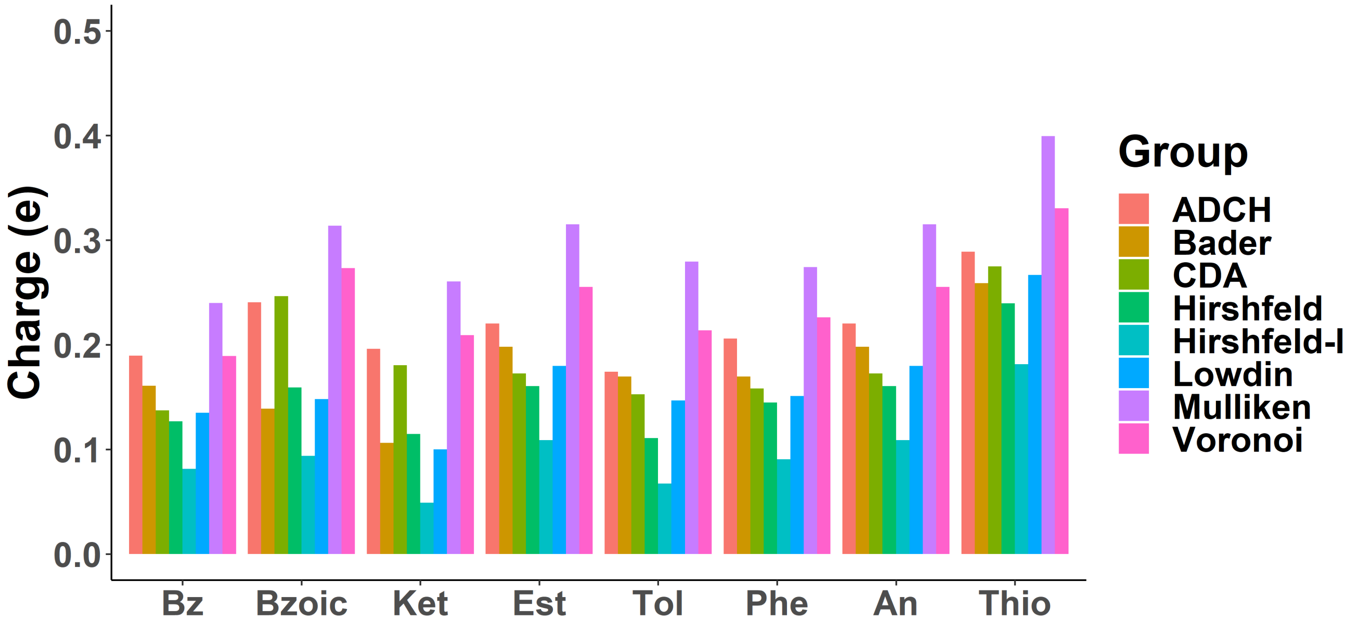

Fig. S6 Charge transfer values between GNP and aromatic fragments, calculated with different populations schemes for flat configurations.

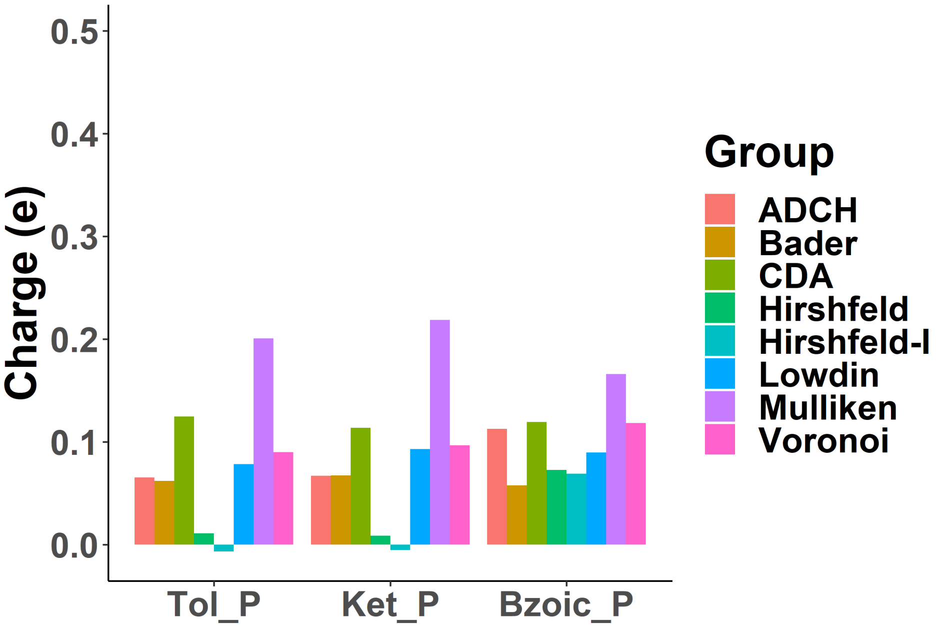

Fig. S7 Charge transfer values between GNP and aromatic fragments, calculated with different populations schemes for perpendicular configurations.

Table S4 Charge Decomposition Analysis framework applied to each of the complex to obtain donation (d), back-donation (b), d−b, polarization, re-arranged electrons, extended CDA (ECDA).

Complex	donation	back-donation	d−b	r (polarization)	re-arranged electron	ECDA
Flat						
Benzene	0.053	-0.085	0.137	-0.475	0.612	0.240
Benzoic Acid	0.104	-0.143	0.247	-0.693	0.939	0.314
Acetophenone	0.057	-0.124	0.180	-0.601	0.781	0.261
Ethyl Benzoate	0.055	-0.102	0.157	-0.591	0.748	0.283
Toluene	0.052	-0.101	0.153	-0.537	0.690	0.280
Phenol	0.064	-0.095	0.158	-0.506	0.664	0.274
Aniline	0.073	-0.099	0.172	-0.554	0.726	0.316
Thiophenol	0.136	-0.139	0.275	-0.783	1.058	0.399
Perpendicular						
Toluene	-0.008	-0.133	0.125	-0.286	0.411	0.201
Acetophenone	-0.022	-0.136	0.114	-0.320	0.434	0.218
Benzoic Acid	0.068	-0.051	0.119	-0.286	0.405	0.166

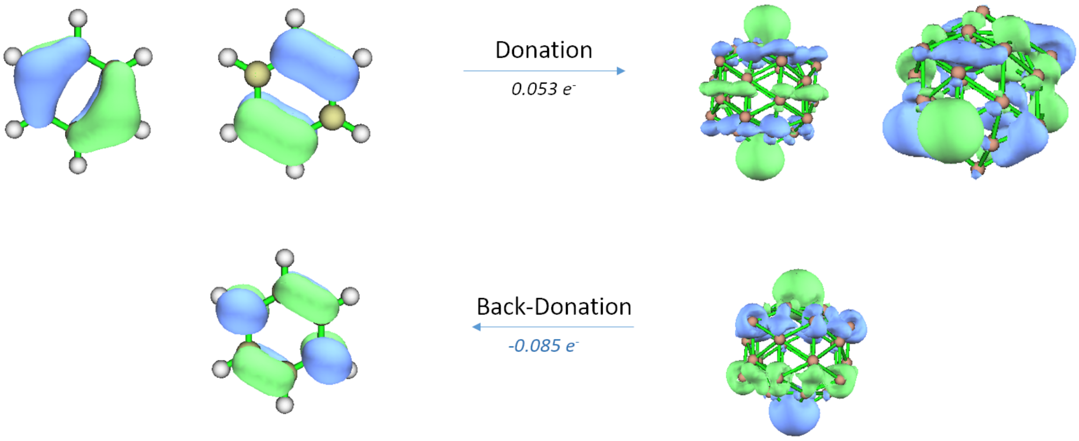

Fig. S8 The interacting molecular orbitals of benzene and GNP as obtained within Charge Decomposition Analysis (CDA) framework.

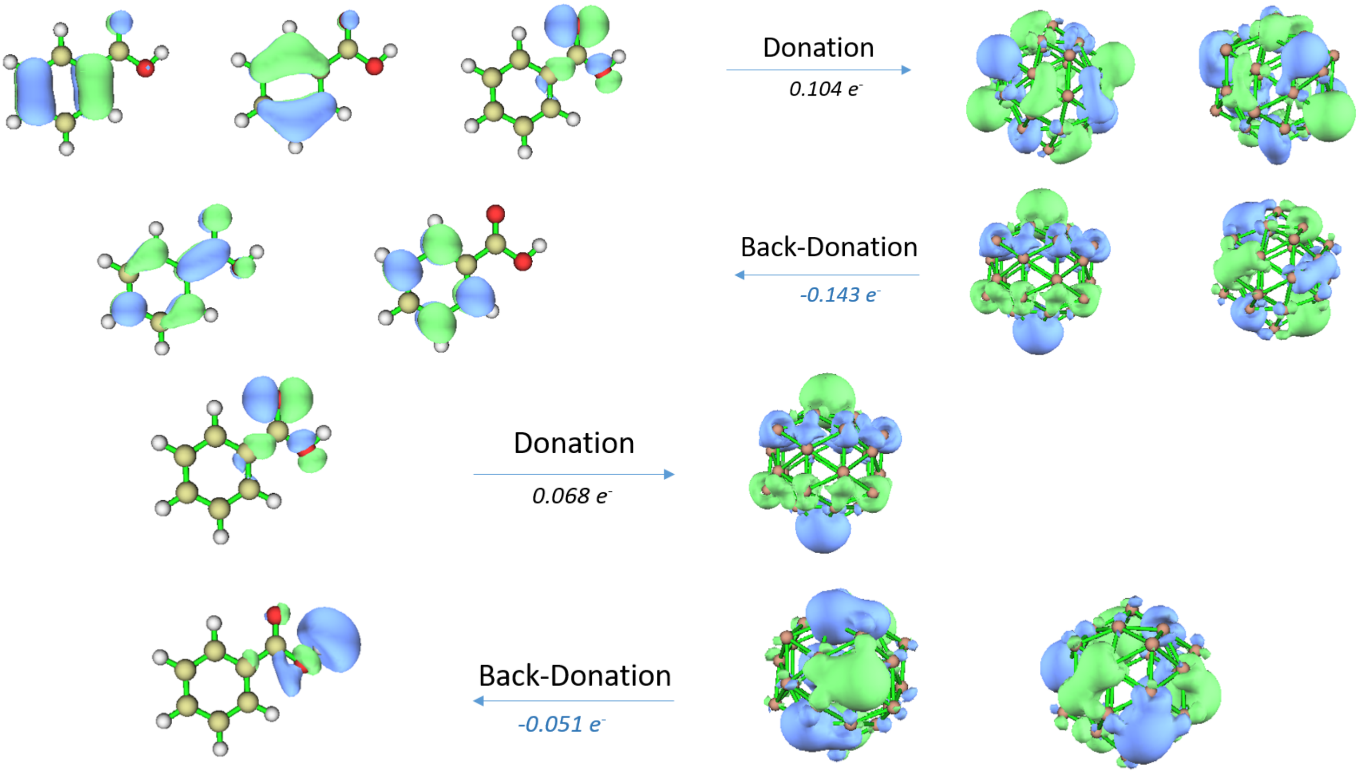

Fig. S9 The interacting molecular orbitals of benzoic acid and GNP adopting either flat (top) or perpendicular (bottom) configuration, as obtained within CDA framework.

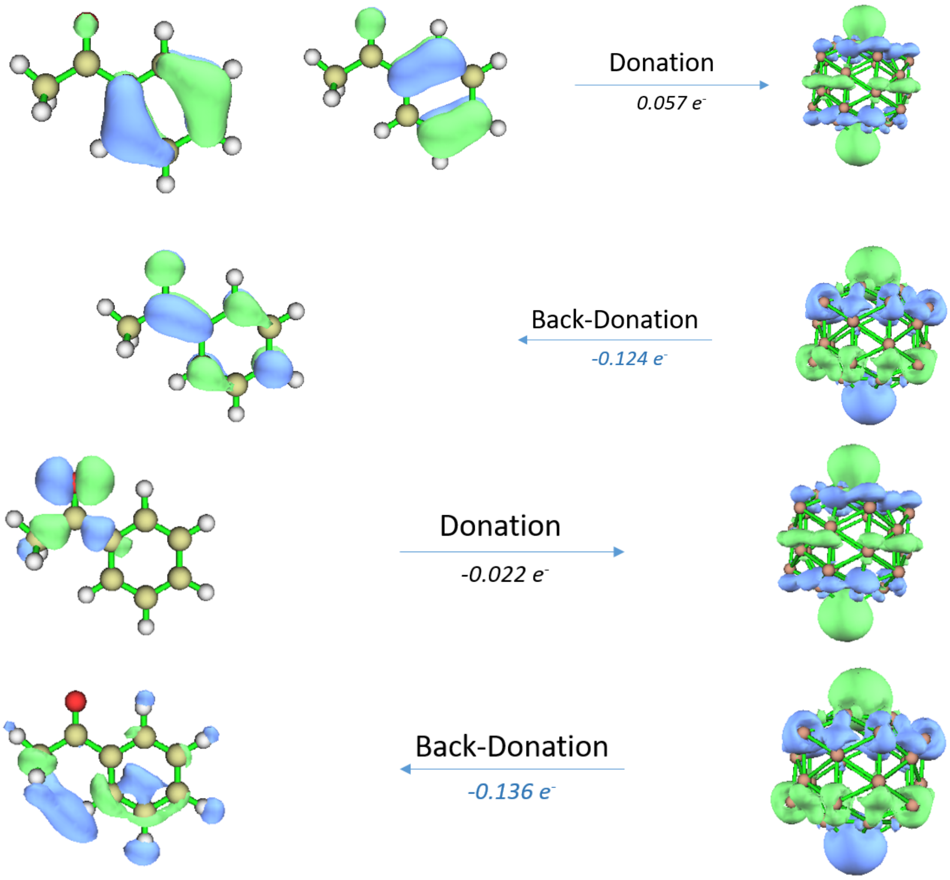

Fig. S10 The interacting molecular orbitals of acetophenone and GNP adopting either flat (top) or perpendicular (bottom) configuration, as obtained within CDA framework.

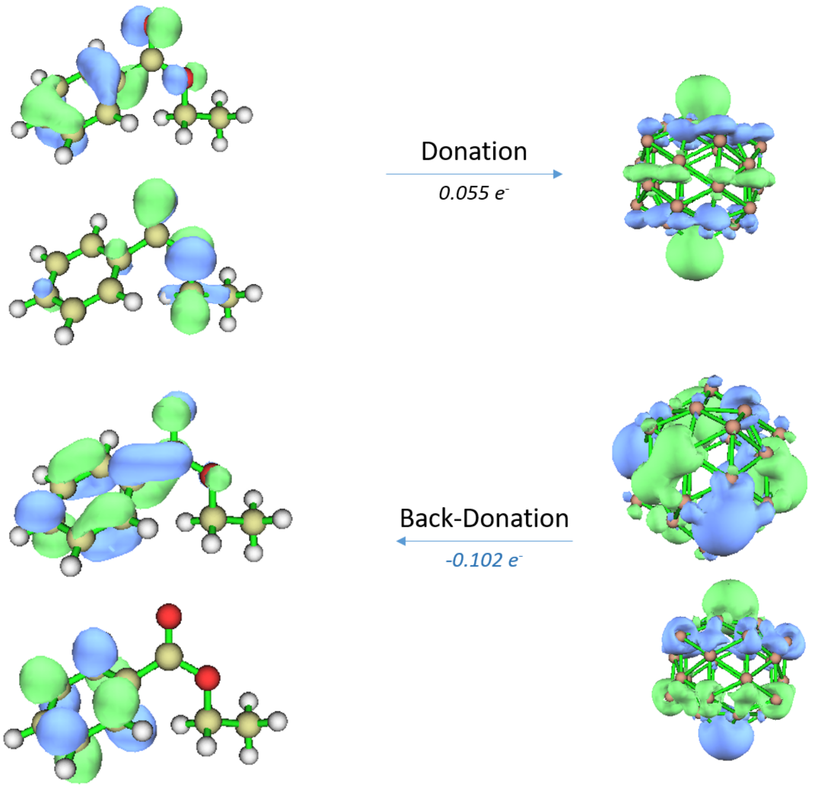

Fig. S11 The interacting molecular orbitals of ethyl benzoate and GNP, as obtained within CDA framework.

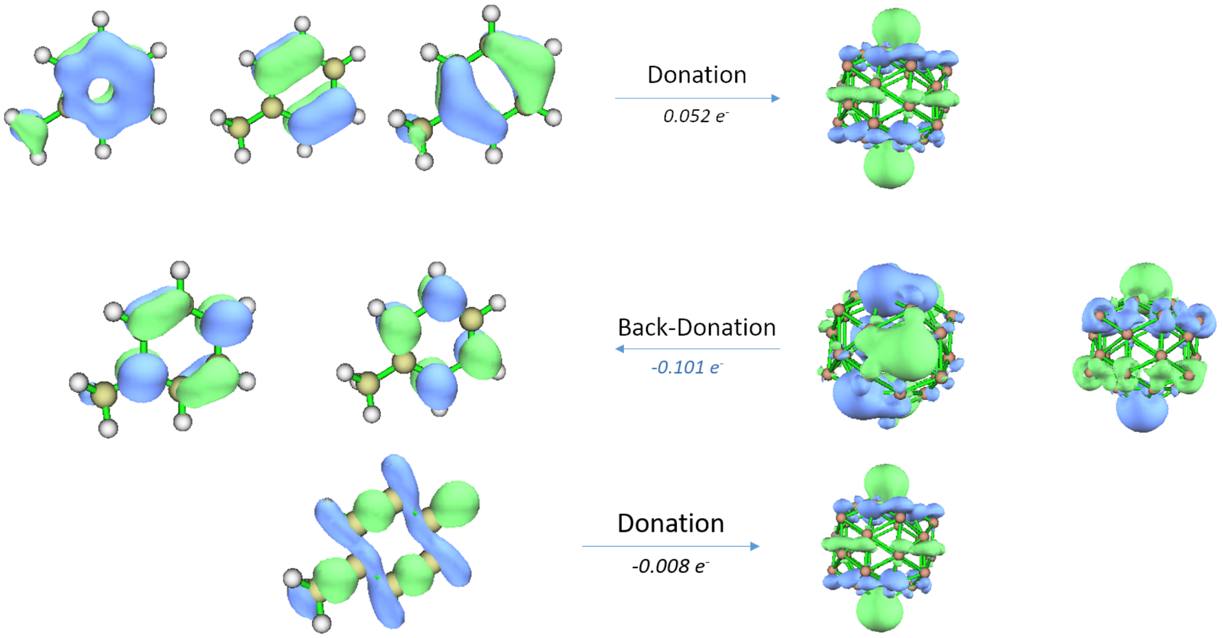

Fig. S12 The interacting molecular orbitals of toluene and GNP adopting either flat (top) or perpendicular (bottom) configuration, as obtained within CDA framework.

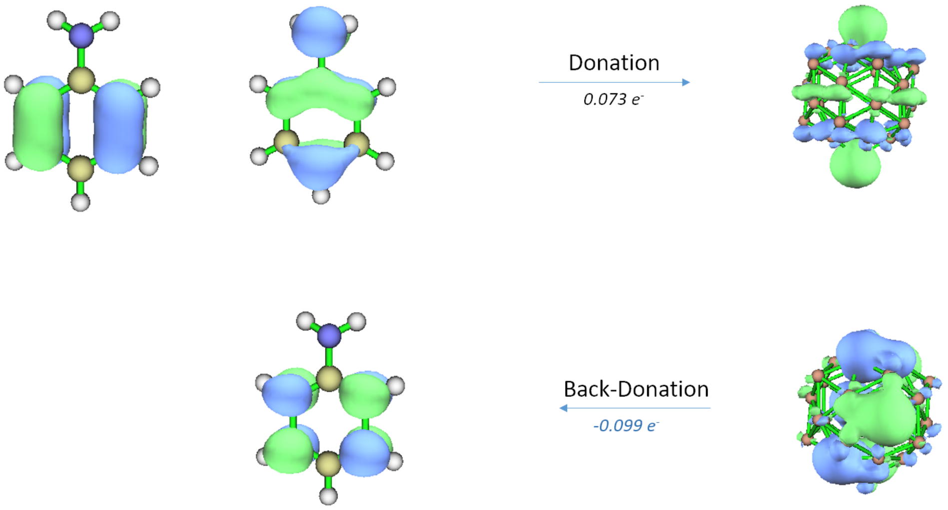

Fig. S13 The interacting molecular orbitals of aniline and GNP, as obtained within CDA framework.

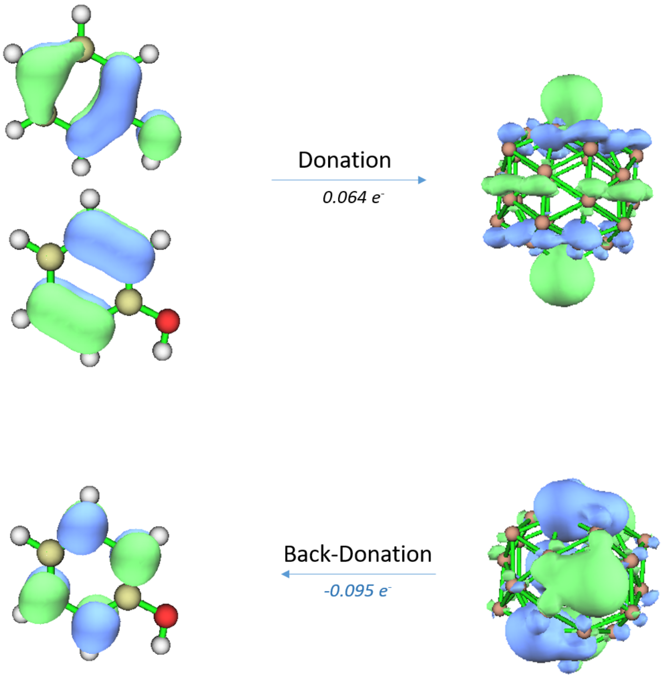

Fig. S14 The interacting molecular orbitals of phenol and GNP, as obtained within CDA framework.

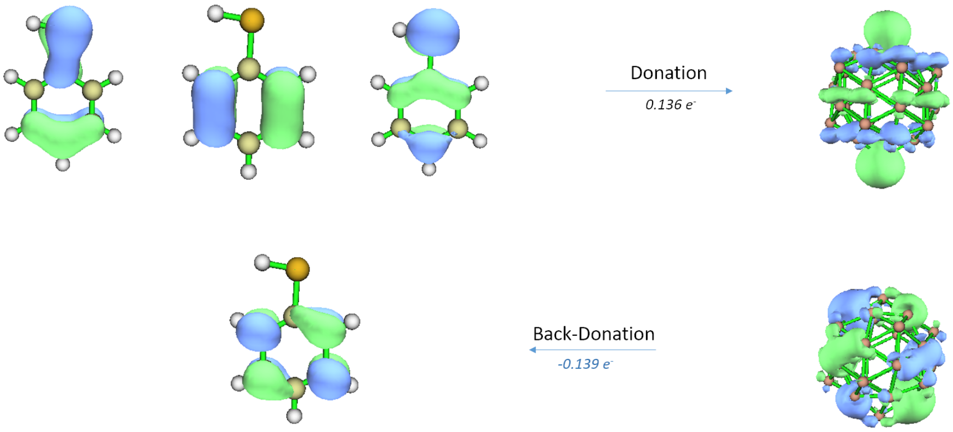

Fig. S15 The interacting molecular orbitals of thiophenol, as obtained within CDA framework

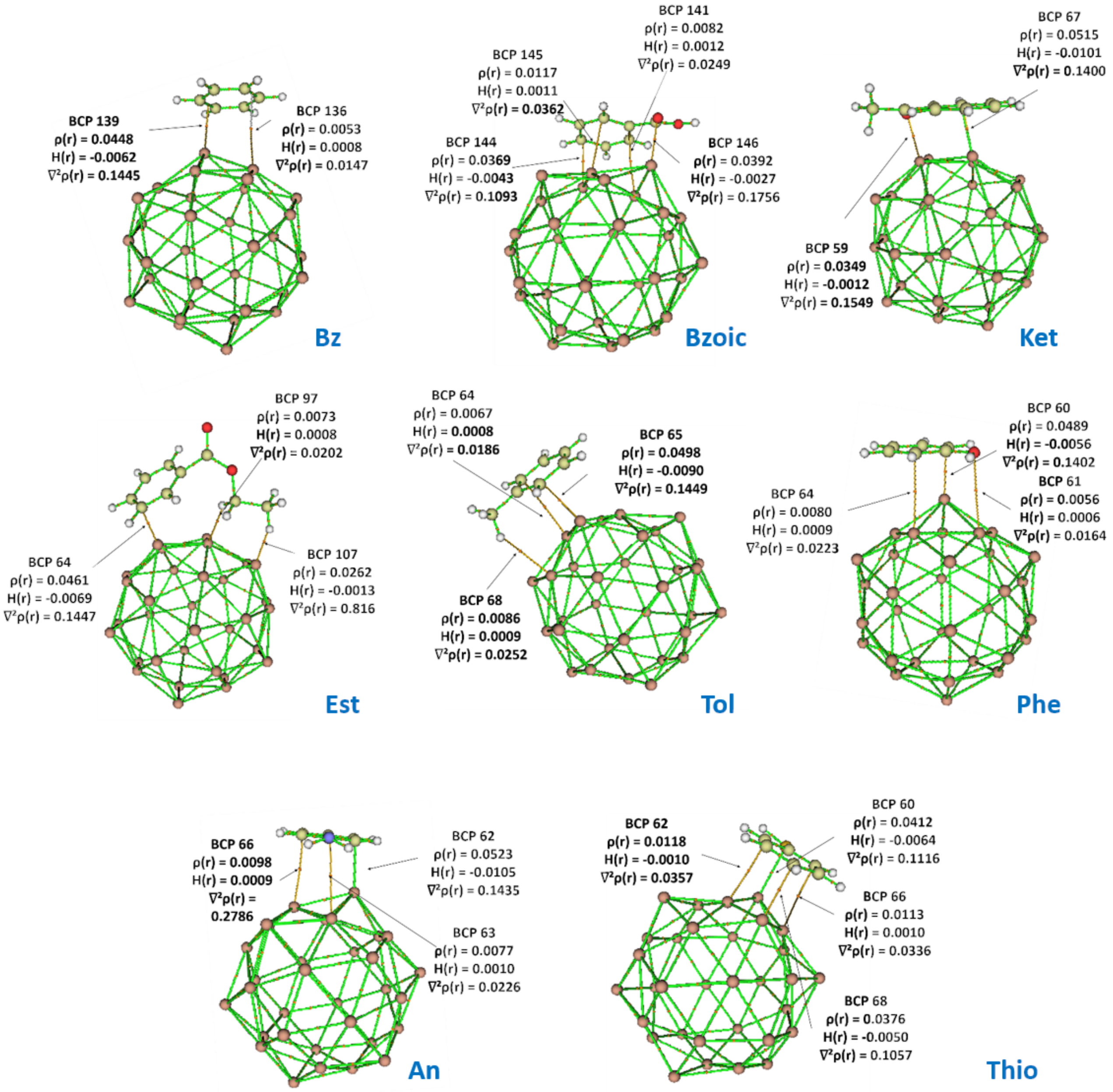

Fig. S16 BCPs calculated within the QTAIM, along with the values of local properties, for flat configurations

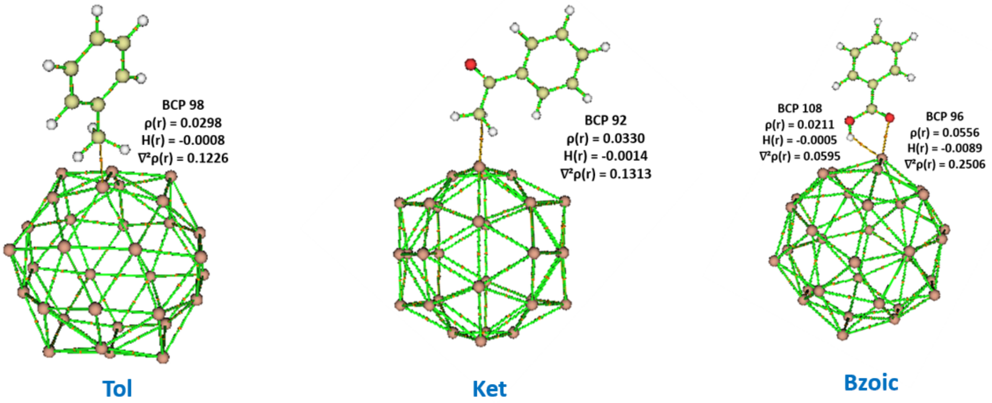

Tol

Ket

Bzoic

Fig. S17 BCPs calculated within the QTAIM, along with the values of local properties, for perpendicular configurations

Table S5 Electron density, Laplacian of electron density and energy density values at respective BCPs.

Compounds	BCP	Electron density (a.u.)	Laplacian (a.u.)	H(rho)	Characterization
Flat					
Benzene	BCP-136	0.0053	0.0147	0.0008	Dispersive
	BCP-139	0.0448	0.1445	-0.0062	Dative
Benzoic Acid	BCP-141	0.0082	0.0249	0.0012	Dispersive
	BCP-144	0.0369	0.1093	-0.0043	Dative
	BCP-145	0.0117	0.0362	0.0011	Dispersive
	BCP-146	0.0392	0.1756	-0.0027	Dative
Acetophenone	BCP-59	0.0349	0.1549	-0.0012	Dative
	BCP-67	0.0515	0.1400	-0.0101	Dative
Ethylbenzoate	BCP-64	0.0461	0.1447	-0.0069	Dative
	BCP-97	0.0073	0.0202	0.0008	Dispersive
	BCP-107	0.0262	0.816	-0.0013	Dative
Toluene	BCP-64	0.0067	0.0186	0.0008	Dispersive
	BCP-65	0.0498	0.1449	-0.0090	Dative
	BCP-68	0.0086	0.0252	0.0009	Dispersive
Phenol	BCP-60	0.0489	0.1402	-0.0056	Dative
	BCP-61	0.0056	0.0164	0.0006	Dispersive
	BCP-64	0.0080	0.0223	0.0009	Dispersive
Aniline	BCP-62	0.0523	0.1435	-0.0105	Dative
	BCP-63	0.0077	0.0226	0.0010	Dispersive
	BCP-66	0.0098	0.2786	0.0009	Dispersive
Thiophenol	BCP-60	0.0412	0.1116	-0.0064	Dative
	BCP-62	0.0118	0.0357	-0.0010	Dative
	BCP-66	0.0113	0.0336	0.0010	Dispersive
	BCP-68	0.0376	0.1057	-0.0050	Dative
Perpendicular					
Toluene	BCP-98	0.0298	0.1226	-0.0008	Dative
Acetophenone	BCP-92	0.0330	0.1313	-0.0014	Dative
Benzoic Acid	BCP-96	0.0556	0.2506	-0.0089	Dative
	BCP-108	0.0211	0.0595	-0.0005	Dative

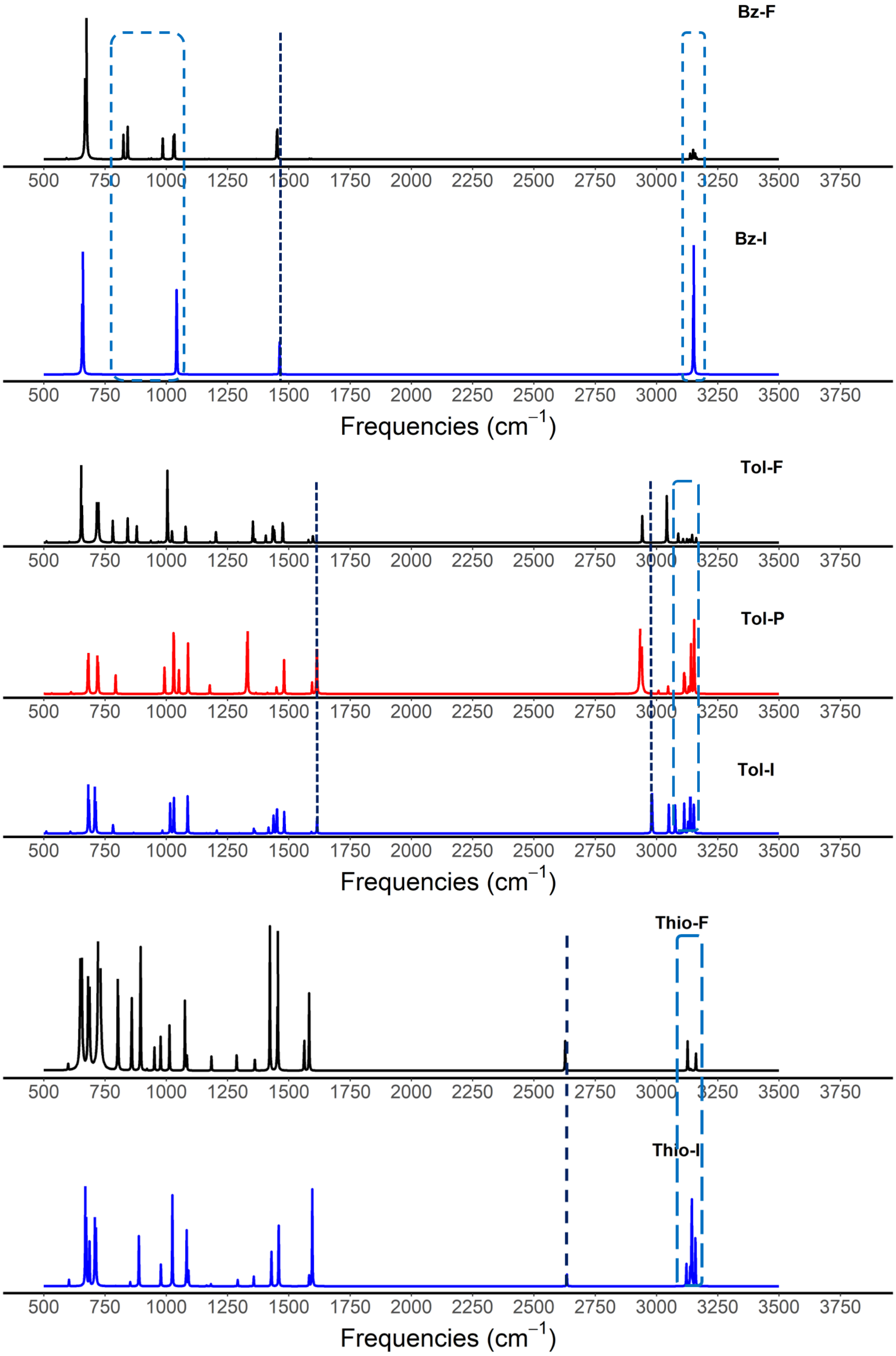

Fig. S18 IR spectra of organic compounds in both isolated (I in blue) and adsorbed state (F/P): benzene, toluene, and thiophenol, respectively. "F" (in black) and "P" (in red) stand for flat and perpendicular configurations, respectively.

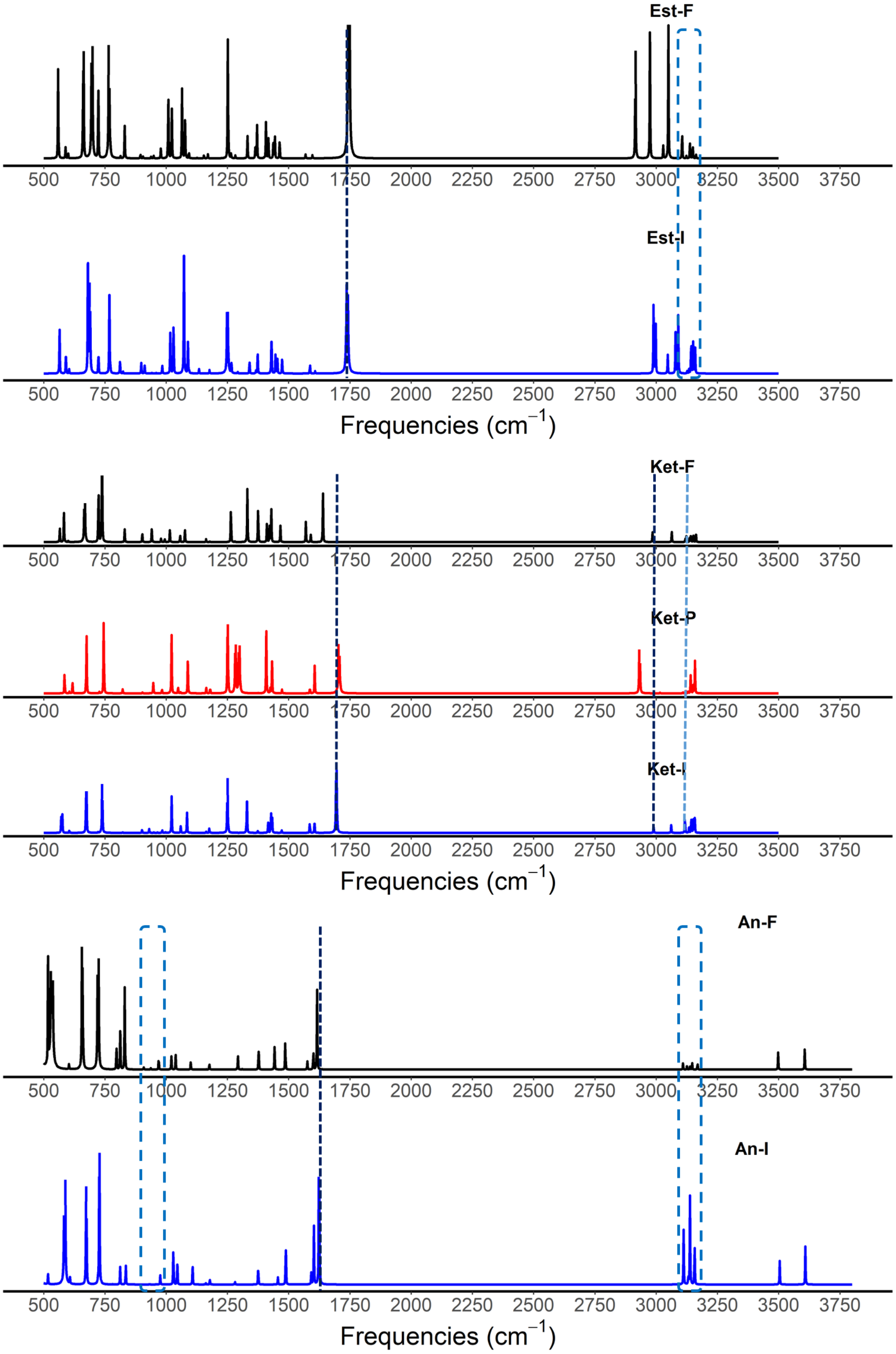

Fig. S19 IR spectra of aromatic compounds in both isolated (I in blue) and adsorbed (F/P) states: ethylbenzoate, acetophenone, and aniline, respectively. "F" (in black) and "P" (in red stand for flat and perpendicular configurations, respectively.

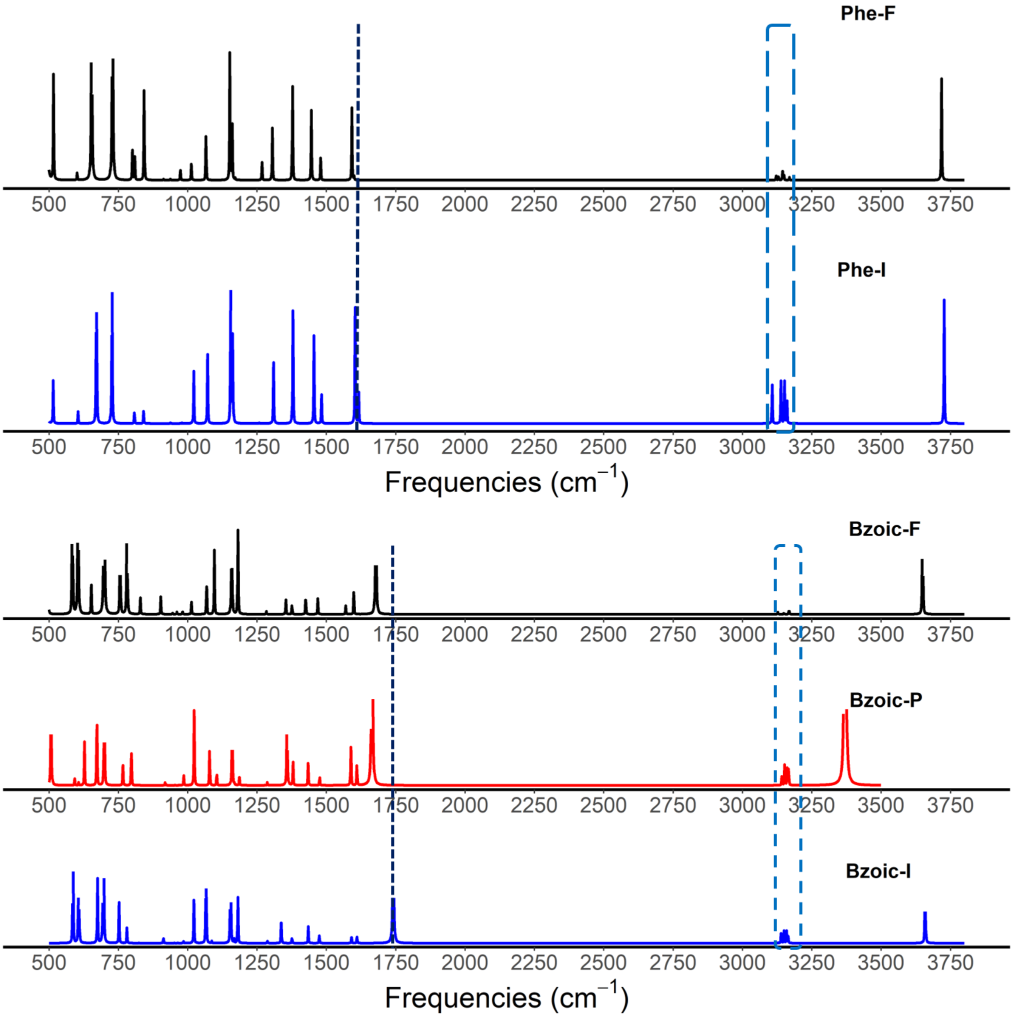

Fig. S20 IR spectra of aromatic compounds in both isolated (I in blue) and adsorbed (F/P) states: phenol and benzoic acid, respectively. "F" (in black) and "P" (in red) stand for flat and perpendicular configurations, respectively.

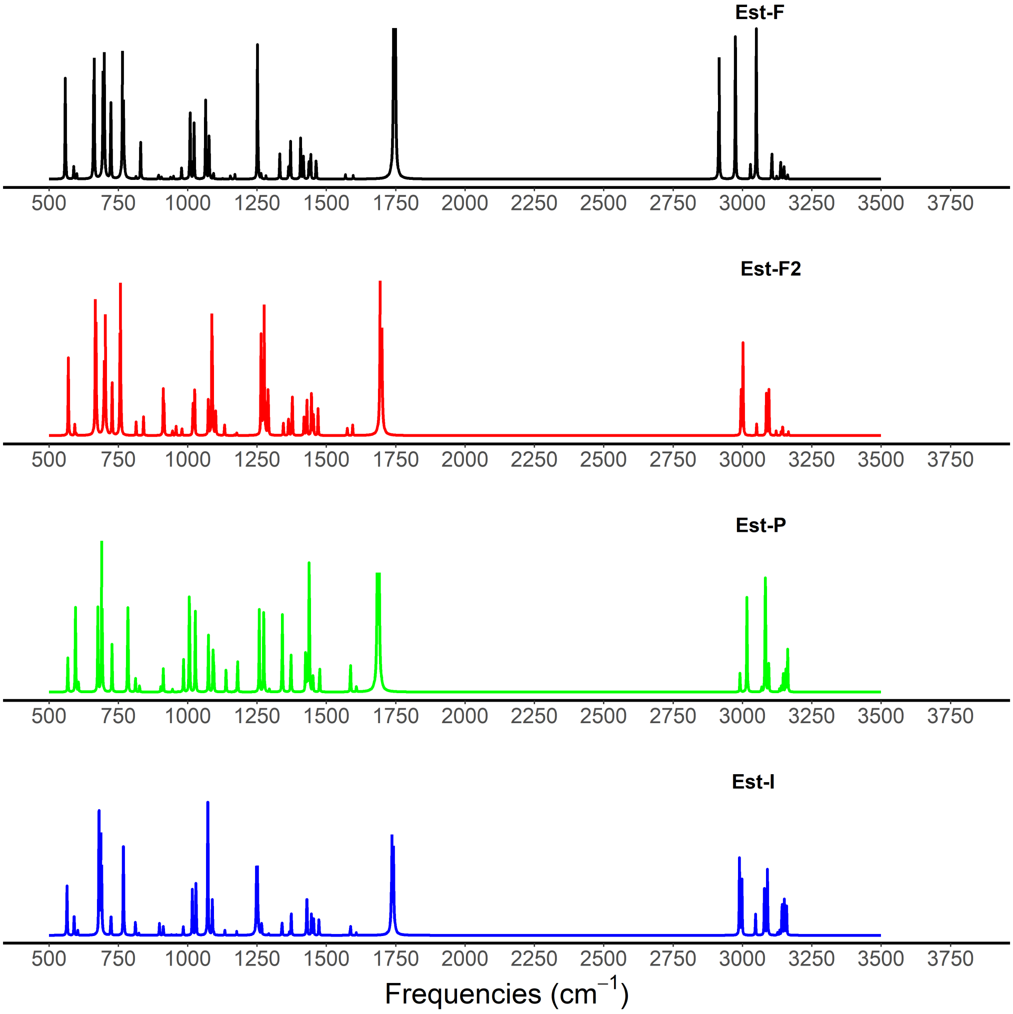

Fig. S21 IR spectra of the different conformations of ethyl benzoate: isolated (I in blue) and adsorbed (F/P) states. "F" and "F2" (in black and red) and "P" (in green) stand for flat and perpendicular configurations, respectively.

Table S6 Integration of NCI basins for the interaction between Au_{32} and aromatic compound.

Compounds	Dative	Dispersive	Repulsive	Volume
Flat				
Benzene	4.05	32.11	12.05	67.30
Benzoic Acid	10.29	33.71	15.17	102.70
Acetophenone	9.79	25.30	9.02	71.67
Ethyl Benzoate	6.95	44.64	8.91	79.62
Toluene	5.38	40.22	9.06	77.78
Phenol	5.44	36.74	9.95	74.98
Aniline	6.10	38.33	11.18	84.16
Thiophenol	20.32	25.49	16.13	113.38
Perpendicular				
Toluene	4.65	0.14	2.73	17.67
Acetophenone	3.94	5.79	3.39	23.37
Benzoic Acid	3.85	5.31	3.62	24.78

Table S7 BLW-EDA decomposition of the interaction energy (kcal/mol) between Au_{32} and aromatic compounds.

Compounds	Frozen Term	Polarization Energy	Charge Transfer Energy	Interaction Energy
Flat				
Benzene	18.44	-7.72	-23.03	-12.31
Benzoic Acid	21.38	-9.35	-25.29	-13.25
Acetophenone	27.24	-10.71	-29.16	-12.63
Ethyl Benzoate	22.77	-8.25	-28.52	-14.00
Toluene	19.03	-8.52	-25.36	-14.85
Phenol	17.74	-8.05	-23.85	-14.16
Aniline	18.91	-9.50	-26.77	-17.36
Thiophenol	22.58	-9.01	-33.23	-19.66
Perpendicular				
Toluene	11.91	-2.82	-7.54	1.54
Acetophenone	13.00	-3.35	-9.84	-0.20
Benzoic Acid	16.53	-10.08	-16.29	-9.84

Table S8 SAPT decomposition of the interaction energy (kcal/mol) between Au_{32} and aromatic compounds.

Compounds	Electrostatic Energy	Exchange Energy	Dispersion Energy	Induction Energy	SAPT
Flat					
Benzene	-35.80	60.80	-35.21	-18.69	-28.90
Benzoic Acid	-50.90	85.74	-49.78	-20.58	-35.52
Acetophenone	-45.32	81.18	-42.16	-24.72	-31.01
Ethyl Benzoate	-38.28	71.37	-42.08	-21.35	-30.33
Toluene	-39.69	67.45	-40.36	-20.39	-32.99
Phenol	-38.60	65.03	-38.30	-19.30	-31.16
Aniline	-44.08	71.96	-42.11	-21.57	-35.79
Thiophenol	-57.16	92.04	-53.39	-23.34	-41.85
Perpendicular					
Toluene	-11.76	26.74	-13.33	-5.52	-3.87
Acetophenone	-12.92	30.14	-15.62	-6.62	-5.02
Benzoic Acid	-29.59	47.36	-17.69	-16.02	-15.94

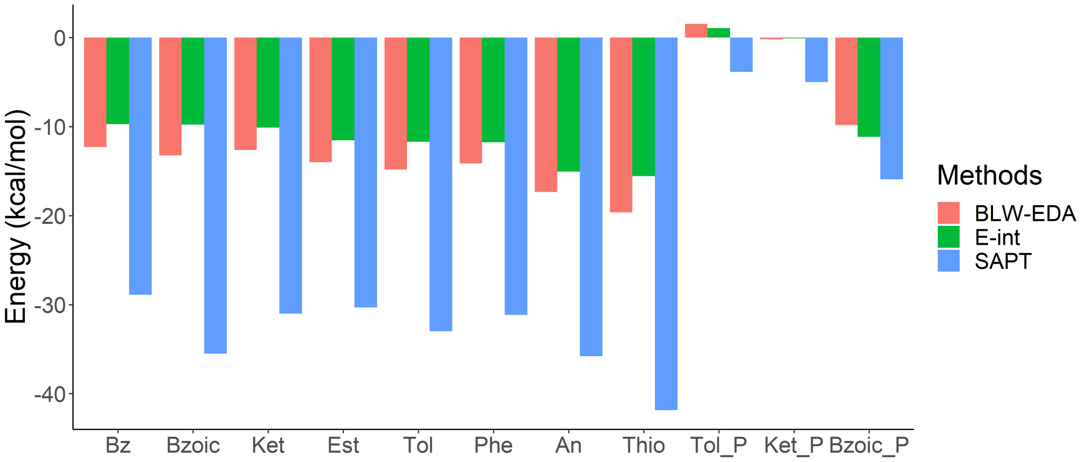

Fig. S22 Comparison between total BLW-EDA, interaction energy, and total SAPT.

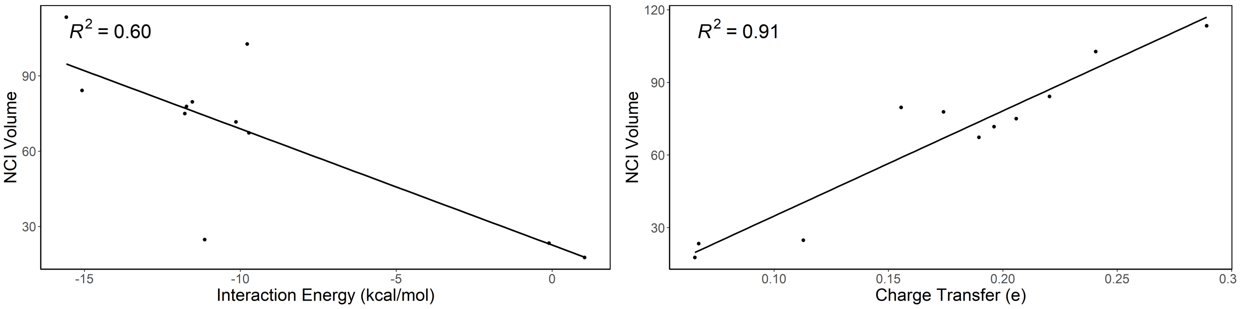

Fig. S23 Correlation between the volume of NCI basins with interaction energy (left) and ADCH charge transfer (right)

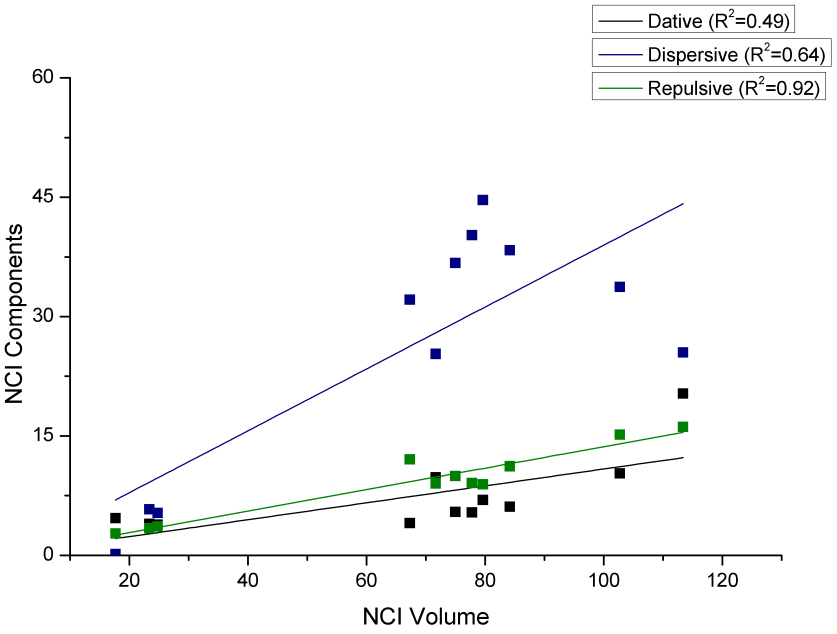

Fig. S24 Correlation of the three NCI basin components with the NCI basin volumes.

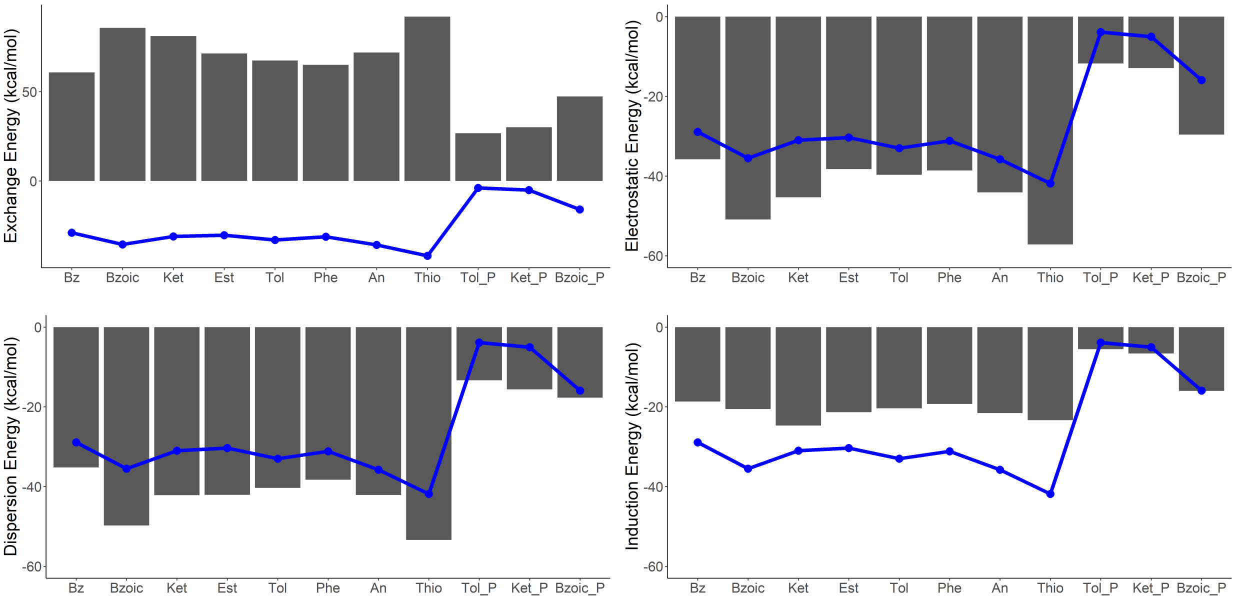

Fig. S25 SAPT decomposition of the interaction energy between Au$_{32}$ and aromatic compounds. The blue line represents the total SAPT energy. Correlation between electrostatic component and the total SAPT energy. "P" stands for perpendicular configuration.

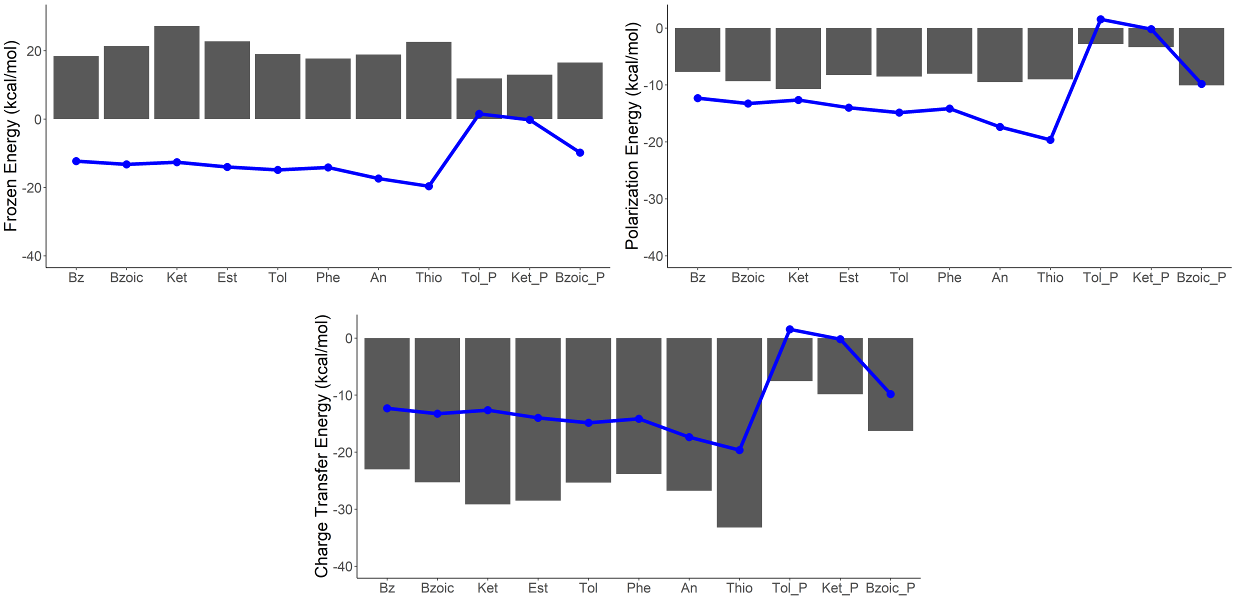

Fig. S26 BLW-EDA decomposition of the interaction energy between Au$_{32}$ and aromatic compounds. The blue line represents the total BLW-EDA energy. "P" stands for perpendicular configuration.

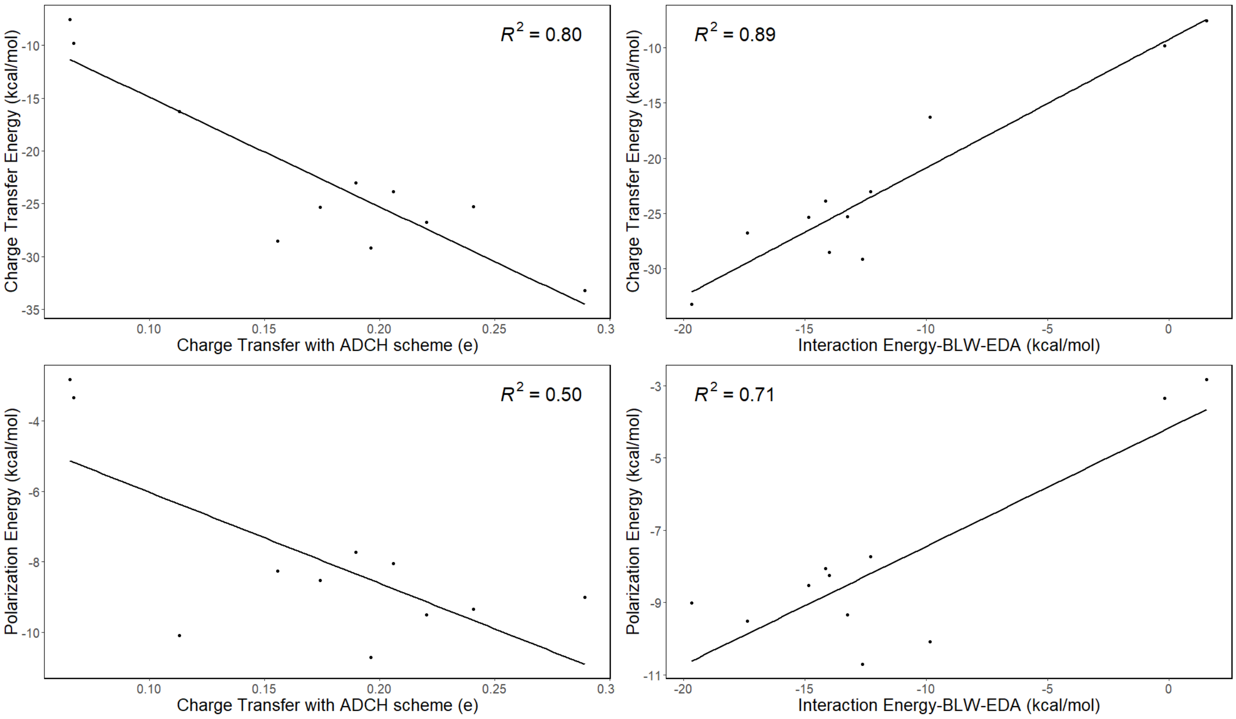

Fig. S27 Correlation between BLW-EDA charge transfer (top) and polarization (bottom) energy components with interaction energy and ADCH charge transfer, respectively.

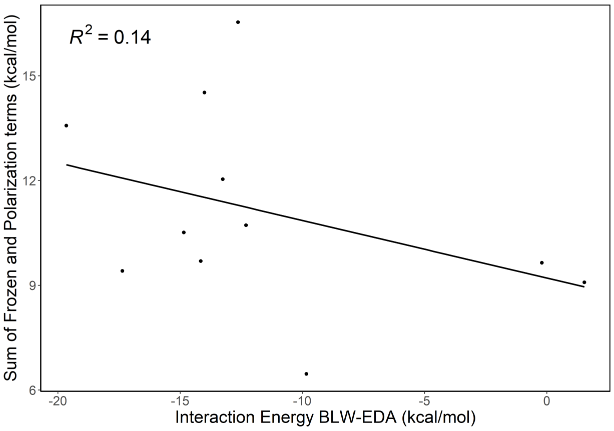

Fig. S28 Correlation between the sum of frozen and polarization terms and interaction energy (slope of -0.165).

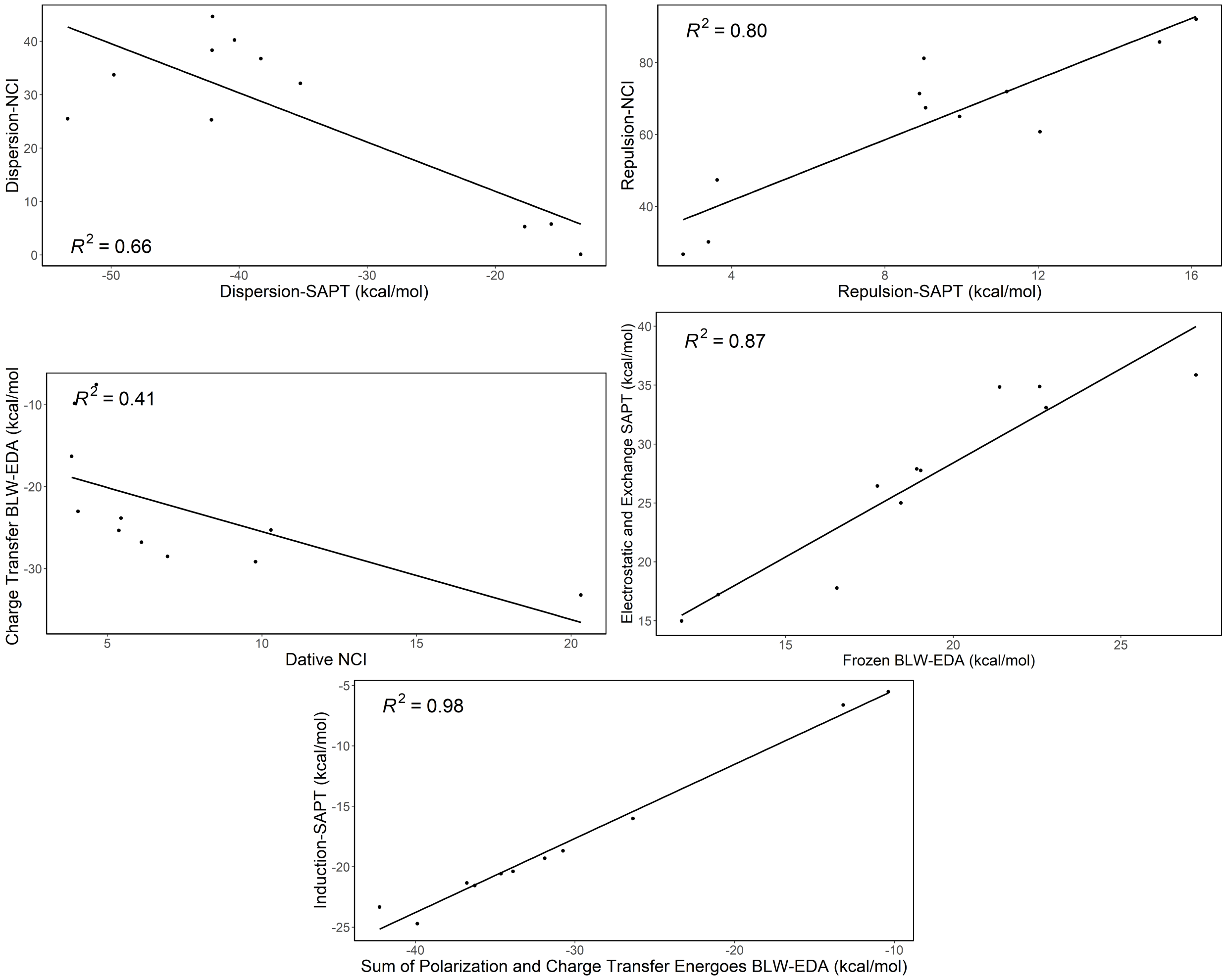

Fig. S29 Correlation across the different approaches: (top) correlation between the terms from NCI and SAPT, for dispersion with slope of -0.92 (left) and repulsion, with slope of 4.22 (right); (middle-left) correlation between charge transfer obtained with BLW-EDA and the dative term from NCI with slope of -1.07, (middle-right) correlation between the sum of electrostatic and exchange terms in SAPT and the frozen term in BLW-EDA with slope of 1.6; (bottom) correlation between the SAPT induction energy term and the sum of BLW-EDA polarization and charge transfer with slope of 0.613.

A.2.3 Vibrational Analysis of Small Organic Molecules Interacting At the Surface of Gold Nanoparticles

Table A.8: SAPT applied to Au_{32} complexes; all energies are reported in kcal/mol

GNP	Complexes	Electrostatic	Exchange	Dispersion	Induction	Total SAPT
Au_{32}	Methane	-11.7	24.9	-11.0	-5.3	-3.2
	Formic Acid	-17.0	35.9	-14.3	-11.4	-6.8
	Methanol	-22.4	31.2	-11.3	-9.0	-11.5
	Hydrogen Sulfide	-25.5	35.8	-14.4	-12.6	-16.7
	Ammonia	-33.9	41.7	-12.5	-15.5	-20.2

Table A.9: The BLW-EDA applied to all complexes; all energies are reported in kcal/mol

GNP	Complexes	Frozen	Polarization	CT	Total BLW-EDA
Au_{32}	Methane	10.9	-2.6	-6.9	1.4
	Formic Acid	13.9	-6.5	-11.8	-4.4
	Methanol	7.4	-5.8	-8.4	-6.9
	Hydrogen Sulfide	10.2	-5.1	-16.9	-11.8
	Ammonia	11.1	-10.3	-15.0	-14.2
$\mathrm{Au}_{55} - c$	Methane	9.3	-2.3	-6.4	0.6
	Formic Acid	13.6	-9.0	-13.9	-9.2
	Methanol	8.5	-6.8	-8.9	-7.2
	Hydrogen Sulfide	11.3	-5.7	-18.0	-12.43
	Ammonia	10.9	-10.5	-15.3	-14.9
$\mathrm{Au}_{55} - e$	Methane	5.2	-1.3	-4.0	-0.1
	Formic Acid	11.9	-7.8	-12.4	-8.4
	Methanol	9.7	-5.4	-10.4	-6.1
	Hydrogen Sulfide	9.6	-4.4	-15.0	-9.8
	Ammonia	13.6	-10.3	-14.8	-11.6